AD:

**Final Report
for the period
September 1980 to
August 1983**

Solid Propellant Nonlinear Constitutive Theory Extension

AD A139957

January 1984

Authors:
E. C. Francis
C. H. Carlton
R. Thompson
W. M. Fisher
W. L. Hufferd

United Technologies Corporation
Chemical Systems Division
P. O. Box 50015
San Jose, California 95150-0015

UTC/CSD 2742
F04611-80-C-0052

Approved for Public Release

APR 1 1 1984

A

prepared for the: **Air Force
Rocket Propulsion
Laboratory**

Air Force Space Technology Center
Space Division, Air Force Systems Command
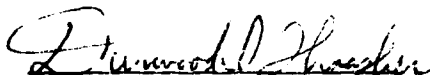Edwards Air Force Base,
California 93523

DTIC FILE COPY

7   030

NOTICES

When U.S. Government drawings, specifications, or other data are used for any purpose other than a definitely related Government procurement operation, the fact that the Government may have formulated, furnished, or in any way supplied the said drawings, specifications, or other data, is not to be regarded by implication or otherwise, or in any manner licensing the holder or any other person or corporation, or conveying any rights or permission to manufacture, use, or sell any patented invention that may be related thereto.
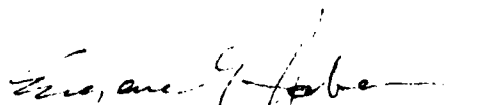
FOREWORD

This report was submitted by United Technologies Corporation/Chemical Systems Division, 1050 E. Arques Avenue, Sunnyvale CA 94086 under Contract F04611-30-C-0052, Job Order No. 2307MIEB with the Air Force Rocket Propulsion Laboratory, Edwards AFB CA 93523. This Final Technical Report is approved for release and publication in accordance with the distribution statement on the cover and in the DD Form 1473.

DURWOOD I. THRASHER
Project Manager

DAVID P. PARKER, 1Lt, USAF
Chief, Structural Integrity Section

FOR THE DIRECTOR

EUGENE G. HABERMAN
Director, Solid Rocket Division

REPORT DOCUMENTATION PAGE		READ INSTRUCTIONS BEFORE COMPLETING FORM
1. REPORT NUMBER AFRPL-TR-83-071	2. GOVT ACCESSION NO. AD-A139 957	3. RECIPIENT'S CATALOG NUMBER
4. TITLE (and Subtitle) Solid Propellant Nonlinear Constitutive Theory Extension: Final Report		5. TYPE OF REPORT & PERIOD COVERED Technical Report, Phases I II, III, and IV; 9/80 - 8/83
		6. PERFORMING ORG. REPORT NUMBER CSD 2742
7. AUTHOR(s) E.C. Francis, D.G. Lemini, C. Carlton, W.L. Hufferd, M. Gurtin, R.A. Schapery, M. Quinlan		8. CONTRACT OR GRANT NUMBER(s) F04611-80-C-0052
9. PERFORMING ORGANIZATION NAME AND ADDRESS Chemical Systems Division 600 Metcalf Rd. San Jose, CA 95138-9602		10. PROGRAM ELEMENT, PROJECT, TASK AREA & WORK UNIT NUMBERS JON: 2307M1EB
11. CONTROLLING OFFICE NAME AND ADDRESS Air Force Rocket Propulsion Laboratory Edwards Air Force Base, CA 93523		12. REPORT DATE JANUARY 1984
		13. NUMBER OF PAGES 332
14. MONITORING AGENCY NAME & ADDRESS(if different from Controlling Office)		15. SECURITY CLASS. (of this report) Unclassified
		15a. DECLASSIFICATION/DOWNGRADING SCHEDULE

16. DISTRIBUTION STATEMENT (of this Report)

APPROVED FOR PUBLIC RELEASE; DISTRIBUTION UNLIMITED
The AFRPL Technical Services Office has reviewed this report, and it is releasable to the National Technical Information Service, where it will be available to the general public, including foreign nationals.

17. DISTRIBUTION STATEMENT (of the abstract entered in Block 20, if different from Report)

18. SUPPLEMENTARY NOTES

19. KEY WORDS (Continue on reverse side if necessary and identify by block number)

Strain	two-dimensional	straining cooling	failure
Stress	three-dimensional	viscoelastic	time-dependent
Modulus	isothermal	nonlinear	elastic
Uniaxial	nonisothermal	linear	damage
Biaxial	constitutive	fracture	healing

20. ABSTRACT (Continue on reverse side if necessary and identify by block number)

This report details the technical effort put forth by CSD and its subcontractors during the four phases of this program for propellant nonlinear constitutive theory extension. This includes the Phase I preliminary study in which the Quinlan theory was critiqued, alternate approaches were studied and detailed research planning accomplished. Also included are the detailed experimental evaluations of propellant during Phases II and III, the uniaxial/isothermal investigation and the two-dimensional variable temperature investigation. The report also covers Phase IV, the validation of the accuracy of the

DD FORM 1473 EDITION OF 1 NOV 65 IS OBSOLETE
1 JAN 73

(cont.)

constitutive theory in a three-dimensional state of stress and strain. Detailed subcontractor theoretical development and predictions are given.

In performing the work required for the program, Chemical Systems Division (CSD) employed under subcontract the services of five scientists of national reputatation: Drs. M. Quinlan, M.E. Gurtin, W.L. Hufferd, R. Wool, and R.A. Schapery. The program effort combined the comprehensive experience and specialized test capabilities of CSD in solid propellant mechanical properties with the theoretical expertise of these scientists. In addition, Dr. J. E. Fitzgerald was retained as a consultant to participate in the periodic technical reviews of the program status.

CONTENTS

CONTENTS (Continued)

ILLUSTRATIONS

ILLUSTRATIONS (Continued)

ILLUSTRATIONS (Continued)

ILLUSTPATIONS (Continued)

7

ILLUSTRATIONS (Continued)

ILLUSTRATIONS (Continued)

ILLUSTRATIONS (Continued)

ILLUSTRATIONS (Continued)

TABLES

14

PREFACE

This report details the technical effort put forth by CSD and its subcontractors during the four phases of this program for propellant nonlinear constitutive theory extension. This includes the Phase I preliminary study in which the Quinlan theory was critiqued, alternate approaches were studied and detailed research planning accomplished. Also included are the detailed experimental evaluations of propellant during Phases II and III, the uniaxial/isothermal investigation and the two-dimensional variable temperature investigation. Detailed subcontractor theoretical development and predictions are presented along with the three-dimensional investigations.

This final technical report on Contract No. F04611-80-C-0052 consists of a summary of the phase II and III laboratory propellant evaluation for UTP-3001 and UTP-19,360B propellants. Phase IV was a validation of the accuracy of the constitutive theory in a three-dimensional state of stress and strain. The detailed experimental results were distributed in Data Packages A through G to all project personnel. Additional details are given in section 1.0.

In performing the work required for the program, Chemical Systems Division (CSD) employed under subcontract the services of five scientists of national reputation: Drs. M. Quinlan, M. E. Gurtin, W. L. Hufferd, R. Wool, and R. A. Schapery. The program effort combined the comprehensive experience and specialized test capabilities of CSD in solid propellant mechanical properties with the theoretical expertise of these scientists. In addition, Dr. J. E. Fitzgerald was retained as a consultant to participate in the periodic technical reviews of the program status.

16

1.0 PROGRAM OBJECTIVES AND OVERVIEW

The objective of the Propellant Nonlinear Constitutive Theory (NLCT)
Program was to develop and demonstrate a nonlinear thermomechanical constitutive
law for solid rocket propellants. The goal was to achieve errors of less than
10% in stress predictions for undamaged propellant and less than 15% for
previously damaged propellant. The program was conducted in four phases:

- Phase I - Preliminary Study
- Phase II - Uniaxial Isothermal Investigation
- Phase III - Two-Dimensional and Variable Temperature Investigation
- Phase IV - Three-Dimensional Investigation.

Each phase had a number of tasks and subtasks. Overall program logic is shown
in Figure 1.

A number of subcontractors were employed to evaluate the several NLCT
approaches considered, and Dr. J. E. Fitzgerald, Director of the School of Civil
Engineering, Georgia Institute of Technology, was retained as a technical
advisor and consultant to the NLCT program.

The objectives of the four phases are summarized in the following
paragraphs:

1.1 PHASE I - PRELIMINARY STUDY

The objective of phase I was to make detailed research plans for evaluating
and modifying candidate nonlinear constitutive laws. Quinlan's nonlinear
constitutive theory[11] was critically reviewed and modifications to the
differential equation for the bonding parameter were proposed. In addition,
five other candidate constitutive approaches were evaluated on a preliminary
basis by subcontractors and CSD personnel:

- Farris Theory - W. Briggs
- Modified Swanson Theory - D. Gutierrez-Lemini
- Russian Theories - W. L. Hufferd

17

- Time-Dependent Bonding - R. A. Schapery

- Softening Approach - M. E. Gurtin.

Dr. S. M. Breitling and Dr. R. P. Wool also provided information of the probability of successfully incorporating a physically based molecular model into any of the NLCT's considered for evaluation.

1.2 PHASE II - UNIAXIAL/ISOTHERMAL INVESTIGATION

The objectives of phase II were to continue theoretical development work on the candidate nonlinear constitutive theories and to evaluate their predictive capabilities for the uniaxial isothermal response to two propellants: an HTPB (UTP-19,360B) and a PBAN (UTP-3001). An extensive test program was conducted on these two propellants. Following the comparative evaluation of the constitutive theories, successful candidates were recommended for continuation into phase III.

1.3 PHASE III - TWO-DIMENSIONAL AND VARIABLE TEMPERATURE INVESTIGATION

The objective of phase III was to extend the theoretical development of the candidate constitutive theories to two-dimensional and variable temperature histories. Stress time predictions were compared with laboratory tests of the two propellants and a decision was reached as to which theories would be inherent within phase IV.

1.4 PHASE IV - THREE-DIMENSIONAL INVESTIGATION

The objective of the final phase was to conduct a critical validation experiment and assess the accuracy of the constitutive theory developed under isothermal and transient temperature conditions for a three-dimensional state of stress and strain.
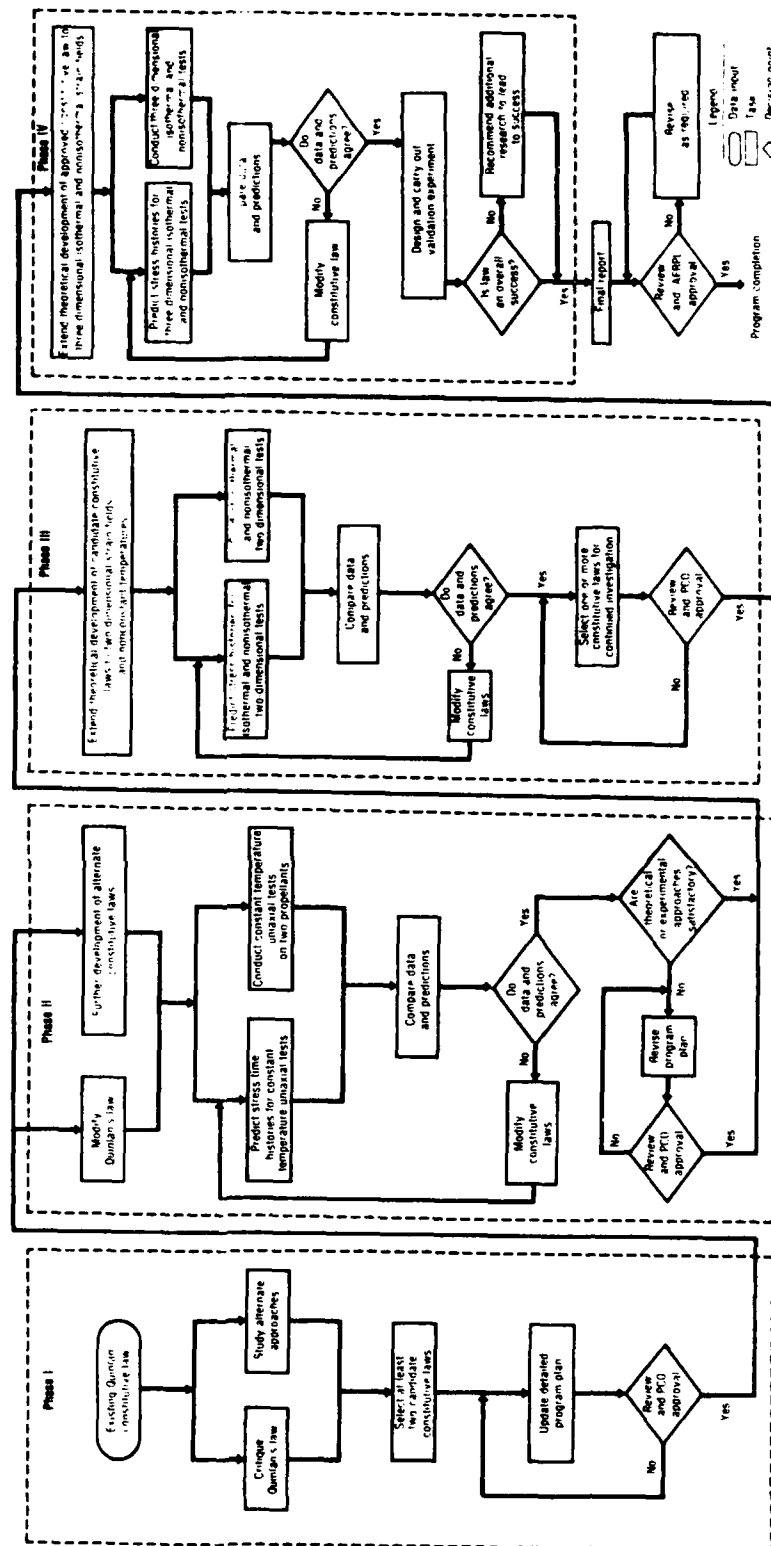
Figure 1. Program Logic

29157

19

2.0 SUMMARY, CONCLUSIONS, AND RECOMMENDATIONS

2.1 SUMMARY AND CONCLUSIONS

The objective of the Propellant Nonlinear Constitutive Theory Extension Program was to develop and demonstrate an accurate, usable, three-dimensional, **thermomechanical** constitutive theory for solid rocket propellants. The target criteria for selection of a candidate constitutive relation were two-fold:

- Less than 10% error in stress predictions for undamaged propellant
- Less than 15% error in stress predictions for previously damaged propellant.

The program was conducted in four phases.

The basis for the program was the limited success achieved by Quinlan in AFRPL-TR-78-37[4] in modeling some of the trends typically observed of solid propellants using a constitutive theory incorporating damage. Accordingly, a significant effort was spent by Dr. M. Quinlan at Cork University, Ireland, and by CSD in an attempt to extend and improve the predictive capabilities of Quinlan's fundamental model. Though some advances were made at the theoretical level to increase our knowledge of the model, the model did not achieve the desired success and was discontinued before the transition to combined straining-cooling and three-dimensional stress states.

Similarly, Gurtin's maximum strain/stress softening approach met with only marginally greater success. The model evolution was capable of describing some trends of solid propellant behavior, but numerical difficulties were encountered in the curve fitting procedures. This method was also discontinued after working with complex uniaxial test histories.

The remaining approaches (namely those of Schapery, Hufferd, and CSD's modification of Swanson's constitutive theory) all achieved greater success. Due to the extensive effort (in time and money) expended during phases I and II with five analytical models, only CSD's modification of Swanson's theory was carried through to actual motor stress predictions.

21

Schapery's approach is based on a micro-cracking model for damage. The theory predicted stresses accurately for uniaxial and biaxial isothermal tests. The approach was not continued to transient thermal nor motor stress predictions due to limitations in time and funding.

Hufferd's modification of Il'yushin's approach to thermovisco-plasticity provided good predictive capabilities for uniaxial isothermal test histories and was comparable to the modified Swanson theory for isothermal biaxial and transient cooling/straining tests. The approach was not continued to motor stress predictions due to a lack of funds.

The Swanson approach modified by CSD achieved the greatest success of all the nonlinear analytical methods. This approach established a major milestone in the solid propellant industry. Using the characterization data from three simple laboratory test modes, a wide variety of very complex uniaxial test histories were predicted to the desired accuracy levels. These successful predictions also included stress and time response ranges outside of the characterization ranges. This was the first known accurate solid propellant stress prediction which extended beyond the nonlinear characterized data base. This analytical model also accurately predicted biaxial and shear test histories which were not included in the characterization.

Because of budget and schedule limitations, this method was not completely adapted for thermomechanical coupling and complete three-dimensional analysis.

2.2 RECOMMENDATIONS

While predictive success was achieved with the modified Swanson theory predicting complex uniaxial, biaxial and shear test histories, there was only preliminary experience with full three-dimensional stress axiality with combined thermal mechanical loads. It is recommended that additional work with the modified Swanson theory be conducted with emphasis on combined thermal and mechanical loads and realistic three-dimensional loading axialities.

All four nonlinear analysis methods could be further developed and could provide alternative methods for analysis of solid propellant structural

response. The modified Swanson method is potentially compatible with inclusion in a finite element analysis, but further work mentioned above is required before this transition can be successful.

23

24

3.0 EXPERIMENTAL PROGRAM

Laboratory testing was divided into categories of uniaxial/isothermal, two-dimensional, and variable temperature and three-dimensional investigations.

The two propellants selected for the program were (1) a PBAN used in the first stage of the Titan missile system (UTP-3001-750/7768) and (2) a HTPB propellant developed for the IUS motor (UTP-19,360B-400/1777). The first numbers are the propellant designation; the next, the mixer size; and the last, a batch number.

In each of the laboratory test groups a specific test of each type has been selected to show the test details.

3.1 UNIAXIAL/ISOTHERMAL INVESTIGATION

Testing uniaxial specimens of UTP-3001 and UTP-19,360B propellants in phase II of the contract was done for the non-damaged material (as indicated in Figure 2) and for damaged material (per Figures 3 and 4). Most of the tests were run with 1/2- x 1/2- x 6-in. bars with redwood end tabs. The exceptions were the stress endurance (test 2) and constant rate (comparison to test 4) data which were obtained with JANNAF Class B specimens.[1] Details of most of the individual test types are discussed in subsections below.

Details of the other tests (which were considered in earlier work but not utilized in this report) may be obtained from AFRPL-TR-83-034[32]. All of the tests are shown in Figures 2 to 4 with sketches of the strain-time histories.

The attachment linkages on both testers were such that the specimens could not be put into compression when the crosshead was returned to an equivalent zero strain position. The strain measurement was done with a linear potentiometer attached to the crosshead; consequently, the data had to be modified to reflect the propellant strain relaxation behavior after the stress had returned to zero (free hanging specimen).

25
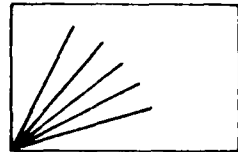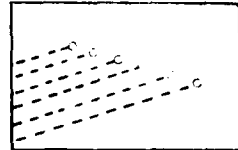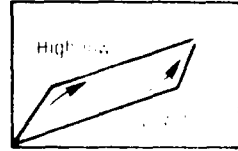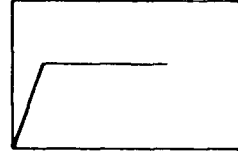
Test No.	Test Description	Temperature, °F	Pressure, psig	Rate, in./min	Strain, %	Experimental Effects	Strain History
1	Constant rate	70 120 40	0 0 0	0.001 • 10	To failure	Time and rate temperature sample type	
2	Stress endurance	70 120 40	0 0	— —	To failure	Time and temperature	
3	Multirate	70	0	0.1-1 1.0 – 0.1	12 12	Rate change	High
4	Stress relaxation	70 120 40 23	0 0 0 0	1 1 1 1	3 3 3 3	Temperature	

Note. Nominal tests were run with three samples per set

Legend
Strain

Figure 2. Uniaxial/Isothermal Non-damaged Tests

24406R1

The uniaxial bars were machined from redwood boxes of propellant. The redwood was sealed then lined in the same manner as a rocket motor. After a partial cure of the liner, propellant was cast into the box and the system cured to provide a good bond to the redwood end tabs. The redwood box assembly and finished specimen are shown in Figure 5. After the specimen is mill finished, a 1/8-in. hole is drilled on the centerline of each end tab for attachment to the testing machine.

All tests were conducted on a Chemical Systems Division (CSD) manufactured six-channel tester and a modified Instron. A Hewlett-Packard computer was used to collect digitized data from the tests (see Appendix A details on the automated data reduction system).

Figure 3. Uniaxial/Isothermal Damaged Tests

Test No.	Test Description	Damage Cycle Temperature, °F	Pressure, psi	Rate, in./min	Strain, %	Remarks	Test Temperature, °F	Pressure, psi	Rate, in./min	Strain, %	Strain Cycle
5	Multiple loading with rest periods, step cycle	70				30 min hold between cycles	70		10	5 to 12	
6	Creep	70 120 -40	0	1	1/4 1/2 ~maximum	3 hr creep periods, first step only for 120 and -40°F	70	0	1	1/4, 1/2 ~maximum	
7	Cyclic loading	70	0	1	4 8 12	20 cycles return to zero stress and monitor E recovery	70	0	1	4, 8, 12	
8	24-hr relaxation	70	0	20	4 8 12	Monitor the unload	70	0	1	4, 8, 12	
9	Predamage relaxation (1 hr)	70	0	01	6 12	30-min hold between loading monitor unload	70	0	20 1	3, 4 8	
10	Complex multiple load	70	0	0.1 1 5	12 8 4	High strain followed by low strain return to zero stress and monitor strain	70	0	0.1 1 5	12, 8 4	

Note: Nominal tests were run with three samples per set

24407R1

27

Test	Test Description	Damage Cycle	Test	Strain Cycle
11	Quinlan complex history	Single samples clamped in rigid Instron jaws were run on UTP-3001 and UTP-19,360B. In returning to zero strain the samples were put into compression.		
12	Similitude	Similitude tests were run with 6-in. bar samples of UTP-3001 and UTP-19,360B.		
13	Three step relaxation	Short and long time tests were run with 6-in. bar samples of UTP-3001 and UTP-19,360B.		

Note: Nominal tests were run with three samples per set

Legend:
ϵ = strain
t = time

Figure 4. Uniaxial Damaged Propellant Tests

28386
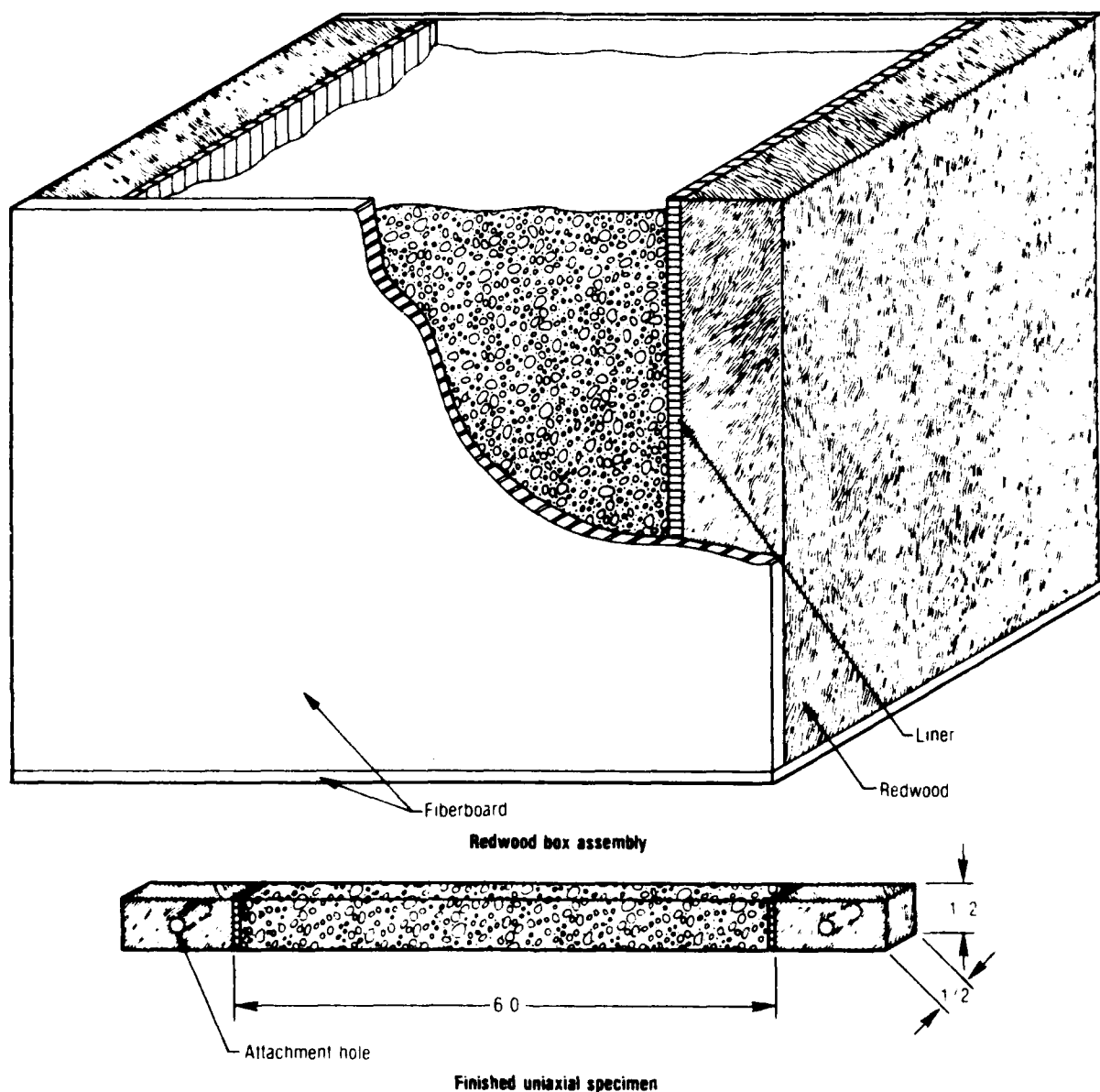
Figure 5. Uniaxial Bar Specimen

28804

Strain relaxation was measured on samples in some of the tests during final unload cycle. Cathetometer measurements were made periodically and strain versus time data were plotted. These data were used to estimate the relaxation behavior on cyclic tests where there was insufficient time for measurements.

A data modification was made to estimate the peak or minimum stress and strain points which were not recorded by the digitized data acquisition system.

The sampling rate limited the crosshead rate that could be used and still obtain enough points to adequately define a ramp. The available computer memory also influenced the sampling rate in some of the longer tests.

3.1.1 Constant Rate Test No. 1

Uniaxial constant rate to failure tests were conducted on 6-in. bars of UTP-3001 and UTP-19,360B. The 70 F tests were at crosshead rates of 10, 1, 0.1, 0.01 and 0.001 in./min, while the 40 and 120 F tests were at 10, 1, and 0.1 in./min.

Typical stress-strain curves for the 3 rates at 120 F are shown in Figure 6 for UTP-3001. To ensure an equivalent time data base, three samples of each propellant were tested at the same time in the six channel testers. The exception was the 10 in./min tests which were tested one propellant at a time due to data sampling rate limitations.

The 6-in. bar specimens always ＾ led at strain levels below the level that would be obtained from JANNAF specimens and always at the propellant to wooden tab interface. Since the objective of the tests was to obtain response data and
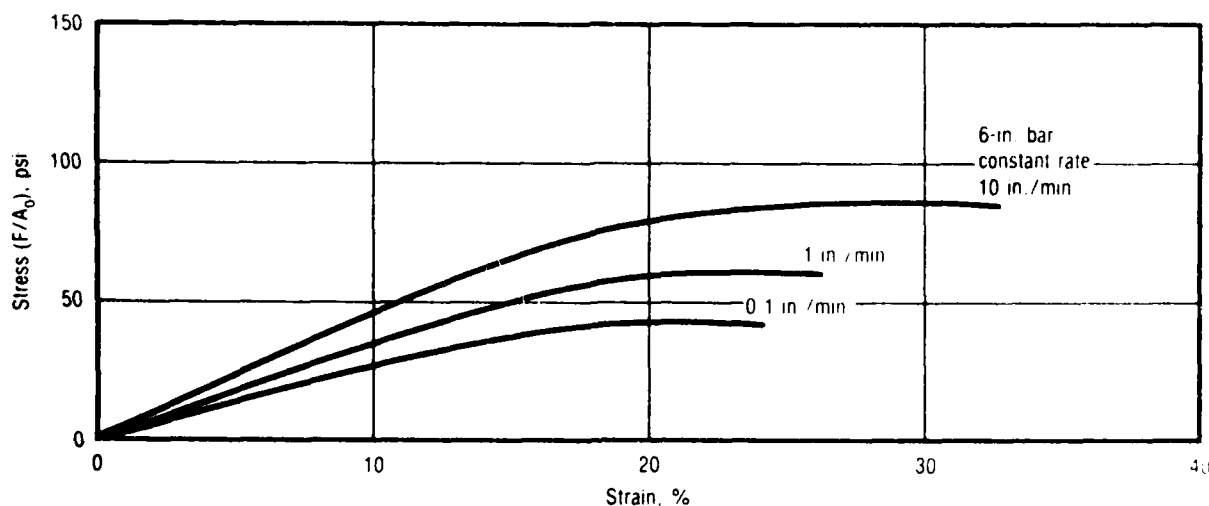
Figure 6. Constant-Rate Tests of UTP-3001-750/7768 at 124 F with 6-in. Bar Specimens

28768

not failure data, the failure strain level was unimportant. The important consideration was to avoid the continually changing effective gage length associated with the JANNAF dogbone specimen.

3.1.2 Multirate Test No. 3

Constant rate tests in which the rate was changed during the test were run on both propellants at 70 F. The 1.0 to 0.1 in./min rate change data for UTP-19,360B are shown in Figure 7 and the 0.1 to 1.0 in./min data are shown in Figure 8. The corresponding data for UTP-3001 are not shown but are similar to the UTP-19,360B results.

3.1.3 Stress Relaxation Modulus Test No. 4

The stress relaxation modulus tests were run at a nominal 3% strain using 1/2- x 1/2- x 6-in. samples of propellant bonded to redwood end tabs for both
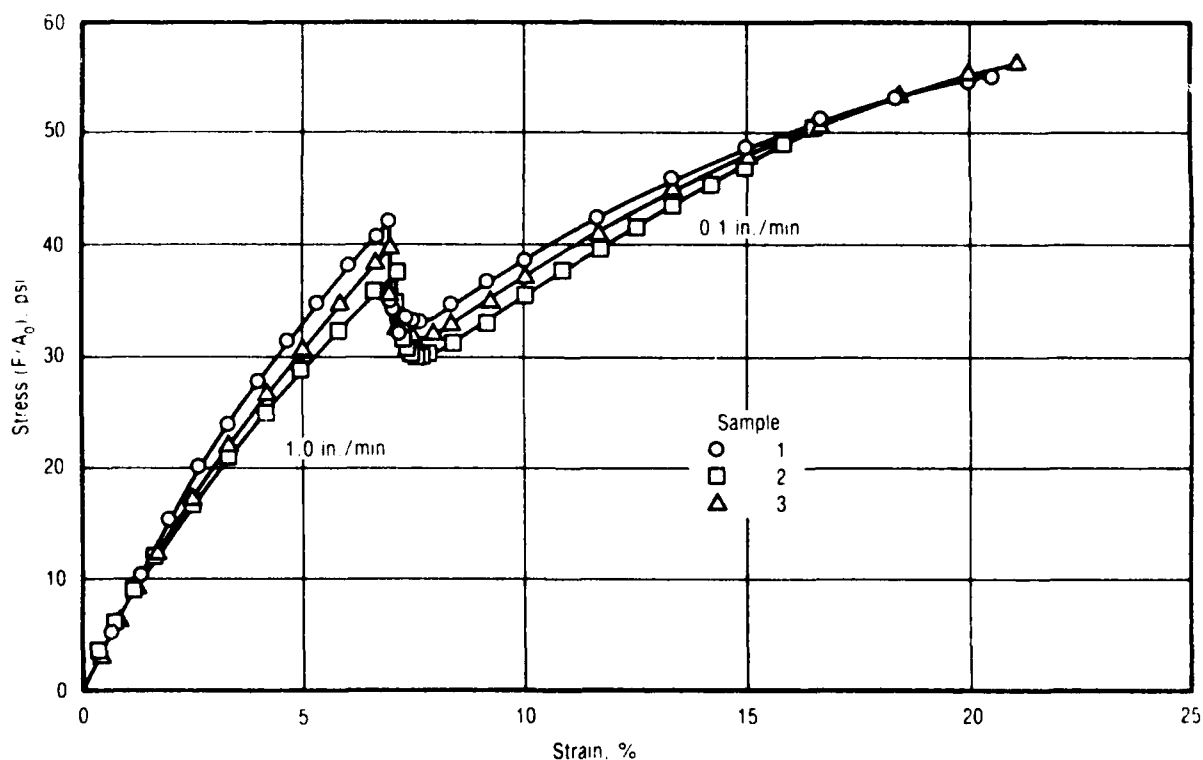
Figure 7. Test No. 3 - High-Low Constant-Rate Tests of
UTP-19,360B-400/1777 at 70 F

28391

31
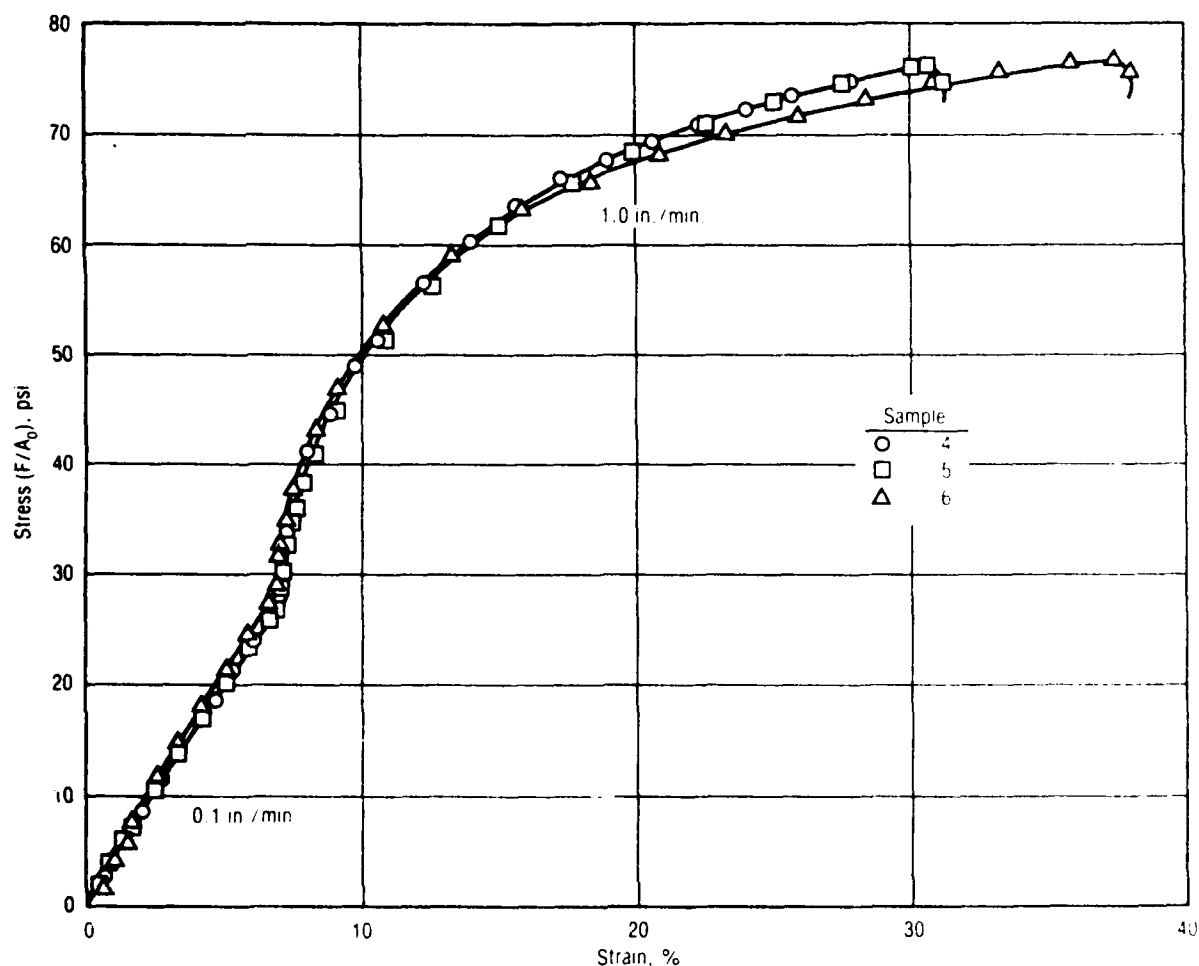
Figure 8. Test No. 3 - Low-High Constant-Rate Tests of
UTP-19,360B-400/1777 at 70 F

28392

propellants. The samples were loaded to 3% strain at a crosshead rate of
1 in./min for temperatures of 20, 43, 73, and 122 F. The load was monitored
with the time while strain was determined from cathetometer measurements
on the samples.

The master stress relaxation modulus data for UTP-3001 are presented in
Figure 9 as typical. Actual data are available from the data bank.

3.1.4 Constant Rate Secant Modulus

Constant rate modulus tests were run on the 6-in. bar samples described
above and on JANNAF class B specimens. The 6-in. bar samples used the
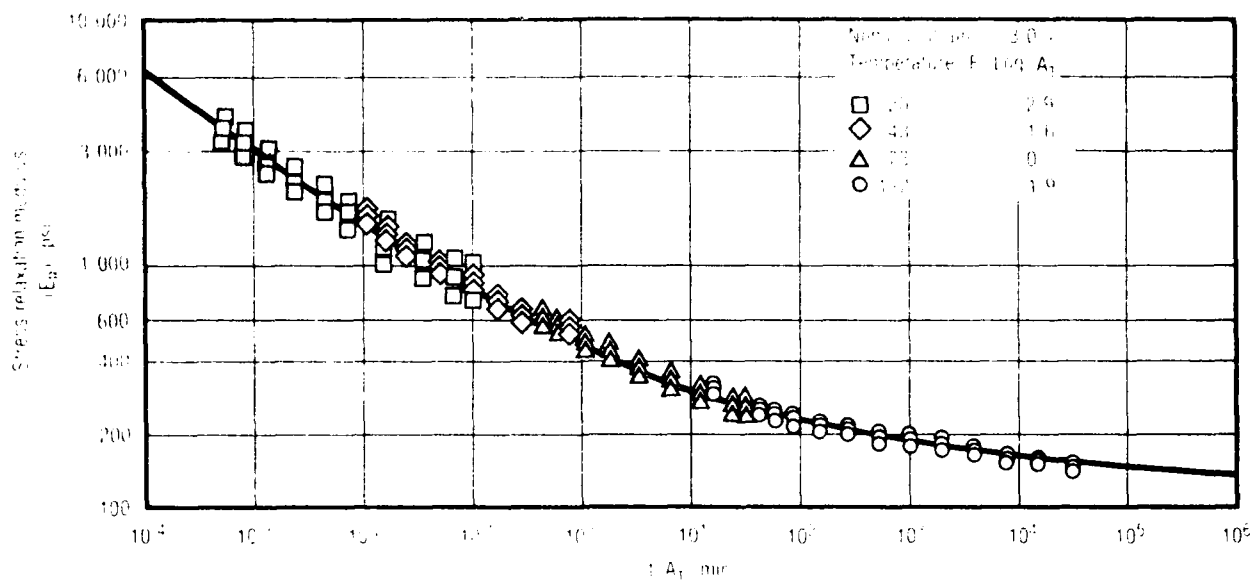
Figure 9.   Master Modulus Data for UTP-3001-750-/7768 with
Experimental Shift

28393

wood-to-wood distance as the effective gage length while the JANNAF's were
analyzed using 2.70-in. effective gage length through the test even though
it is varying. Strain was determined by the crosshead travel.

Constant rate modulus data for UTP-3001, with the curve drawn through
the small strain portion of the results, are compared to the relaxation modulus
in Figure 10. Similar data for UTP-19,360B are available in the data bank.

3.1.5 Cyclic Loading Test No. 5

The multiple loading tests on 6-in. bars of UTP-3001 and UTP-19,360B were
run in five cycles with increasing strain levels for each cycle and a rest
period between cycles. All tests were at 70 F and at crosshead rates of
5, 1, and 0.1 in./min. An attempt was made with UTP-3001 to run at 10 in./min
(i.e., planned rate instead of five), but the data sampling rate did not provide
sufficient data points to clearly define the load-time curve, particularly
on the first low strain cycle. As previously mentioned, this data had to
be reworked.
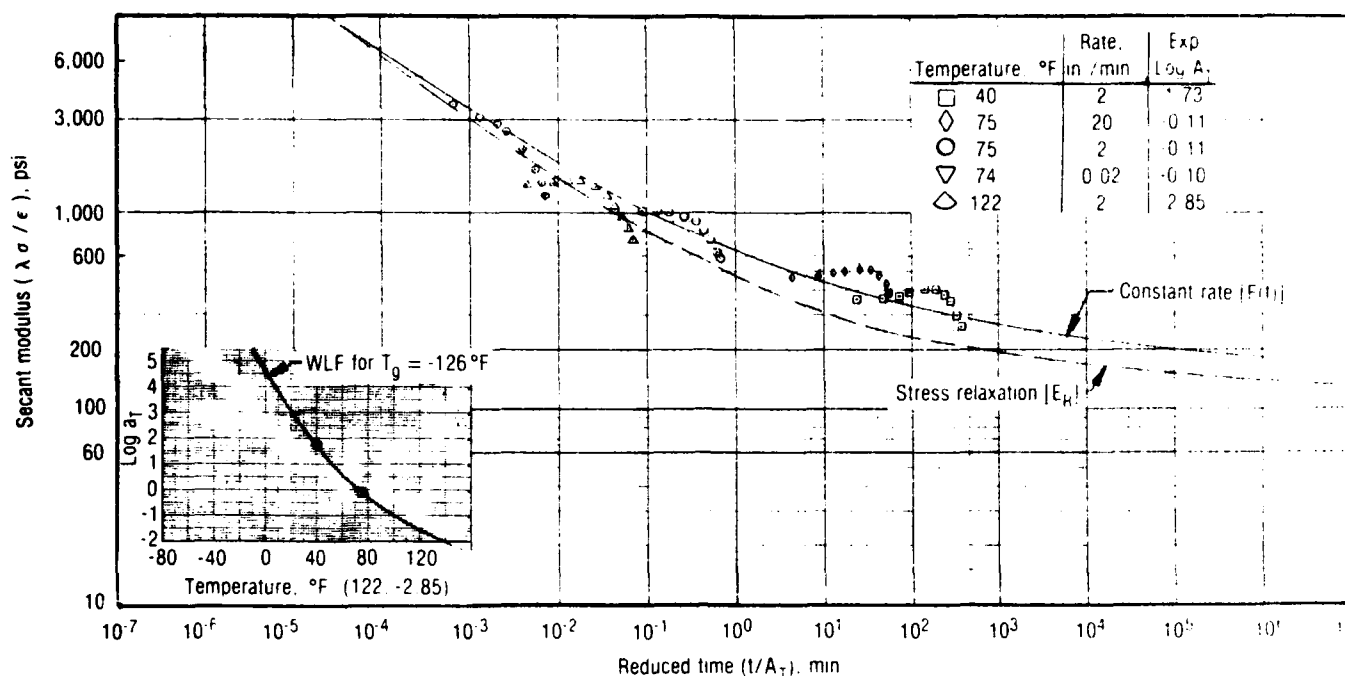
Figure 10. Master Constant-Rate Secant Modulus Data for UTP-3001-750/7768
JANNAF Specimens

28394

The rework of the data consisted of estimating maximum and minimum stress
and strain points that were not detected by the digitized data acquisition
system. The data reduction system computed strain from crosshead travel;
this was satisfactory except at and below zero stress. The sample linkage
attachment was such that specimens would not be put into compression with the
exception of test No. 11, which was run in an Instron with rigid clamp jaws. The
actual propellant strain decay was estimated from other tests where strain
recovery was monitored by cathetometer measurements for the part of the tests at
zero stress (i.e., no load on the samples). The 5-in./min crosshead test for
UTP-19,360B was selected as typical and is shown in Figure 11.

3.1.6 Cyclic Loading Test No. 7

Cyclic loading tests were run on 6-in. bars of UTP-3001 and UTP-19,360B
propellants at ambient temperature. The cycling was for 20 cycles at nominal
strain levels of 4, 8, and 12% for UTP-19,360B with UTP-3001 limited to 1.3%. At
the end of the test (after unloading to zero stress) the strain was monitored on
the samples with a cathetometer. The test at a nominal 12% strain is shown in

34
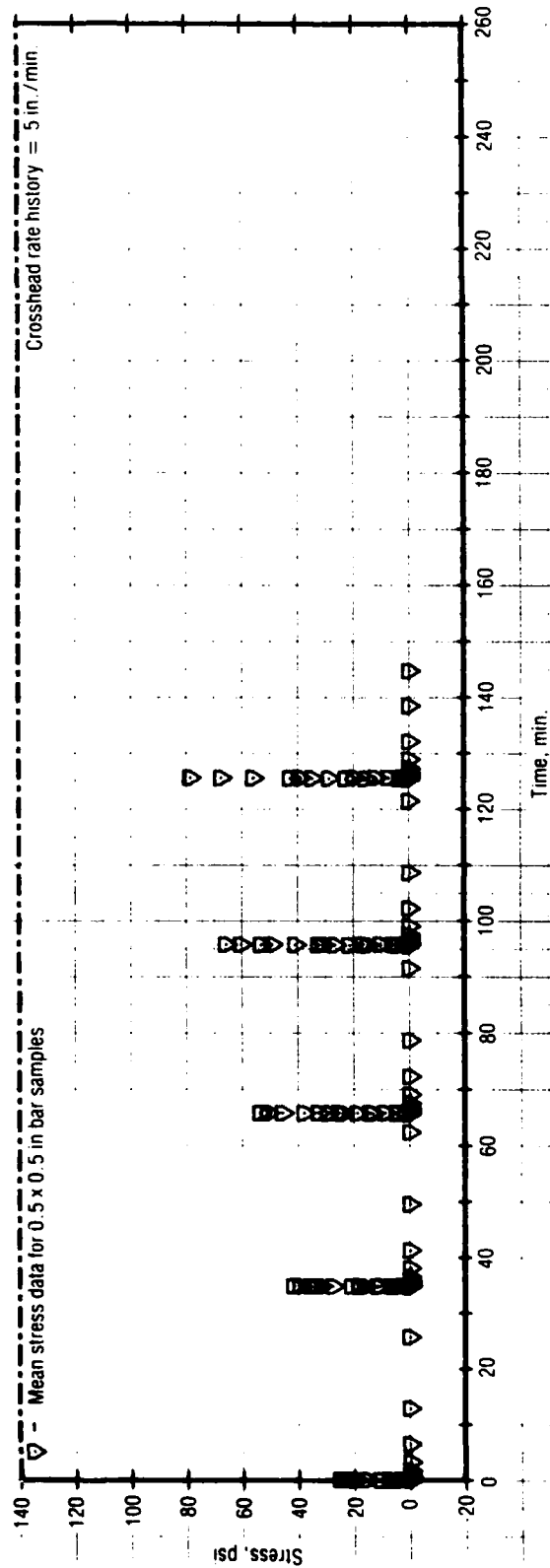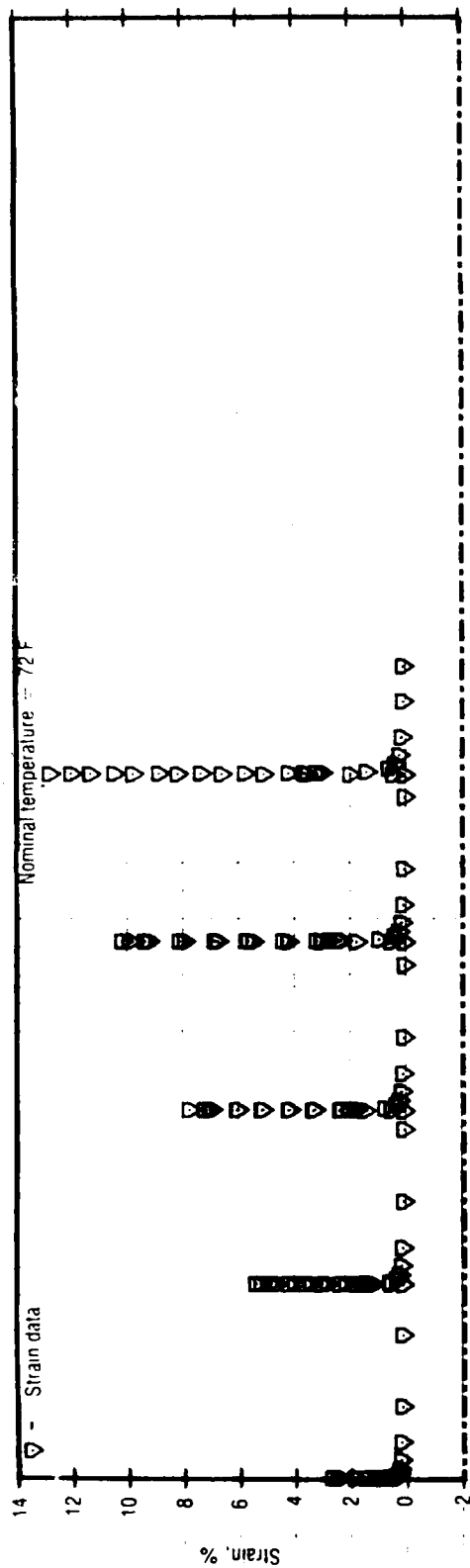
Figure 11. Test No. 5 - Stress While Cycling for UTP-19,360B-400/1777

28746

35

Figure 12 for UTP-19,360B as typical. These data were modified to insert the estimated maximum stress points and the propellant strain decay while at zero stress.

3.1.7 Relaxation Test No. 8

Stress relaxation tests are run on 6-in. bars of UTP-3001 and UTP-19,360B propellant for a 24-hr period and then monitored for strain decay after being unloaded. The tests at ambient temperature were repeated for 4, 8, and 12% nominal strain levels. They were loaded at a crosshead rate of 20 in./min and unloaded at 1 in./min after the 24-hr relaxation. Typical test data are shown in Figure 13.

3.1.8 Predamaged-Relaxation Test No. 9

The predamaged-relaxation tests were run with 6-in. bars on UTP-3001 and UTP-19,360B propellants at ambient temperature. They were preloaded to 12% and unloaded at a crosshead rate of 0.1 in./min allowed to rest, then reloaded to 8 or 4% strain at 20 in./min. After relaxing 1 hr, the samples were unloaded at 1.0 in./min and strain was monitored after unloading. These tests were repeated for a 6% predamage strain followed by a reload to 4 or 2% as above. These data were modified to obtain the peak stress and strain relaxation after the samples were unloaded. Strain was monitored with a cathetometer after the relaxation part of the test. Typical test data are shown in Figure 14 for UTP-19,360B.

3.1.9 Complex Multiple Load Test No. 10

The complex multiple load tests were run with 6-in. bars on UTP-3001 and UTP-19,360B propellants. Tests were run at crosshead rates of 5, 1, and 0.1 in./min. The test sequence was 12 to 8 to 12 to 4% strain, then unloaded, reloaded to 4% strain, and unloaded (four cycles) with cathetometer monitoring of strain decay on the last unload. The same type of sequence was repeated with maximum strains of 8 and then 4% where the 4% maximum strain was shortened by one cycle. The 5 in./min, 12% maximum strain test with UTP-19,360B propellant is typical and is shown in Figure 15. The data were reworked to obtain maximum and minimum stress values as well as strain decay for unloaded specimens. The cathetometer strain after the final unload was incorporated into the data.

36

Figure 12. Test No. 7 - Stress While Cycling for UTP-19,360B-400/1777

28754

37
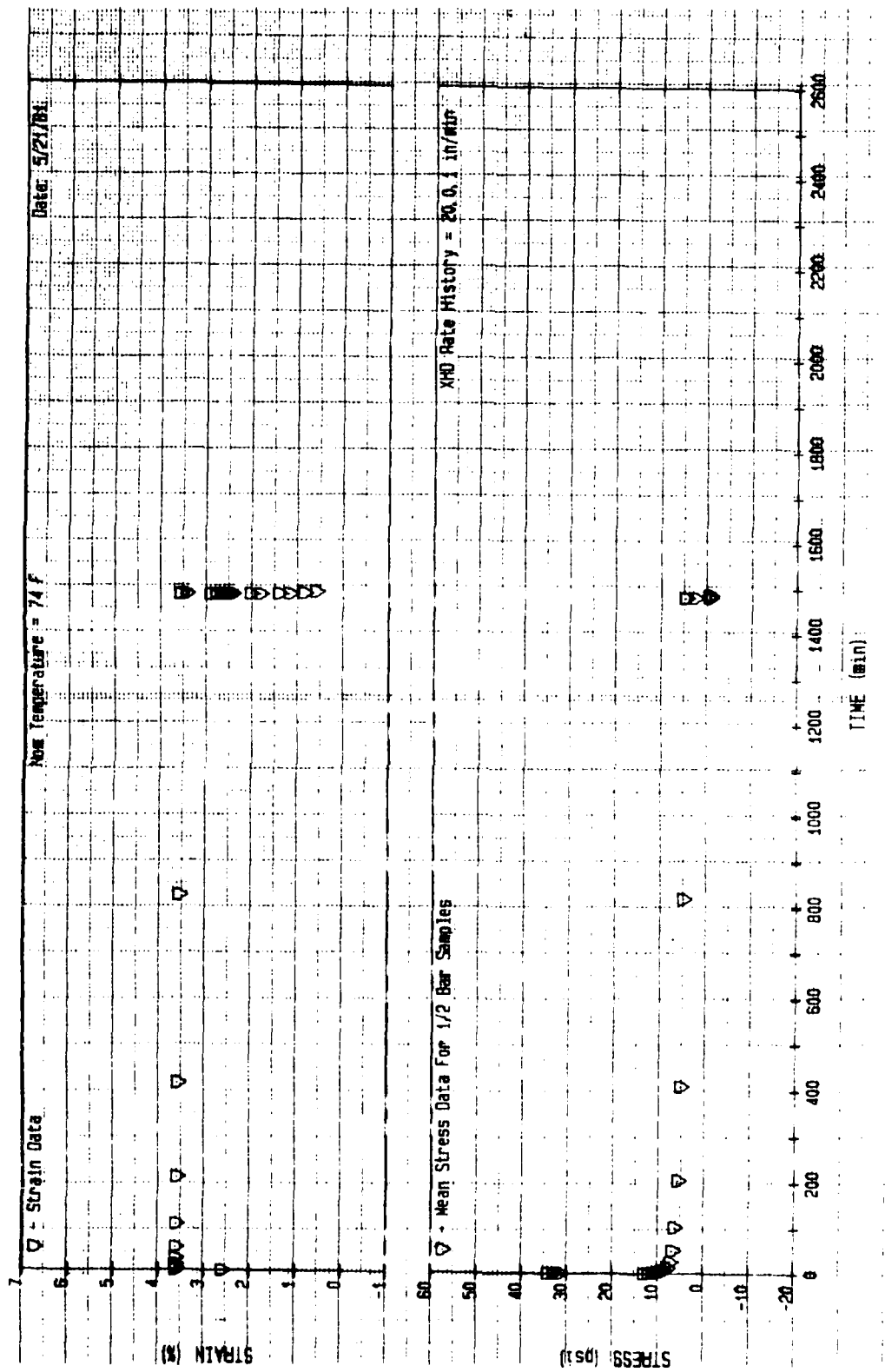
Figure 13. Test No. 8 - Stress While Step Straining for UTP-3001-750/7768

28755

38
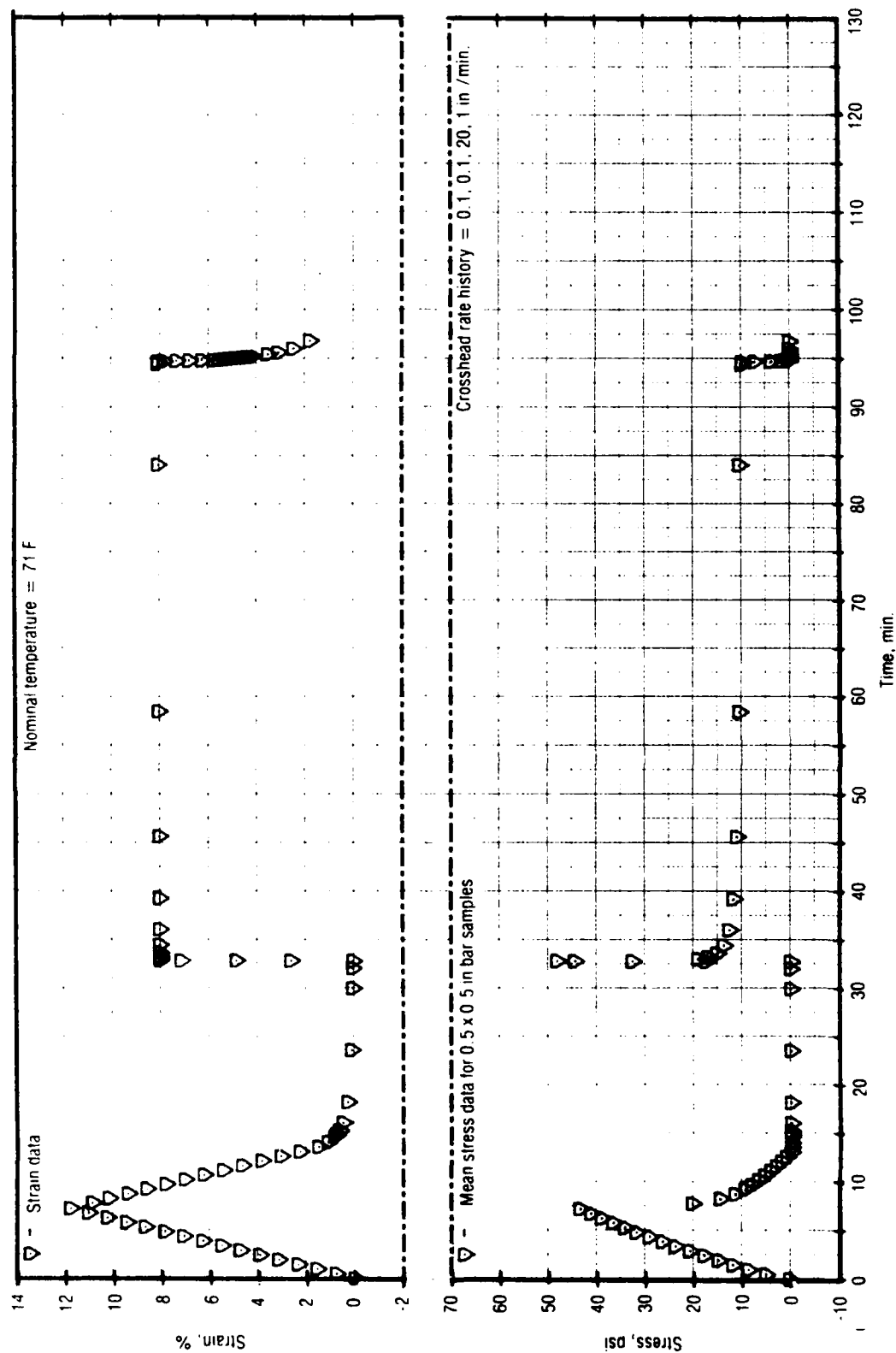
Figure 14. Test No. 9 – Stress While Step Straining for UTP-19, 360B-400/1777

28753
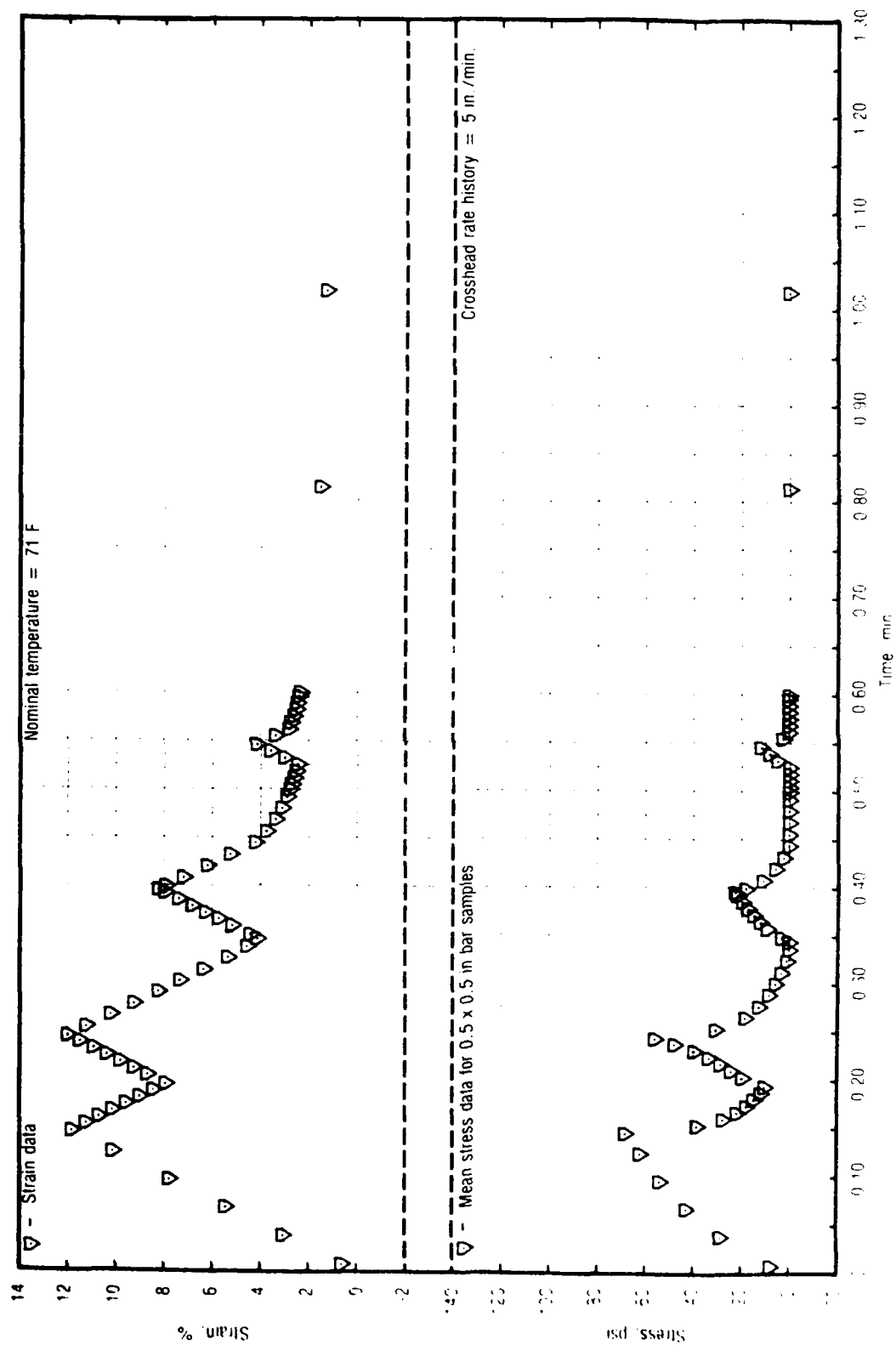
Figure 15. Test No. 10 - Stress While Complex Straining for UTP-19, 360B-400/1777

28709

The 5-in./min, 12% strain test for UTP-3001 was deleted because the modulus was outside the range of the remainder of the data (i.e., carton-to-carton difference).

3.1.10 Complex History Test No. 11

This particular test is very complex and required two full months to complete. It was run with a single sample (one at a time) in an Instron using single 6-in. bar specimens of UTP-3001 and UTP-19,360B propellant. The samples were pinned through the redwood end tabs and clamped onto the pins to avoid crushing the redwood (i.e., that would generate a compression load on the sample) during attachment. All coupling joints were heavy and tightly pinned so that the sample would be put into compression when returned to the zero strain position.

Only the test on UTP-3001 is selected for presentation here, but it is very similar to the UTP-19,360B test. Since the test is so complex, it has been divided into three parts. Part 1 is described in Table 1. Since an actual Instron trace of the load-time curve was obtained, the peaks and minimum (compression) stresses were selected data reduction points. Part 1 of the test is expanded in time scale to show some detail of the process (Figures 16 through 19). Part 2 is described in Table 2. Test sequence for Part 2 is shown in Figures 20 through 22. Part 3 (selected cycle maximum and minimum) are given in Table 3. The last figure of this part (Figure 23) is some of the cyclic loading at the end of the test. The chart speed was set such that good definition of the cycle could be recorded.

The latter part of the cycling represented only by the maximum and minimum stress-strain points. Part 3 of this test (the balance of cycling to failure) is recorded in Table 3 as maxima and minima for selected cycles sufficiently close to describe the upper and lower bounds. A plot of the data would be similar to Figure 22. The strain values in Table 3 are stable, while the maximum stress shows a continual decay, and compressive (negative values) stresses are less compressive.

41

TABLE 1.   TEST NO. 11, PART 1 - QUINLAN COMPLEX HISTORY FOR UTP-3001

Test No.	Cycle	Rate, in./min	Remarks
1 to 7	Load Unload	2 2	Approximately 15-min rest after cycle Approximately 15-min rest after cycle
8	Load Unload	1 1	Approximately 15-min rest after cycle
9	Load Unload	5 5	Approximately 15-min rest after cycle
10	Load Unload	0.5 0.5	Approximately 15-min rest after cycle
11	Load Unload	10 10	Approximately 15-min rest after cycle
12	Load Unload	0.2 0.2	Approximately 15-min rest after cycle
13	Load Relax Unload	2 1/2 hr 2	Approximately 30-min rest after cycle
14	Load Relax Unload	2 1 hr 2	4-day rest after cycle
15	Load Relax Unload	2 1 hr 2	7-day rest after cycle

3.2 TWO-DIMENSIONAL AND VARIABLE TEMPERATURE INVESTIGATION

The biaxial and nonisothermal testing was conducted on specimens of UTP-3001 and UTP-19,360B propellants as detailed in Figure 23. The biaxial samples were cast into prelined redwood boxes with a 1.25-in. gage length by 6-in. wide and machined flat to a 0.25-in. thickness. The response properties rather than failure properties were of interest so the discontinuity at the redwood interface did not affect the desired behavior. The 1/2- x 1/2- x 6-in. specimens were used for straining-cooling and cyclic strain tests. Shear
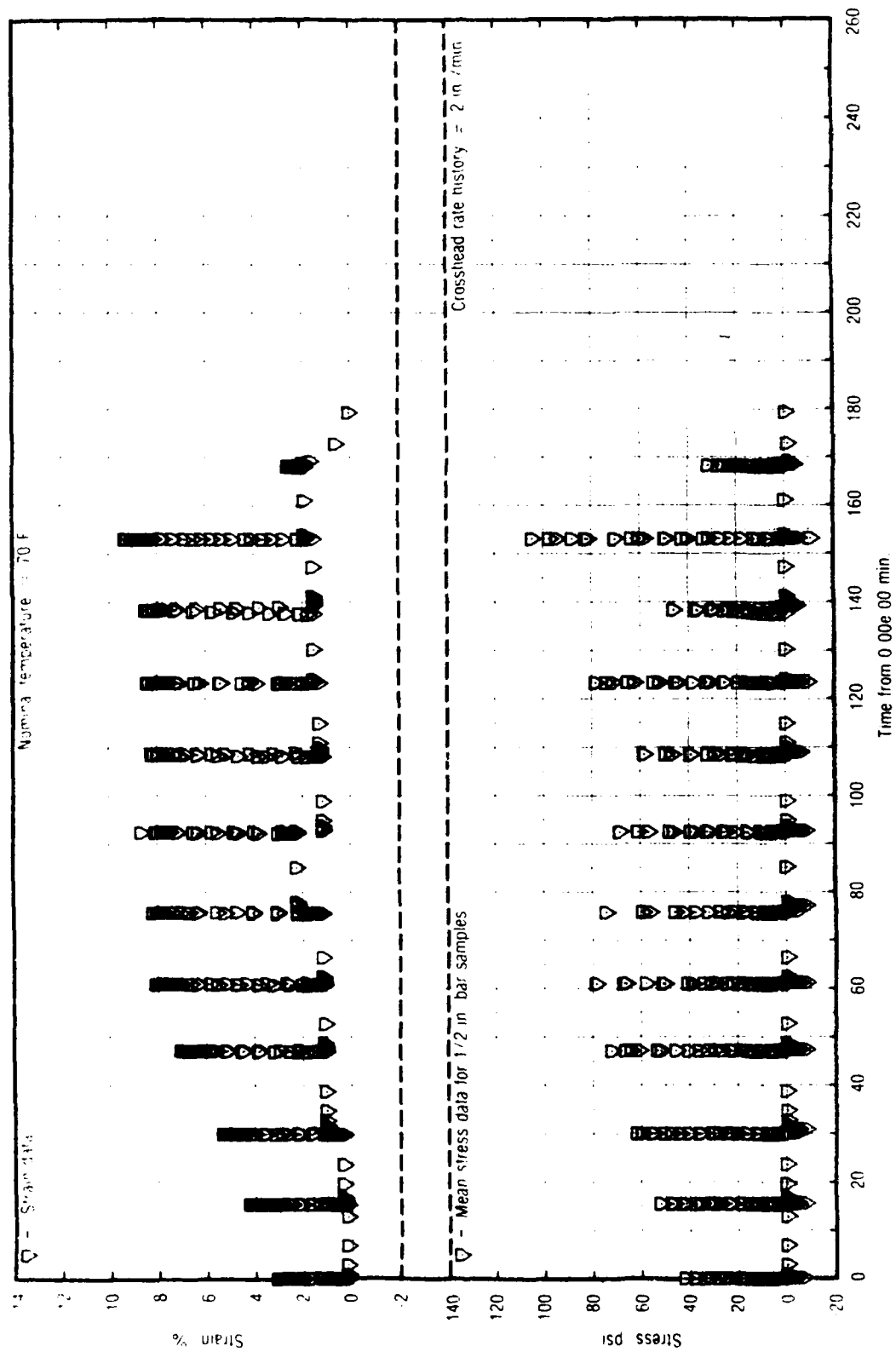
Figure 16. Test No. 11, Part 1 – Stress While Cycling for UTP-3001-750/7768

28757

43
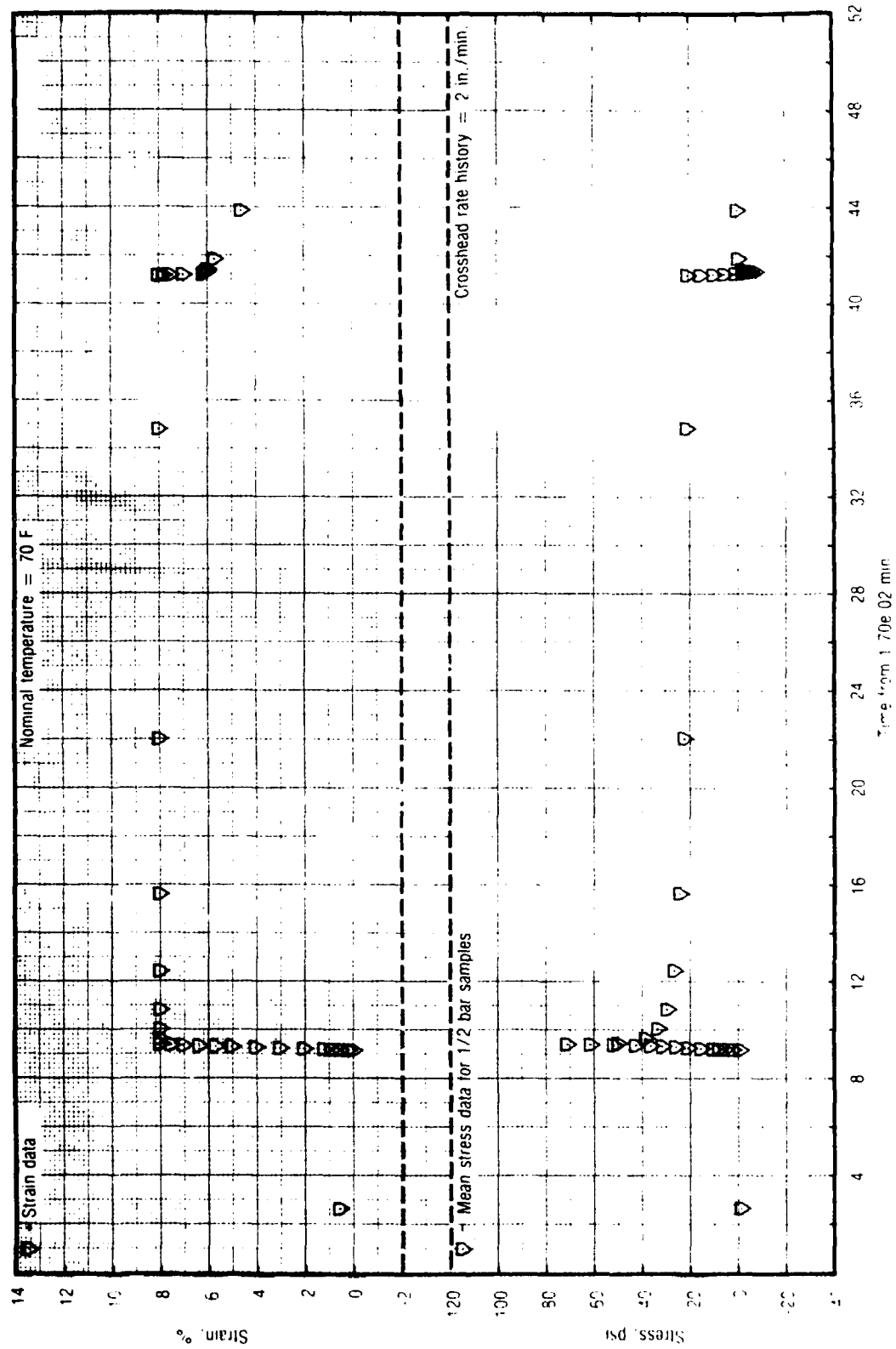
Figure 17. Test No. 11, Part 1 - Stress While Cycling for UTP-3001-750/7768

28758

44
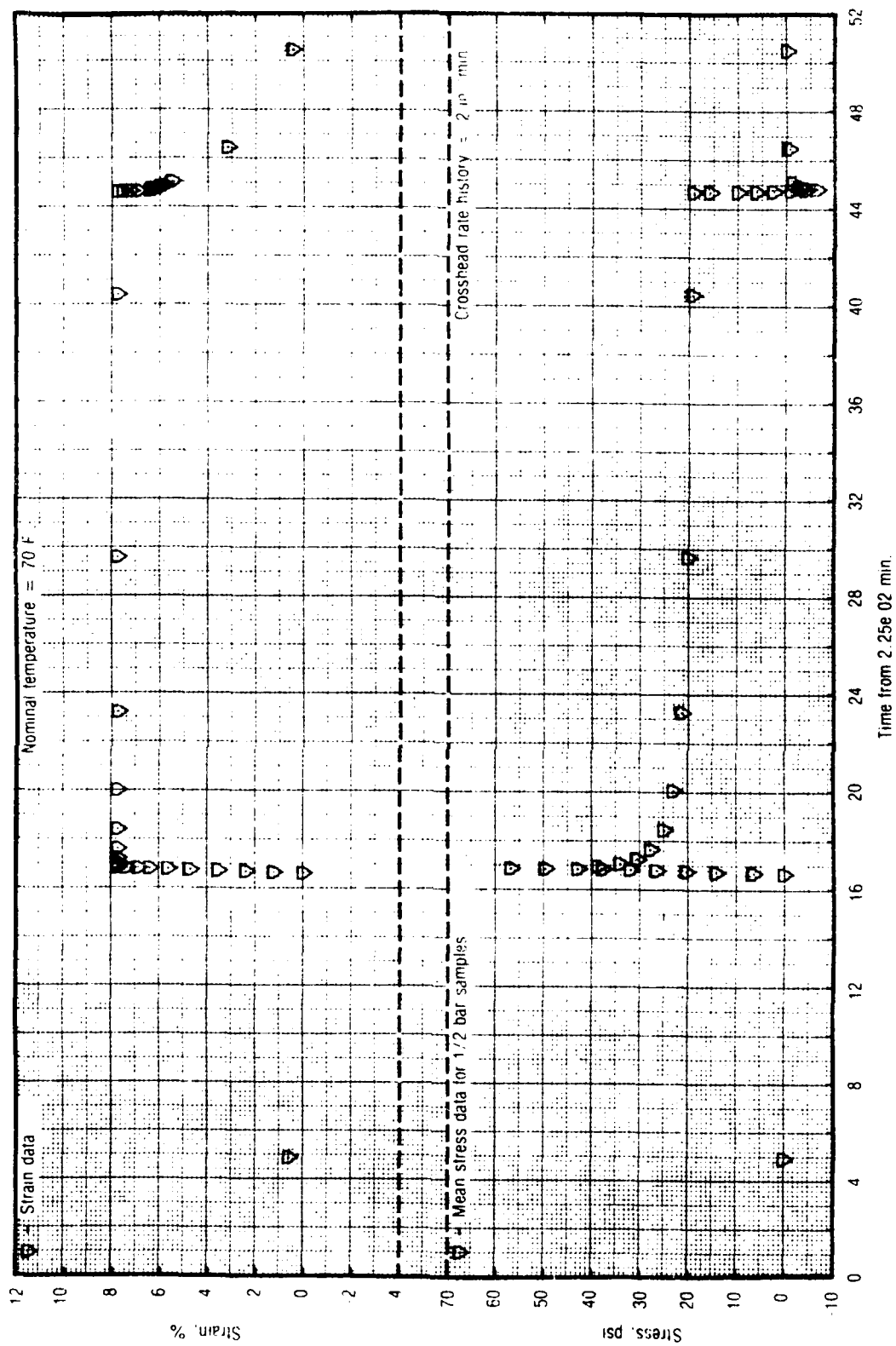
Figure 18. Test No. 11, Part 1 - Stress While Cycling for UTP-3001-750/7768

28797
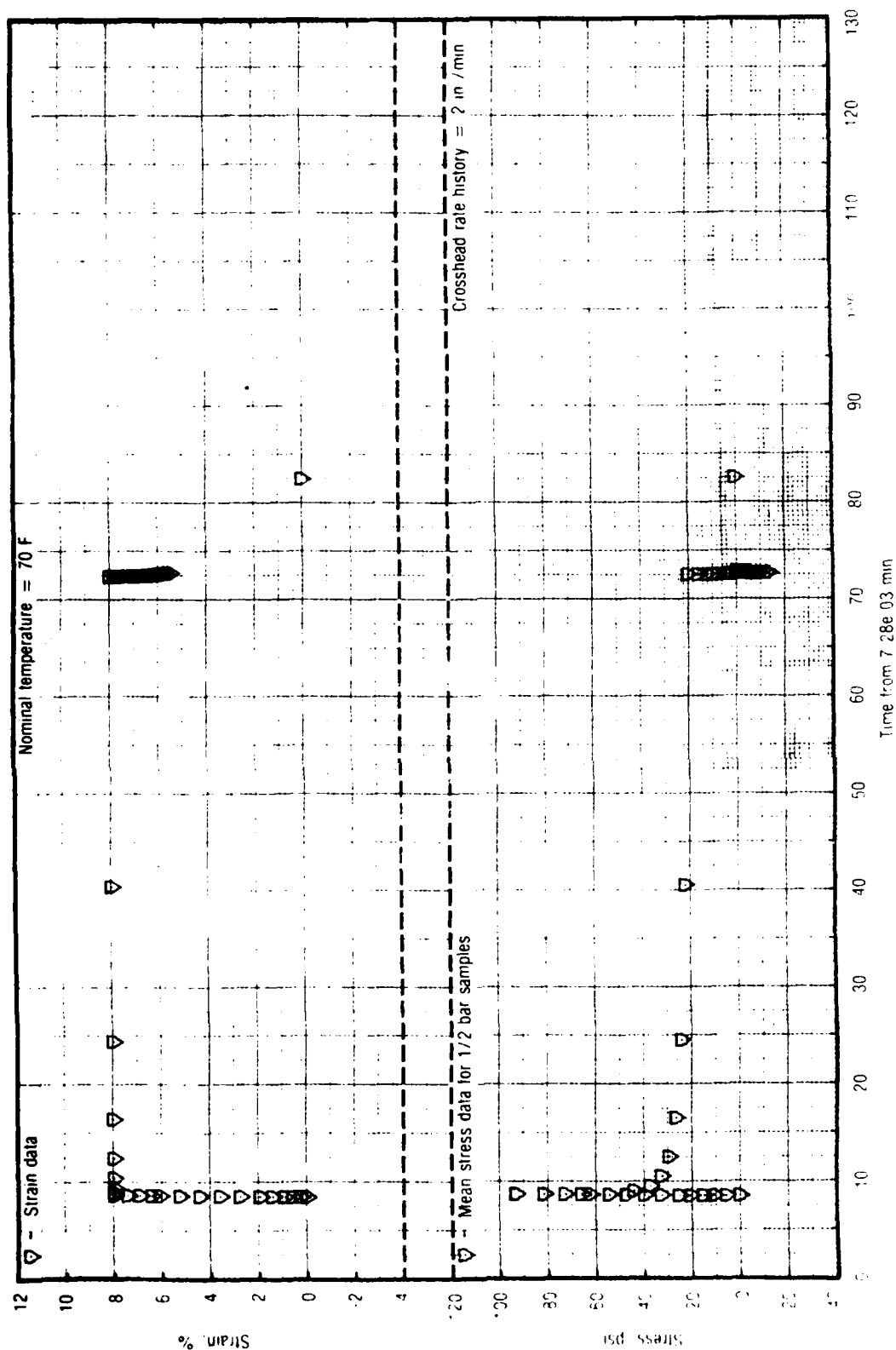
Figure 19. Test No. 11, Part 1 – Stress While Cycling for UTP-2001-750/7768

28798

46

TABLE 2. TEST NO. 11, PART 2 - QUINLAN COMPLEX HISTORY FOR UTP-3001

Test No.	Cycle	Rate, in./min	Remarks
16	Load	0.02	
	Unload	0.02	Approximately 30-min rest after cycle
17	Load	0.02	
	Unload	0.02	Approximately 30-min rest after cycle
18	Load	0.05	
	Relax	3 hr	
	Unload	0.05	2-weeks rest after cycle
19	Load	0.02	
	Unload	0.02	Approximately 30-min rest after cycle
20	Load	0.02	
	Unload	0.02	Approximately 30-min rest after cycle
21	Load	0.05	
	Relax	3 hr	
	Unload	0.05	1-month rest after cycle
22 to 42	Cycling	5	Several cycles monitored, followed by several with only maximum and minimum recorded

relaxation tests were run with 1- x 1- x 3-in. specimens bonded directly to steel anvils. Details are given in later sections, except for test 21 in Figure 23 which was uniaxial. The six-channel test equipment discussed in subsection 3.1 was used for this testing; however, only three biaxial specimens could be tested at once because of space limitations in the conditioning boxes.

The biaxial specimens used in this part of the program were cast into redwood boxes similar to that shown in Figure 5. The space between redwood blocks was 1.25-in. instead of the 6-in. for the uniaxial bars. The mill finished geometry is shown in Figure 24. The propellant was left flat rather than necking it down as is done with standard JANNAF biaxial specimens. The gage length was designated as the wood-to-wood distance for strain evaluation.
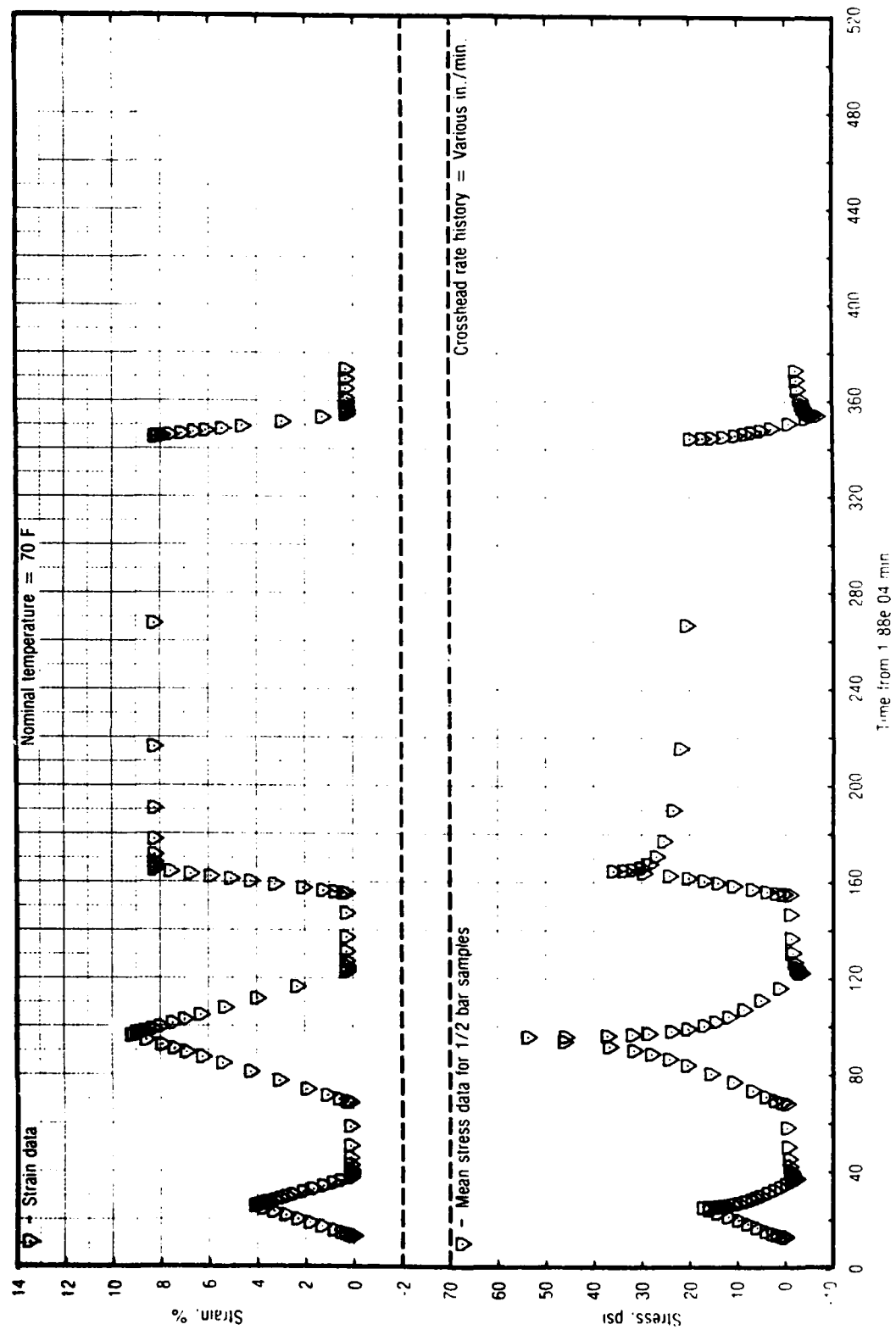
Figure 20. Test No. 11, Part 2 - Stress While Cycling for UTP-3001-750/7768

48
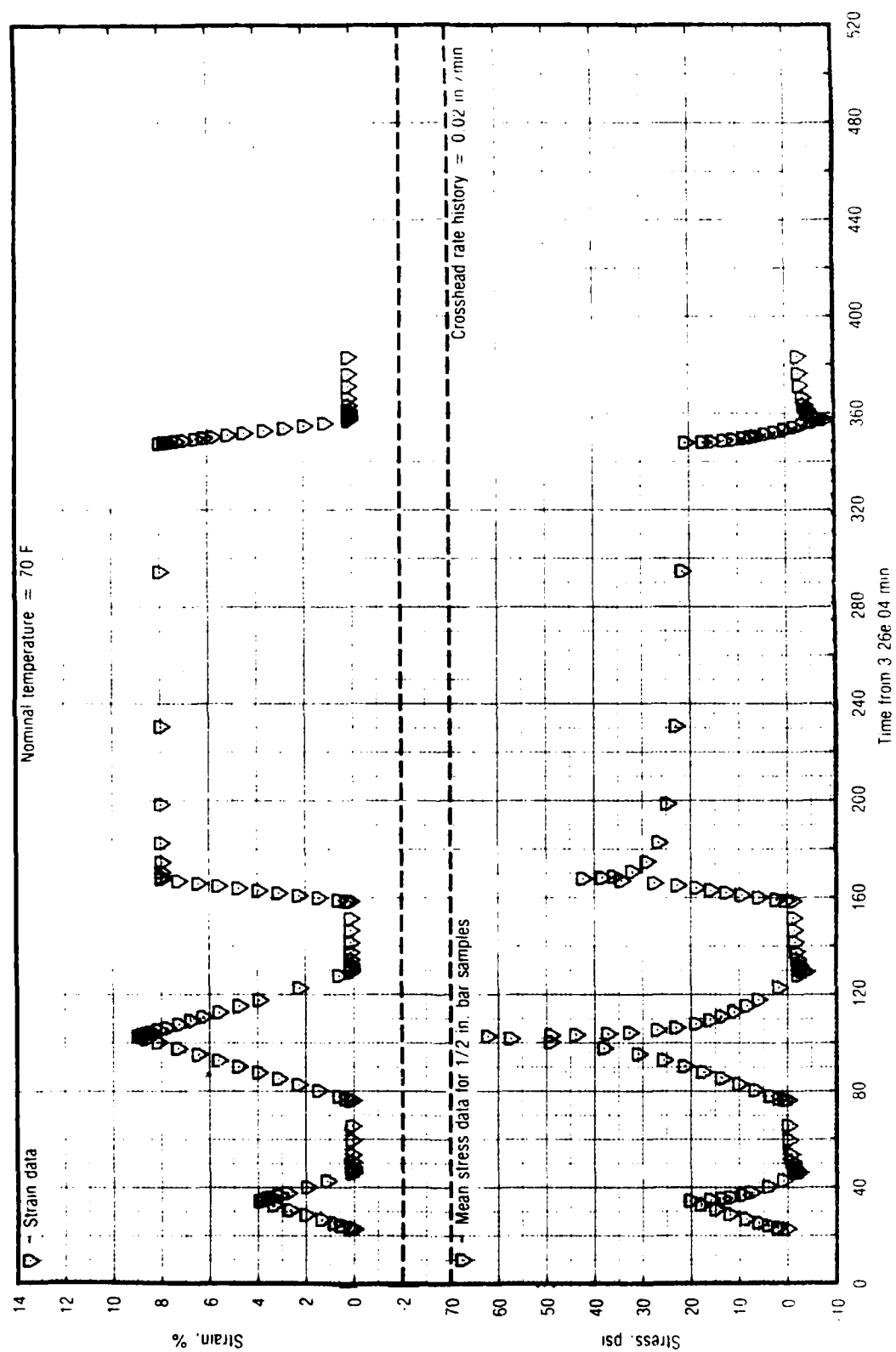
Figure 21. Test No. 11, Part 2 — Stress While Cycling for UTP-3001-750/7768

28760

49
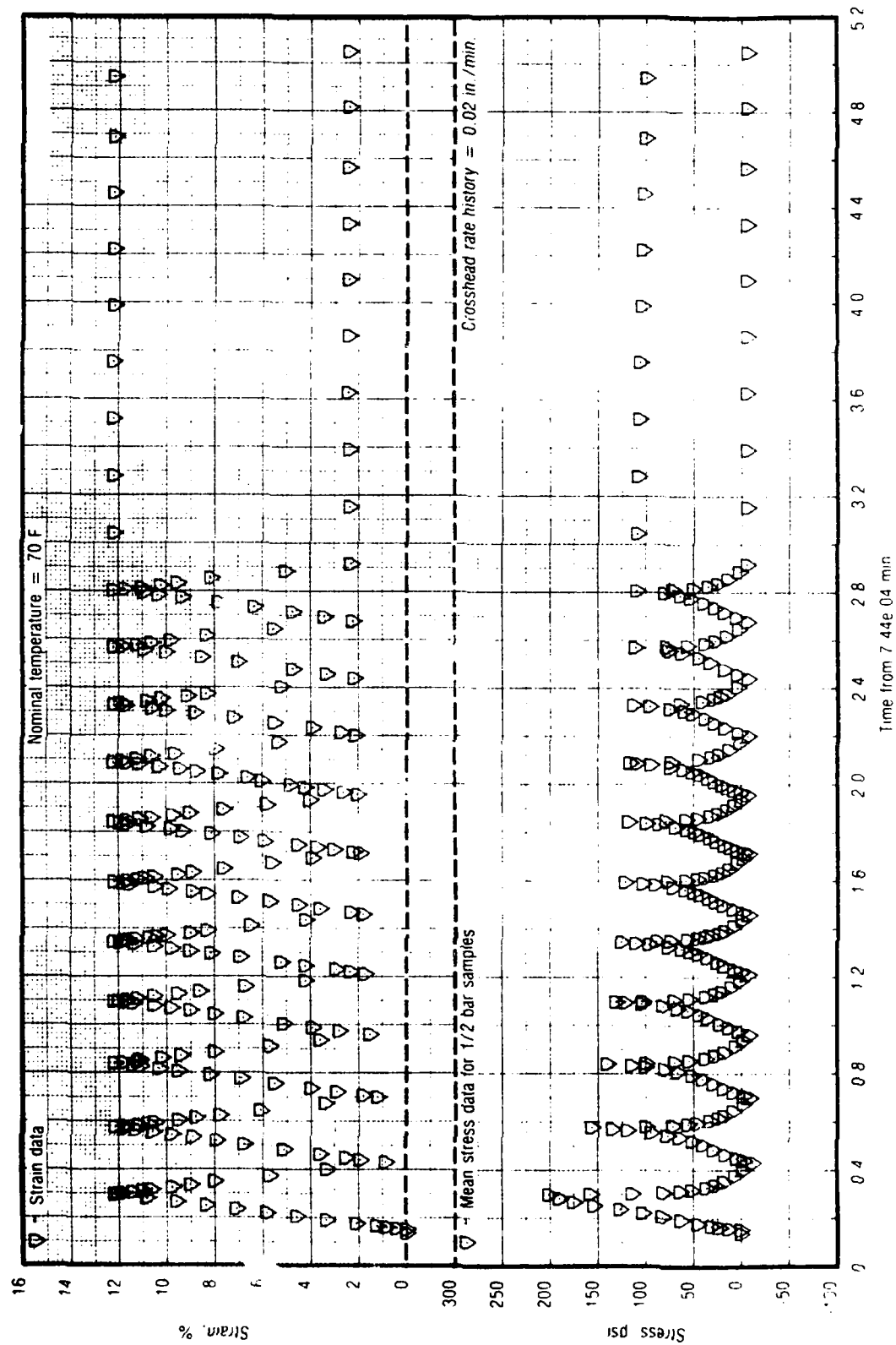
Figure 22. Test No. 11, Part 2 - Stress While Cycling for UTP-3001-750/7768

28761

50

TABLE 3.   TEST NO. 11, PART 3 - UTP-3001-750/7768 1/2-IN. BAR STRESS
WHILE CYCLING
(Sheet 1 of 2)   T8715

Time	Strain	Stress	Remarks
74388.0479	2.40	-6.37	End of cycle 20
74390.3479	12.17	93.23	Peak of cycle 30
74390.4539	2.40	-5.98	End of cycle 30
74391.3819	12.17	92.03	Peak of cycle 34
74391.4239	2.40	-5.58	End of cycle 34
74391.9432	12.17	91.24	Peak of cycle 40
74391.9859	2.40	-5.58	End of cycle 40
74392.0799	12.17	89.64	Peak of cycle 50
74392.1219	2.40	-5.18	End of cycle 50
74393.0099	12.17	88.45	Peak of cycle 60
74393.0519	2.40	-5.18	End of cycle 60
74394.7799	12.17	84.86	Peak of cycle 80
74394.8219	2.40	-4.78	End of cycle 80
74395.7279	12.17	80.10	Peak of cycle 102
74395.7479	2.40	-4.78	End of cycle 102
74418.3479	12.17	76.49	Peak of cycle 164
74418.3979	2.40	-4.78	End of cycle 164
74451.5979	12.17	71.71	Peak of cycle 330
74451.8779	2.40	-4.38	End of cycle 330
74474.2779	12.17	68.92	Peak of cycle 442
74474.3179	2.40	-3.98	End of cycle 442
74698.0179	12.17	62.95	Peak of cycle 980
	2.40	-3.59	End of cycle 980
74928.0179	12.17	60.16	Peak of cycle 1980
	2.40	-3.59	End of cycle 1980
75158.0179	12.17	56.97	Peak of cycle 2980
	2.40	-3.59	End of cycle 2980
75388.0179	12.17	56.18	Peak of cycle 3980
	2.40	-3.59	End of cycle 3980

51

Time	Strain	Stress	Remarks
75618.0179	12.17	53.39	Peak of cycle 4980
	2.40	-3.59	End of cycle 4980
75695.5179	12.17	51.39	Peak of cycle 5317
	2.40	-3.59	End of cycle 5317*
* Sample broke			
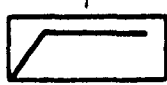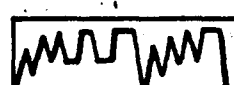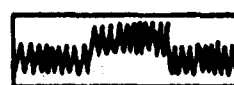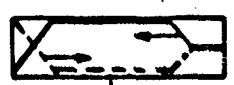
Test	Test Description	Damage Cycle/Test	Strain Cycle
14	Biaxial constant rate	Biaxial samples of UTP-3001 and UTP-19.360B were ramp loaded to failure at rates of 2, 0.2, and 0.02 in./min at temperatures of 41, 70, and 120 °F	
15	Biaxial straining-cooling	Biaxial samples of UTP-3001 and UTP 19.360B were simultaneously strain and cooled from 120 to 40 °F c e a 40 hr period	
16	Biaxial relaxation	Biaxial samples of UTP-3001 and UTP-19.360B were run in stress relaxation tests at 40, 70, and 120 °F	
17	Shear relaxation	Shear samples of UTP-3001 and UTP-19.360B were run in stress relaxation tests at 70 °F	See above
18	6-in. bar straining- cooling	6-in. bars of UTP-3001 and UTP-19.360B were simultaneously strain and cooled from 120 to 40 °F at three slow rates	
19	Biaxial Quinlan complex history	Biaxial samples of UTP-3001 and UTP-19.360B were cycled for the Quinlan complex history test at 70 °F	
20	6-in. bar cyclic test	6-in. bars of UTP-3001 and UTP-19.360B were run in cyclic strain tests at 0.1 in./min and 70 °F	
21	Biaxial thermal similitude	Biaxial samples of UTP-3001 and UTP-19.360B were run in ramp relaxation-ramp tests with simultaneous cooling or heating (i.e. for reverse ramp)	See above plus last half thermal cycled
	Note: Nominally three samples were run for each test and condition		Legend T = temperature ↑ time ε strain

Figure 23. Biaxial and Nonisothermal Phase III Testing

28774
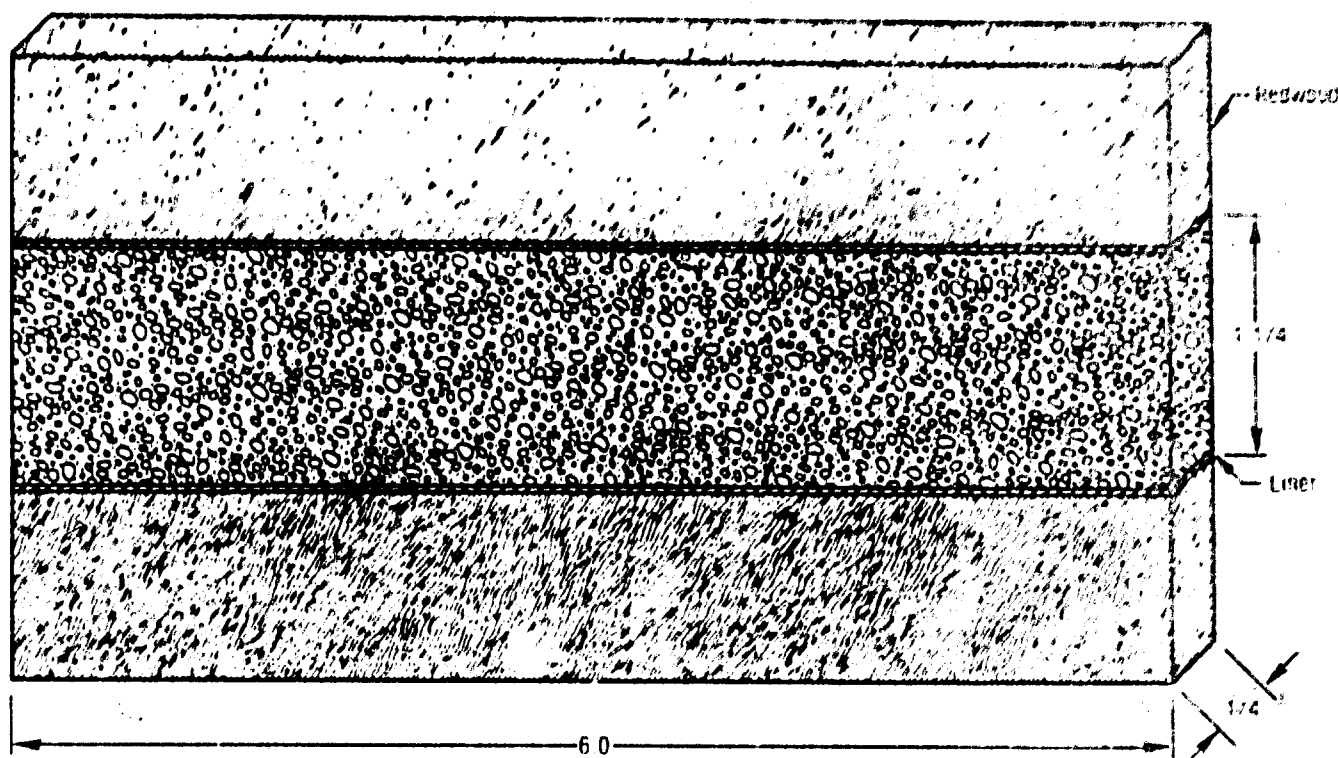
Figure 24. Finished Biaxial Specimen

28806

Response properties rather than failure properties were of interest, so the boundary perturbation was neglected.

The shear samples (test No. 17) were 1- x 1- x 3-in. blocks of propellant that were bonded to the test fixture (shown in Figure 25) after being machined. The pull rods were attached to the offset plates so that the load was transmitted through the center of the sample as shown. Since strain was limited to 5% for the shear relaxation test, the sample was assumed to be in simple shear. The shear strain (γ) was calculated as the tangent of the displacement angle or $\Delta L/G.L.$ The shear stress (τ) was calculated as force/area (area = 3 in.^{2}).

The data modification to insert peak and minimum stress points previously discussed for uniaxial cyclic tests was also used for the biaxial and nonisothermal tests.

53

Load

Load

a. Propellant and Loading Fixture

b. Propellant
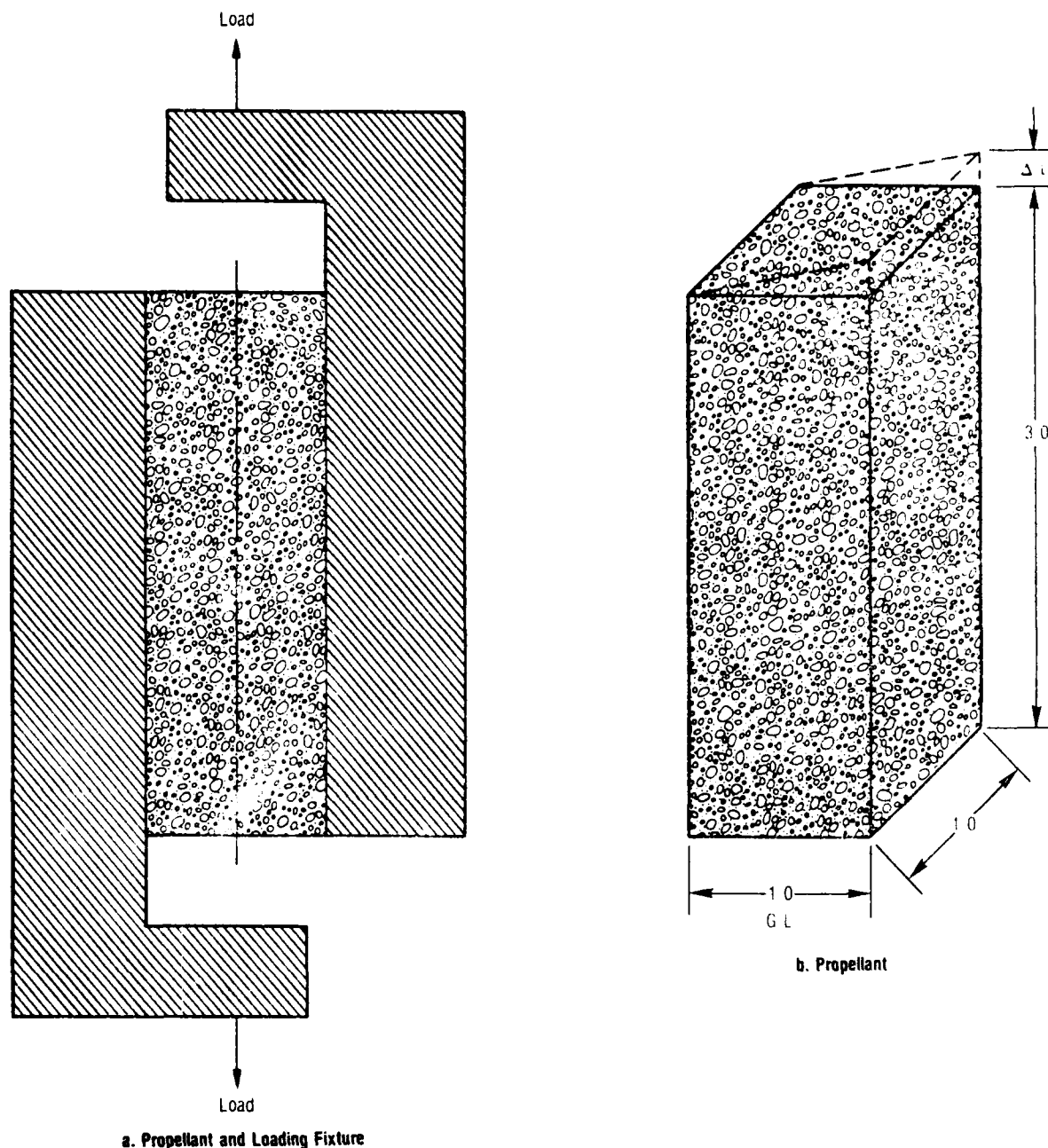
Figure 25.   Shear Sample and Test Attachment

28811

3.2.1 Biaxial Constant Rate Test No. 14

The biaxial constant rate tests to failure were run with the
1/4- x 1-1/4- x 6-in. specimens of UTP-3001 and UTP-19,360B. The tests were
conducted at 40, 70, and 120 F at crosshead rates of 2, 0.2, and 0.02 in./min.
The typical stress-strain response is shown in Figure 26 for UTP-19,360B
at 71 F and 2 in./min. Because of the fixtures and more difficulty in adjusting

54
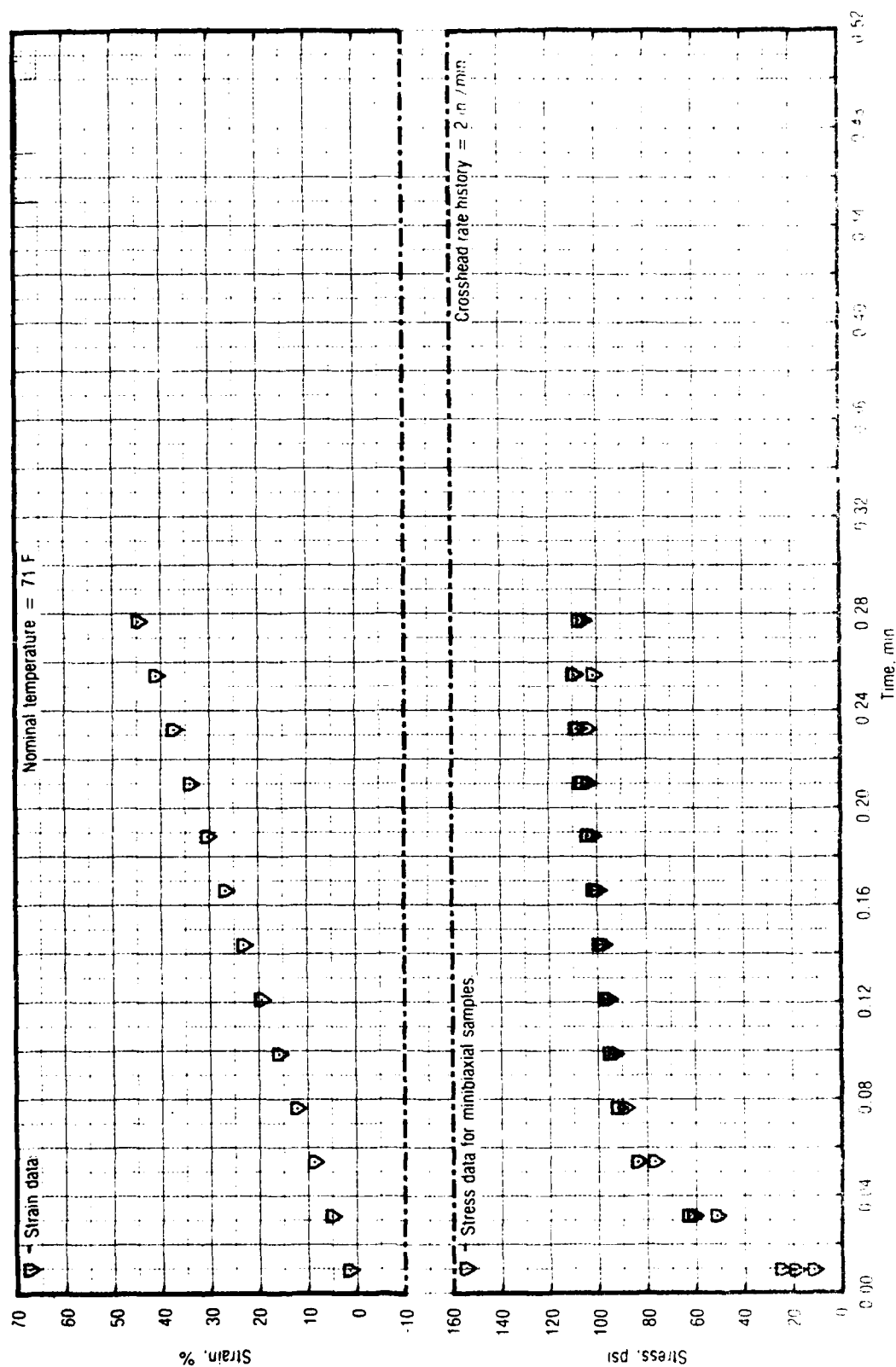
Figure 26. Test No. 14 - Stress for UTP-19, 3608-H00/1777

28812

55

linkage than with the 6-in. bar specimens, the three samples did not load simultaneously. Consequently, it was necessary to adjust the data for each sample to have a common starting point.

3.2.2 Biaxial Straining-Cooling Test No. 15

Biaxial specimens of UTP-3001 and UTP-19,360B propellants were simultaneously strained and cooled from 115 to 40 F at a crosshead rate of approximately 3×10^{-5} in./min over a 40-hr period. Typical test results are shown in Figure 27 for UTP-3001. The stress-time traces for all three samples appear to start together but spread out as the test progressed.

3.2.3 Biaxial Stress Relaxation Test No. 16

Biaxial stress relaxation tests were run with the 1/4- x 1-1/4- x 6-in. specimens of UTP-3001 and UTP-19,360B propellants at a nominal 3% strain and temperatures of 40, 70, and 120 F. The loading ramp rate was 0.2 in./min. Typical relaxation data for UTP-19,360B at 40 F are shown in Figure 28.

3.2.4 Shear Relaxation Test No. 17

Shear relaxation tests were run on 1- x 1- x 3-in. samples of UTP-3001 and UTP-19,360B propellants. The samples were post-bonded to steel plates as shown in Figure 25 and run one at a time by loading them at 0.2 in./min and ambient temperature with offset fixtures so the load was transmitted through the centerline of the sample. The three samples for each propellant were hand-reduced and digitized for computer storage and printout. Typical test data are presented in Figure 29 for UTP-3001.

Peak stresses and strain were very close, as was the 1 hr relaxation stress on each propellant, even though the samples were run separately.

3.2.5 Uniaxial Straining-Cooling Multiple Rates Test No. 18

The rate effect on the straining-cooling response was determined on UTP-3001 and UTP-19,360B propellants. The 1/2- x 1/2- x 6-in. uniaxial bar sample was used so that testing could be completed in the shortest time possible. The rate effect for the uniaxial specimens was then applied to biaxial test No. 15. Cooling was from 110 to 40 F at the crosshead rates of 0.002, 0.0002, and
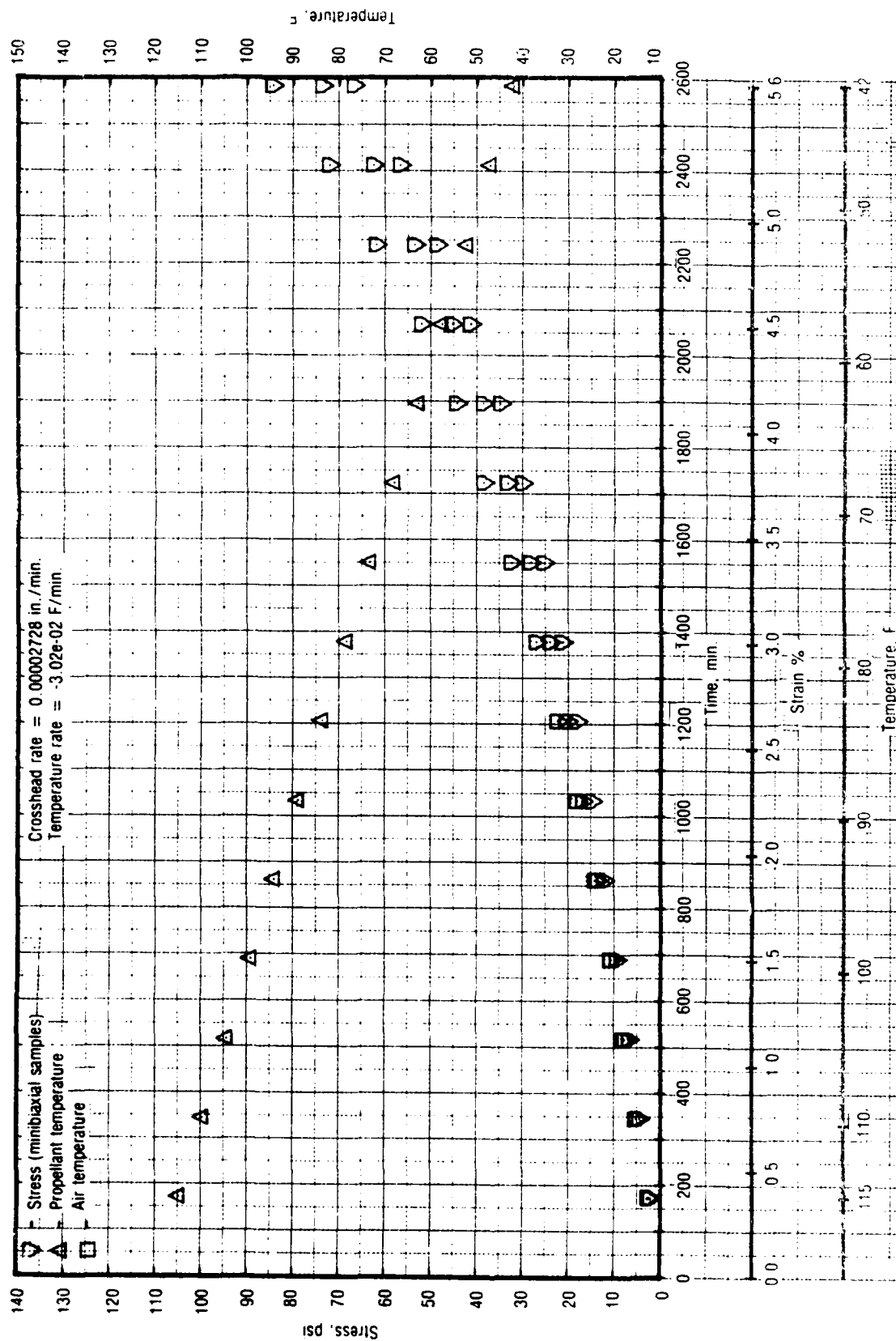
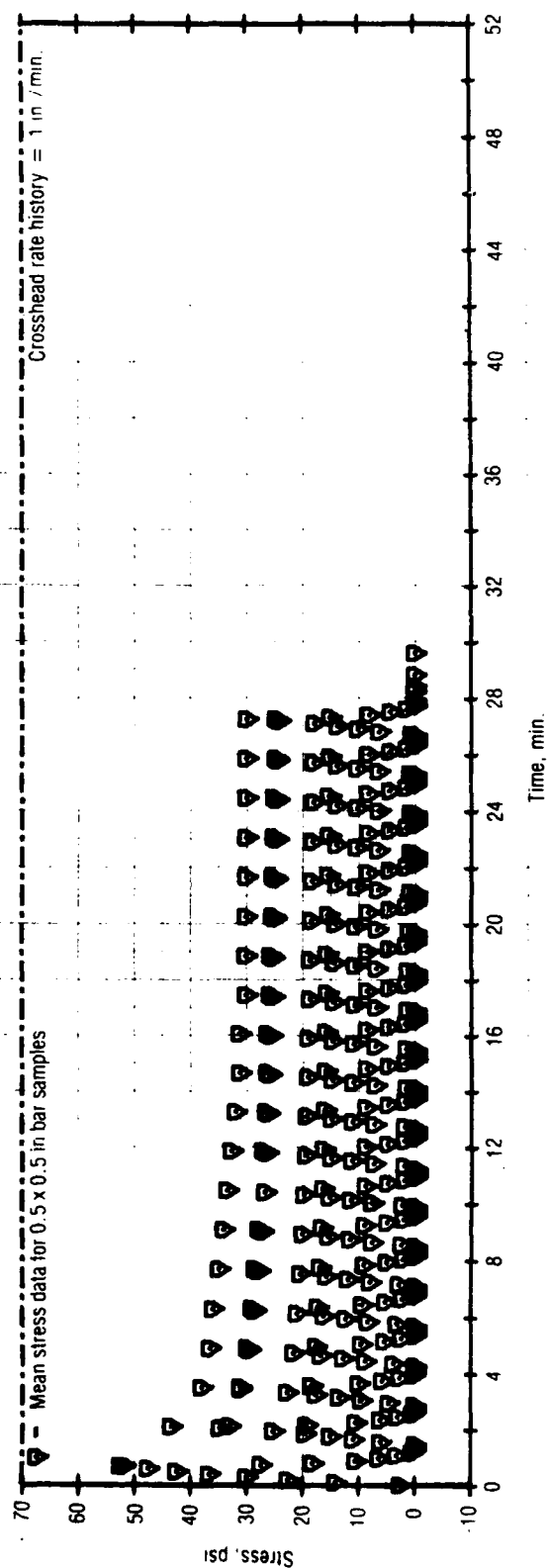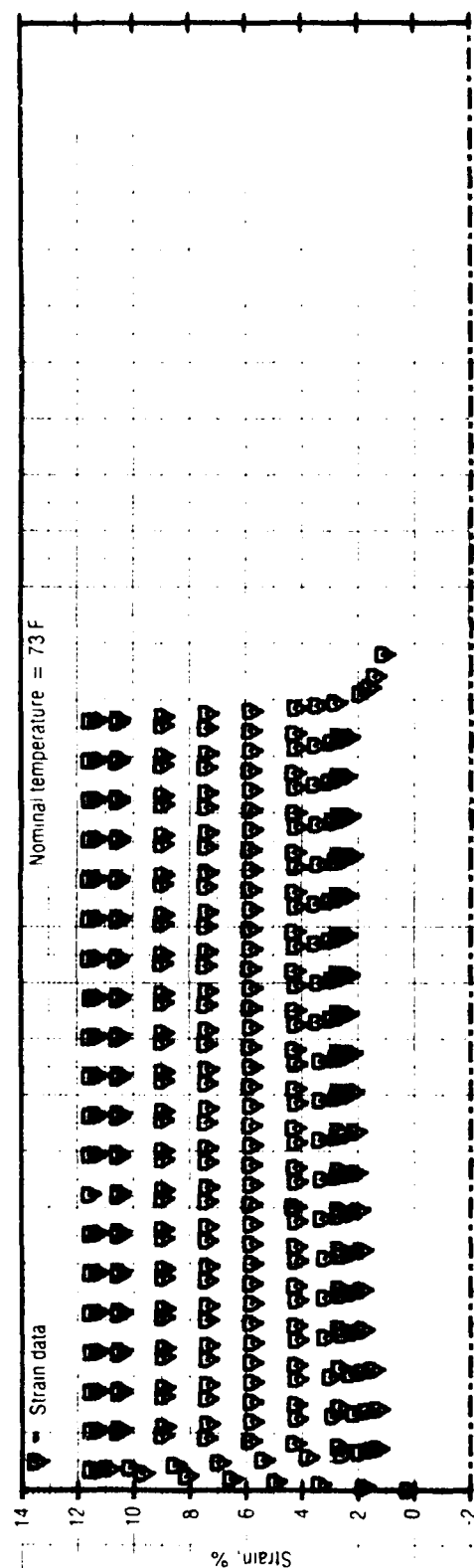Figure 27. Stress While Straining and Cooling for UTP-3001-750/7768
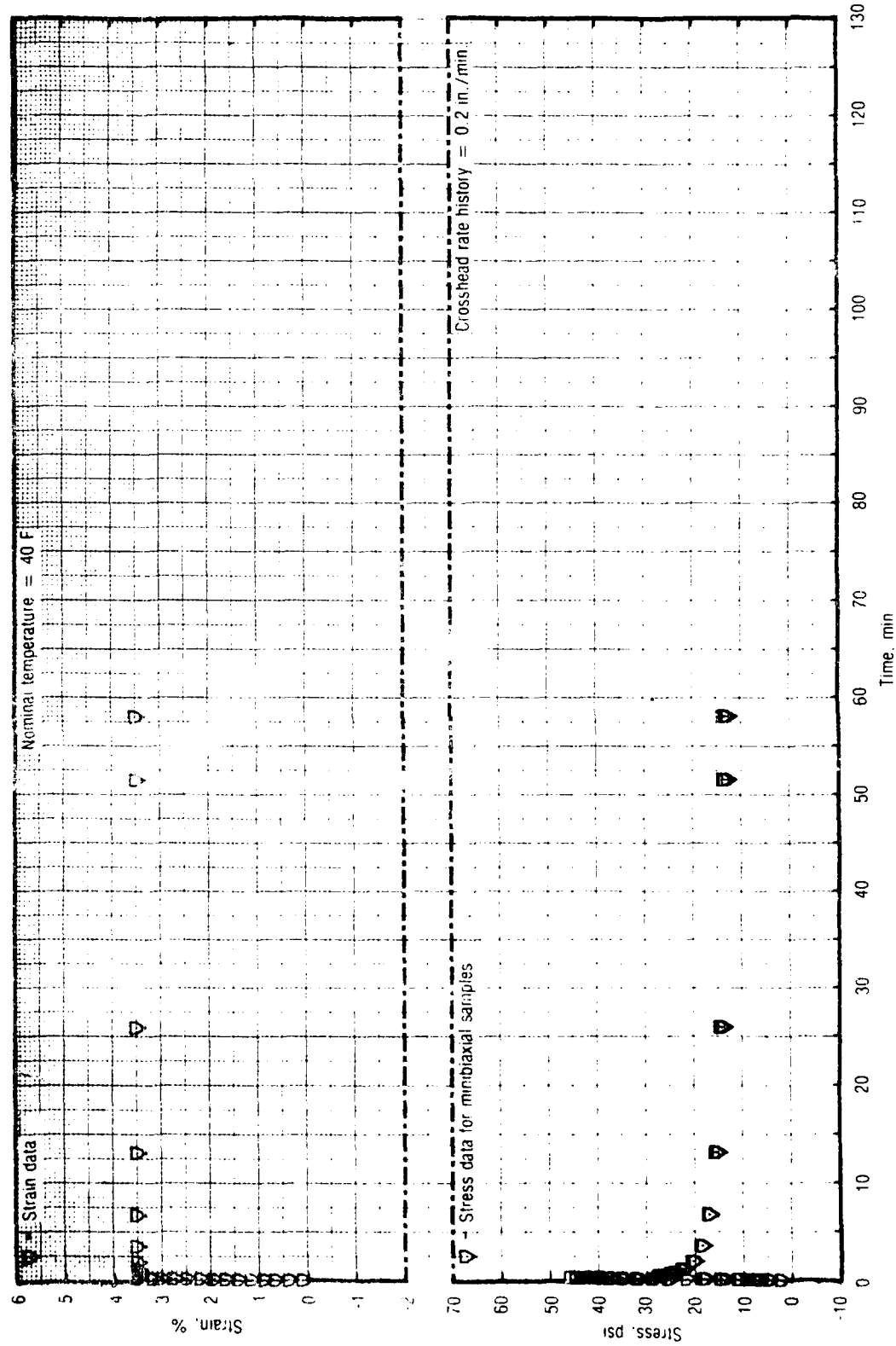
Figure 28. Test No. 16 - Stress While Step Straining for UTP-19,360B-400/177

28815
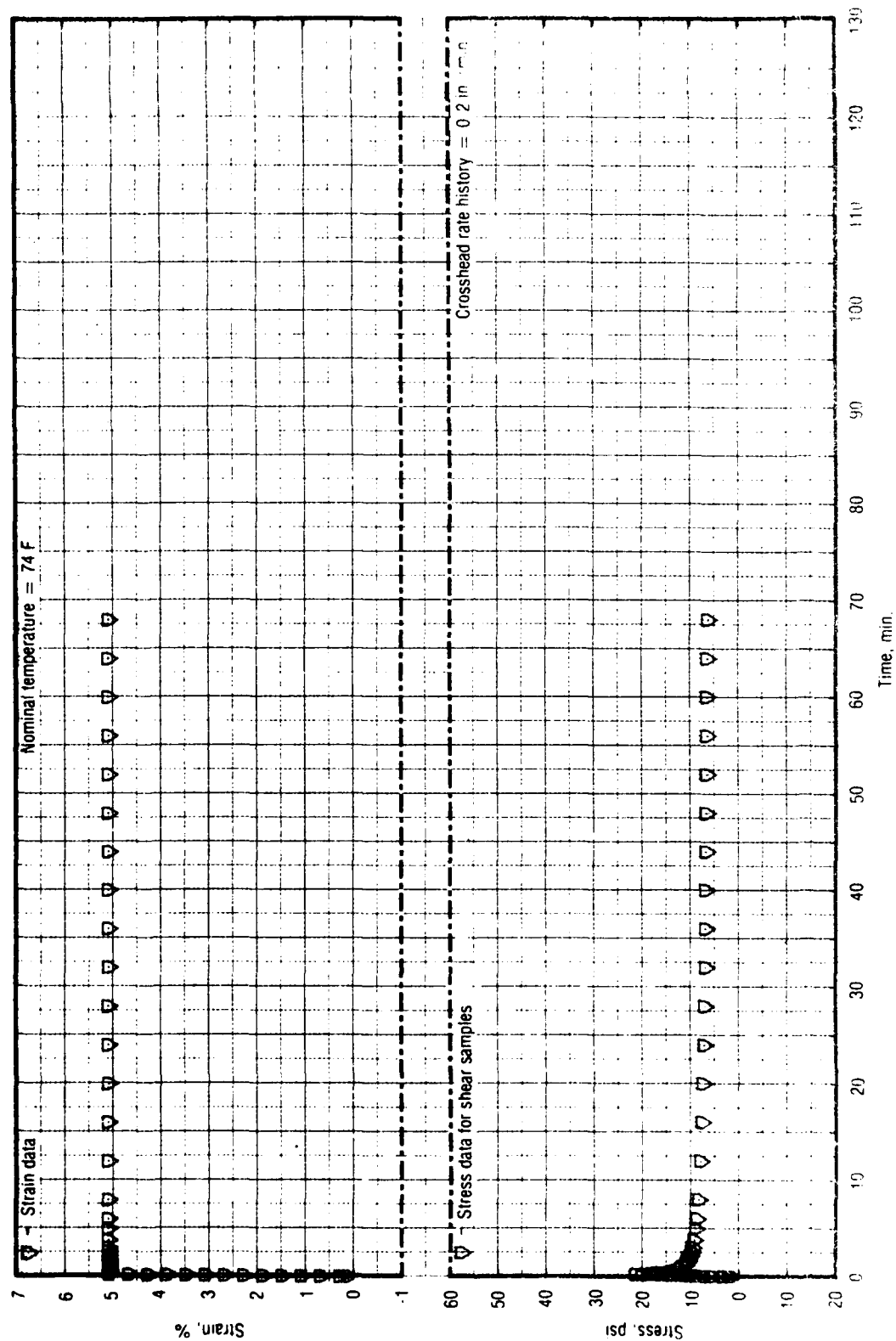
Figure 29. Test No. 17 - Stress While Step Straining for UTP-3001-750/7768

59

0.0004 in./min. Typical data are shown in Figures 30 for UTP-3001. Good reproducibility is shown within the set of three samples.

3.2.6 Biaxial Quinlan Complex History Test No. 19

The 1/4- x 1-1/4- x 6-in. biaxial samples of UTP-3001 and UTP-19,360B were subjected to the complex cycling and relaxation history indicated in Figure 23. When the tests were run, the linkage (misalignment, etc.) was such that the samples were not loaded with an equivalent amount. The first sample to be loaded had the correct strain determined but strain on the other samples had to be adjusted to the time the ramp started on each. Each sample was separately reduced and data were modified to pick up the peak and minimum stress points. Sample 1 for UTP-3001 is shown in Figures 31 through 33 where the complex test has been divided into segments on an expanded time scale to show test details. The first cycle in Figure 31 shows no load and the second cycle shows very little. By contrast sample 3 (not included here) had a first peak stress-strain of 37 psi, 2.26% and a second peak of 76 psi and 4.97%. During the unload part of the cycle after the stress reached zero, strain decay was estimated from other tests in which the strain was measured using a cathetometer.

3.2.7 Biaxial Ramp-Relax-Ramp Test No. 21

Ramp-relaxation-ramp tests were run on UTP-3001 and UTP-19,360B propellants with the 1/4- x 1-1/4- x 6-in. biaxial specimens. The first test was ramped at 0.0005 in./min to 6% strain and simultaneously cooled from 120 to 70F. It was held at 6% strain nearly 23 hr, then ramp-loaded to failure, while cooling towards 40 F. Data for UTP-3001 are shown in Figure 34; those for UTP-19,360B were similar. The cooling cycle did not end at the peak strain; consequently, the relaxation of stress was not the normal type behavior. The continued cooling increased the propellant stress so that the normal relaxation behavior did not start until the propellant temperature stabilized.

This test was repeated starting at 110 F and taken to 6% strain with a peak stress of 70 psi compared to 30 psi for the above test. The longer ramp time allowed the cooling to reach 40 F at the peak stress. The samples were allowed
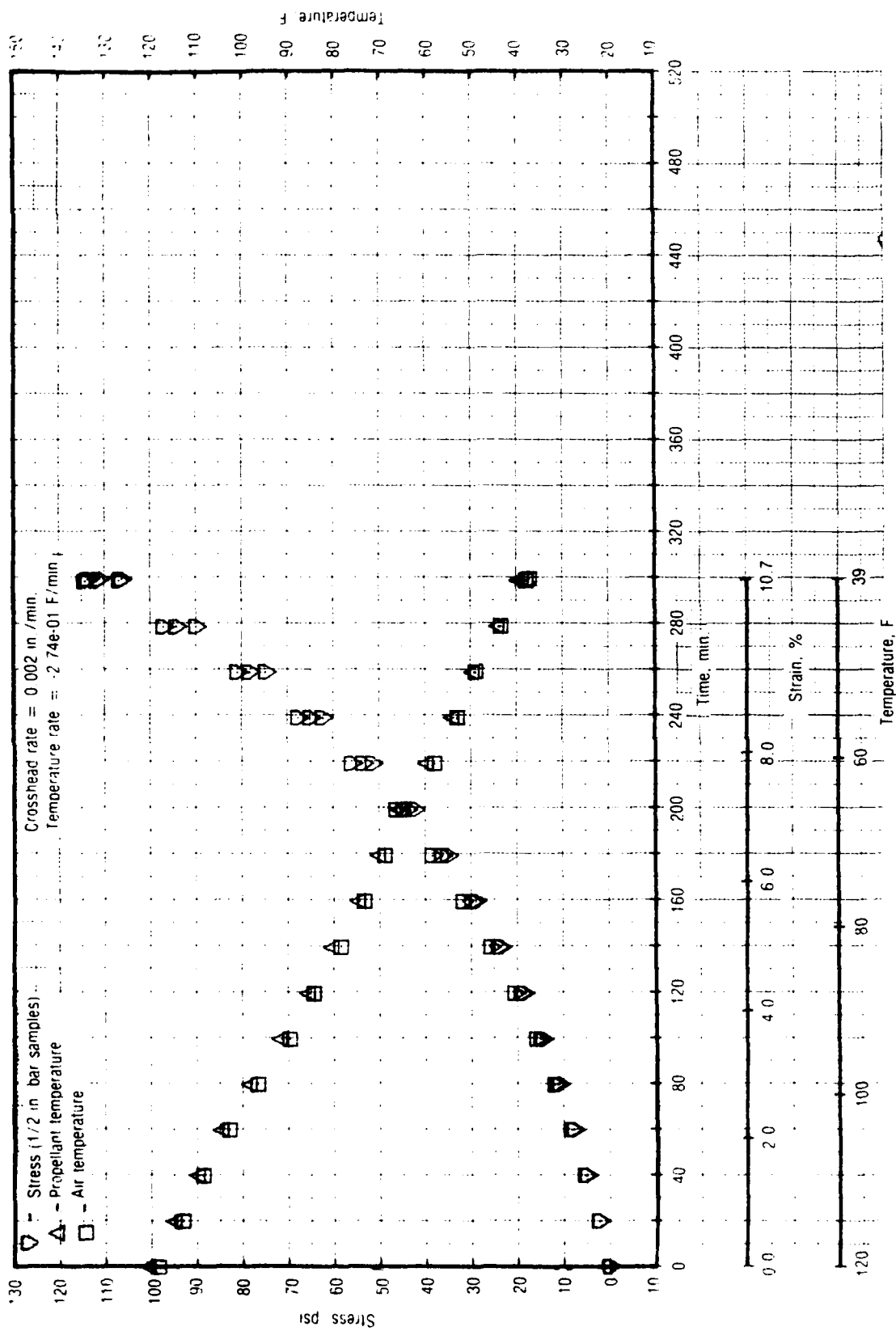
Figure 30. Test No. 18 - Stress While Straining and Cooling for UTP-3001-750/7768

28817

61
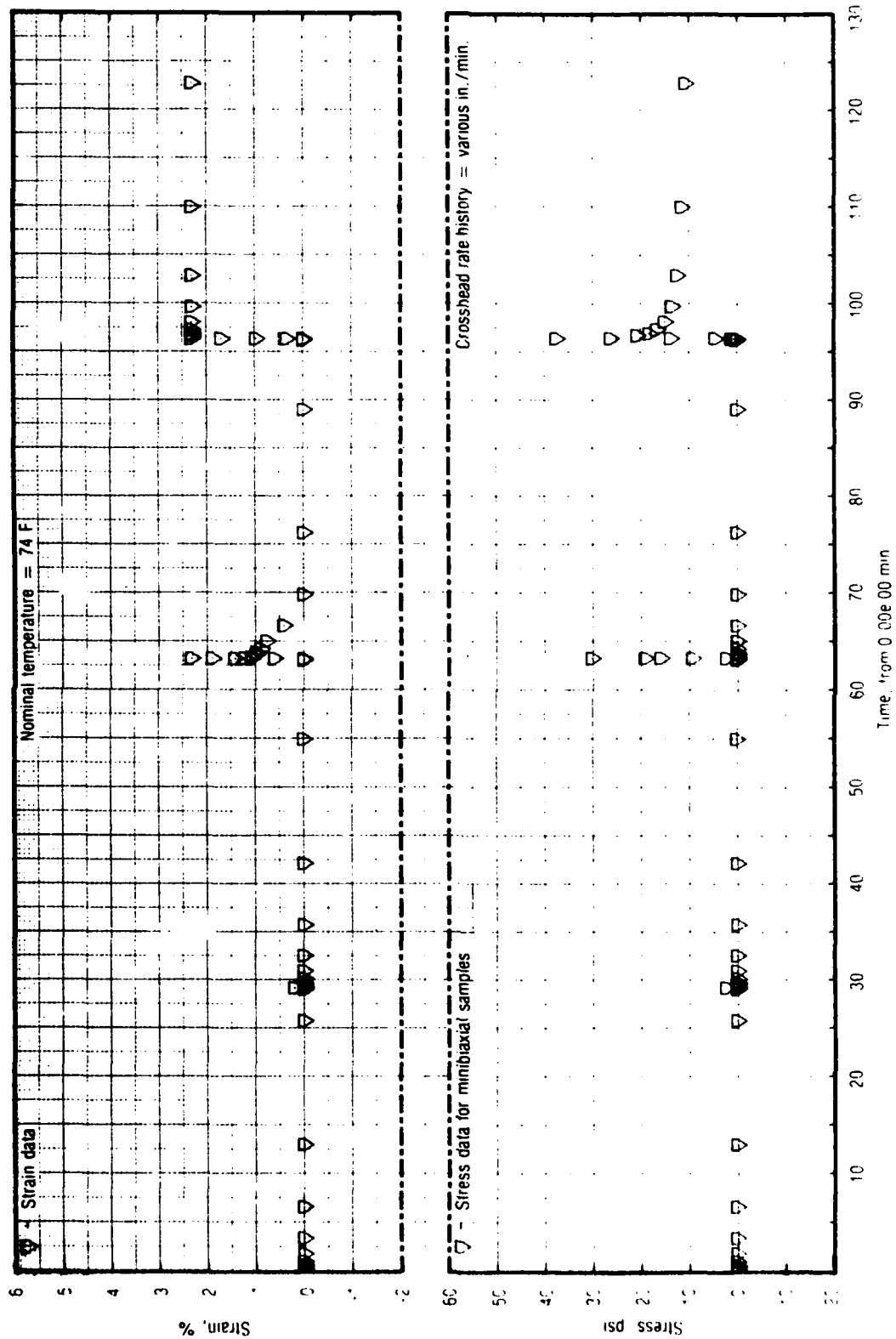
Figure 31. Test No. 10, Part 1 - Stress for UTP-2001-750/7768

62
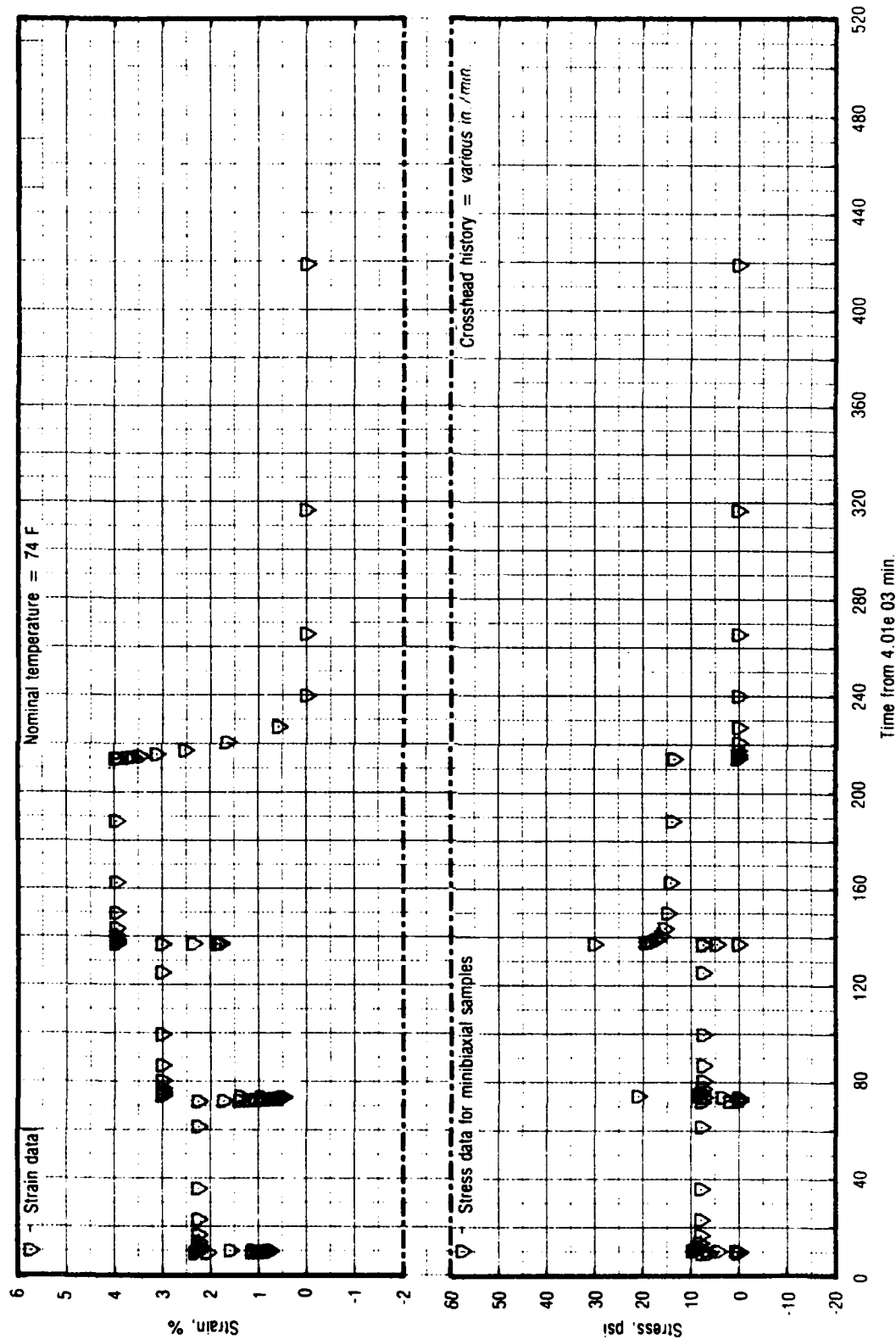
Figure 32. Test No. 19, Part 2 - Stress for UTP-3001-750/7768

63

28819
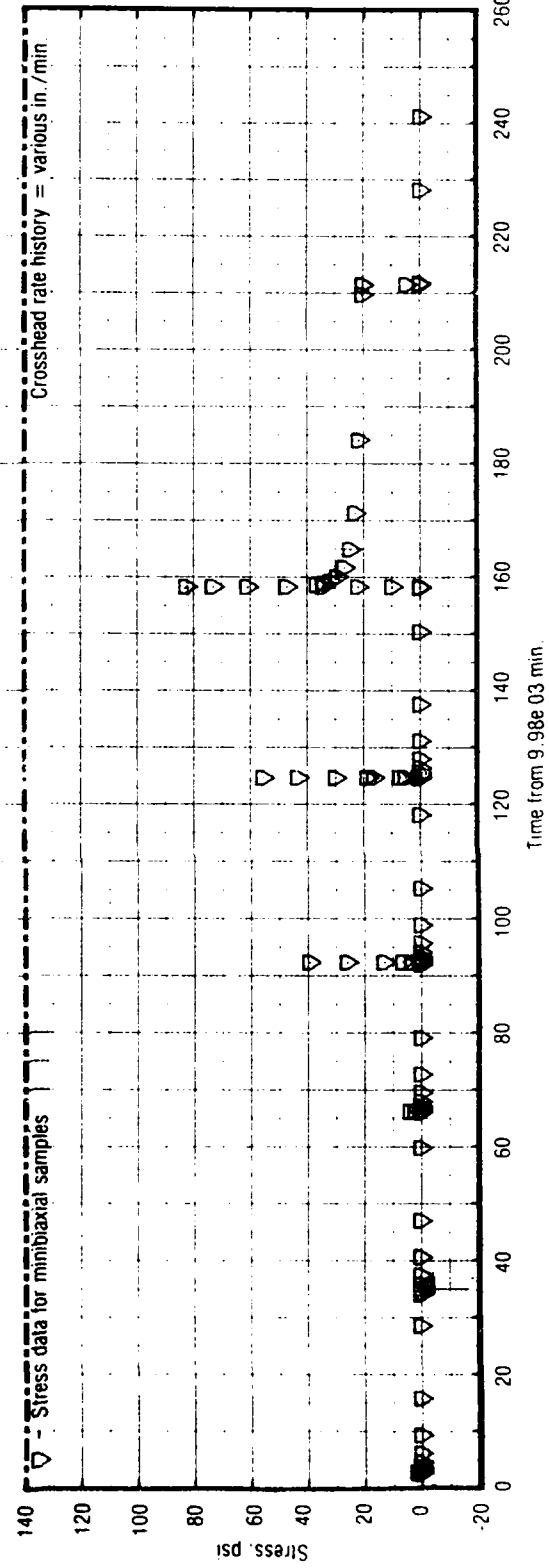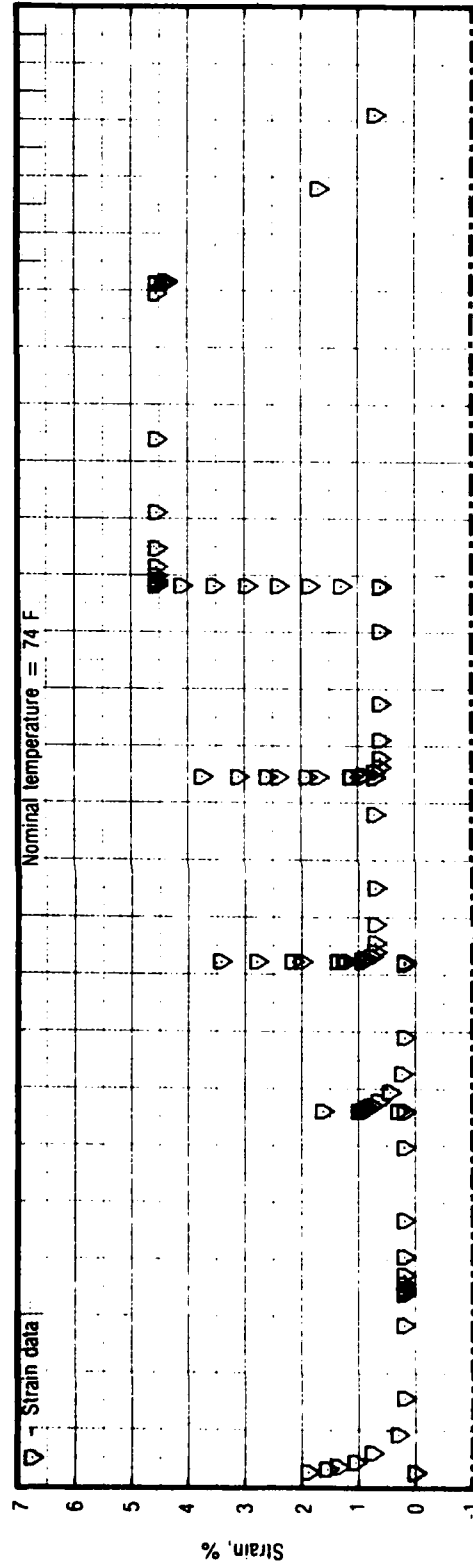
Figure 33. Test No. 19, Part 3 - Stress for UTP-3001-750/7768

28820

64
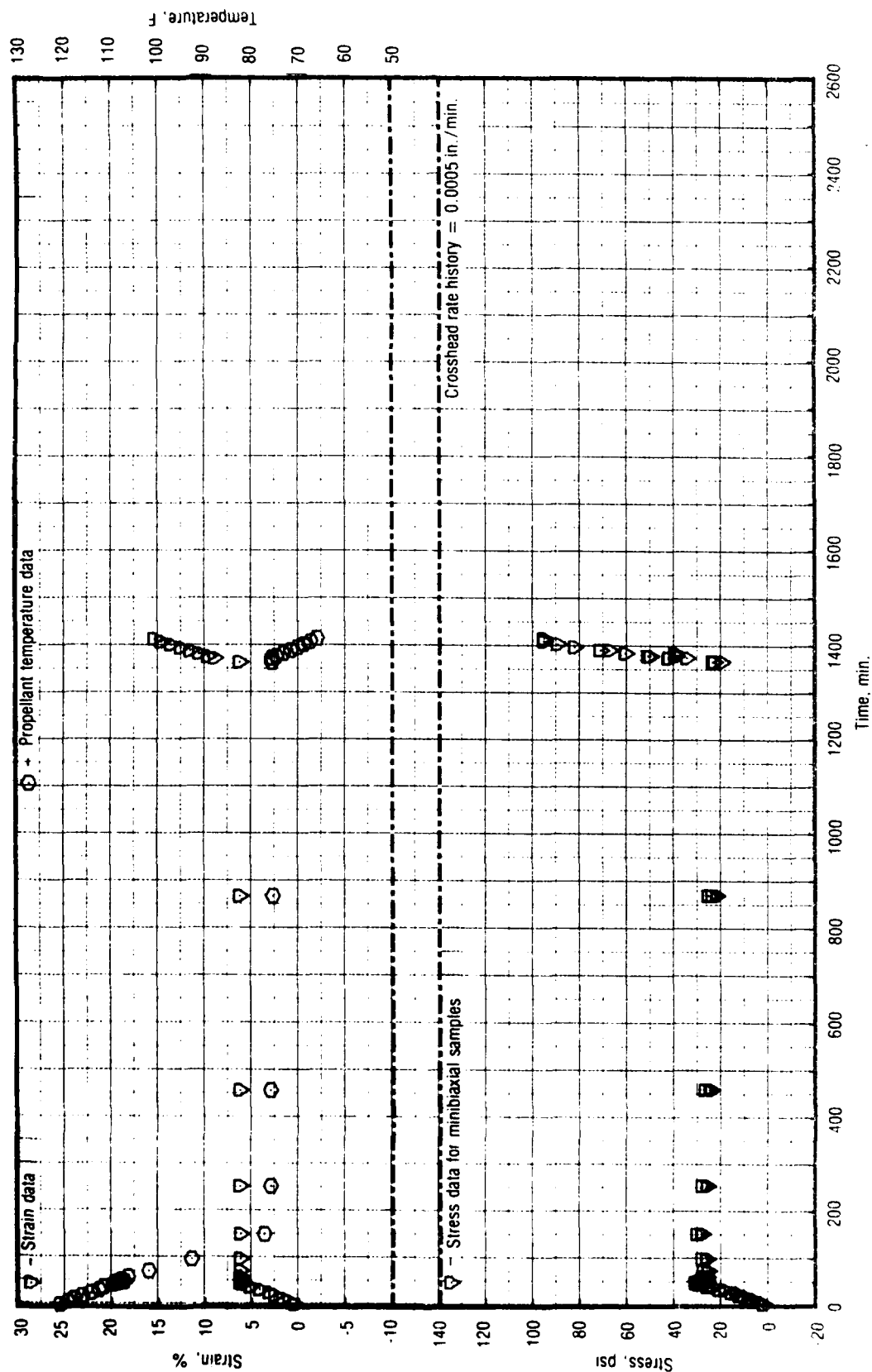
Figure 34. Test No. 21 -- Stress While Complex Straining and Cooling
for UTP-3001-750/7768

65

to relax overnight and then unloaded to 3% while warming the samples to room temperature.

3.2.8 Uniaxial, Biaxial, and Shear Comparison

Comparisons of the different samples were made in order to show that the pro-pellant used in each of the tests was of the same family. These comparisons were done at ambient temperatures for selected rates and were limited to strain rates that were close to each other. Such testing minimized the time-temperature equivalence shifts to small changes for negligible data input errors. The adjustments made for strain levels are given in Table 4.

The comparisons between uniaxial and biaxial in the table are close to the theoretical ratio of 75 to 80%. The shear to uniaxial ratios of 0.28 and 0.39 bracket the nominal theoretical value of 1/3. For the comparisons made in Table 4, the UTP-3001 and UTP-19,360B propellants have to be considered part of the same family. Any minor differences can be attributed to carton-to-carton variations.

Uniaxial and biaxial stress relaxation modulus data for UTP-19,360B are compared in Figure 35. The biaxial modulus was shifted using the uniaxial A_T shift factor. Figure 35 also shows that excellent agreement is obtained when the uniaxial modulus is multiplied by the theoretical value of 4/3 to correct it to a 2:1 principal state of stress.

66

TABLE 4. COMPARISON OF UNIAXIAL, BIAXIAL, AND SHEAR TEST DATA FROM PHASE III

Sample	Temperature, F	Rate, in./min	Strain Rate, in./in./min	UTP-3001 Strain, %	UTP-3001 Stress, psi	UTP-19,360B Strain, %	UTP-19,360B Stress, psi
Uniaxial Adjusted to	70	1	0.1667	10.0 5.8	128 86.8	10.0 5.6	57.7 38.9
Biaxial	70	0.2	0.160	10.0	148	10.0	65.0
Shear Adjusted to	70	0.2	0.2 0.150	5.8	23.3 24.0	5.6	14.3 15.0

Stress ratios for:

	UTP-3001	UTP-19,360B
Uniaxial/biaxial	128/148 = 0.86	57.7/65.0 = 0.89
Shear/uniaxial	24.0/86.8 = 0.28	15.0/38.9 = 0.39
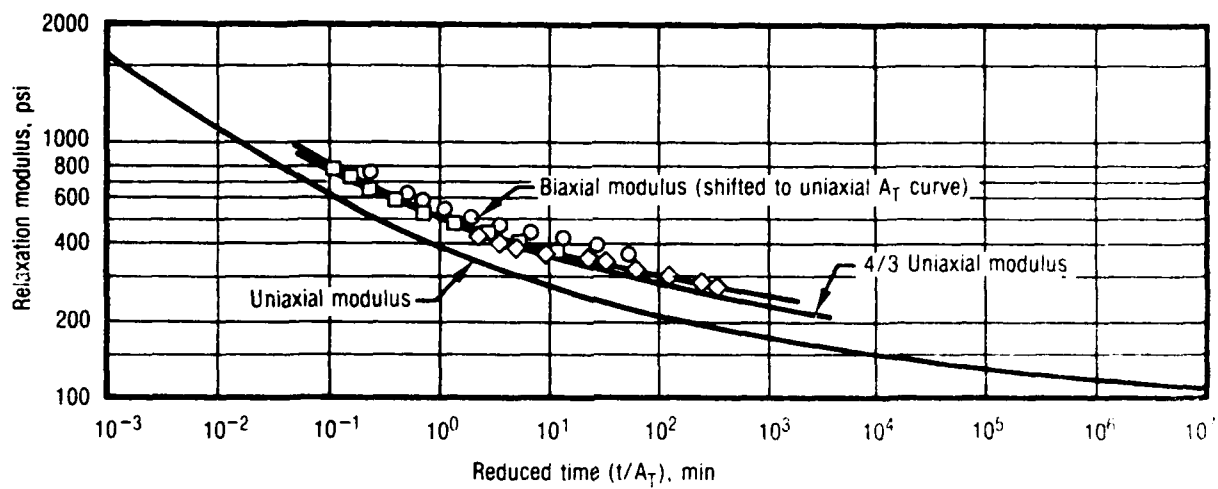
Figure 35. Comparison of Uniaxial and Biaxial Modulus
Curves for UTP-19,360B

30977

4.0 THEORETICAL DEVELOPMENT

4.1 INTRODUCTION AND PRELIMINARY STUDY

Generally speaking, solid propellants may be considered as lightly crosslinked long-chain polymers, highly filled with coarse solid particles. They respond viscoelastically to the action of external stimuli. But certain aspects of their behavior cannot be reproduced by classical linear or nonlinear theories of fading-memory materials. Thus, in recent years, much work has been concerned with the development of appropriate models to predict the mechanical response of solid propellants. A current trend is to express the observed response in terms of some measure of "damage" at the continuum level where damage is described as the difference between the observed response and that predicted by a fading-theory, such as linear viscoelasticity. There is now sufficient experimental evidence to show that damage per se is a microscopic phenomenon associated with the initiation and growth of flaws, debonding between matrix and solid filler particles, and molecular chain scission. Although it is largely irreversible, damage is partially recoverable shortly after removal of the loading system. This recovery from damage is termed as "healing." It is clear that, depending on the propellant and service requirements, it may also have to be accounted for in a constitutive theory for solid propellants.

In the present program, two approaches to characterizing damage have been followed. In the first one, damage is treated as the algebraic difference between the measured stress and that predicted by linear viscoelasticity, so that:

$$\sigma_c(t) = \sigma(t) - \sigma_\ell(t)$$

(1)

in which σ_ℓ and σ_c are the linear-viscoelastic and correction terms, respectively, with σ, the measured stress. In the second approach, the difference between measured and fading-memory type stresses is handled through a stress-correction function in the following form:

$$\sigma(t) = C\,(\epsilon_{max}, \ldots)\,\sigma_f(t)$$

(2)

69

The softening function (C) is made to depend on the past maximum strain or stress and $\sigma_f(t)$ represents an appropriate function of the fading-memory type stresses.

Broadly speaking, the models of R. Farris, M. Gurtin and M. Quinlan are of the type presented in equation (1) above, while those of R. Schapery, W. Hufferd and Swanson are of the form given by equation (2).

The following section presents some experimental evidence on the types of nonlinearities exhibited by solid propellants, and briefly discusses the pioneering work of Mullins and Tobin in treating the large hysteresis observed in tire rubbers. During the preliminary phase a brief evaluation of the potential of basing constitutive models on molecular dynamics considerations was reviewed by Dr. S. M. Breitling, subcontractor to CSD, and Dr. R. P. Wool of the University of Illinois. Their conclusions and recommendations are discussed next. Subsequently, the nonlinear theory of Farris[5] is presented. This theory was used during the first pha.. of the program to predict the response of TP-H1011 and to compare with preliminary results of the other five constitutive laws investigated.

Next, the theory of linear viscoelasticity is applied to predict the response of UTP-19,360B and UTP-3001 under various strain histories. The ensuing results are the basis for comparing the propellant response as predicted by each of the constitutive laws. This comparison is most meaningful because each of the theories considered evolved from a set of modifications to linear viscoelasticity.

Finally, a detailed description is given of each of these five stress-strain relations. These include the original concept of the models, their current versions, comparisons of predicted and measured stresses for a variety of strain histories, and some pertinent guidelines for characterizing solid propellant according to each theory.

4.1.1 Experimental Background

The complex behavior of solid propellants, as well as some attempts at developing usable stress-strain laws for these materials, are well documented in

70

numerous studies.[3-31] These studies show that a given deformation process causes a change in the response properties of solid propellants, for instance a drop in the relaxation modulus. As stated before, this deviation from some expected response is what has been called damage. It is evidenced as phenomenological microscopic changes that are caused by undefined, but real, irreversible or partially reversible microscopic changes. Polymer bond breakage, vacuole formation in the polymer matrix, dewetting between the polymer matrix and solid filler particles, microcracking, etc., are among the possible microscopic causes of observed permanent-memory effects in propellants.

Studies on uniaxial solid propellant samples have indicated that these materials exhibit large hysteresis even at small strains. These studies have also revealed that the state of damage in solid propellants is determined primarily by the maximum strain or stress undergone during the loading histories.

The typical nonlinear hysteresis and permanent-memory effects exhibited by solid propellants are illustrated in Figure 36. A series of finite-duration, variable-strain-level ramp pulses were used to obtain the propellant response subsequent to a given damage history.[12, 13] All ramps had the same initial moderate rise rate, with two exceptions to be noted later, and all ramps had the same very slow decline rate.

Observations of the load on the specimen after returning to its original length (zero strain) showed that it took approximately 30 min for the stress to relax to zero.

A series of tests was run on a 1/4- x 1/4- x 4-in. tab-end sample. The virgin specimen was initially strained to a level of 7.04% and allowed to relax to achieve a rest-state condition. The first part of the testing is shown in the lower half of Figure 36 (curves A-H) and the last part in the upper half (curves H-M).

Curve A shows the load response to the first pulse. The specimen was then subjected to four successive ramp strain pulses ranging from $\epsilon^\circ = 3.82\%$ to $\epsilon^\circ = 6.34\%$. There was a rest period allowed between each pulse. The results are shown in Figure 36 as curves B through E.

71
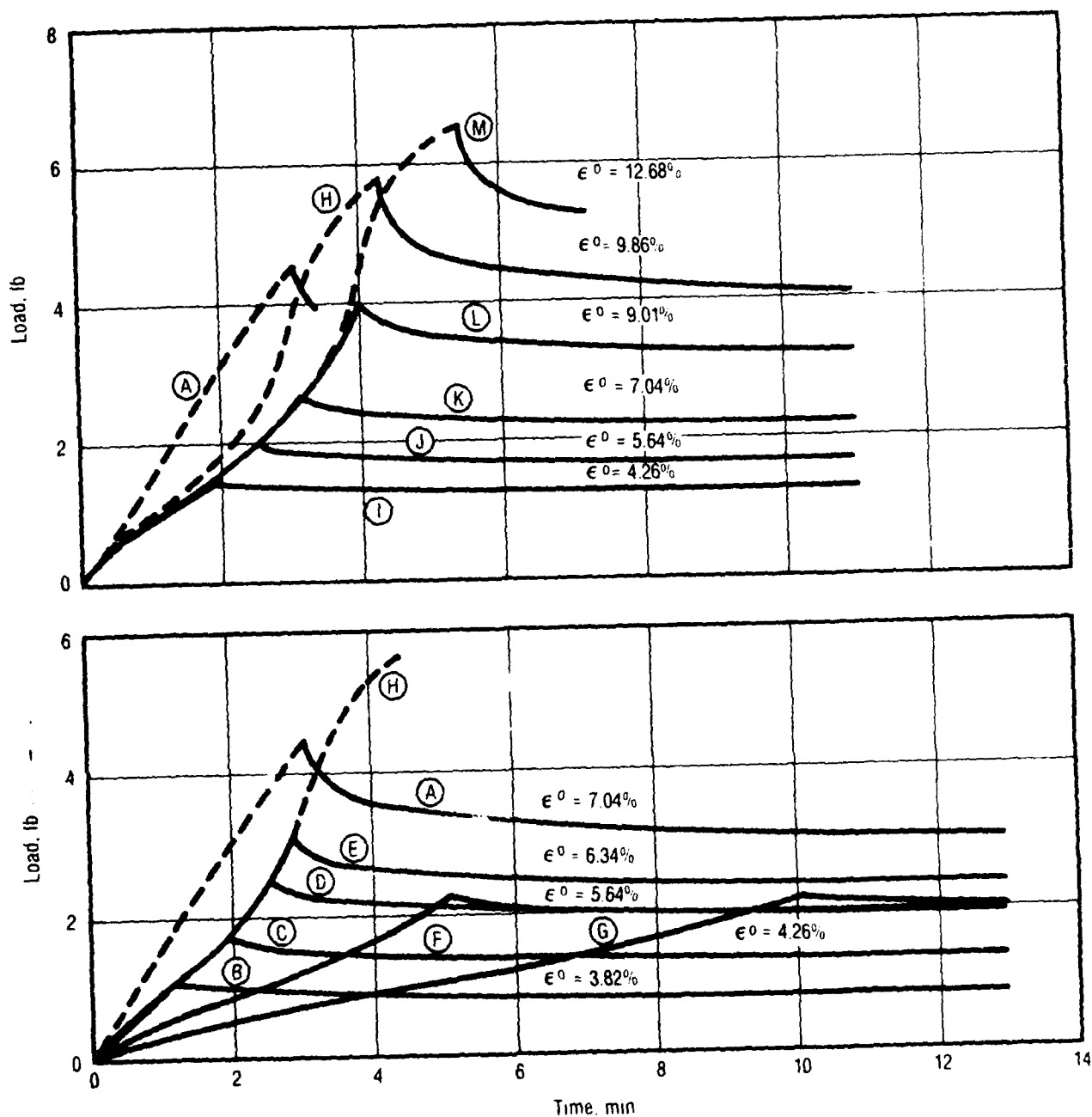
Figure 36. Relaxation After Damage

22019

Two aspects of the propellant's behavior are worth noting. First, during the constant strain rate portion of the ramp, each successive load-time curve is essentially identical. This phenomenon indicates that the "new material" has the same nonlinear rate-dependency under repeated strain conditions as long as the strain levels are below the previous maximum strain of $c^0 = 7.04\%$. Second,

72

the relaxation portions of the curves are essentially homologous, indicating that a viscoelastic relaxation process is taking place.

Curves F and G present the results of two additional tests at two successively lower strain rates where the sample was loaded to 5.64% strain each time. A strong rate dependency is observed during the rise portion of the ramp; however, curves F and G rapidly rejoin curve D indicating that the material is behaving in a viscoelastic fading-memory fashion.

The specimen was next subjected to a ramp strain pulse reaching a higher strain level (ϵ^0 = 9.86%) than the maximum 7.04% previously experienced (Figure 36, curve H). The first part of curve H repeats the loading ramp portion of curves B-E to indicate the same "new material" rest-state. Note that the load-time curve returns to the initial or virgin constant strain rate curve once the previous maximum strain (7.04%) has been passed.

Subsequently, the specimen was strained with the ramp pulse to four different strain levels less than 9.86% (ϵ^0 = 4.26%, 5.64%, 7.04%, and 9.01%), as shown in curves I through L. The results show that a new rate-dependency has developed (compare the rising portions of I through L with the rising portion of H). Thus, another "new-material" rest-state has been produced as a result of the second maximum strain level of 9.86%. Lastly, the specimen was strained to another new maximum of ϵ^0 = 12.68% as shown in curve M. It returned again to the virgin undamaged curve once the 9.86% strain level was exceeded.

The above experimental evidence suggests that the form of the constitutive equation should remain unchanged with respect to the material's current rest-state. This condition should remain as long as the damage is unchanged (i.e., the ϵ_{max} is unchanged during its subsequent strain histories).

Figure 37 shows a replot (curves N and O) of some of the results just discussed. After an initial maximum strain (7.04%) the specimen was allowed to return to a rest-state and then strained to a value of ϵ^0 = 5.64%, with the result shown as curve P. These three identical strain history tests of three different material states indicate that the higher the state of damage (primarily ϵ_{max}), the softer the material response upon subsequent testing.

73

Strain (ϵ), %

.10

5

0

Load, lb

8

6

$\epsilon_{max} = 12.68\%$

$\epsilon_{max} = 9.86\%$

$\epsilon_{max} = 7.04\%$

Note Curve N is the same as
curve D in Figure 65. curve O is
the same as curve J in Figure 65

$\epsilon = 5.64\%$

$\epsilon = 5.64\%$

$\epsilon = 5.64\%$

4

Ⓝ

2

Ⓞ

Ⓟ

0

0   2   4   6   8   10   12   13

Time, min
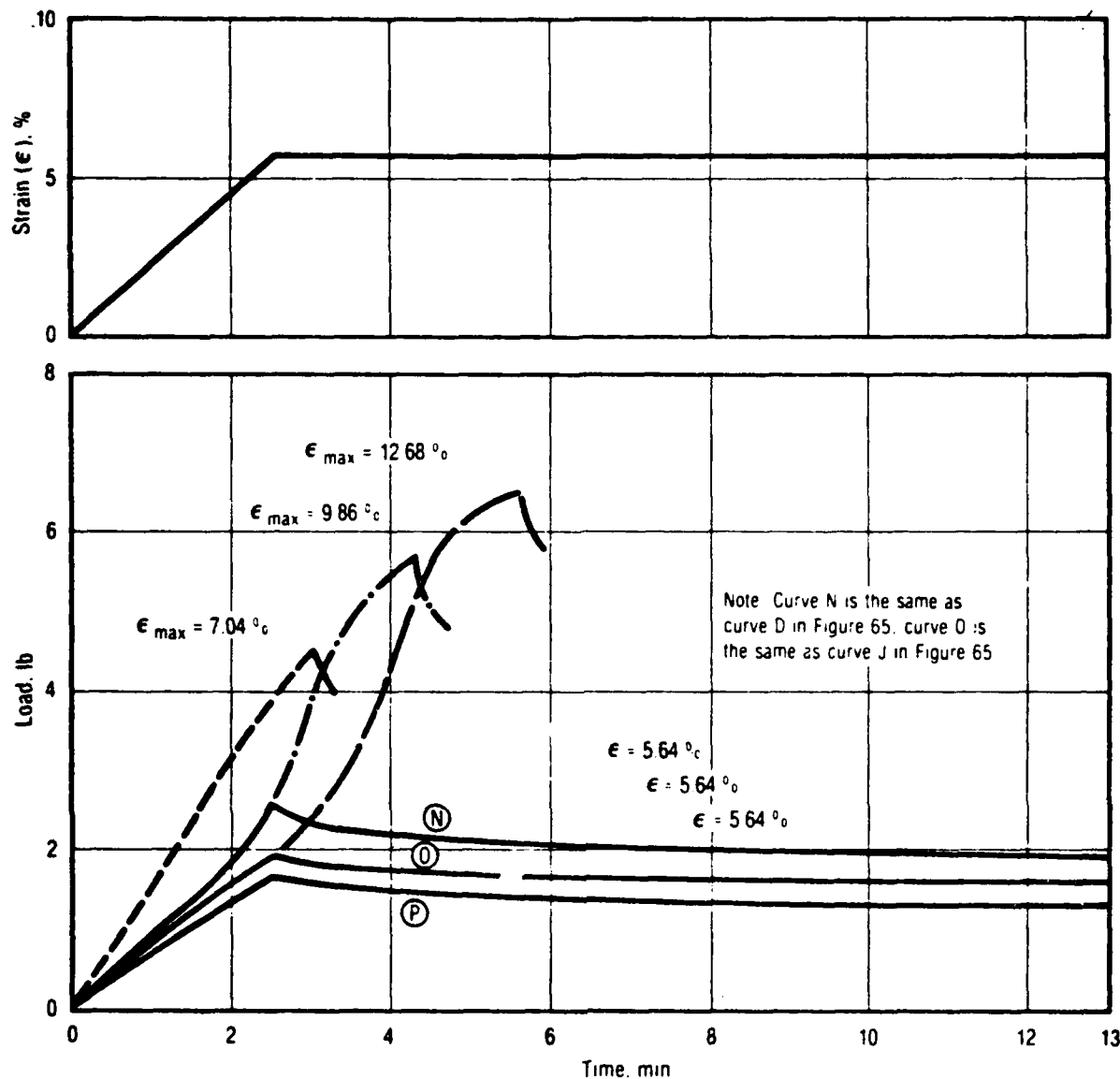
Figure 37.   Relaxation after Damage

22020

In addition, other experimental studies have pointed out the importance of
healing effects, load duration, and initial strain rate.[12, 13, 14, 15] Finally,
it is important to note that the behavior of solid propellant, depicted in
Figures 36 and 37, is similar to that exhibited by rubber. The nonlinear
uniaxial stress response of rubber, with or without carbon black filler and
in the absence of time effects, was well characterized by Mullins and Tobin[27]
with equation (3).

$$\epsilon = \epsilon_u \ F$$

(3)

74

where:

ϵ = engineering strain. The Mullins-Tobin model is not limited to small strains.

$\epsilon_u = \epsilon_u(\sigma)$ = strain as a function of engineering stress for the polymer without filler and without damage. The characteristic shape of this function is shown in Figure 38.

$F = F(\sigma_{max}, N)$ = damage or softening function which depends on the maximum stress experienced by the rubber and the number N of loading and unloading cycles. F is not very sensitive to N, but depends strongly on any hard filler particles that may be present.

A large amount of rubber data can be predicted by means of this equation when the samples are not allowed to rest between cycles. Recovery or healing occurs as a function of the rest time. Therefore, healing would have to be considered in an accurate characterization of rubber.

Introducing the inverse of $\epsilon_u = \epsilon_u(\sigma)$, equation (3) may be put in the form:

$$\epsilon = f\ (\epsilon/F) \qquad (4)$$

which shows that F (where $F \leqslant 1$) is a strain-magnification factor. The ratio ϵ/F is interpreted by Mullins and Tobin to be the average strain in the rubber phase
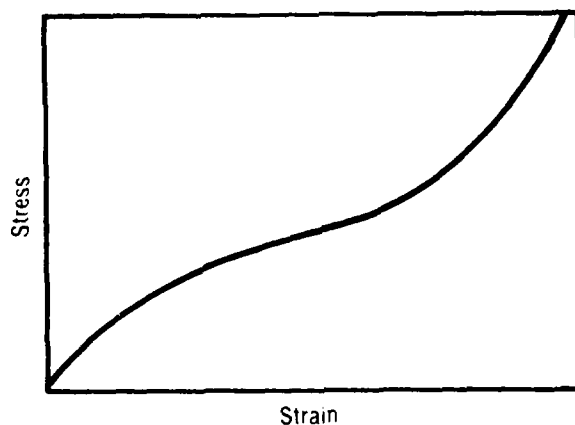
Figure 38. Stress-Strain Curve for Rubber

22074

of a hard particle-filled rubber. Without damage in a highly-filled rubber, $F \ll 1$. As the rubber is cycled between the strains $\epsilon = 0$ and $\epsilon = \epsilon_{max}$, the ratio ϵ/F at any strain decreases, and therefore the stress decreases. The shape of the stress-strain curve is still as shown in Figure 38. It is similar to that for solid propellant after first-time loading. This fact and the ability of the model presented in equation (3) to reproduce a large amount of rubber data explain the great influence of the Mullins-Tobin approach on the development of nonlinear constitutive theories for solid propellants.

4.1.2 Potential Physical Parameters for Damage and Healing

A fundamental problem of continuum mechanics is the rationalization of mathematical models with a body of experimental data. As the complexity of the physics increases it becomes progressively difficult to identify unambiguously those theories and models which properly treat the critical mechanisms operating in the physical process. Nowhere is this more apparent than in viscoelastic materials undergoing damage. Frequently, a theory is a product of years of evaluation with layer upon layer of parametric refinements that lead to better numerical fits of given data sets which may not elucidate the underlying physics. It becomes very difficult to transfer the acquired experience with a given model to a new material system or a markedly different application in the same system.

Preoccupation with chemical-physics is equally fascinating and unproductive. The detailed investigation of molecular and chemical properties has been the domain of many investigators for long periods of time with little information that is applicable to real problems. However, several trends have been developing in the last decade that may prove productive if prudently implemented and coordinated with an applied effort. Boyd and associates at the University of Utah have successfully treated cooperative molecular motions in crystals and in the pseudo-amorphous state. The results of this work has not been applied to the development of continuum models.

A relevant question may be asked: "Is it possible to apply molecular dynamic methods directly to continuum mechanics?" The answer is clearly "no". Continuum theories do not consider the discrete molecular processes, just as the

molecular dynamics neglect microscopic deformations and stresses. However, the point of commonality between the two approaches is the treatment of energy. Both methods must consider energy as a function of movement and dissipative processes. Thus, it may be possible to use the molecular dynamic work done to date to guide in the selection of mathematical continuum models by evaluation of model functional forms and parameters based on molecular energetics. We were unable to accomplish this goal within the resources available to this program. Still, this is a laudable objective and should be continued in future constitutive theory development programs.

The evaluation would not be of a formulation of models based on first principles nor a calculation of model parameters. Rather, both functional form and parametric values could be judged for physical appropriateness using the molecular dynamic information. Conversely, the experimental continuum data could eliminate many molecular processes that do not contribute significantly to the macroscopic viscoelastic-damage mechanism. The interplay of a more fundamental molecular viewpoint with the mathematical models and an expanded experimental data base could prove extremely useful not only in the rapid identification of the fruitful, productive mathematical formulations, but in the elimination of poor models.

Included in the area of molecular dynamics is rate theory applications to macromolecular mechanical and dielectric loss experiments, cooperative polymer motion energetics, fracture and electron microscope fracture studies. These studies do not represent a coherent single field of study but rather a wide range of studies conducted on many types of materials, most frequently unfilled. The initial effort in this program was to collect and review some material likely to be of most interest and relevance to the propellant behavior. An evaluation should lead to the identification of a few molecular modes of motion and associated energetics applicable to the binder. This information can then be interpreted in a form (e.g., energy density, surface energy) helpful to the mathematical continuum model. Implicit in this interpretation is the descriptive physical model of molecular behavior that gives rise to the macroscopic observations.

A small cooperative effort between molecular and continuum approaches was carried out in this program to identify the compatibility of the mathematics and physics. Only minimal molecular dynamics experimentation was conducted. The objective of this initial effort was to capitalize on the molecular information presently available and evaluate the productiveness of the initial approach.

Table 5 briefly outlines potential areas where molecular dynamics can be expected to make an impact on damage-healing phenomena.

Processes occurring at the molecular and microstructural levels control the macroscopic response of materials. Therefore, a knowledge of these events, particularly to the extent of controlling damage, would provide guidelines for constructing the constitutive relations for the material. The nature of mechanically induced damage can be investigated in experiments which monitor both the occurrence of the damage and disappearance of damage (healing). Damage may express itself mechanically as a stress-softening effect, similar to the "Mullin's effect" in filled elastomer·, and may or may not involve cavitation, crazing, or bond rupture. Damage can of·an occur in a time scale and manner which create difficulty in evaluation or detection. However, healing studies provide a method of reversing the process, or "turning back the clock" in a controllable (via temperature) manner. Thus, the damage reversibility concept provides a method of evaluating damage mechanisms. This consideration was investigated briefly and at a preliminary level by Dr. Richard Wool of the University of Illinois during the initial preliminary studies of the program. Available methods for evaluating crack or damage healing are summarized in Table 6.

Damage healing studies were conducted with the intent of learning the mechanism of material damage at the molecular and microstructural levels because processes occurring at these material levels control the macroscopic response of the material. The approach is to study the nature of mechanically induced damage through experiments which monitor both the occurrence and disappearance (i.e., healing) of damage. Dr. Wool at the University of Illinois, Urbana, has conducted recent healing studies on the polymeric materials shown in Table 7.

78

TABLE 5. POTENTIAL AREAS OF IMPACT ON CONTINUUM MECHANICS BY MOLECULAR DYNAMICS

Molecular Considerations	Probable Functional Forms
Polymer intra-chain energetics	Chemical bond stretching, $U = K_1 (r - r_o)^2$
	Chemical bond angle bending, $U = K_2 (\theta - \theta_o)^2$
	Chemical bond torsion, $U = K_3(1-\cos 3\phi)$
	Atomic non-bonded interactions, $U = K_4\exp(-K_5 r) - \dfrac{K_6}{r^6}$
Polymer interchain energetics	Chemical bond rupture, U = bond strength
	Chain twisting, $U = K_7\cos\psi$
	Chain slip, $U = K_8\exp(-K_9 r) - \dfrac{K_{10}}{r^6}$
	Cooperative group motions, U = numerical results from computer simulations
Rate controlled processes	Diffusion of liquid components, $\dfrac{\partial c}{\partial t} = D\dfrac{\partial^2 c}{\partial x^2}$
	Chemical aging, $\dfrac{dc}{dt} = -kc$
	Continued crosslinking, $\dfrac{dc'}{dt} = k'c^n$
Fracture processes	Cohesive failure, $\gamma_c = \dfrac{\partial U}{\partial A}$
	Adhesive failure, $\gamma_a = \dfrac{\partial U}{\partial A}$

TABLE 6. METHODS OF EVALUATING CRACK HEALING

T9987

Mechanical	Spectroscopic
Tensile testing (MTS, Instron) Dynamic mechanical (Rheovibron) Izod impact fracture	Infrared with stress and temperature dispersive and Fourier transform (FTIR) X-ray, SAXD, WAXD NMR, broadline, pulse, magic angle
Optical	Eximer flourescence
Bright field plus stress plus temperature Dark field plus stress plus temperature Birefringence plus stress plus temperature	**Electron microscopy** Transmission (TEM) with stress Scanning (SEM) with stress Scanning-transmission (STEM)
Videorecording Photometric Small and wide angle light scattering	**Other** Picometry (density gradient) Dilatometry Visual Neutron scattering

TABLE 7. RECENT HEALING STUDIES

T9988

Materials Studied	Damage Investigated
Crystalline polymers	Microvoids <1 micron
Amorphous polymers	Crazes >1 micron
Glassy polymers	Izod fracture
Block copolymers	Microvoids
Filled composites	Stress softening

Studies of these materials have reached the following conclusions:

- In each material, complete healing was usually observed; i.e., all cracks, crazes, and microvoids disappear as heat in the mechanical sense.
- In each case, the virgin mechanical strength was restored.
- The kinetics of healing could be excellently modeled by the following equations:

$$-\frac{dD}{dt} = kD^n \tag{5}$$

k, n constants

D = Damage

$$R = 1 - \frac{1 - R_0}{(1 + Kt)^\alpha} \tag{6}$$

$$K = K_0 \exp - E/kT \tag{7}$$

K, α constants

- There exists a master healing curve (equation 6) for each material which is obtained by similar WLF approach to viscoelastic materials. The activation energy, E, is obtained from a plot of log (shift factor) versus 1/T. The master healing curve is sigmoidal with respect to log t, with a lower plateau at R = R_0 and an upper plateau at R = 1, at long times.

From these studies it has been concluded that the general mechanisms of healing consist of four stages:

1. <u>Surface Rearrangement</u> - Molecular motion on newly formed crack surfaces may cause new configurations which affect the following stages. The concept of damage history is therefore important. If significant rearrangement occurs, healing can be prevented.
2. <u>Wetting</u> - The surfaces of the crack can wet and the crack disappears optically, but only a minor fraction of the local mechanical strength is restored.

81

3. **Diffusion** - The chains on contacting surfaces interdiffuse and establish the virgin configuration of interpenetrated chains with a subsequent increase in mechanical strength. This step is the slowest (rate determining) and is responsible for the major fraction of mechanical strength recovery.

4. **Randomization** - The final stage is subtle and involves long time molecular motion which completely erases the damage memory.

From these observations, it may be postulated that with mechanical loading the mechanisms of damage consist of:

- Derandomization
- Diffusional demixing
- Dewetting
- Surface rearrangement.

Voids or cracks appear at step 3. The majority of stress softening damage, however, occurs at step 2. Therefore, considerable damage can occur under conditions approximating constant volume.

In the present limited study, the objectives were to:

- Obtain a master healing curve
- Study matrix molecular mechanisms
- Determine voiding processes
- Investigate molecular theories which may have an impact on constitutive applications.

Two propellants were investigated, an inert (NaCl-fill)Thiokol propellant and a "live" PBAN propellant supplied to Dr. Wool by CSD. The strain temperature history which was investigated is shown in Figure 39.

Recovery data were fitted to Wool's empirical kinetic theory:

$$R = 1 - \frac{1 - R_o}{(1 + Kt)^\alpha} \qquad (8)$$

82

with

$$K = K_o \exp(-Ea/KT) \qquad (9)$$

Experimental parameters are compared in Table 8.

One interesting observation was that the rate parameter, K, in equation (9) was constant for the inert propellant, whereas it was not for CSD live propellant.

The experimental results are shown in Figures 40 to 46. It can be seen that a master healing curve does, indeed, exist.
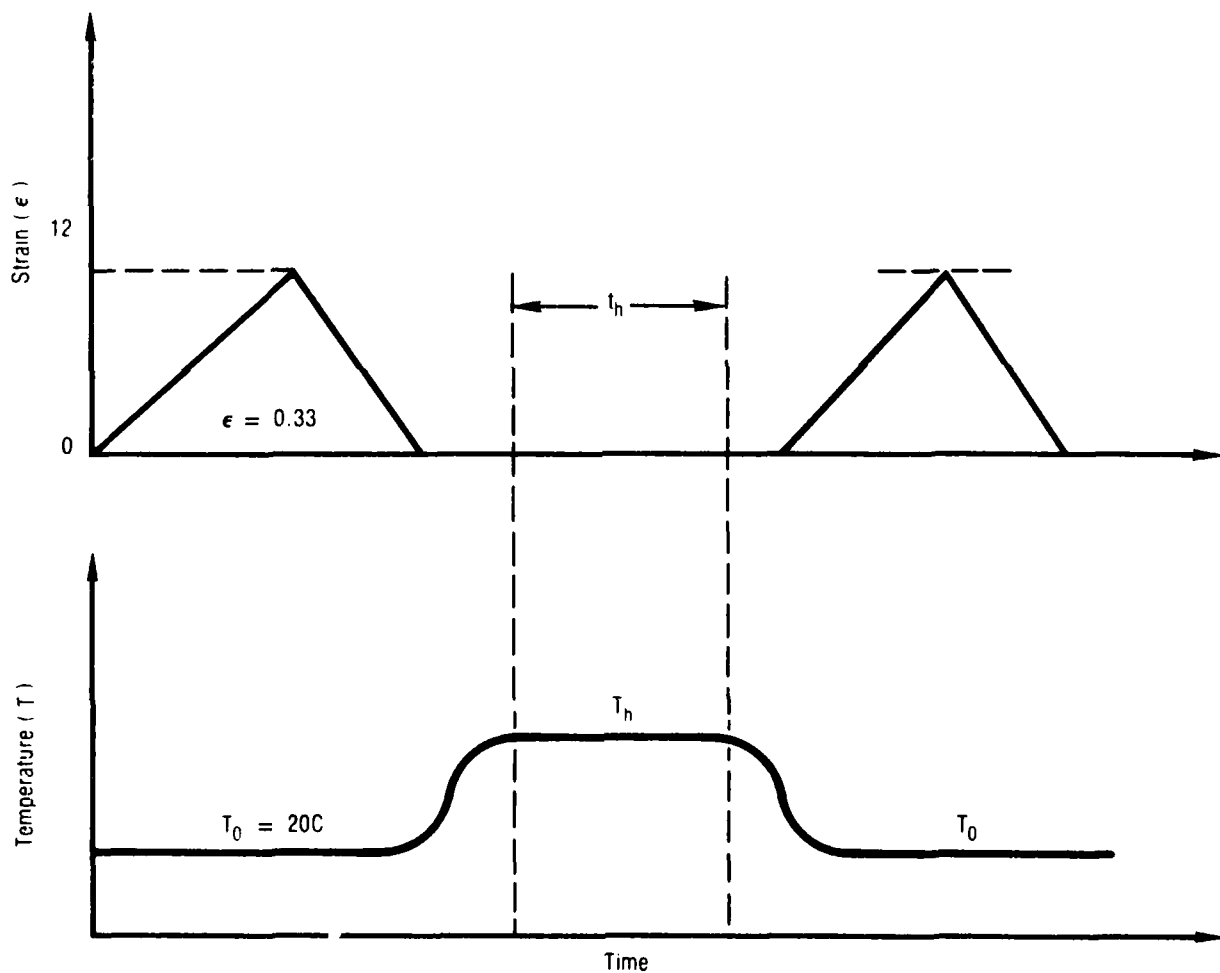
Figure 39. Strain Temperature Healing History

30953

TABLE 8. HEALING RESULTS

T9989

Inert Propellant	Live Propellant
NaCl-filled (Thiokol)	$K_0 = 18.3 \times 10^{36}$
$K = 18.443 \text{ min}^{-1}$	$\alpha = \alpha_0 - 3.747 \times 10^{-4} (T - T_0)$
$\alpha = 0.071$	$\alpha_0 = 0.053$
$R_0 = 0.26$	$T_0 = 20 \text{ C}$
$T = 24 \text{ C}$	$R_0 = 0.66$
$\epsilon_M = 12\%$	$E_a = 50 \text{ kcal/mole, K}$

Based upon this limited study, a new theory of healing as a function of stress level and time was proposed in the following form:

$$R(\sigma,t) = \int_{\tau=-\infty}^{\tau=t} \left[\sigma_0 + \frac{(T)}{\sigma_\infty} (t-\tau)^{\frac{1}{4}} \right] \frac{d\phi}{d\tau} (\tau,x) \, d\tau \qquad (10)$$

with several forms possible for $\phi(t)$ or $\dot{\phi}(H)$:

$$\delta(t) \sim \begin{array}{l} e^{-at} \\ K_s \ U(t) \\ K_0 \exp(-k_1(t-\tau_0)^2) \end{array} \qquad (11)$$

Analytical solutions are obtainable for these forms; however, the "new" constitutive theory, which would be based on a physical molecular model, is even more complicated at the present time than available phenomenological continuum models.

4.1.3 Farris Nonlinear Theory for Solid Propellants

The work of R. Farris[3] was a major attempt at predicting the nonlinear response of solid propellants in rocket motor analyses.
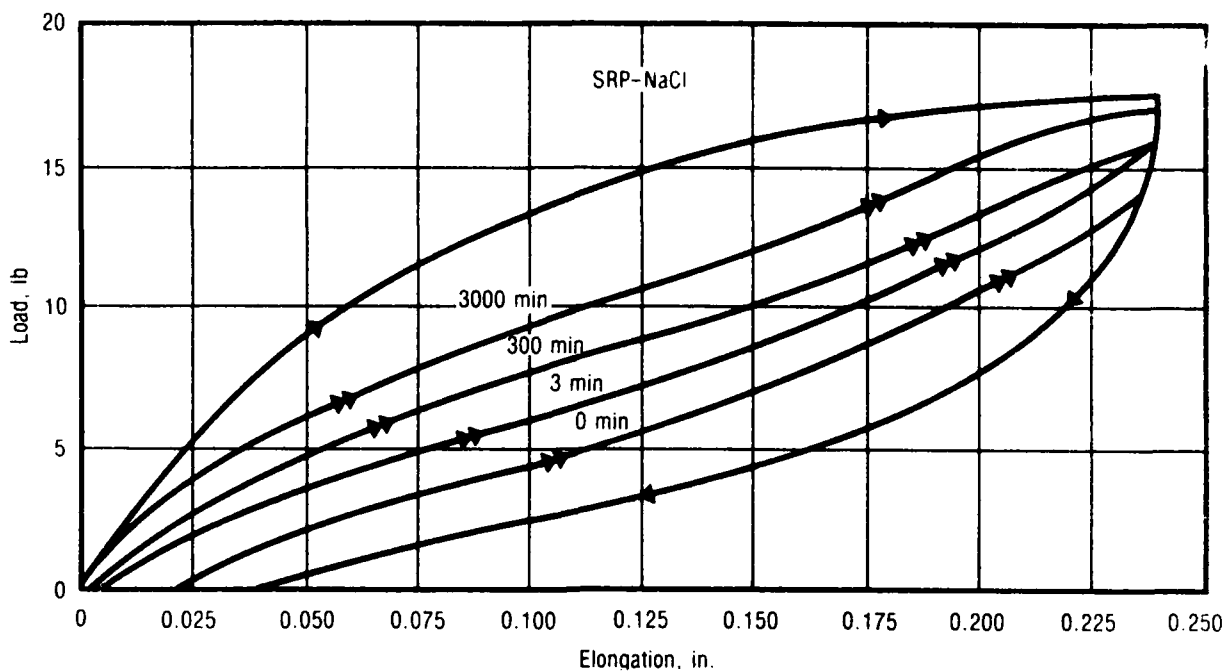
Figure 40. Healing Curves for Inert Propellant

30954
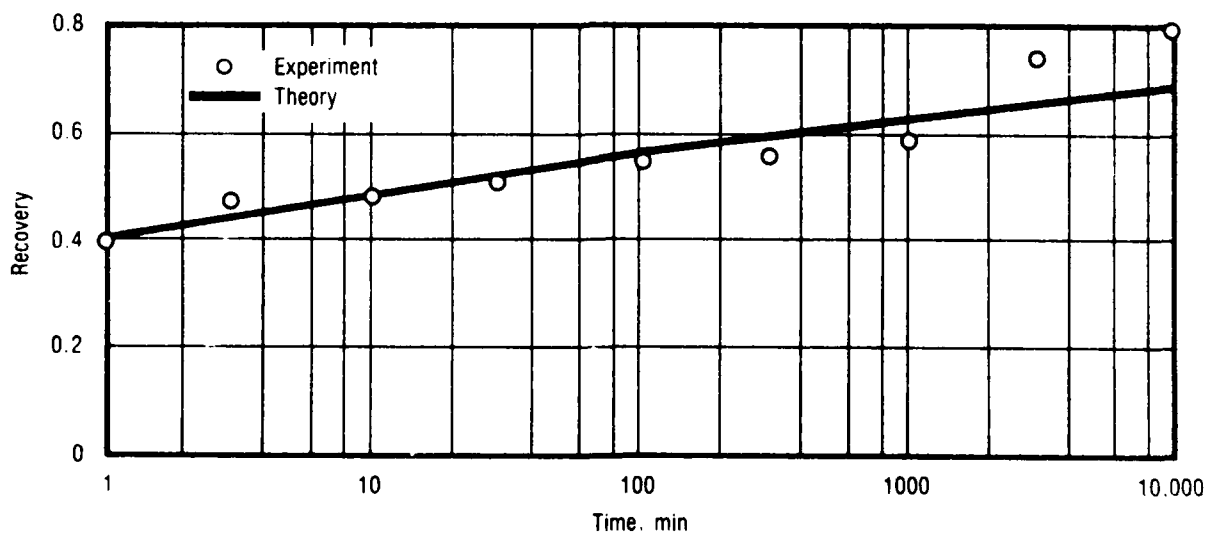
Figure 41. Inert Propellant Recovery

30955

85
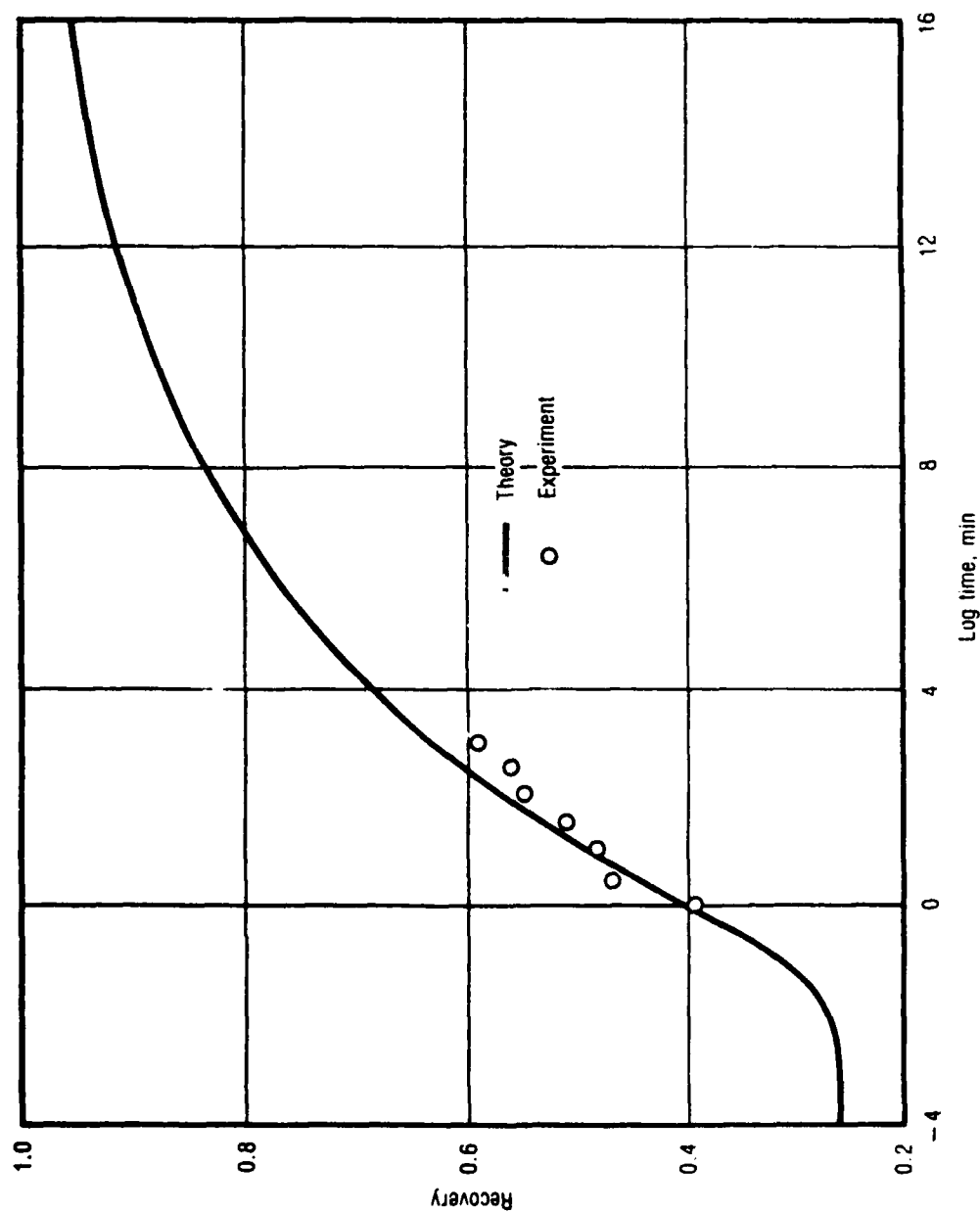
Figure 42. Healing Master Curve for Inert Propellant

30956
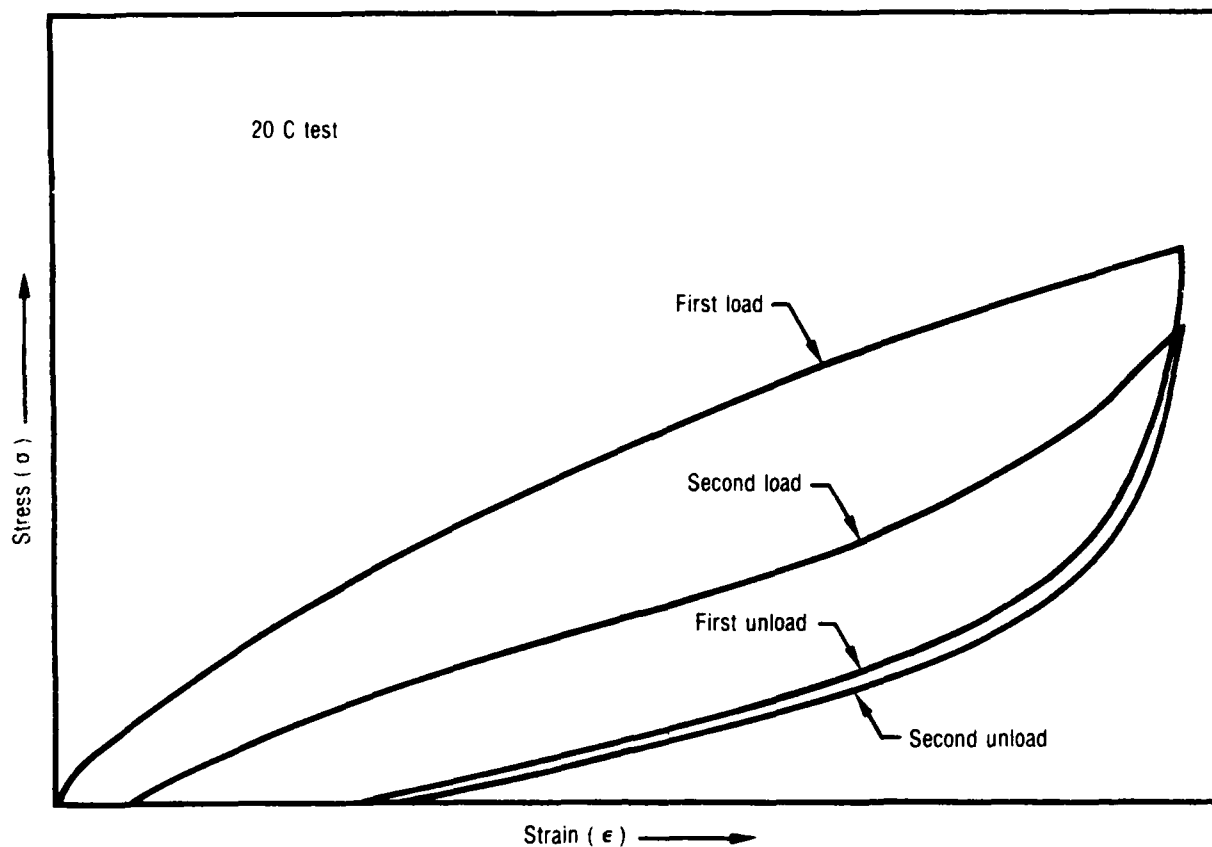
Figure 43. Load-Unload Curves for PBAN Propellant with Zero Healing Time

30957
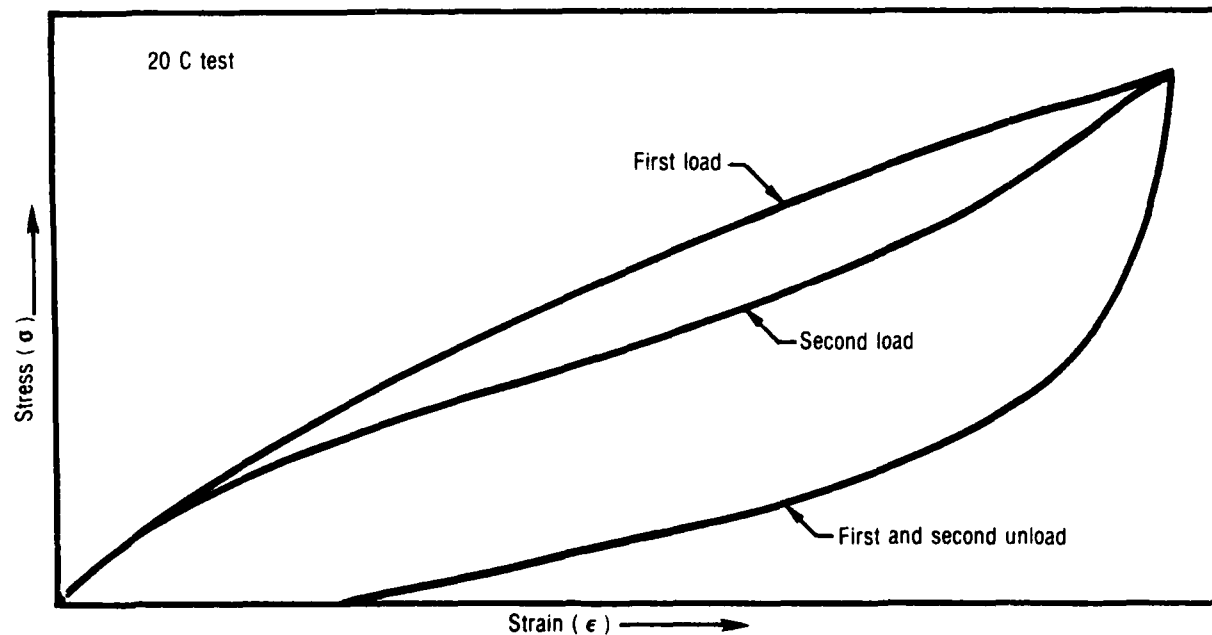
Figure 44. Load-Unload Curves for PBAN Propellant with 1000-min Healing Time

30958
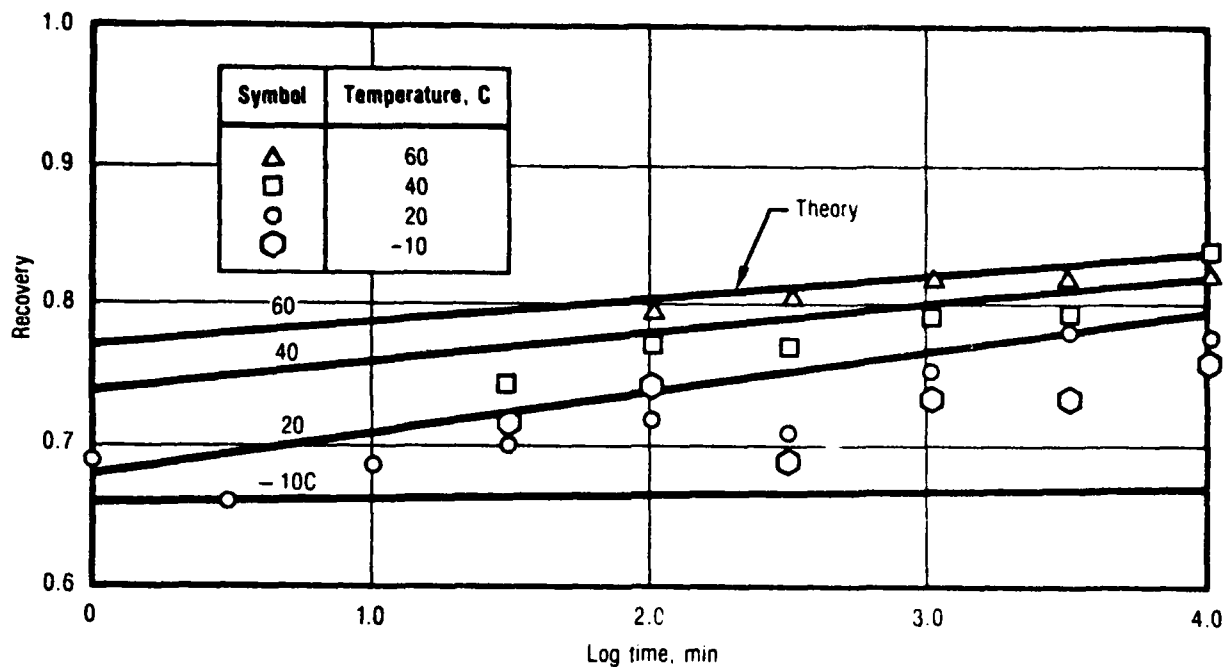
Figure 45. PBAN Propellant Recovery

30959
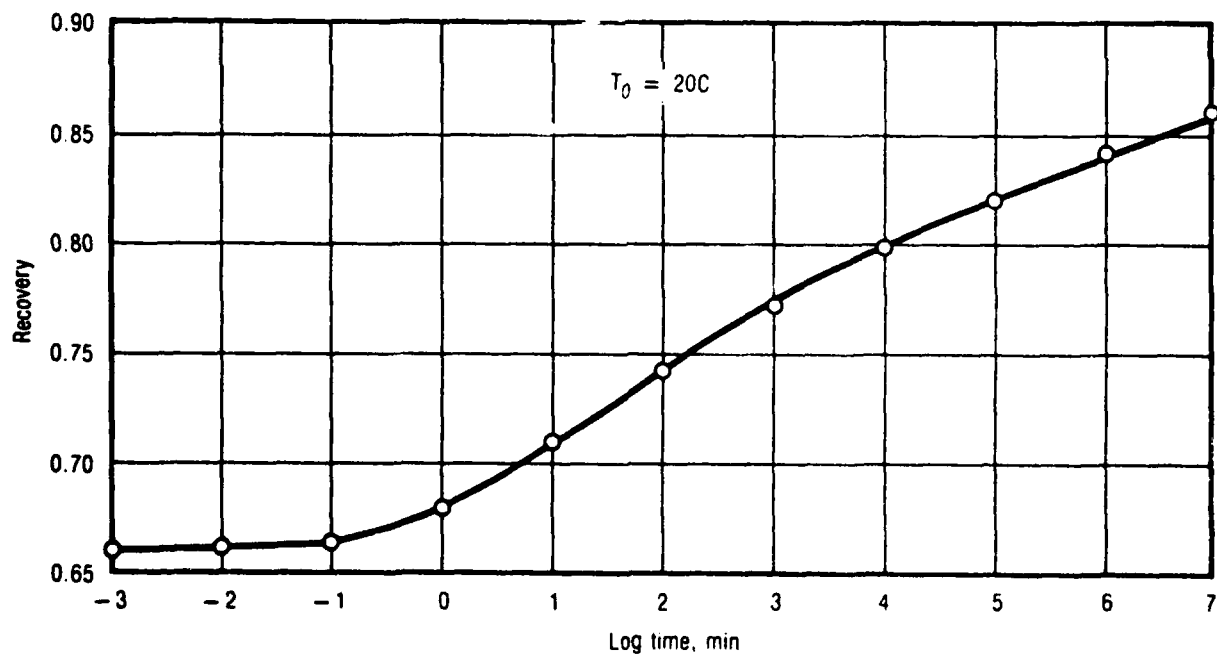
Figure 46. PBAN Propellant Master Healing Curve

30960

Experience with Farris' stress-strain law at CSD showed that this theory could not predict the response of solid propellants under strain histories that were not included in the set used for material characterization. For loading histories of the types included in such a set, however, the predictions were generally acceptable.

Farris' nonlinear theory, in the form presented next, was considered in the first phase of the program to compare it with the other five approaches originally proposed.

Based upon previous work on rubber elasticity, Farris postulated a model to account for the permanent-memory effects exhibited by many solid propellants under uniaxial loading. This model presumes the existence of inhomogeneities in the local strain field between filler particles, a distribution of polymer chain lengths between filler particles, and a uniform failure strain for each polymer chain. This model has been successful in predicting the nonlinear permanent memory response of solid propellants before dewetting when the models predict the same response in compression as in tension. This prediction is in agreement with experimental observations, although the molecular mechanisms contributing to the permanent memory response in compression are clearly different from those in tension.

Once dewetting occurs, the model is modified to account for vacuole formation and different results in compression and tension are expected. Farris presented the constitutive equation as the sum of an essentially time independent bulk stress σ_B and a time-dependent deviatoric stress σ_{ij}^d, so that in general

$$\sigma_{ij}(t) = \sigma_B \delta_{ij} + \sigma_{ij}^d (t) \tag{12}$$

where δ_{ij} is the Kronecker delta equal to unity if $i = j$ and zer otherwise. The form developed for the deviatoric stress is

$$\sigma_{ij}^{d}(t) = e^{-BI_{d}/I_{\gamma}} \left| A_1 e_{ij}^{d}(t) + A_2 \left(\frac{I_{\gamma}}{\| I_{\gamma} \|_{P_2}} \right)^{m_2} e_{ij}^{d}(t) \right.$$

$$\left. + \int_{0}^{t} A_3 (t - \xi) \dot{e}_{ij}^{d}(\xi) d\xi + \left(\frac{I_{\gamma}}{\| I_{\gamma} \|_{P_4}} \right)^{m_4} \int_{0}^{t} A_4 (t - \xi) \dot{e}_{ij}^{d}(\xi) d\xi \right| \quad (13)$$

where:

I_d = volume dilatation = $e_{11} + e_{22} + e_{33}$ for small strains

I_{γ} = octahedral shear strain = $\frac{1}{3} \left[(e_{11} - e_{22})^2 + (e_{22} - e_{33})^2 \right.$
$$\left. + (e_{33} - e_{11})^2 \right]^{1/2}$$

e_{ij}^{d} = deviatoric strain tensor

$B, A_1, A_2, A_3, A_4, M_2, M_4, P_2, P_4,$ = constants

and

$$\| I_{\gamma} \|_{P_i} = \left[\int_{0}^{t} \left| I_{\gamma}(\xi) \right|^{P_i} d\xi \right]^{1/P_i} \quad (14)$$

Equation (13) has been applied to reasonably complex deformation histories using unpressurized and pressurized uniaxial and biaxial test specimens. The agreement was not as good as would have been desirable, but it was still better than with linear viscoelasticity. Time-temperature superposition was included in equation (13) by introducing a time-temperature shift factor, A_T, and redefining the L_p norm of equation (14) in the form:

$$\| I_{\gamma} \|_{P_i} = \left(\int_{0}^{t} \frac{\left| I_{\gamma}(\xi) \right|^{P_i}}{a_T(\xi)} d\xi \right)^{1/p_i} \quad (15)$$

with $|\cdot|$ denoting the absolute value. Experimental data for simultaneous cooling and straining have been fit using equation (13) with the introduction

of a time-temperature shift function A_T through equation (15). The justification for introducing an A_T in the above manner, however, is not immediately obvious nor adequately explained in the available literature.

To represent the response to interrupted and cyclic constant strain rate tests, equation (13) was modified by setting $P_4 = \infty$ and $A_3 = -A_4$ so that:

$$\sigma^d_{ij}(t) = e^{-BI} d/I_\gamma \left\{ A_1 \overset{d}{e}_{ij}(t) + A_2 \left(\frac{I_\gamma}{\| I_\gamma \|_{p2}} \right)^{m_2} \overset{d}{e}_{ij}(t) \right.$$

$$\left. + \left[1 - \left(\frac{I_\gamma}{\| I_\gamma \|_\infty} \right)^{m_4} \right] \int_0^t A_3 (t - \xi) \overset{d}{\dot{e}}_{ij}(\xi) d\xi \right\} \qquad (16)$$

where:

$$\| I_\gamma \|_\infty = \max \left| I_\gamma(\xi) \right|, \quad 0 \leqslant \xi \leqslant t$$

The multiplier for the hereditary integral in equation (16) vanishes whenever the current value of I_γ is at its largest and is non-zero for all other values. This representation allows for viscoelastic (fading memory) response on unloading.

The bulk stress, σ_B in equation (12), was taken to be essentially time-independent, although there is coupling between distortion and dilatation as indicated in the exponential multiplier in equations (13) and (16).

The first attempt to represent the bulk stress took the form of a series:

$$\frac{\sigma_{kk}}{3} = \sum_{i,j=0}^{N} A_{ij} I_d^i I_\gamma^j \quad ; \quad A_\infty = 0 \qquad (17)$$

This equation adequately predicts the bulk stress as long as it does not vary greatly. When a hydrostatic pressure is superimposed, however, very poor results are obtained. In an attempt to overcome this difficulty, Farris modeled the compressibility of the gas voids caused by vacuole dilatation by treating them as spherical voids contained in an elastic medium. Assuming that the voids themselves offer no resistance so that all void dilatation is caused by distortion of the surrounding elastic material, the void content at zero pressure may be represented as a power law in terms of the octahedral shear strain I_γ, and assuming that the bulk behavior varies linearly with hydrostatic pressure, P, yields:

$$I_d = C_1 P + C_2 I_\gamma^n e^{\left(\frac{-3P}{4G}\right)} \tag{18}$$

for the dilatation, where C_1, C_2, and n are constants, and G is the shear modulus of the elastic matrix material.

The Farris approach to nonlinear characterization was only superficially investigated at the start of this program, since our previous experience on the Failure Mechanism Program had demonstrated that this approach was not useful. However, it was felt that the Farris code could give a meaningful baseline for comparison to the Quinlan theory, at least the predictions made in AFRPL-TR-78-37. Consequently, the same 12 cycle test data that were reported in AFRPL-TR-78-37 were input into the Farris nonlinear code. Results of this computation are shown for the first two cycles in Figures 47 and 48. Note that during the first cycle (Figure 47), the Farris fit gives much better correlation on both the loading and unloading parts of the cycle. The second cycle shows less clear agreement on the loading part of the cycle, similar agreement at the peak stress, and better agreement with the measured stress on the unloading cycle. Figure 49 shows the error in peak stress calculation for each cycle for both the Quinlan fit and the Farris fit. This measure of error also shows that the Farris theory fit the data quite well. The eleventh cycle data is questionable. This is the highest strain rate test and in fact could be erroneous as the test rate is specified as 4.0 in./min, which is not common nor even possible on some
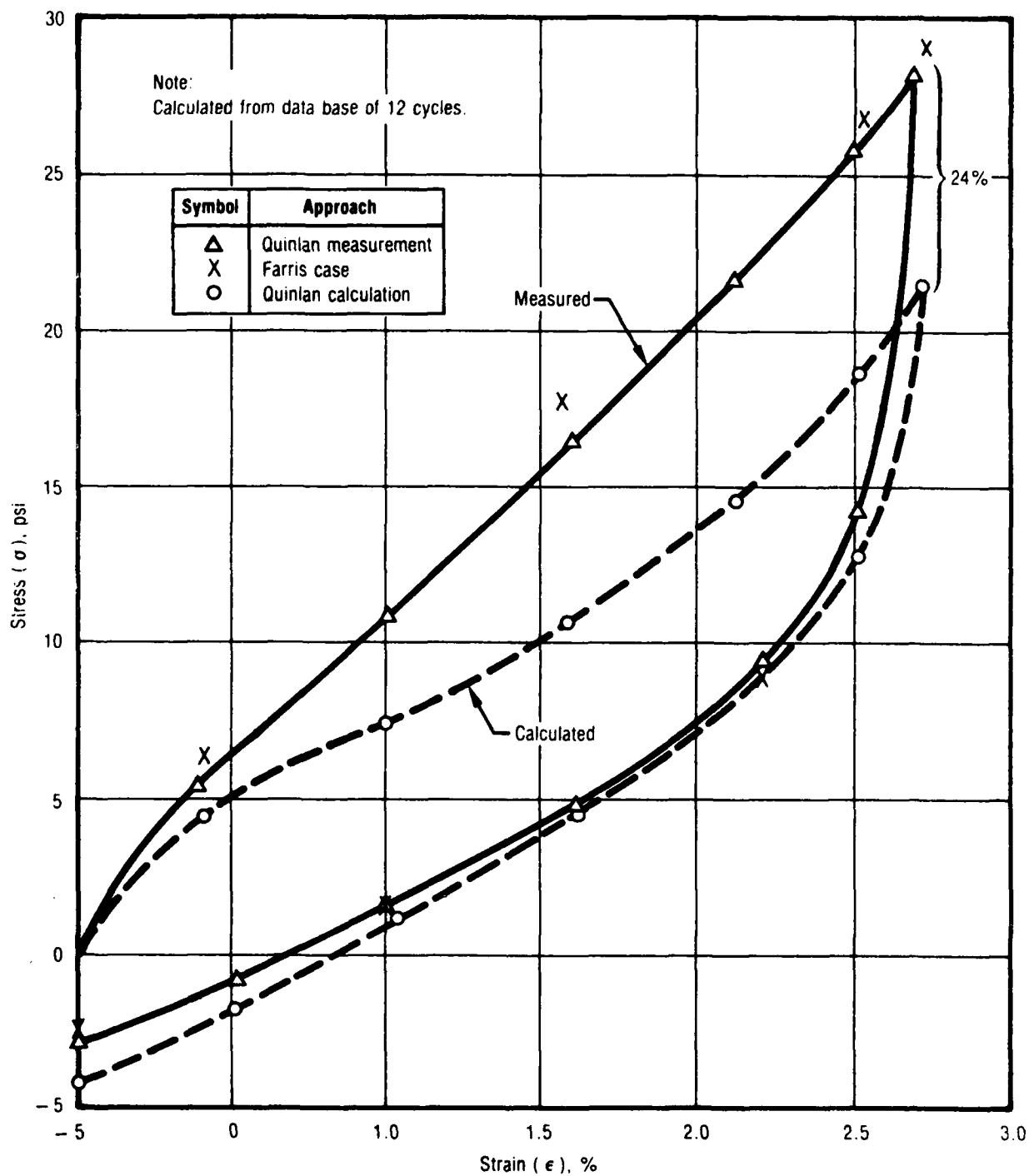
Figure 47.   Quinlan N.C. Calculation with TPH 1011 Propellant (First Cycle)
30961
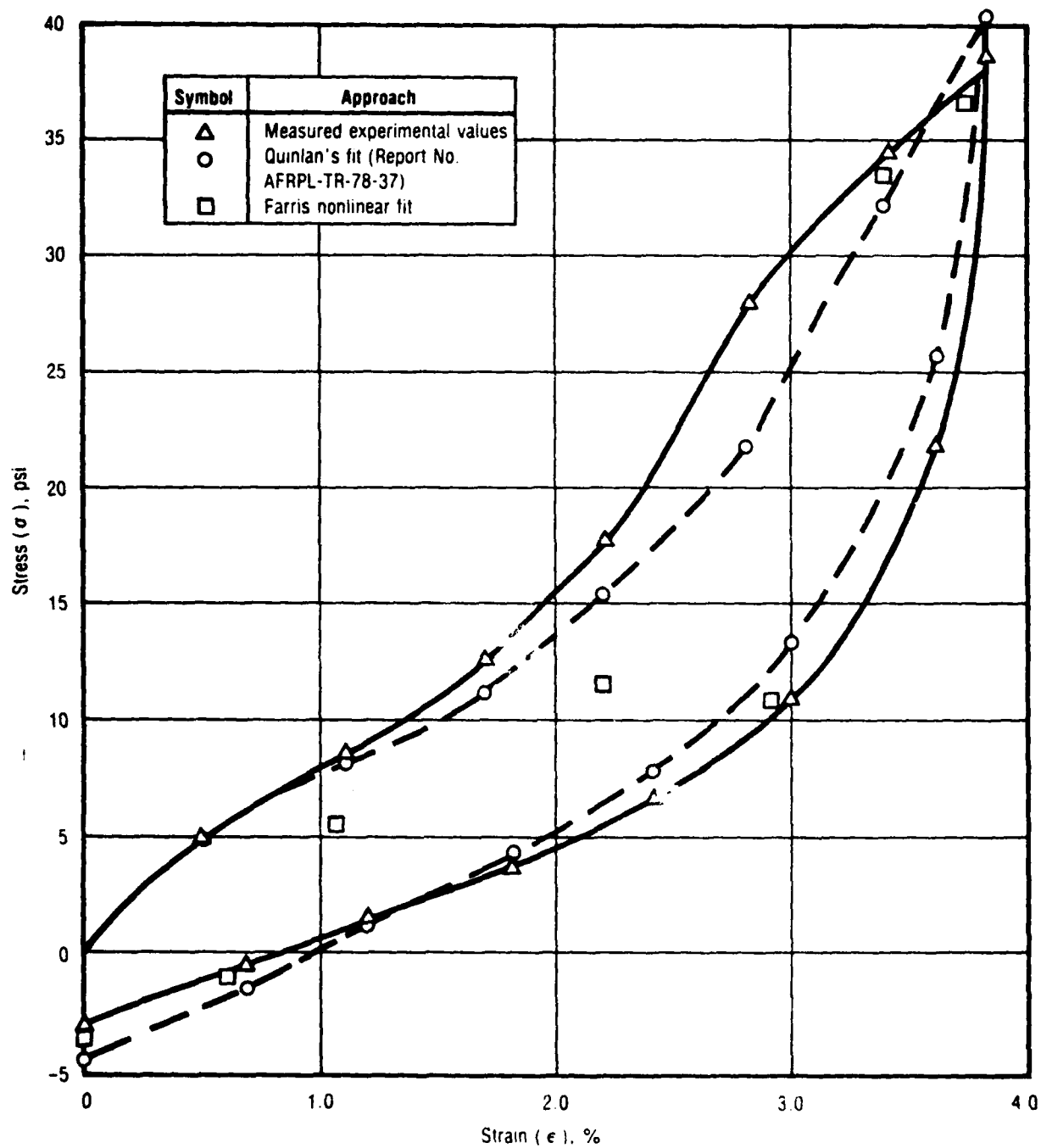
Figure 48. Quinlan's 12 Cycle Sawtooth-Rest Test (Cycle No. 2)

30962
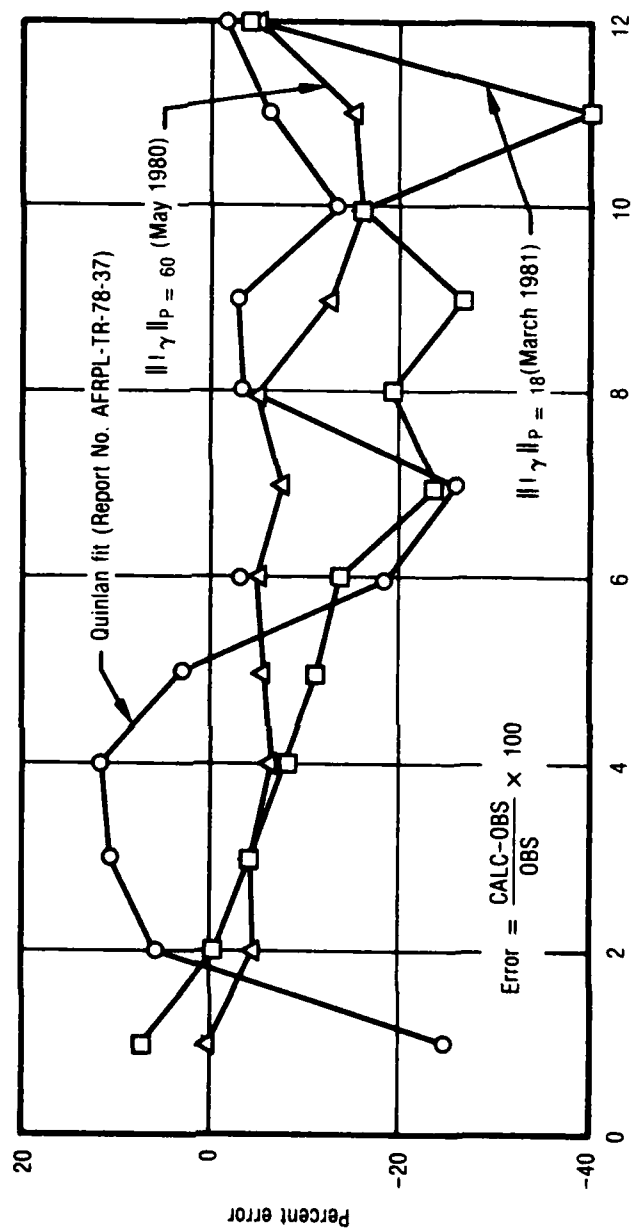
Figure 49. Error in Peak Stress for 12-Cycle Experiment

TABLE 9. FARRIS COMPUTED N-L PARAMETERS

Constants	Farris ASPC Final Report TPH 1011 (54 Tests)	Quinlan Test			
		Run 21	Run 22	Run 23	Run 24
$B_{NT} + 1$	60	60*	94.0	60.0*	93.8
B_{NC}	-0.150	-0.150*	-0.150*	-0.45	-0.237
$B_{NC} + 1$	-1.69	3.94	-3.32	8.15	-3.92
$B_{NC} + 2$	-1.23	-1.23	-1.23	-1.23	-1.23
$B_{NC} + 3$	10.5	12.5	8.1	18.4	10.8
$B_{NC} + 4$	2.00	19.9	19.6	19.1	18.1
$B_{NC} + 5$	102.0	-44.0	15.4	129.0	128.0
$B_{NC} + 6$	239.0	151	426	48.0	352.0
$B_{NC} + 7$	56.5	167	90.9	17.8	32.0
Average deviation		-4.1	-14.2	-4.5	-9.0
Standard deviation		18.9	24.1	15.3	26.3

* Denotes held fixed

Instron machines, whereas all other cycles were at the usual intervals of 1, 2, and 5 in./min. Table 9 shows the values for the Farris parameters from several solutions to the Quinlan data. Shown for comparison in the first column are data generated by Aerojet during the development of the Farris constitutive theory on the same propellant (circa 1972), TPH 1011. Note the range in values from the various runs. This is reminiscent of the CSD experiences with the failure mechanisms program.

It might also be noted in passing that each of these solutions cost about $1.50 in computer time as compared to about $100.00 for the CSD program to evaluate the Quinlan theory. Hence, computation costs may be highly dependent on the theory chosen and the sophistication of the techniques used to evaluate the constitutive expressions.

One additional test was run at the request of Dr. J. E. Fitzgerald, a consultant to CSD on this program. He requested a prediction for a test in which a 24-hr rest period was included in the test history. The results are shown in Figure 50 for the parameters selected from Table 10. Contrary to what was expected, the predicted response did not show anomalous behavior on the reloading following the rest period.
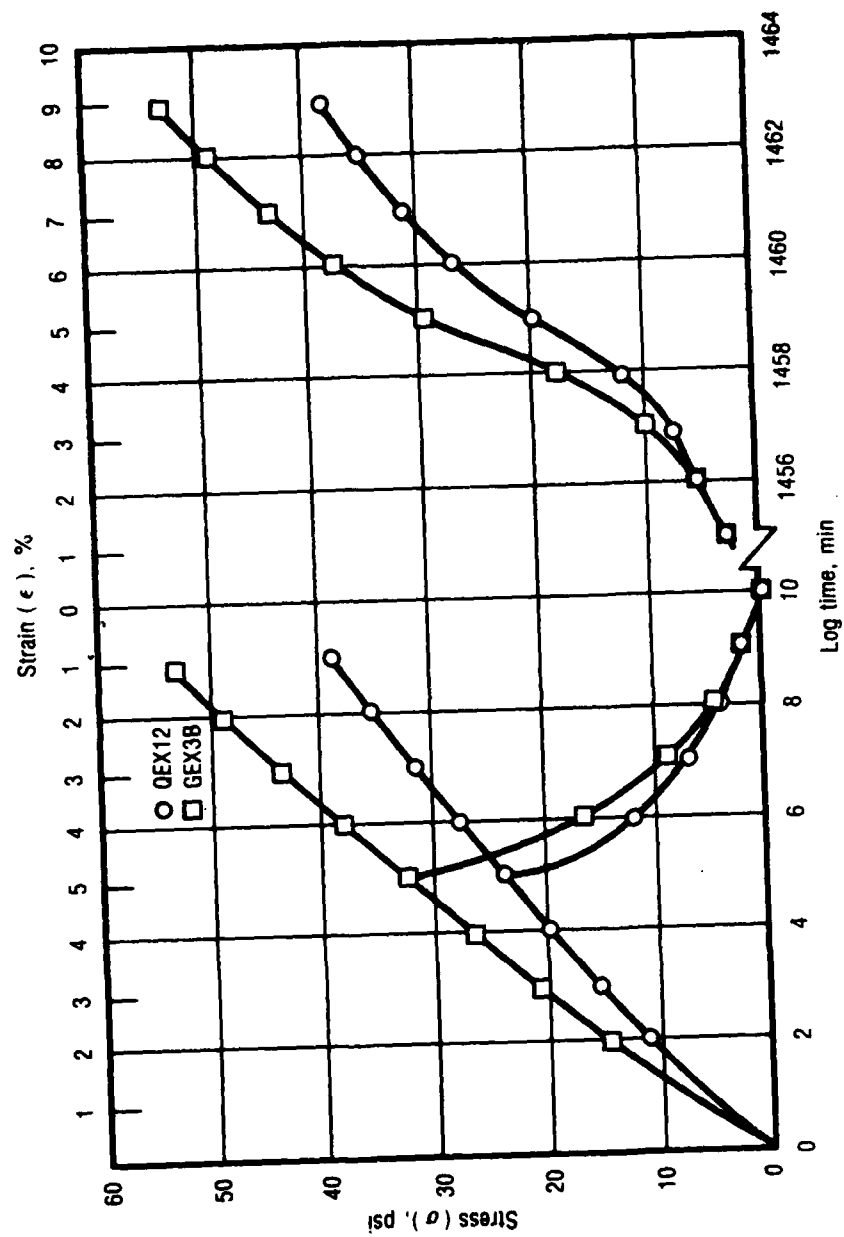
Figure 50. Fitzgerald 24-hr "Dip" Test

30964

97

TABLE 10. PARAMETERS FOR FARRIS FIT

T9991

Contstants	QEX12	GEX3A	GEX3B
B_{NT}	18	18	18
B_{NC}	-0.49	-0.27	-0.61
B_{NC+3}	5.44	2.90	3.00
B_{NC+4}	2.20	13.0	19.0
B_{NC+5}	152	30	140
B_{NC+6}	102	360	225
B_{NC+7}	15	22	11

4.2 LINEAR VISCOELASTIC CONSTITUTIVE EQUATION

4.2.1 Isothermal Tests

The one-dimensional stress-strain law for a thermorheologically simple linear viscoelastic solid may be expressed as:

$$\sigma(t) = \int_0^t E\ (S_t - S_\tau)\ \frac{d\epsilon}{d\tau}\ (\tau)\ d\tau \tag{19}$$

where:

   σ = stress

   ϵ = strain

E(t)   = relaxation modulus (PRONY series representation
       using a matrix solution for curve fitting data;
       CSD Data Analysis Procedure No. 7.3)

$S_t - S_\tau$ = temperature-shifted time, given by:

$$S_t - S_\tau = \int_\tau^t \frac{d\tau}{A_T\left[T\left(\tau\right)\right]} \qquad (20)$$

and

A_T = time-temperature shift function, taken in the form:

$$A_T = \left(\frac{T_R - T_a}{T - T_a}\right)^m \qquad (21)$$

in which T_R is the shift reference temperature, and both T_a and m are material parameters. The material parameters were obtained using CSD Data Analysis Procedure No. 7.4, which is curve fit routine using Powell's algorithms.

The linear viscoelastic model was used to predict the response of UTP-19,360B and UTP-3001 under several strain histories. The corresponding results are included here as a basis against which to compare the stress predictions obtained using the nonlinear stress-strain laws considered in the program.

4.2.2 Isothermal Stress Predictions

The measured response is compared against that predicted by linear viscoelasticity for UTP-19,360B in the following order (Figures 51 through 76).

The results for the lowest and highest constant-rate tests (Test No. 1) appear in Figures 51 and 52. Those for the dual-rate tests (high-to-low and low-to-high, Test No. 3) are shown in Figures 53 and 54. Figure 55 contains the comparisons for a saw-tooth strain history (Test No. 5) with increasing strain peaks and rest periods between cycles. The results corresponding to complex multiple loading, 24-hour relaxation, long-duration similitude, three-step relaxation, and predamage relaxation are presented in Figures 56 to 60. In addition, the time-temperature superposition principle is put to use with constant

99
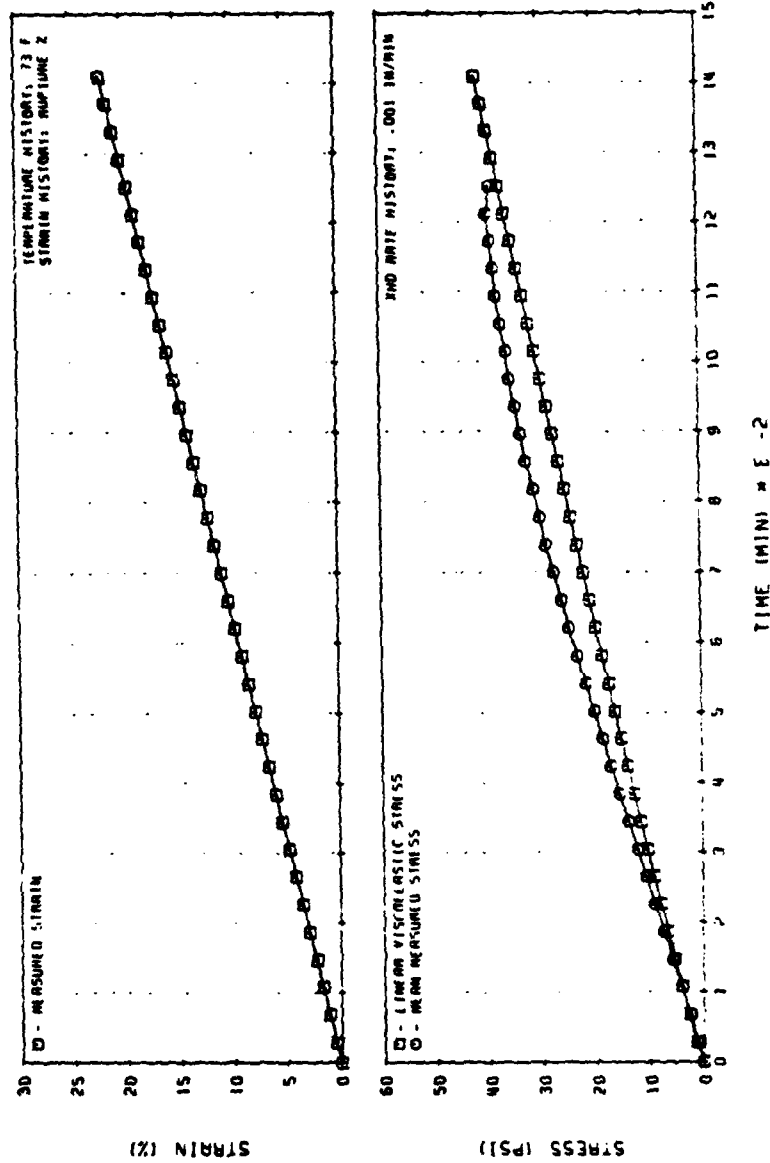
Figure 51. Linear Viscoelastic Stress Predictions for UTP-19,360B-400/1777 Constant-Rate Test History (Code No. 1)

30993

100
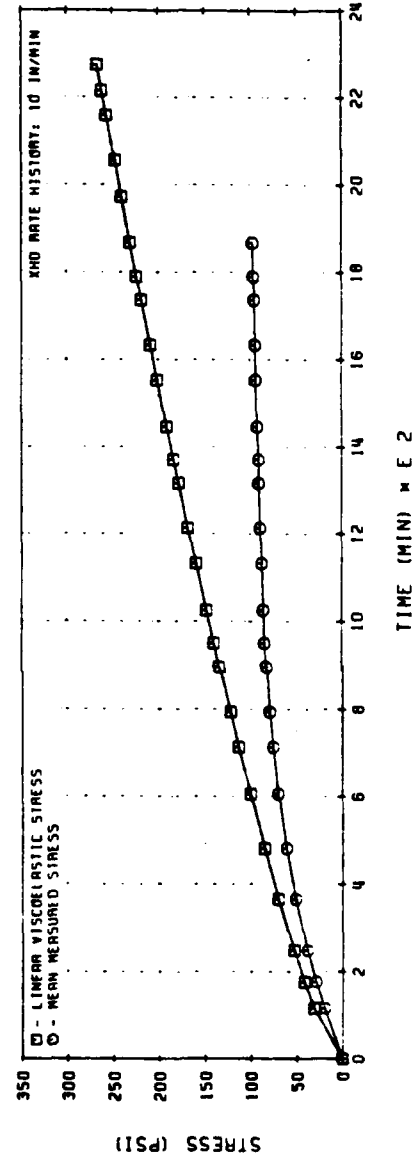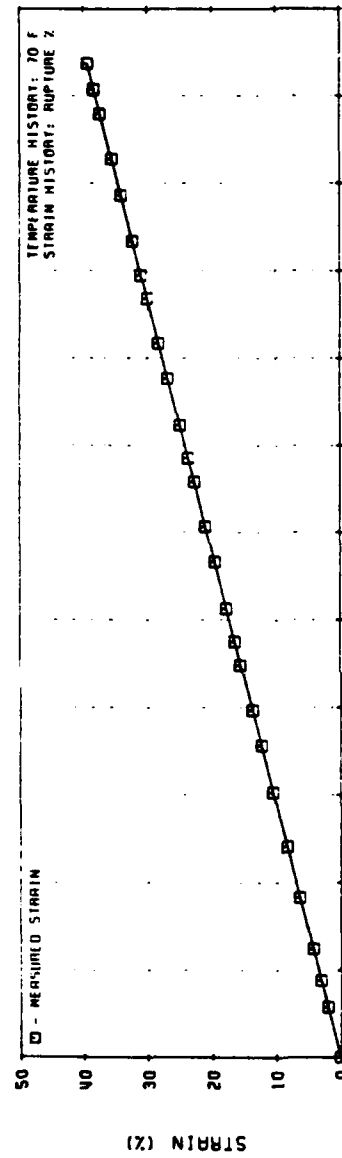
Figure 52. Linear Viscoelastic Stress Predictions for UTP-19,360B-400/1777 Constant-Rate Test History (Code No. 1)

30994
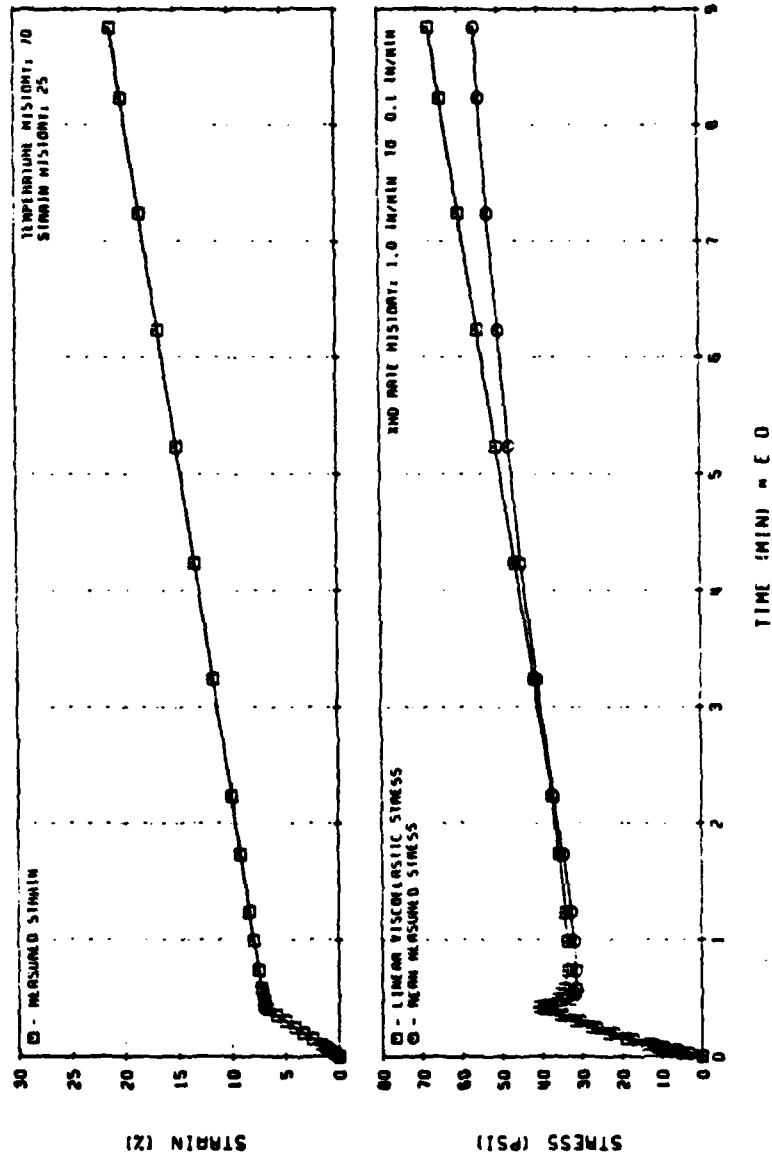
Figure 53. Linear Viscoelastic Predictions for UTP-19,360B-400/1777 Two-Rate Test History (Code No. 3)

30995
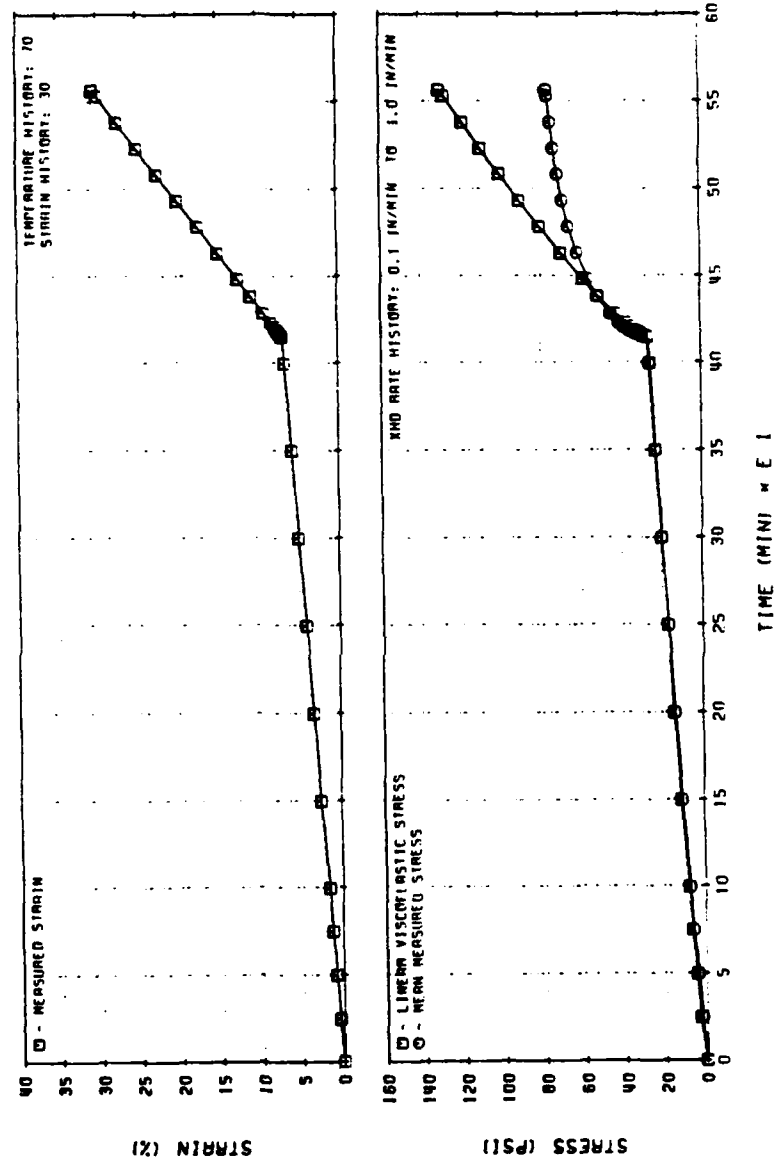
Figure 54. Linear Viscoelastic Stress Predictions for UTP-19,360B-400/1777 Two-Rate Test History (Code No. 3)

30996

103
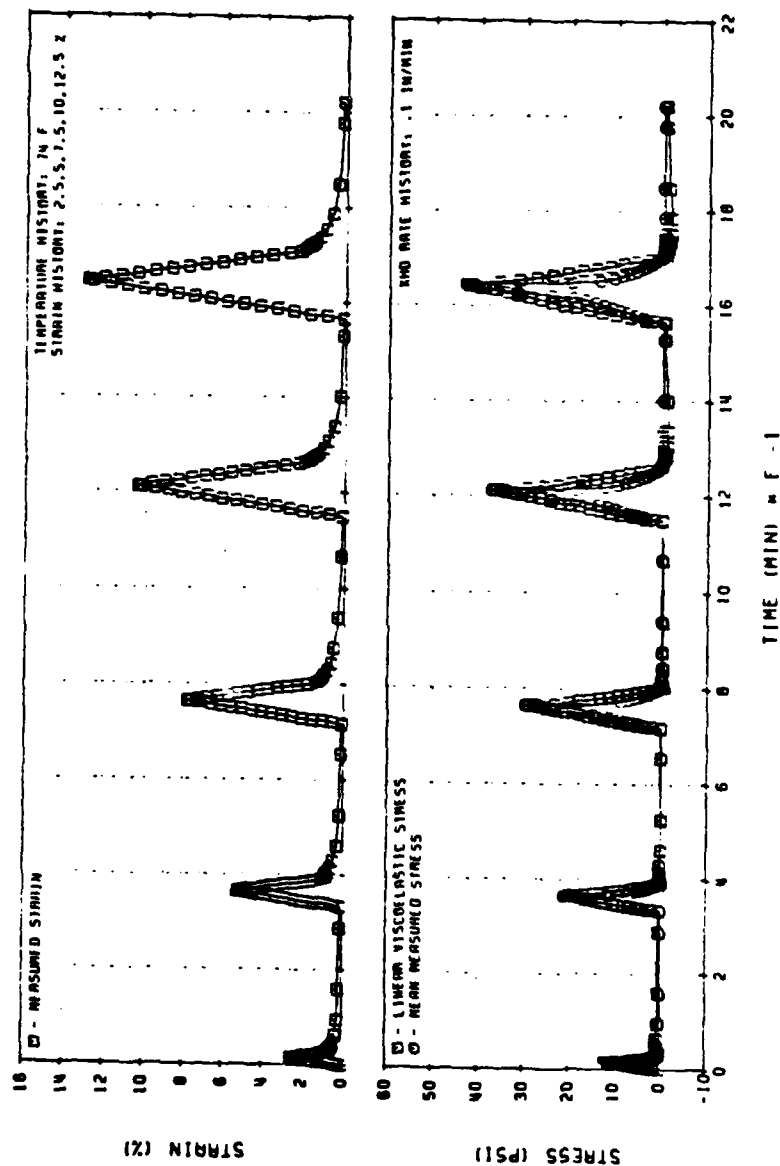
Figure 55. Linear Viscoelastic Stress Predictions for UTP-19,360B-400/1777 Multiple Loading Test History (Code No. 5)

30997
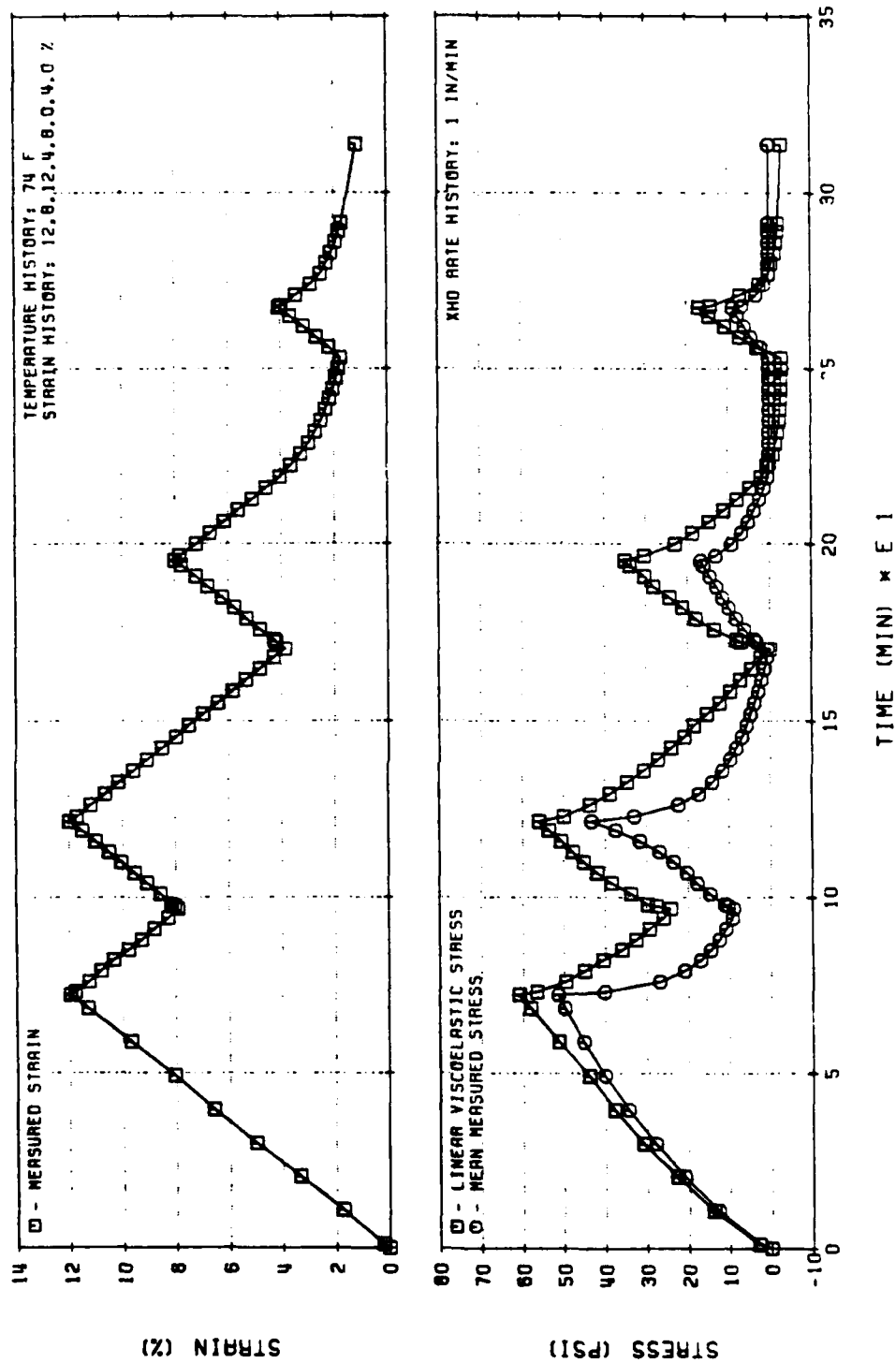
Figure 56. Linear Viscoelastic Stress Predictions for UTP-19,360B-400/1777 Complex Multiple Loading
(Test No. 10)

30998

105
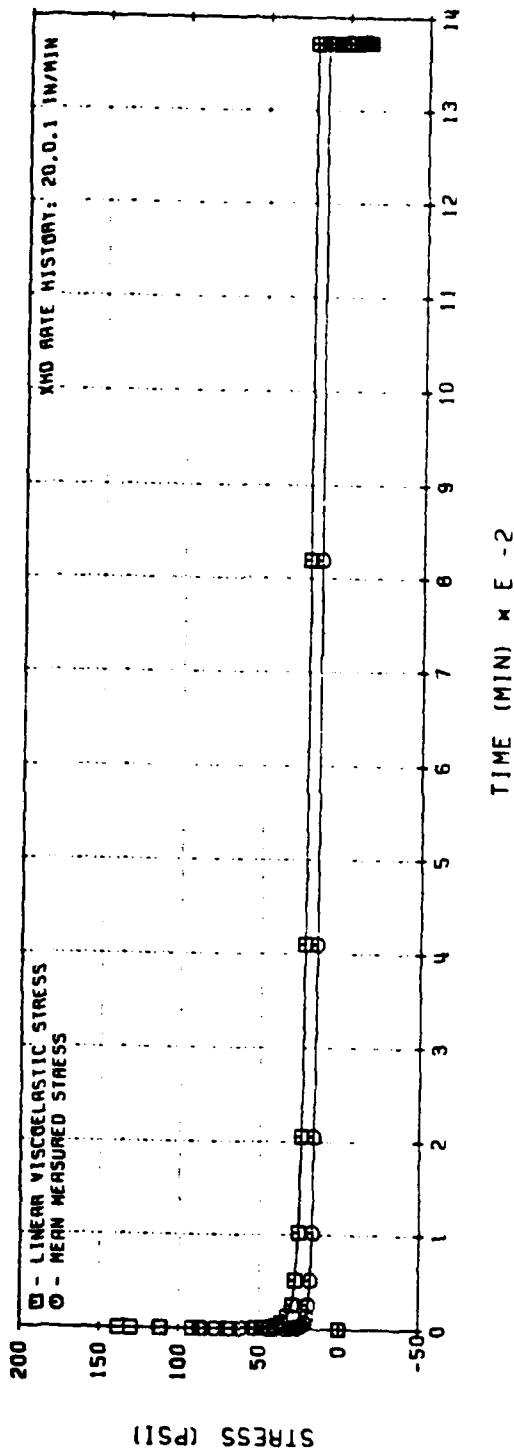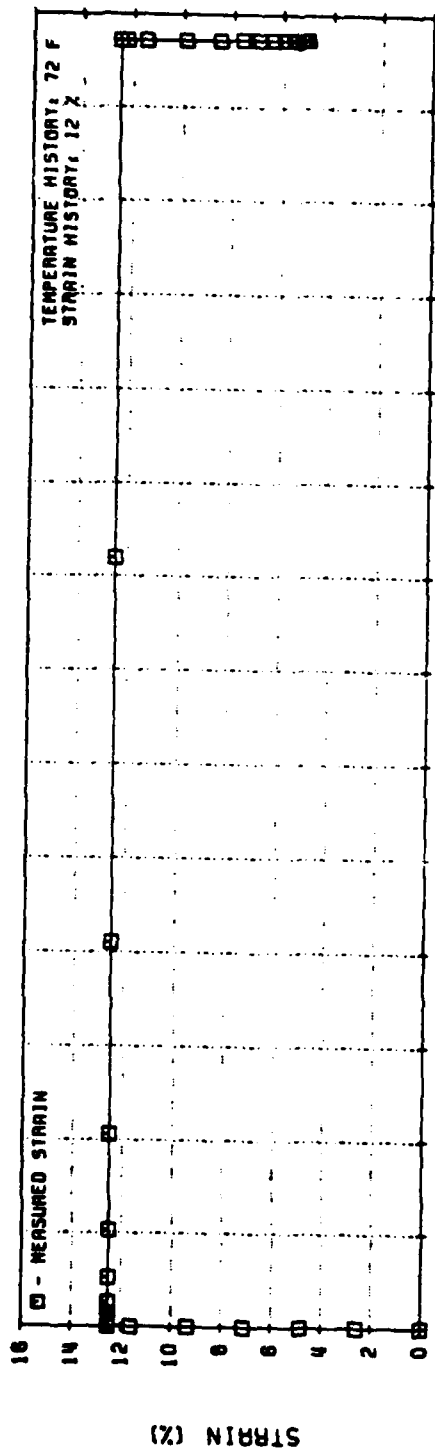
Figure 57. Linear Viscoelastic Stress Predictions for UTP-19,360B-400/1777 24-hr Relaxation (Test No. 8)

30999
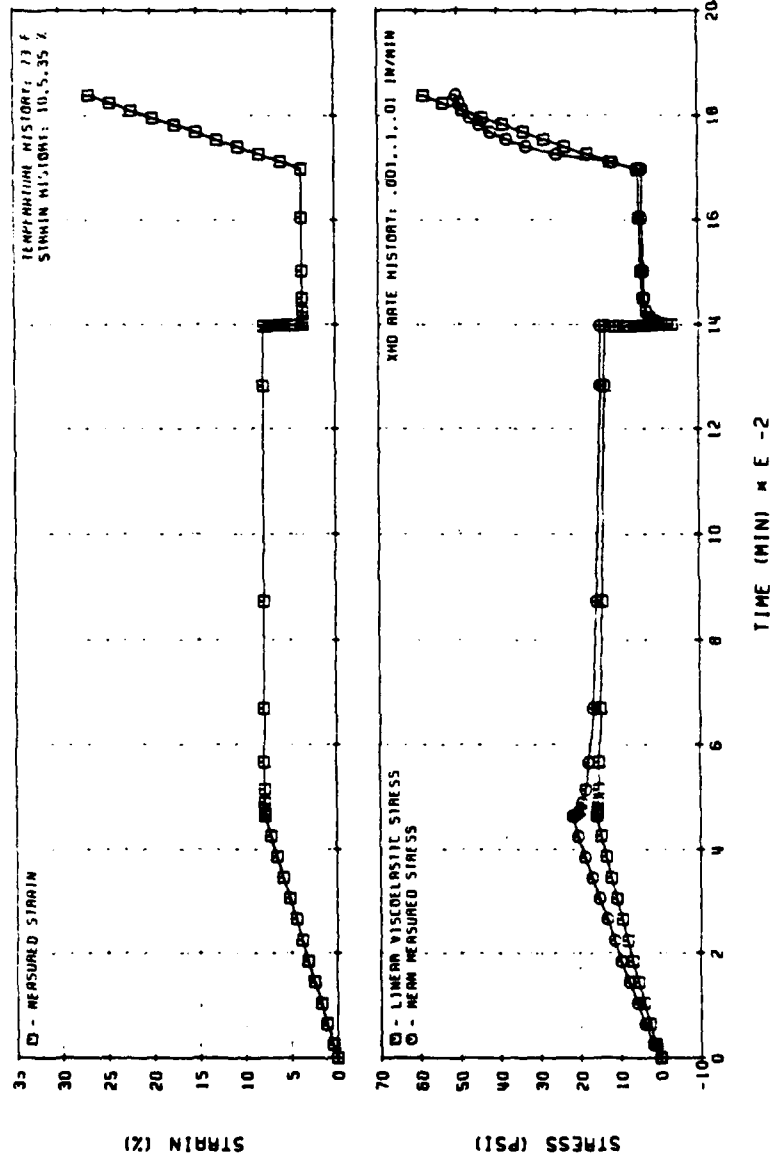
Figure 58. Linear Viscoelastic Stress Predictions for UTP-19,360B-400/1777 Similitude Test History
(Code No. 12)

31000
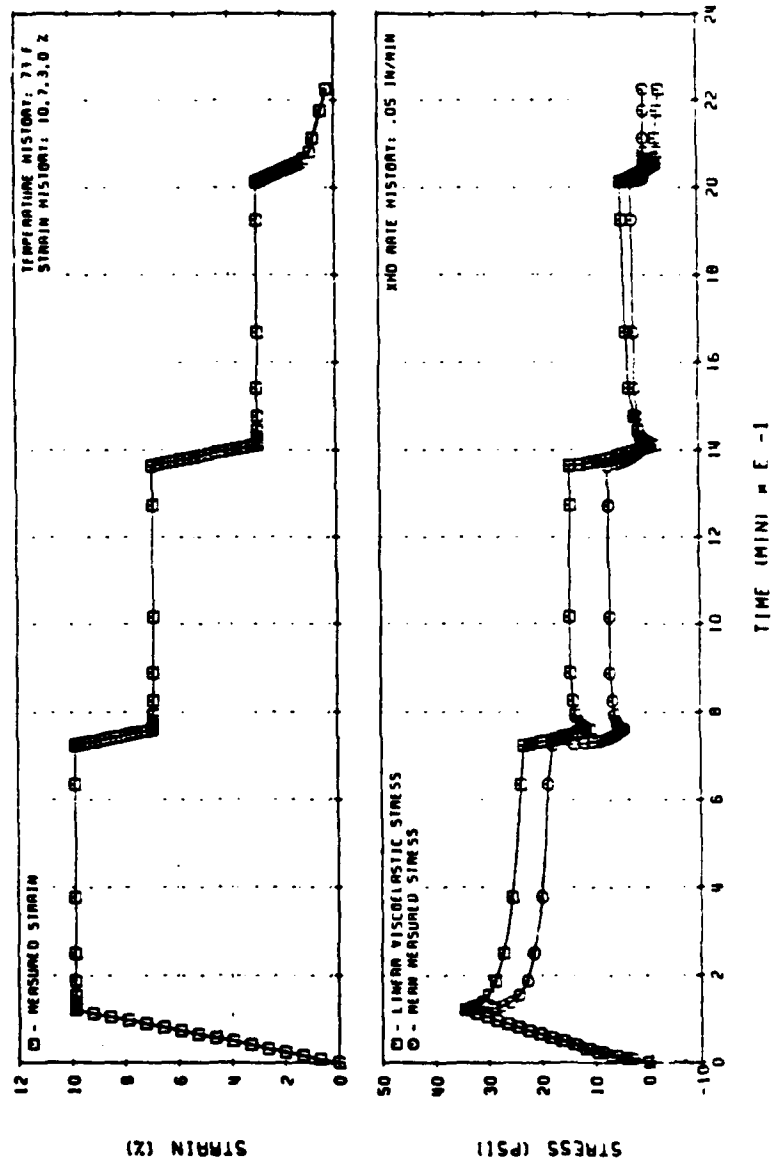
Figure 59. Linear Viscoelastic Stress Predictions for UTP-19,360-B-400/1777 Three-Step Relaxation Test History (Code No. 13)

31001
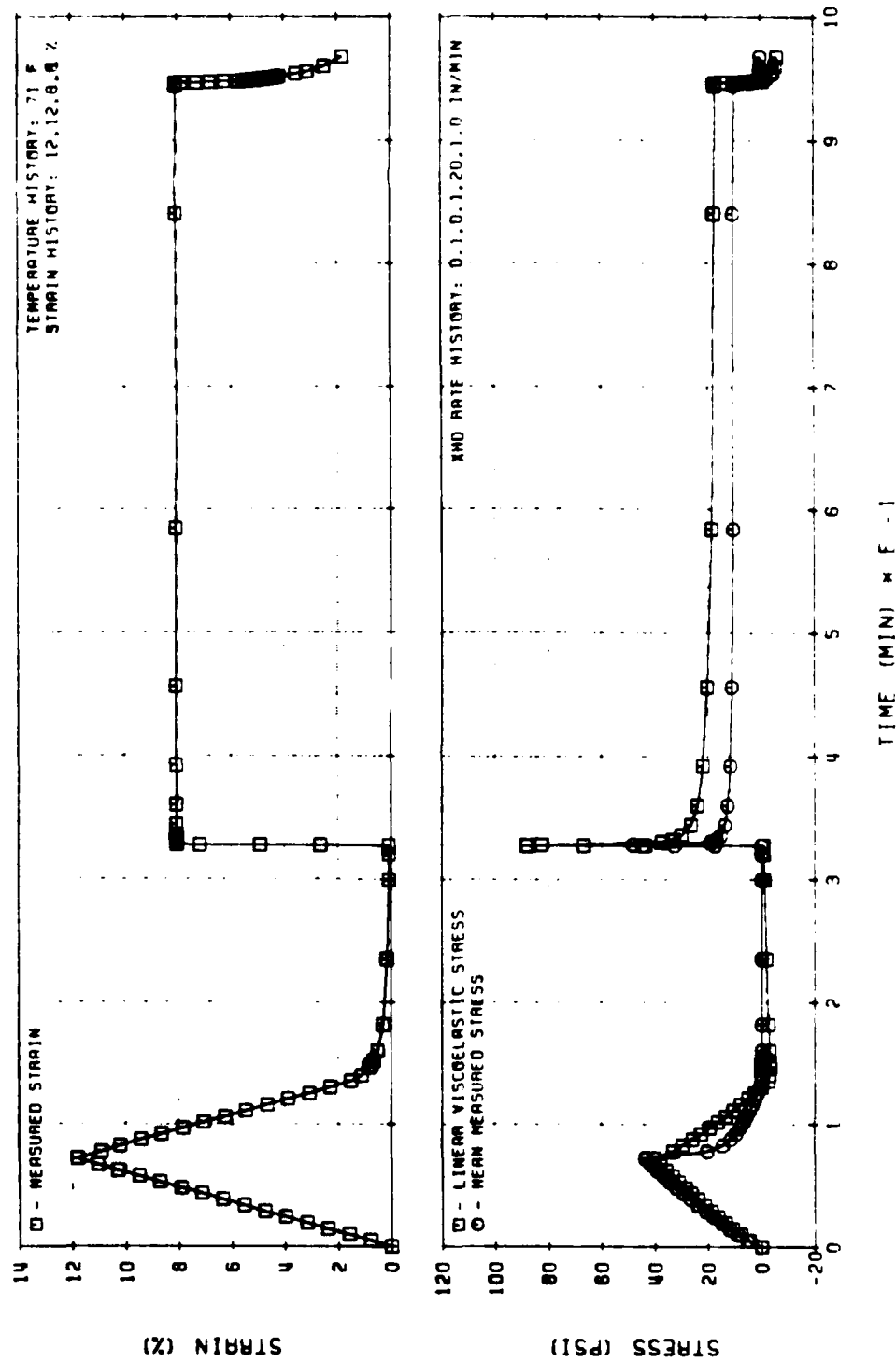
Figure 60. Linear Viscoelastic Stress Predictions for UTP-19,360B-400/1777 Predamaged Relaxation (Test No. 9)

109
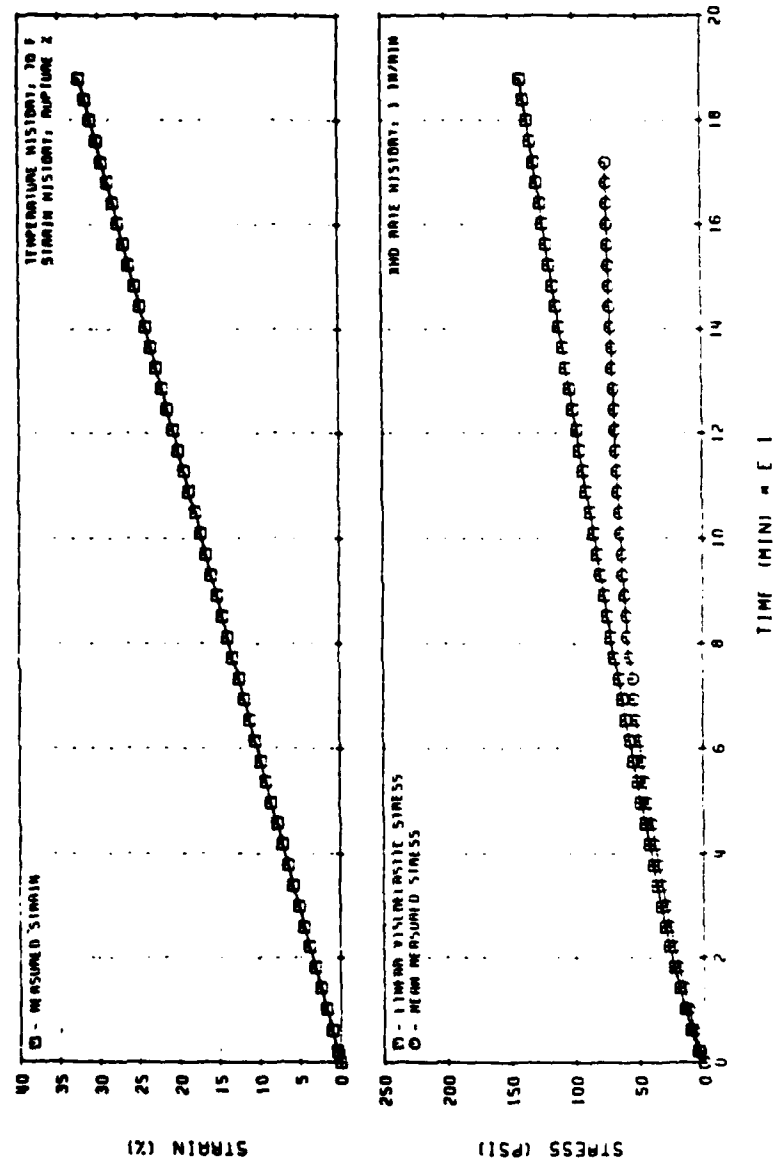
Figure 61. Linear Viscoelastic Stress Predictions for UTP-19,360B-400/1777 Constant-Rate History (Code No. 1)

31003
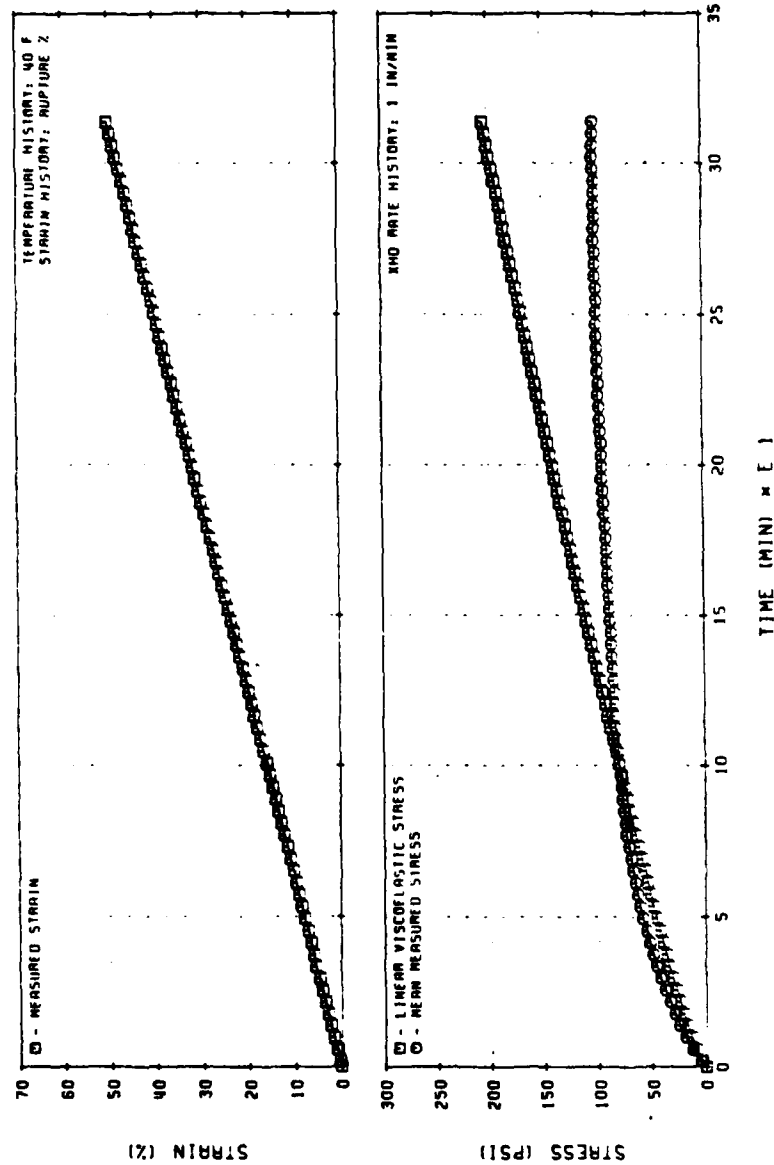
Figure 62. Linear Viscoelastic Stress Predictions for UTP-19,360B-400/1777 Constant-Rate Test History
(Code No. 1)

31004
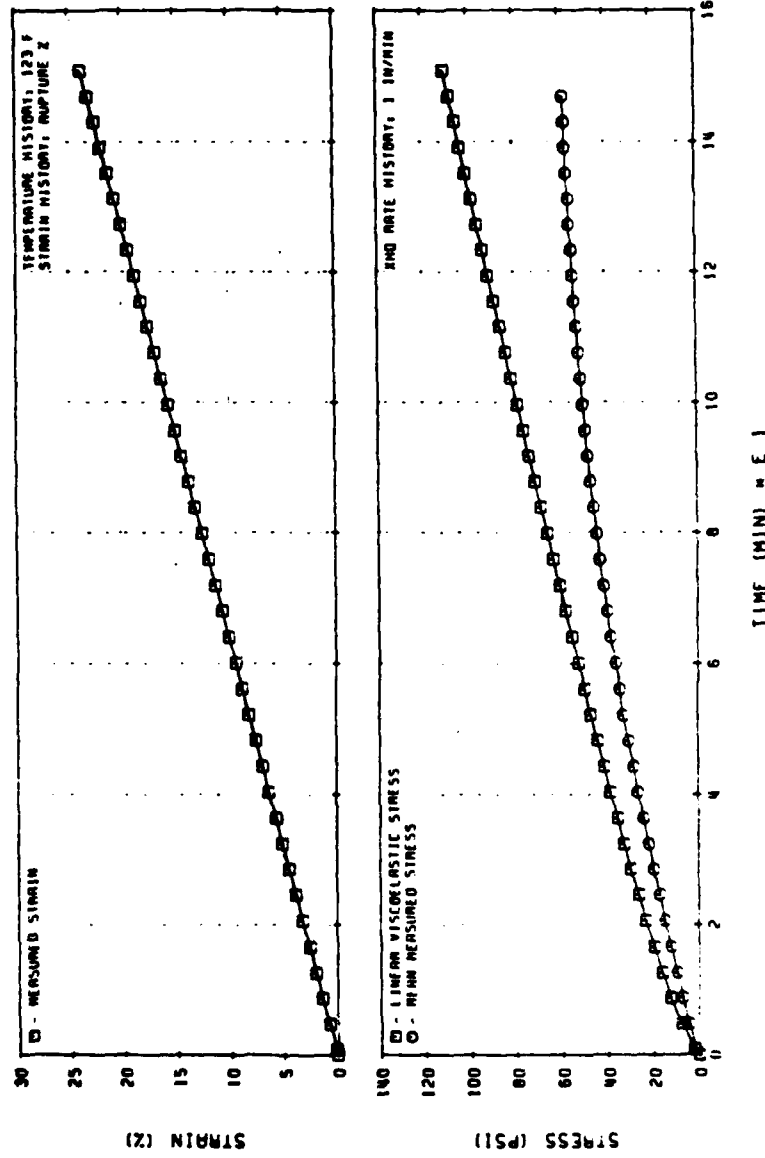
Figure 63.   Linear Viscoelastic Stress Predictions for UTP-19,360B-400/1777 Constant-Rate Test History
(Code No. 1)

31005
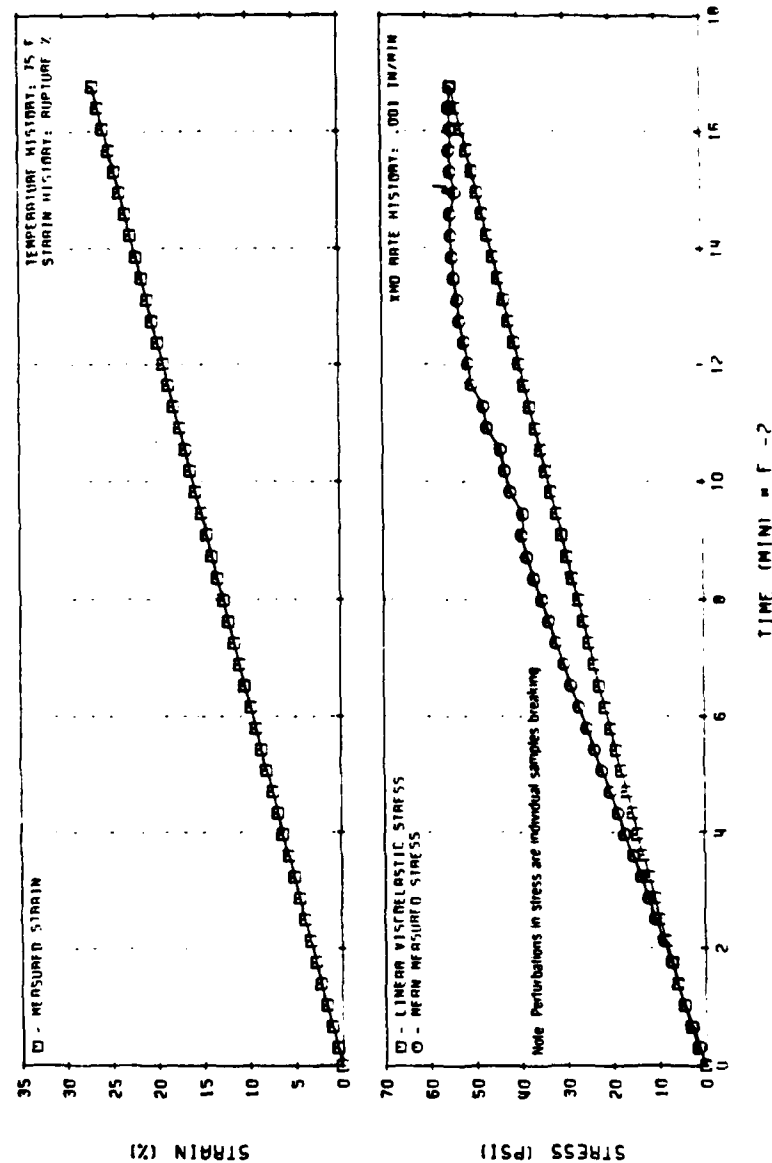
Figure 64. Linear Viscoelastic Stress Predictions for UTP-3001-750/7768 Constant-Rate Test History (Code No. 1)

31006

113
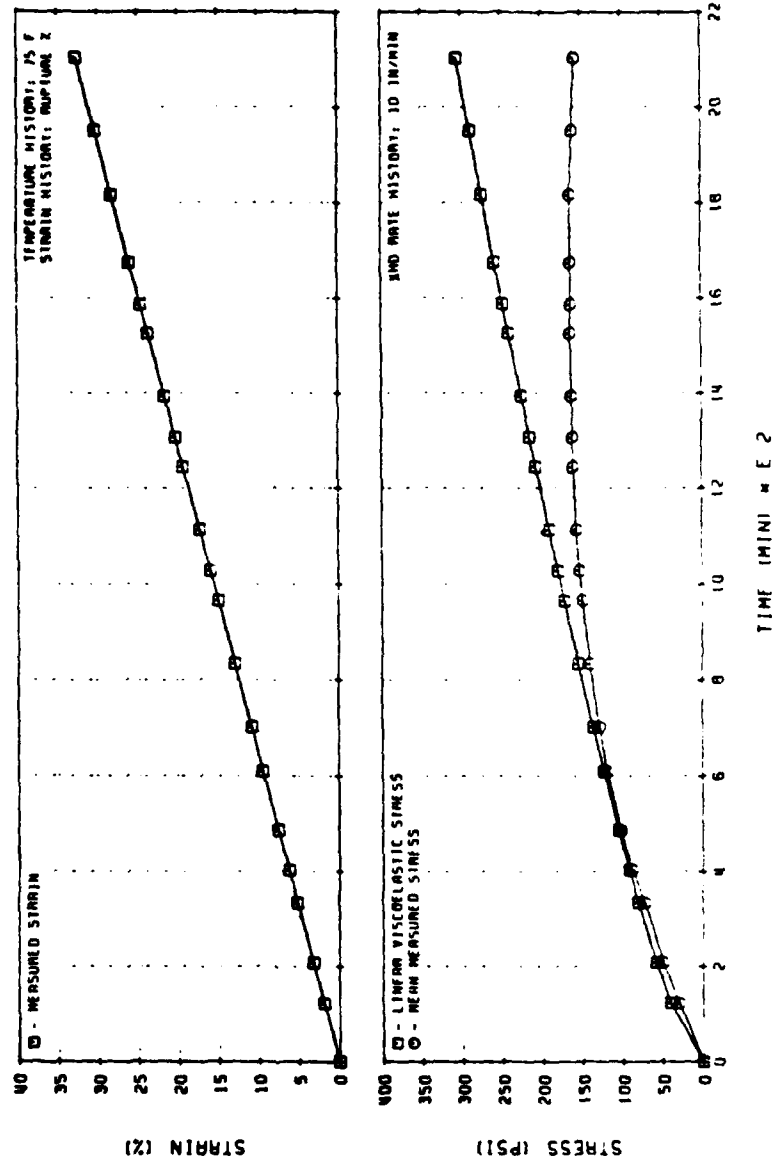
Figure 65. Linear Viscoelastic Stress Predictions for UTP-3001-750/7768 Constant-Rate Test History
(Code No. 1)

31007

114

TIME (MIN) * E 1
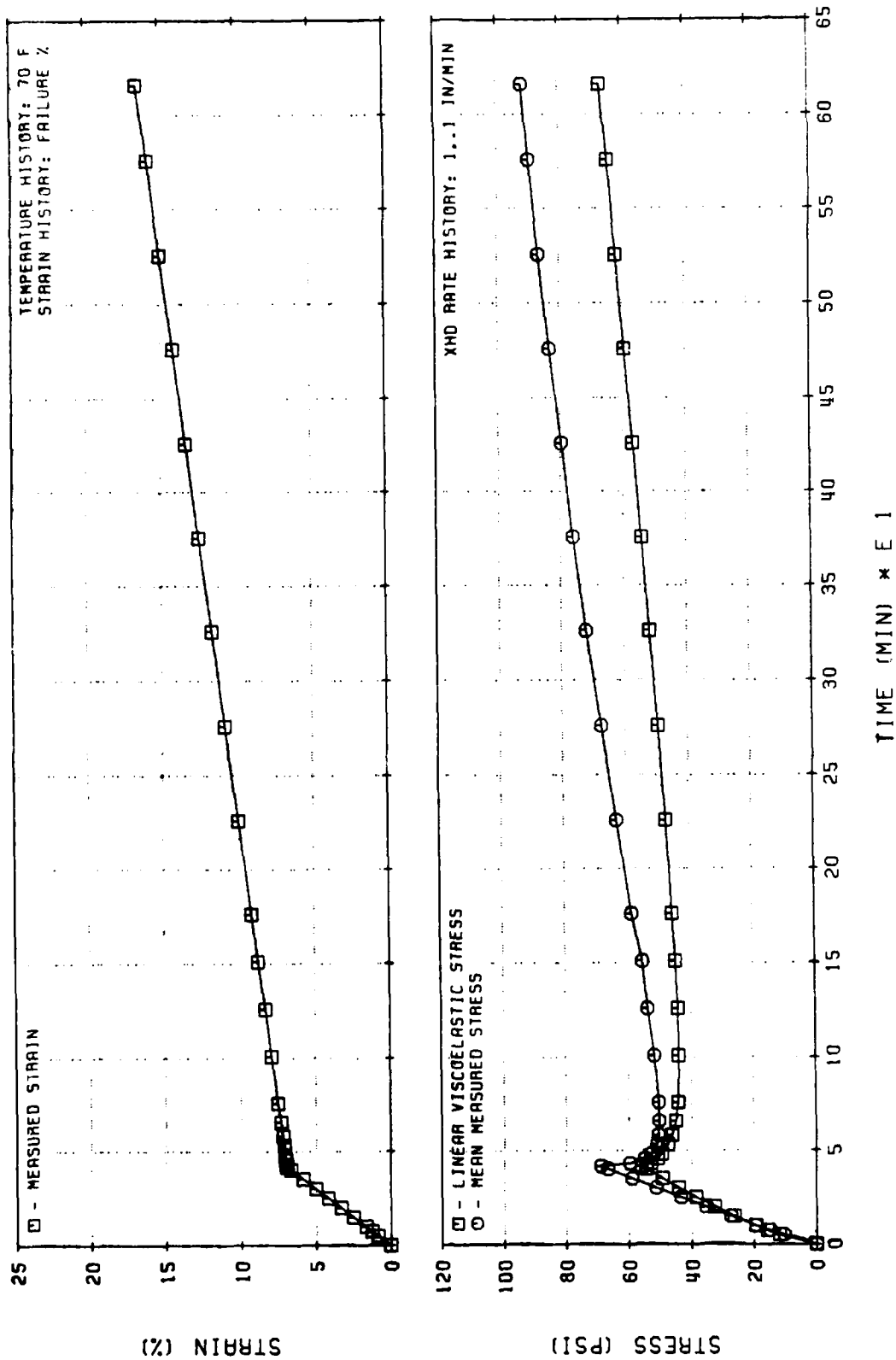
Figure 66. Linear Viscoelastic Stress Predictions for UTP-3001-750/7768 (Sample No. 2)
Multiple Rate: High to Low (Test No. 3)

31008

115
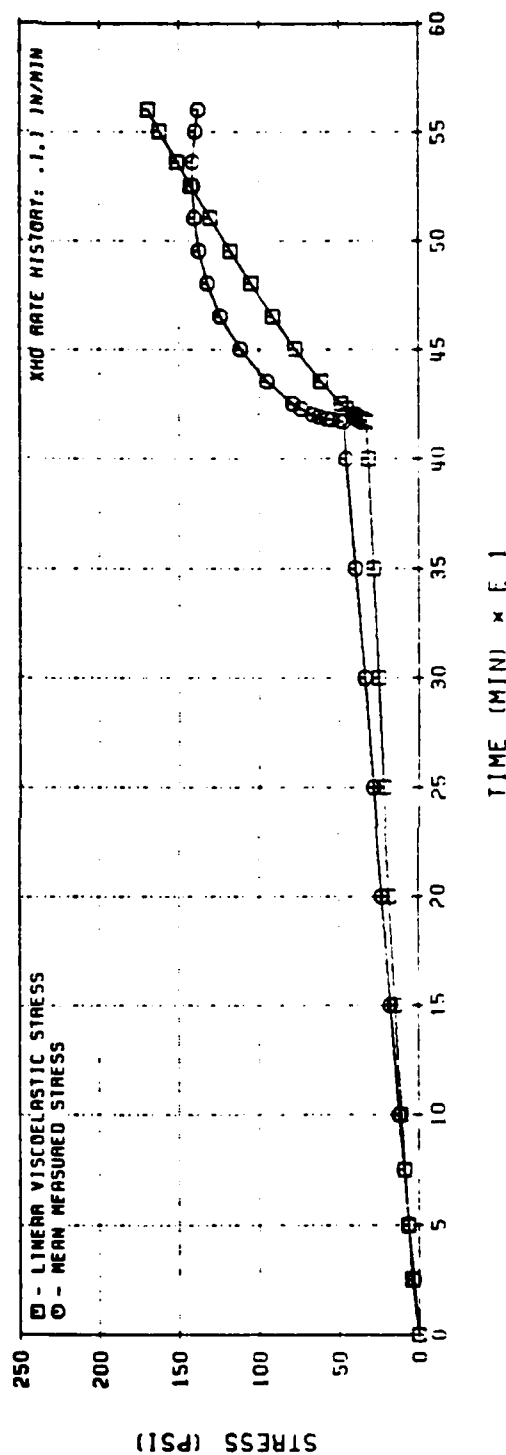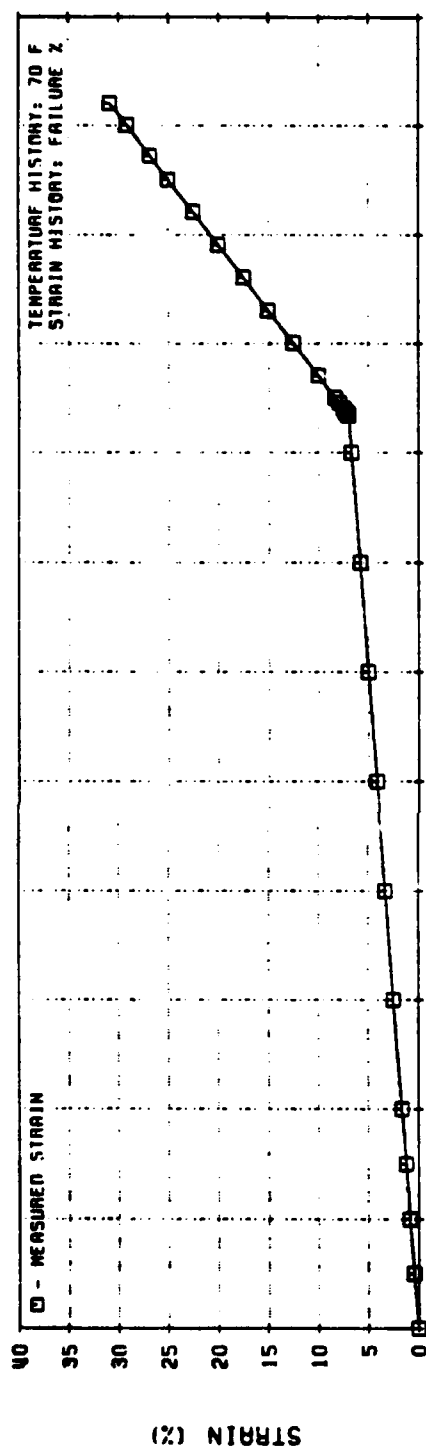
Figure 67. Linear Viscoelastic Stress Predictions for UTP-3001-750/7768 (Sample No. 4)
Multiple Rate: Low to High (Test No. 3)

116
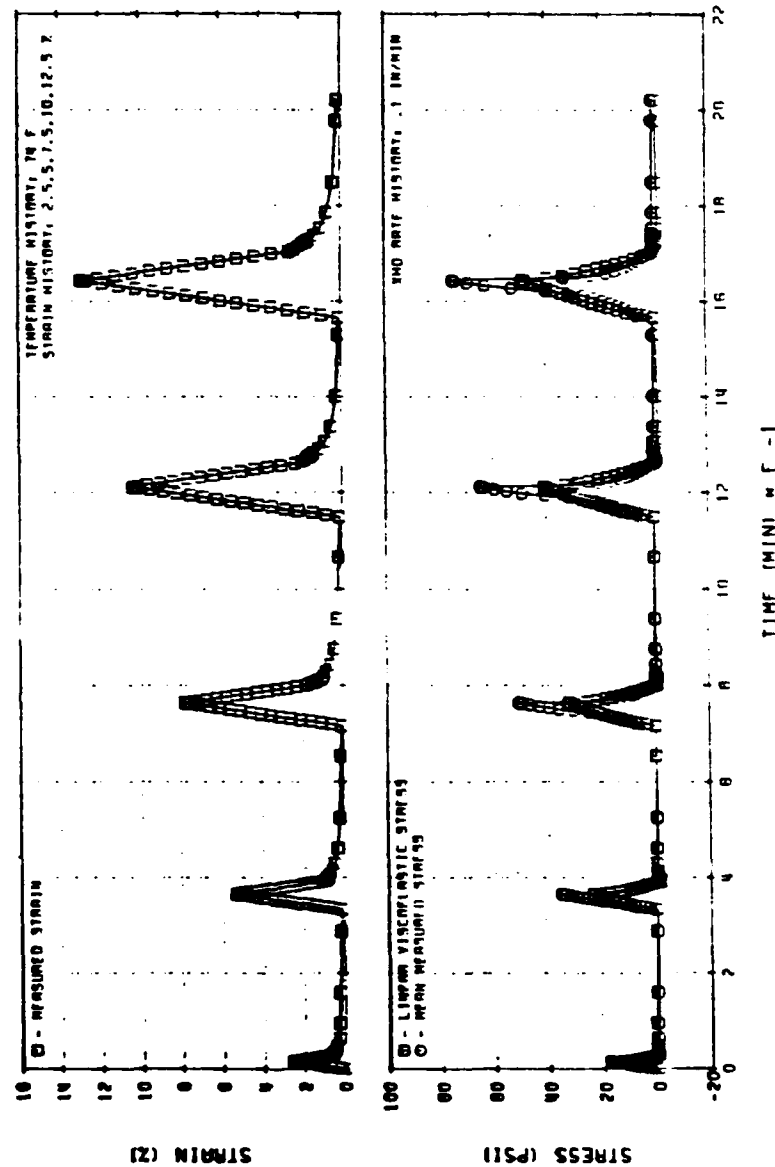
Figure 68. Linear Viscoelastic Stress Predictions for UTP-3001-750/7768 Multiple Loading Test History (Code No. 5)

31010

117
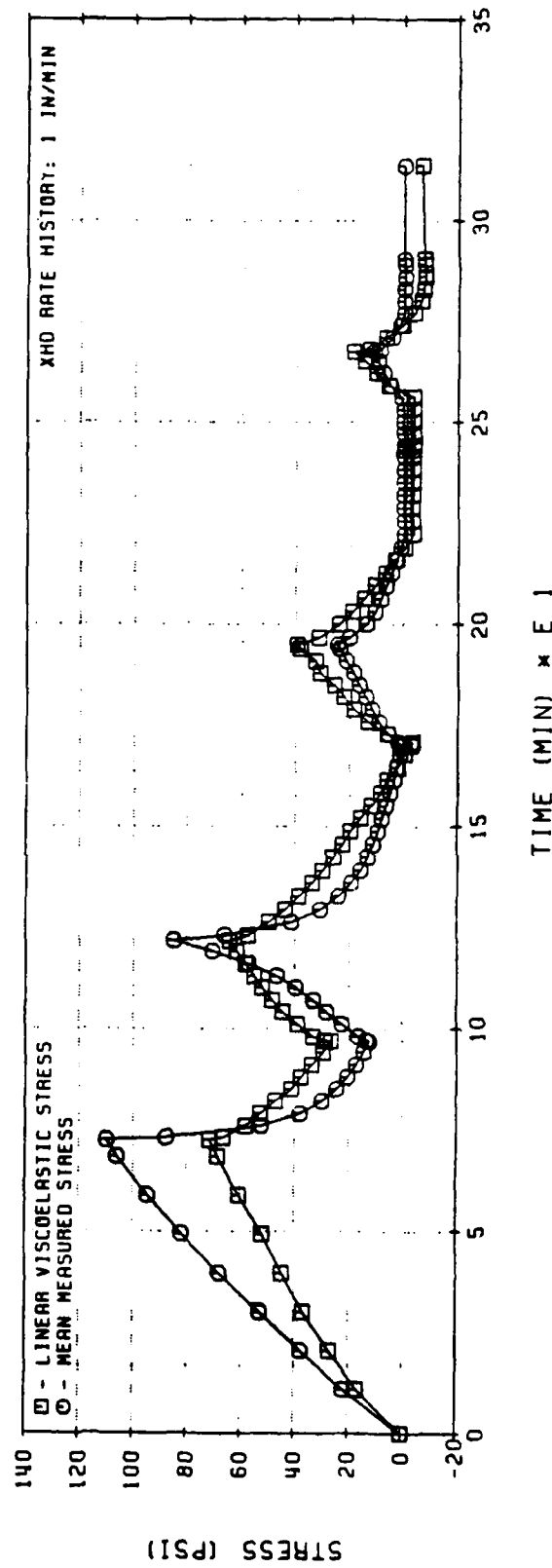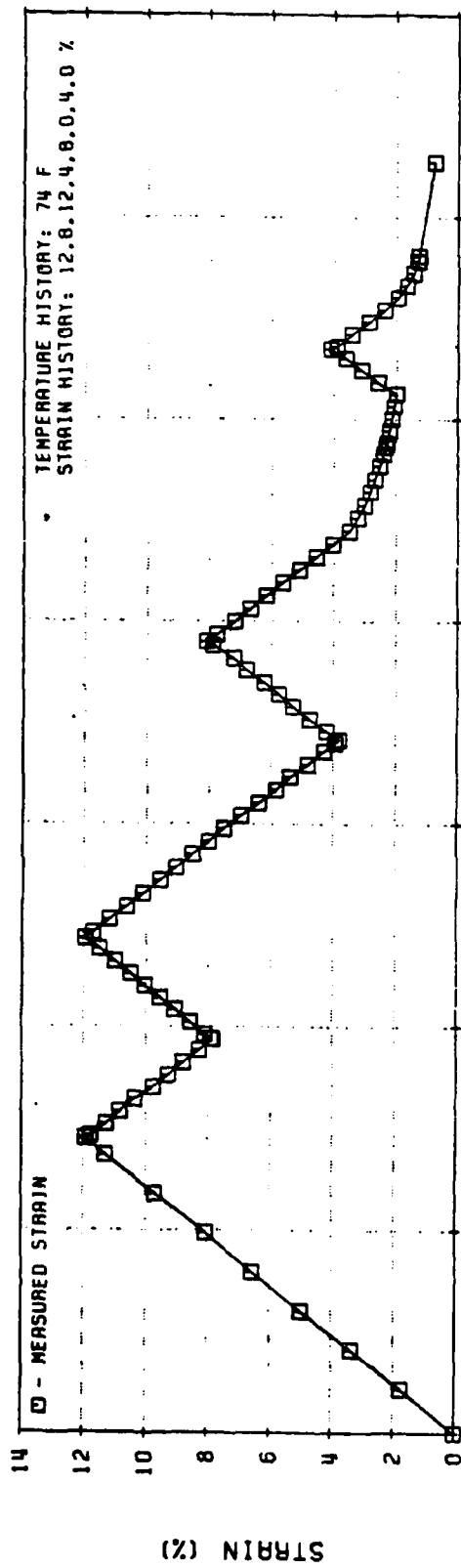
Figure 69. Linear Viscoelastic Stress Predictions for UTP-3001-750/7768 Complex Multiple Loading (Test No. 10)

118
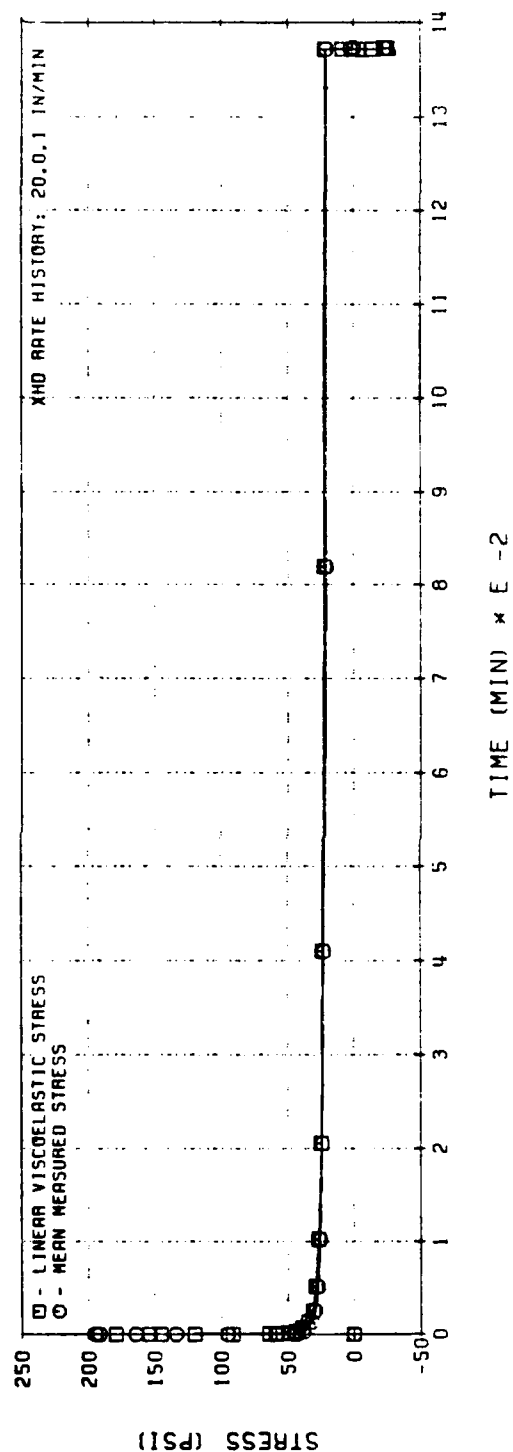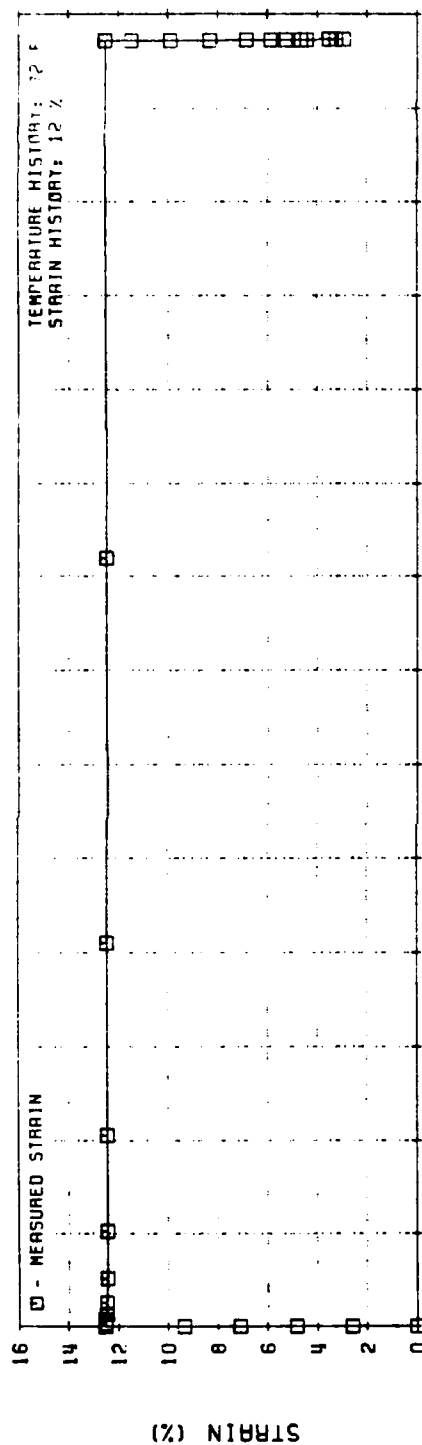
Figure 70. Linear Viscoelastic Stress Predictions for UTP-3001-750/7768 2½-hr Relaxation (Test No. 8)

31012

119
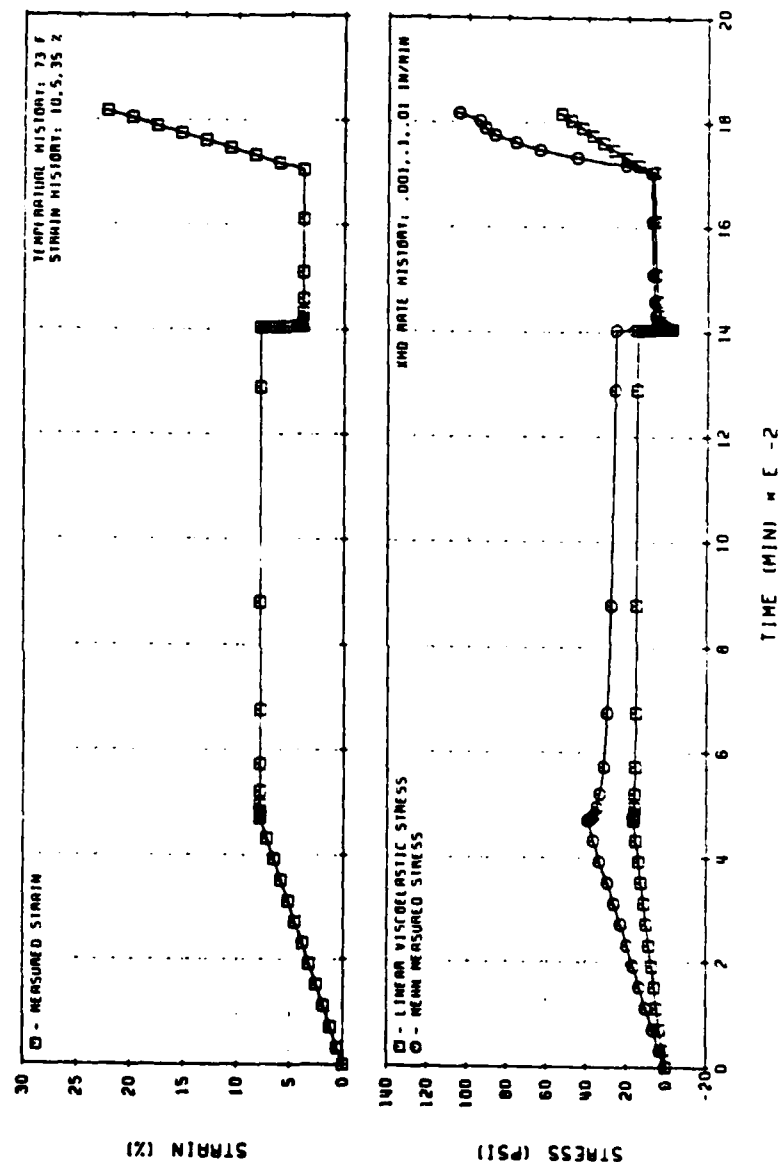
Figure 71. Linear Viscoelastic Stress Predictions for UTP-3001-750/7768 Similitude Test History (Code No. 12)

31013

120
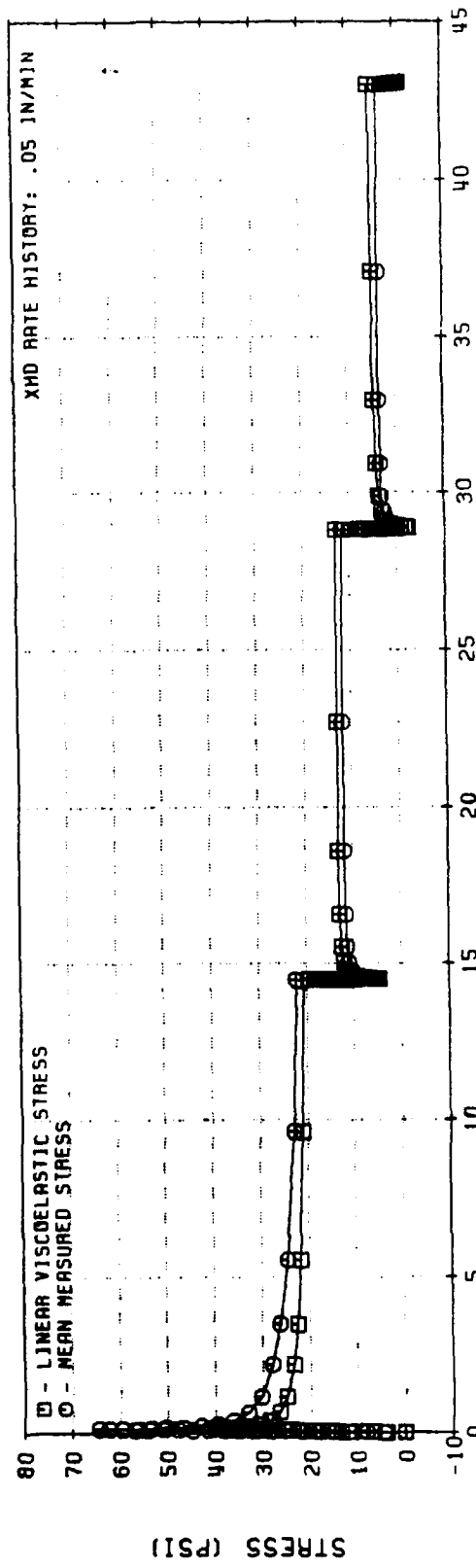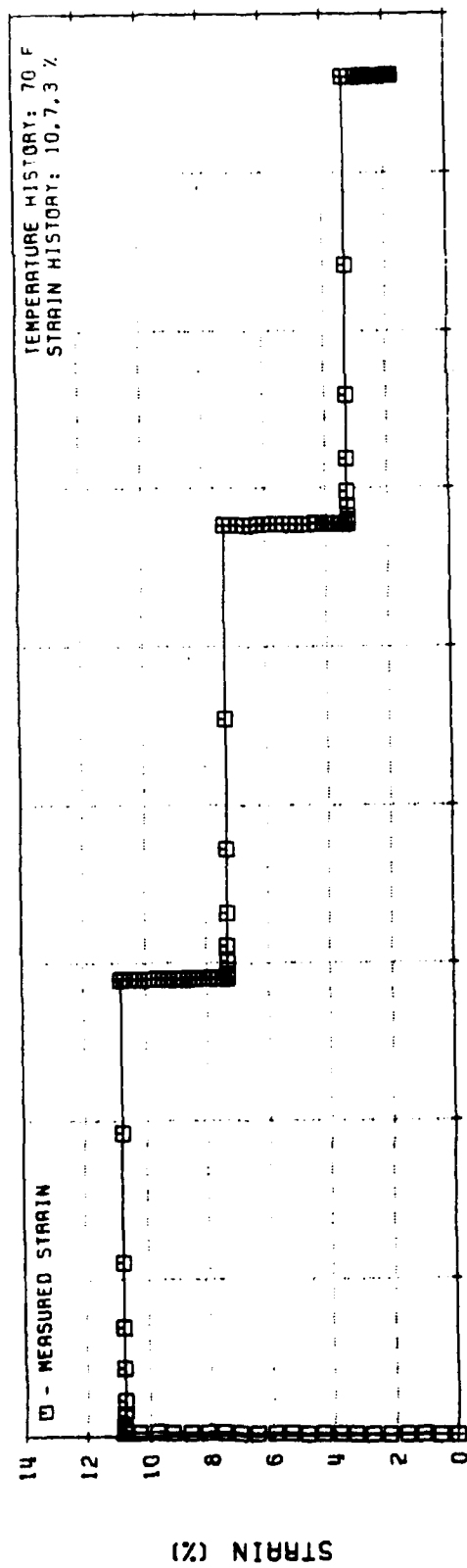
Figure 72. Linear Viscoelastic Stress Predictions for UTP-3001-750/7768
Short and Long Time Relaxation (Test No. 13)
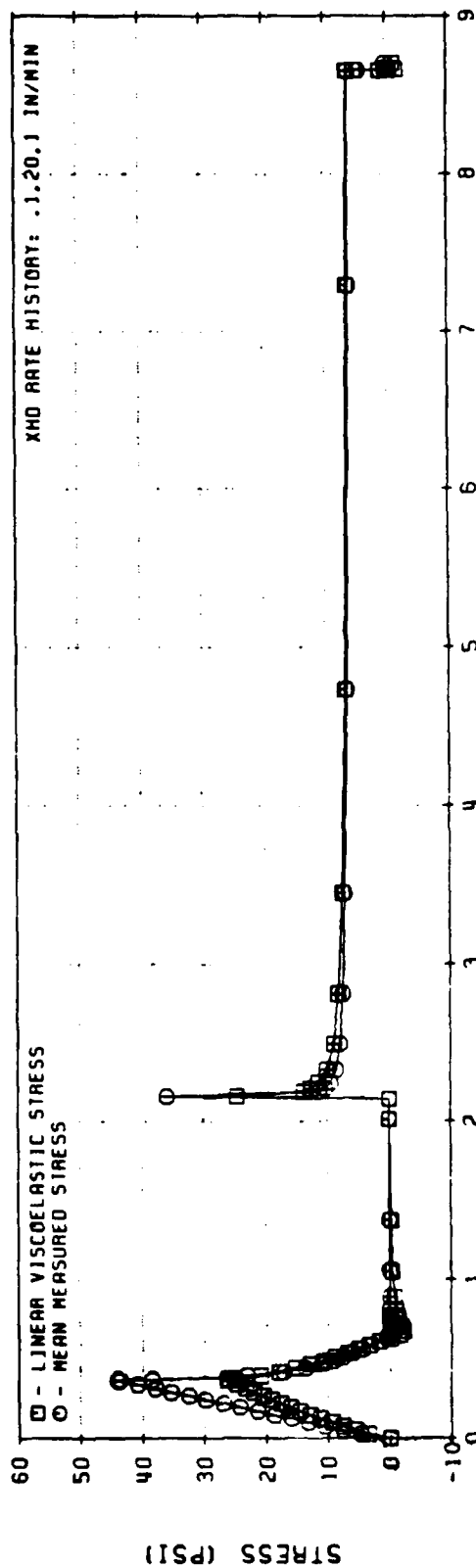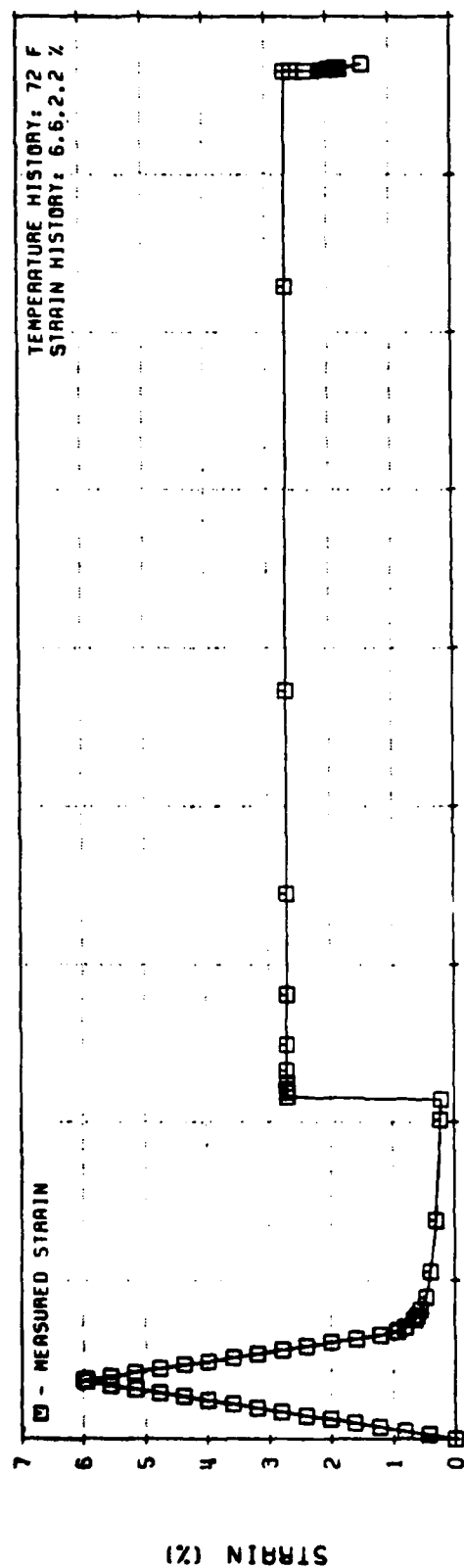
121

Figure 73. Linear Viscoelastic Stress Predictions for UTP-3001-750-7768 Predamage Relaxation (Test No. 9)

122
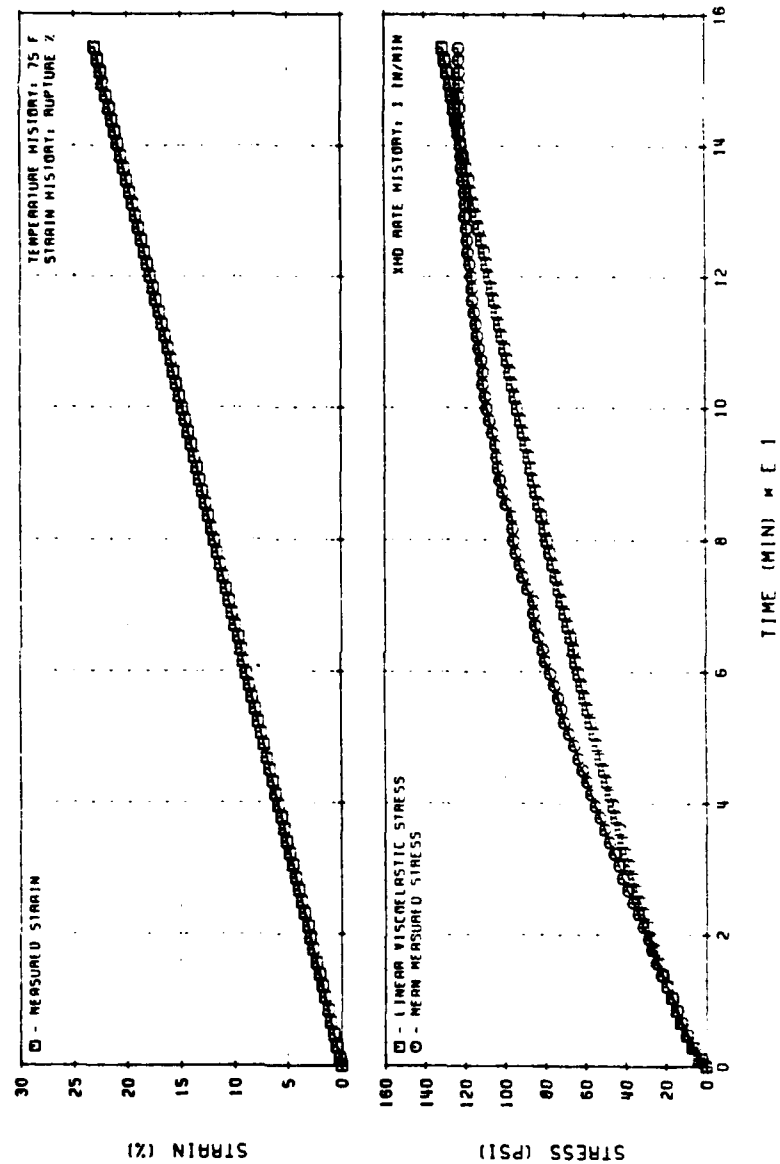
Figure 74. Linear Viscoelastic Stress Predictions for UTP-3001-750/7768 Constant-Rate Test History (Code No. 1)

31016

123
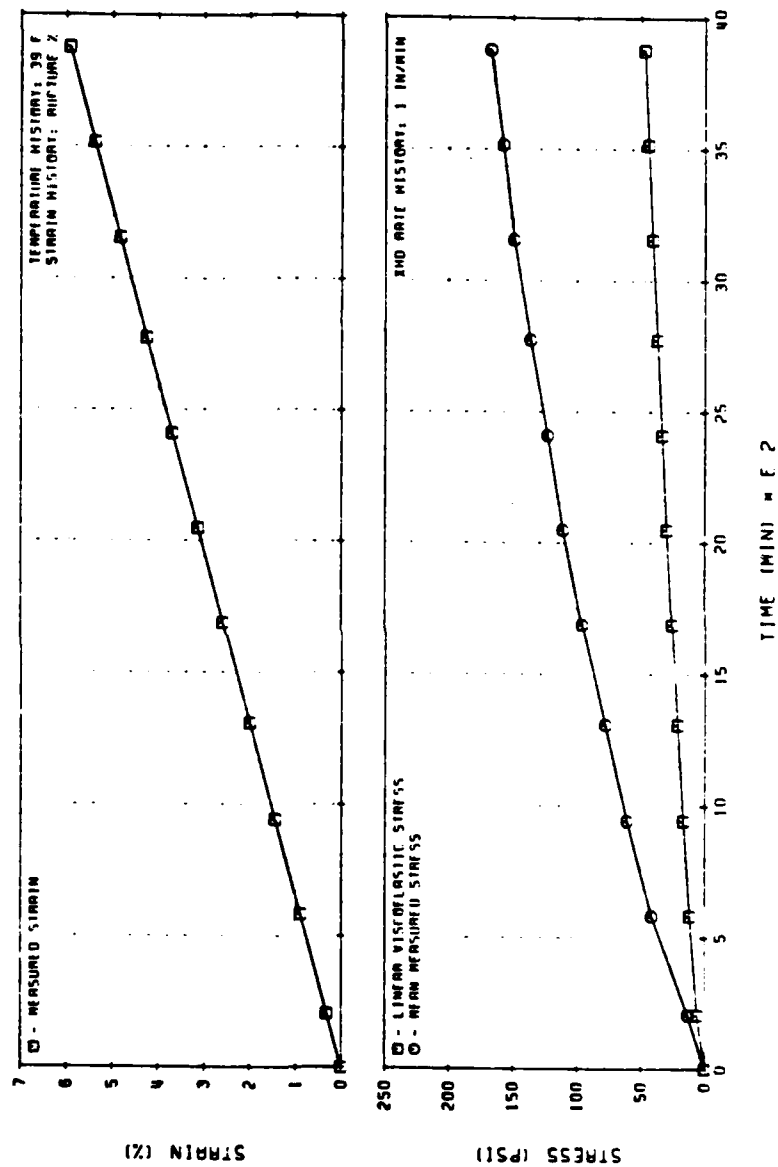
Figure 75. Linear Viscoelastic Stress Predictions for UTP-3001-750/7768 Constant-Rate Test History (Code No. 1)

124

31017
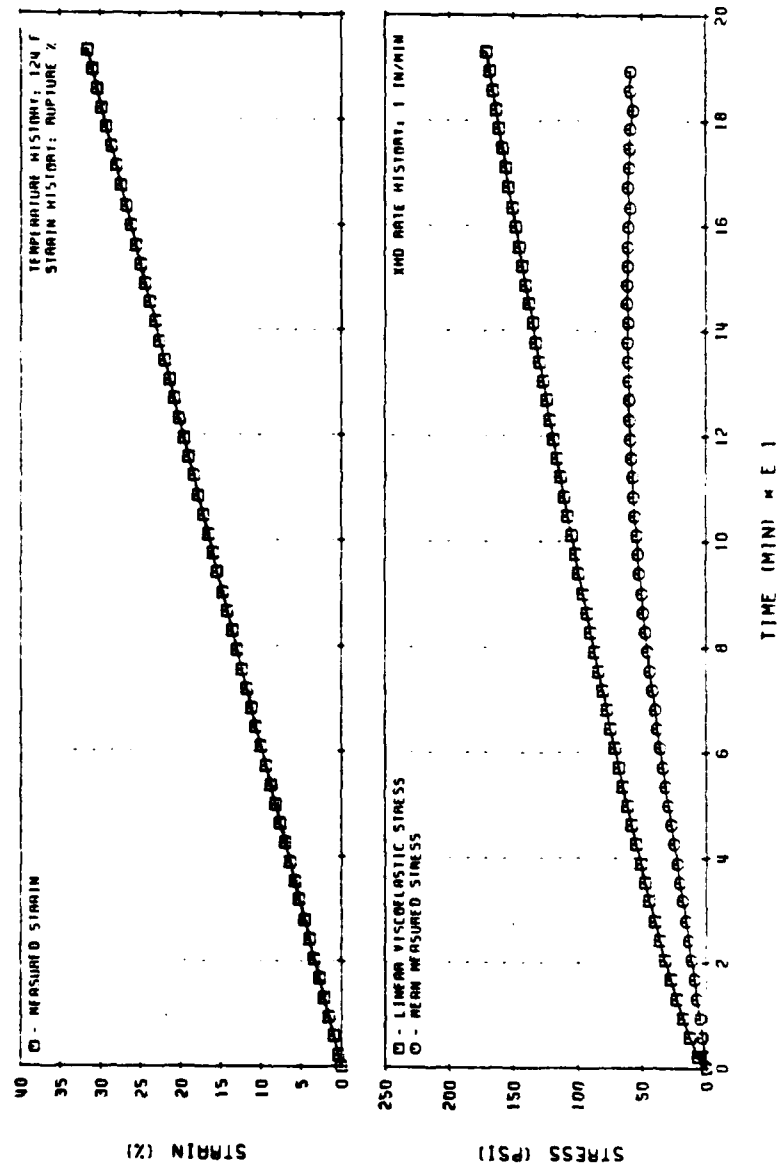
Figure 76. Linear Viscoelastic Stress Predictions for UTP-3001-750/7768 Constant-Rate Test History (Code No. 1)

125

31018

rate tests (Test No. 1) at 70, 40, and 123 F, as shown in Figures 61 to 65, respectively. Stress predictions for the same tests on UTP-3001 are shown in Figures 66 through 76.

Predictions for biaxial samples were also made using equation (19). For UTP-19,360B, it was assumed that $E_{biaxial} = 4/3 \ E_{uniaxial}$. This assumption is supported by the limited biaxial modulus tests conducted on the program. Predictions for UTP-3001 were made by substituting the biaxial relaxation modulus for that of the uniaxial.

The results for UTP-19,360B are given as follow. The lowest and highest constant rate tests (Test No. 14) are shown in Figures 77 and 78. Figure 79 contains the comparisons for the stress relaxation history (Test No. 16). The results for UTP-3001 for the same tests are given in Figures 80 to 82.

4.2.3 Linear Thermoviscoelasticity Analyses of UTP-19,360B Propellant

Simultaneous cooling and straining tests of uniaxial and biaxial specimens and the complex biaxial ramp-relaxation ramp-test while cooling and heating have been analyzed according to linear viscoelasticity theory in order to provide a baseline for comparison with the nonlinear theoretical predictions and to evaluate the error between linear predictions and measured experimental results.

The one-dimensional equations are as shown in equation (19), with the exception that ϵ is replaced by $\epsilon - \alpha\Delta T$ and $\Delta T = T_o - T(t)$. In order to simplify numerical calculations, the time-temperature shift function was represented by the power law given in equation (21).

Calculations have been made for prony series and power-law representations of the relaxation modulus. Both types of computations give comparable results and the computer codes have been verified with handbook type calculations.
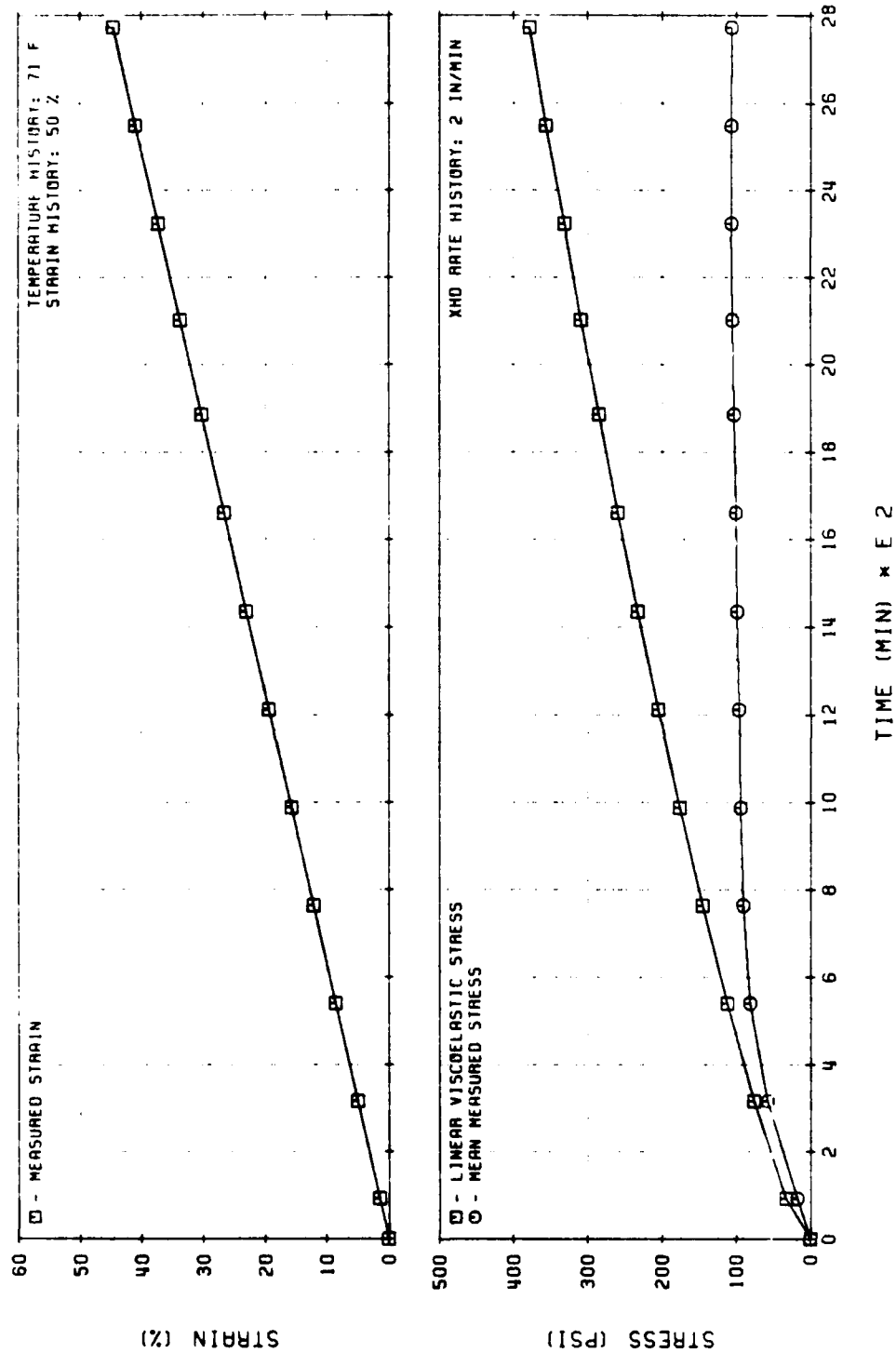
Figure 77. Linear Viscoelastic Stress Predictions for UTP-19,360B-400/1777 Biaxial Constant-Rate (Test No. 14)

31019

127
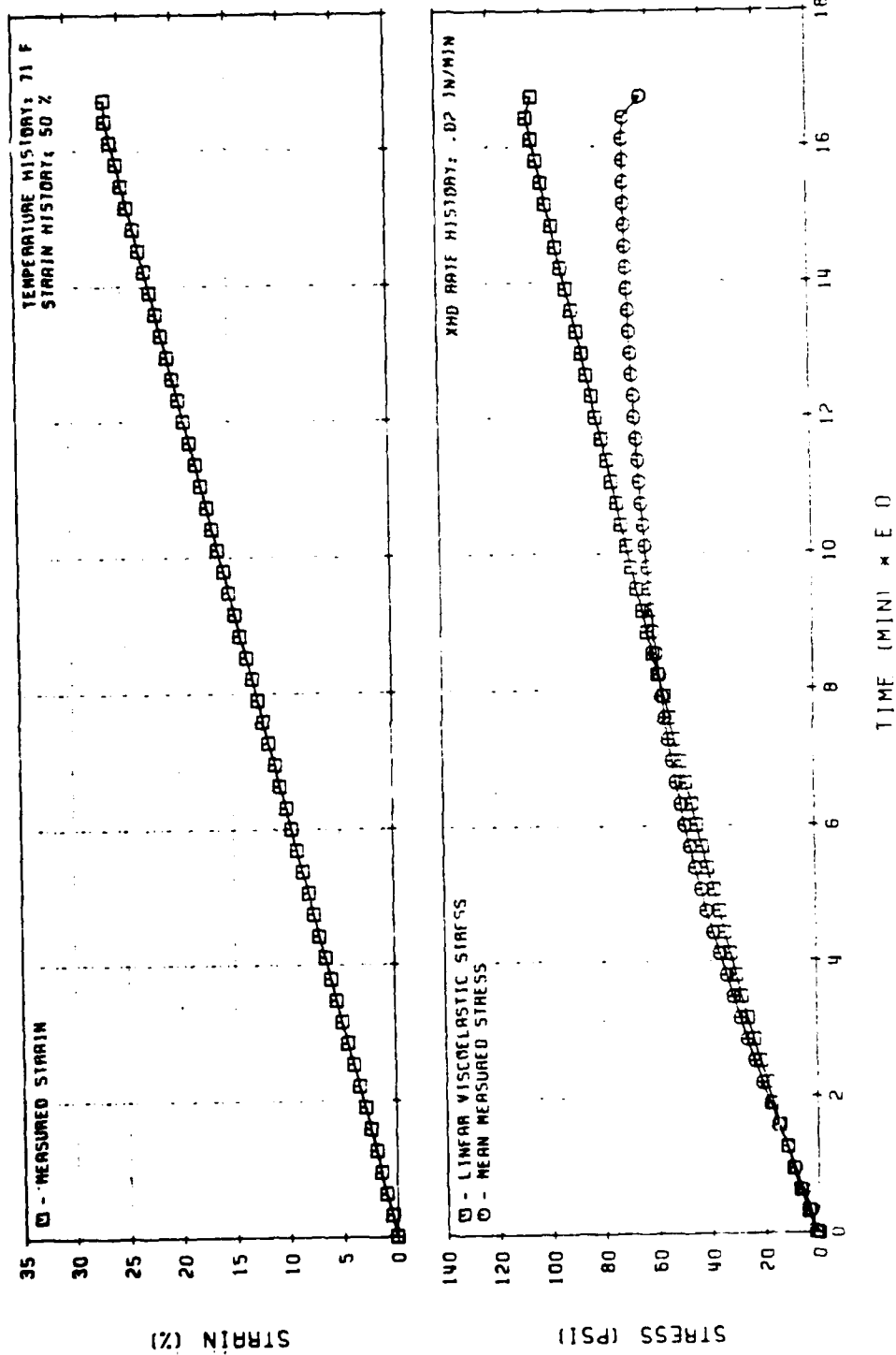
Figure 78. Linear Viscoelastic Stress Predictions for UTP-19,360B-400/1777 Biaxial Constant-Rate (Test No. 14)

128
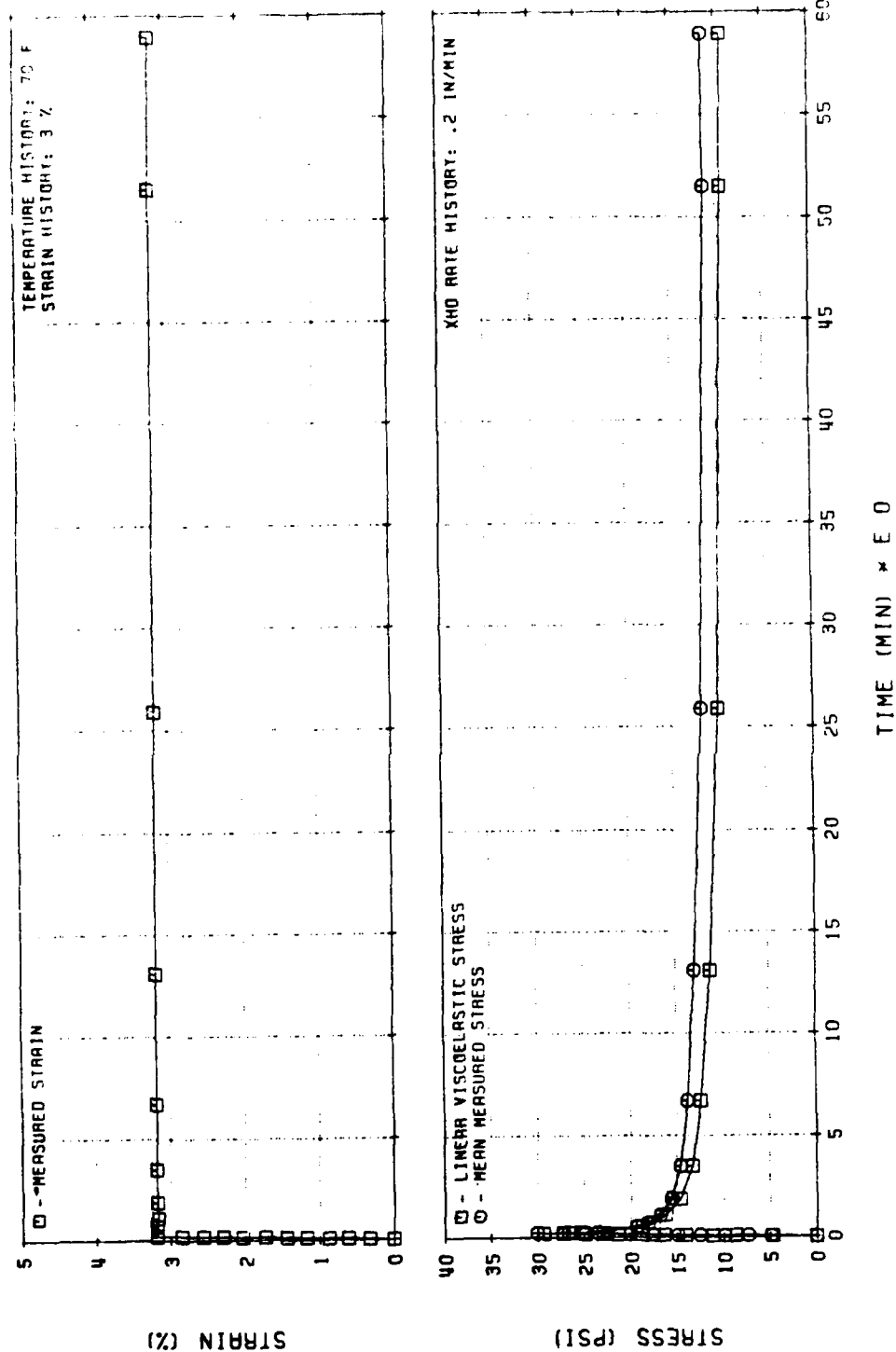
Figure 79. Linear Viscoelastic Stress Predictions for UTP-19,360B-400/1777 Biaxial Stress Relaxation (Test No. 16)

129

31076
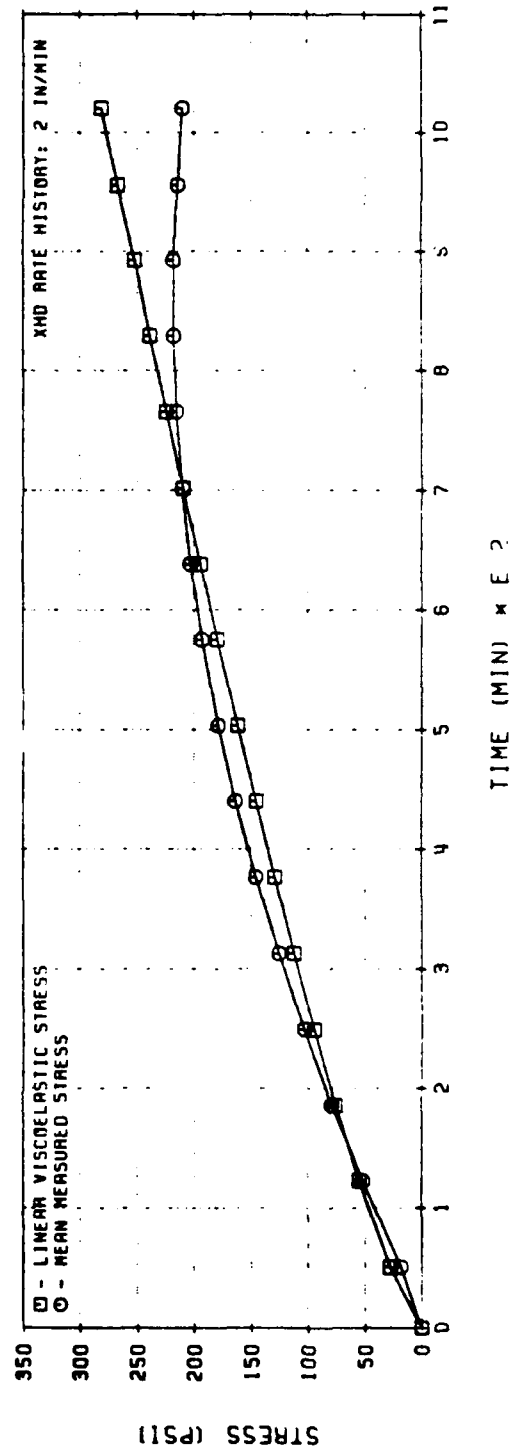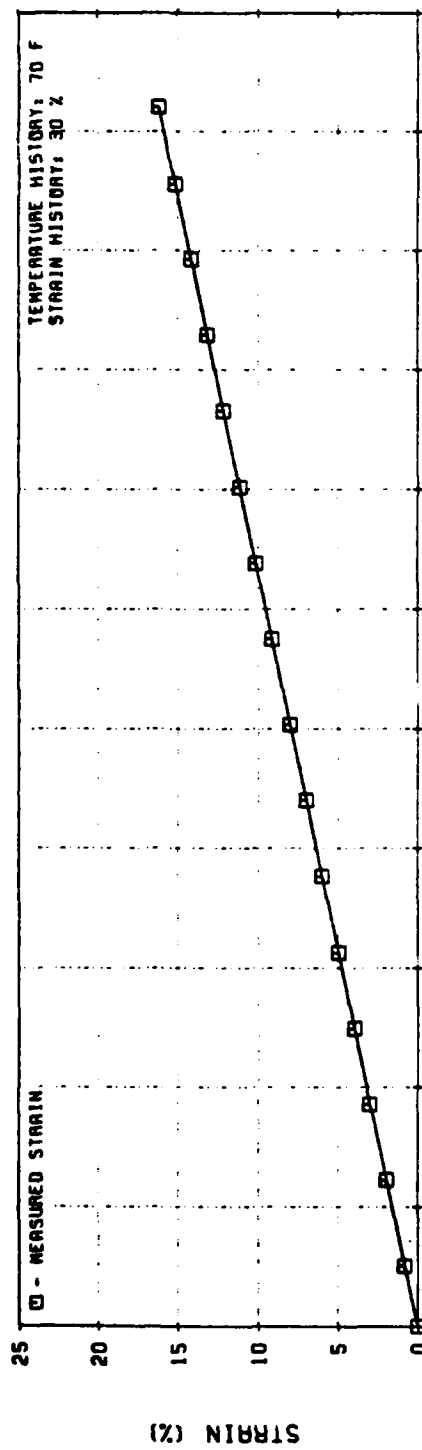
Figure 80. Linear Viscoelastic Stress Predictions for UTP-3001-750/7768 Biaxial Constant-Rate (Test No. 14)

130
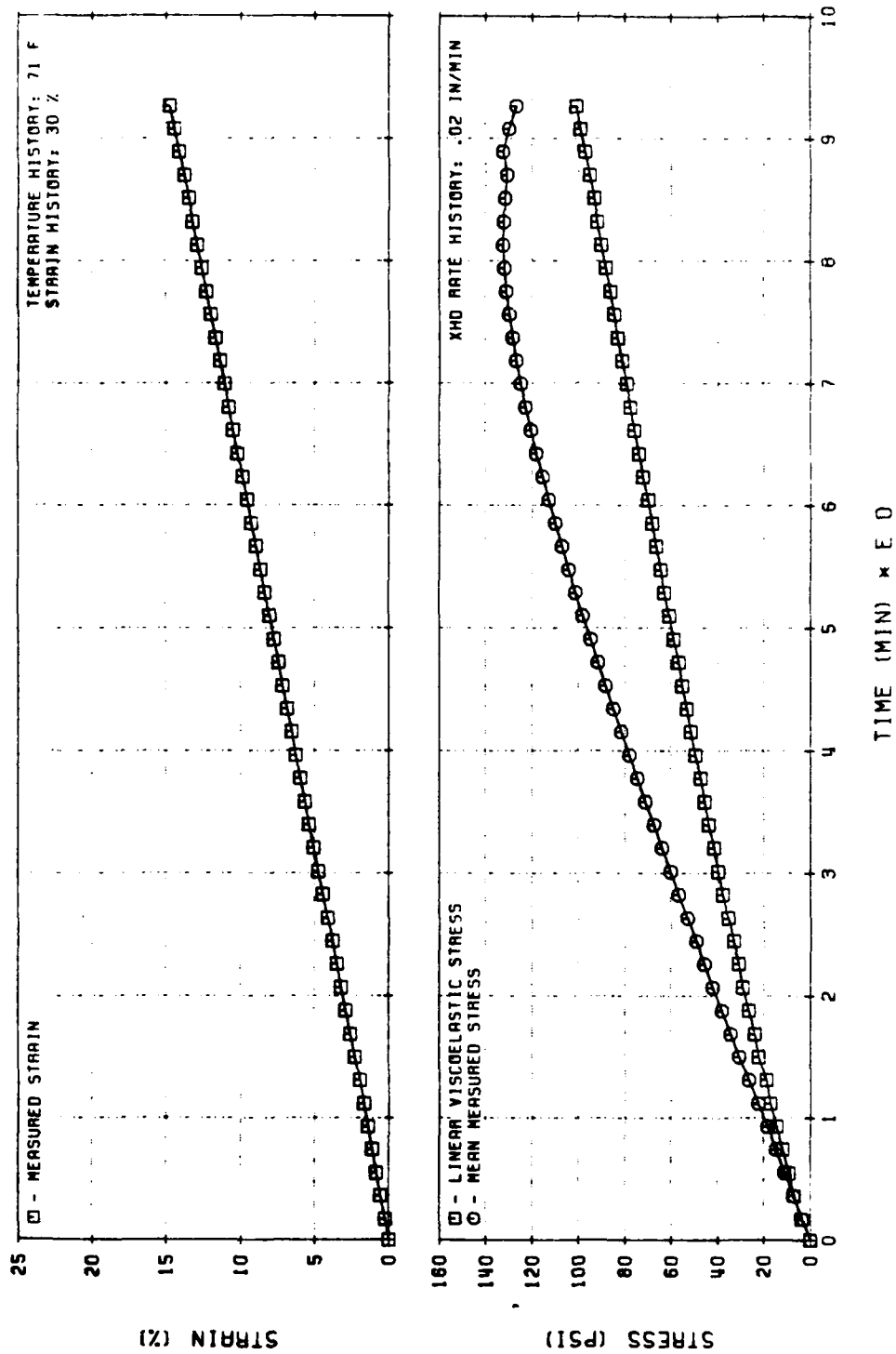
Figure 81. Linear Viscoelastic Stress Predictions for UTP-3001-750/7768
Biaxial Constant-Rate (Test No. 14)

31078

131
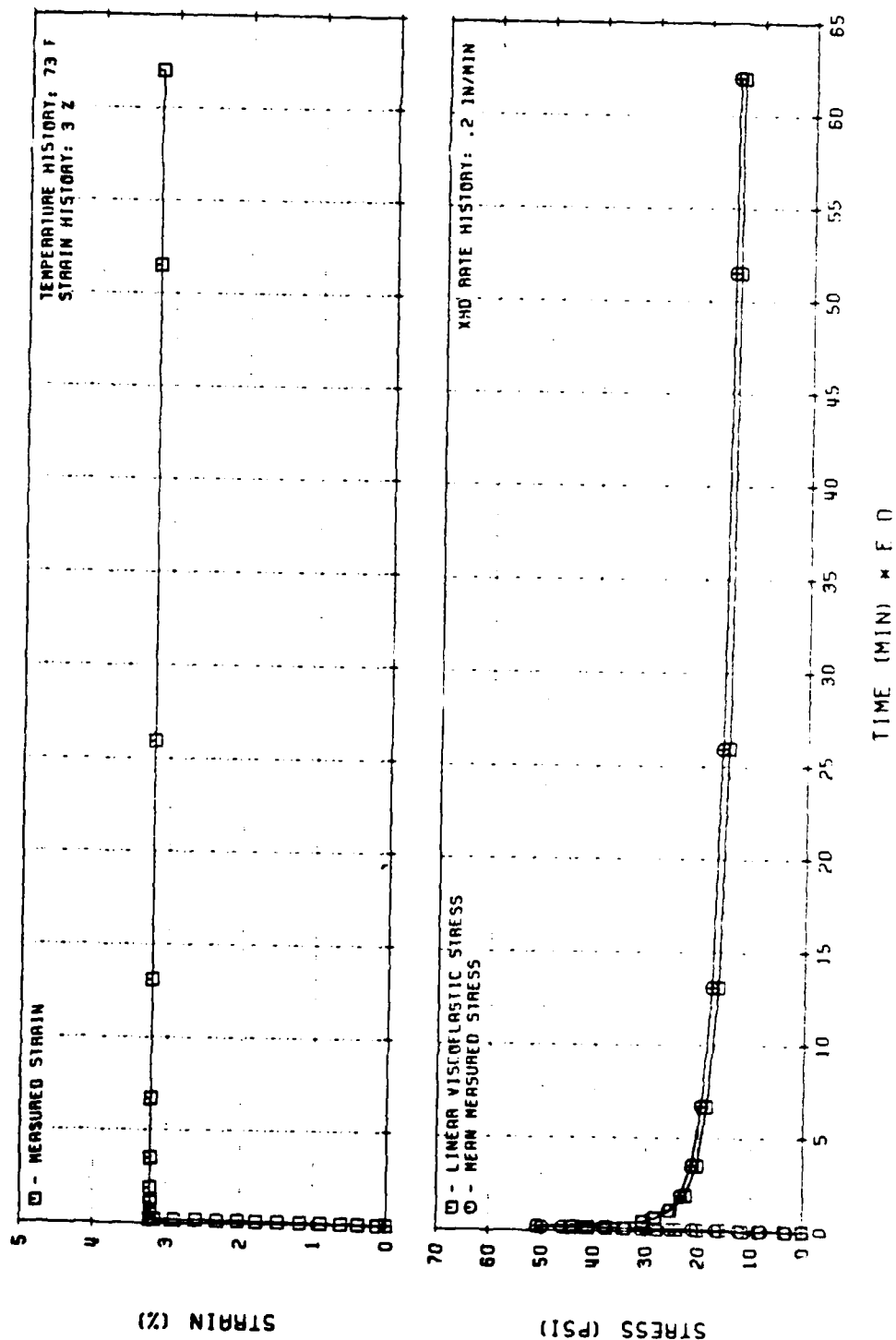
Figure 82. Linear Viscoelastic Stress Predictions for UTP-3001-750/7768 Biaxial Stress Relaxation (Test No. 16)

31079

132

Using Prony series representation for the modulus and assuming a constant coefficient of linear thermal expansion, equation (19) can be written in the form

$$\sigma(t) = (\epsilon - \alpha \Delta T) \left\{ E_e + \frac{1}{t} \sum_{i=1}^{N} \int_0^t E_i \, e^{-\lambda_i(t' - \xi')} \, d\tau \right\}$$

where it is also assumed that $\dot{\epsilon}$ and $\dot{\Delta T}$ are constant. Substituting equation (21) into equation (20) and performing the indicated integrations leads to

$$\sigma(t) = (\epsilon - \alpha \Delta T) \left\{ E_e + \frac{1}{t} \sum_{i=1}^{N} E_i \int_0^t e^{-au^{1+m}} \, du \right\} \qquad (22)$$

where:

$$a = \frac{1}{(1 + m)} \left(\frac{\dot{T}}{T_R - T_a} \right)^m \lambda_i \qquad (23)$$

Equation (22) was evaluated numerically calculating the constant $\dot{\epsilon}$ and $\dot{T}$ at each data point.

Assuming a power law representation for the modulus of the form

$$E(t) = E_e + E_1 t^{-n} \qquad (24)$$

leads to

$$\sigma(t) = (\epsilon - \alpha \Delta T) \left\{ E_e + \frac{E_1(t/A_T)^{-n}}{1 - n} - I_T \right\} \qquad (25)$$

133

where

$$I_T = \frac{1-n}{(1+m)} -n \left(-1 + \frac{1}{T_n}\right)^{1-n} \int_{(H + \Delta T_n)}^{1} (1-u)^{-m} \cdot u^{\left(\frac{m}{m+1} + n-2\right)} du \qquad (26)$$

Figures 83 through 85 compare the measured and predicted stresses for the uniaxial tests and Figure 86 compares stresses for the biaxial test. The good agreement with the biaxial straining and cooling test is believed to be fortuitous. In fact, the test data is questionable, since the linear predictions did not agree even during the initial cooldown of the biaxial ramp-relaxation ramp test as shown in Figure 87.

Handbook type calculations were also made to determine a thermomechanical coupling coefficient, A_F, with the results shown in Figures 88 through 90. The results obtained using a constant A_F agree reasonably well with experiment, with the exception of the biaxial tests. Using an A_F calculated from uniaxial tests, the predictions shown in Figures 91 and 92 were made. Observe that the initial cooldown of the biaxial ramp-relaxation-ramp test is matched well, but the cooling-only test is not, giving further credence to our contention that these test results are invalid.

4.3 M. QUINLAN'S THEORY OF MATERIALS WITH VARIABLE BONDING
4.3.1 Original Model

In developing a mathematical framework for his stress-strain law, Qunilan,[4] reasoned that since propellants consist of minute rigid particles embedded in a polymer matrix, such materials would respond to a deformation process with a change in the amount of species to species bonding. He thus proposed to correct the deficiencies of fading-memory type theories by introducing a correction term that accounted for the changes in the state of bonding that

134
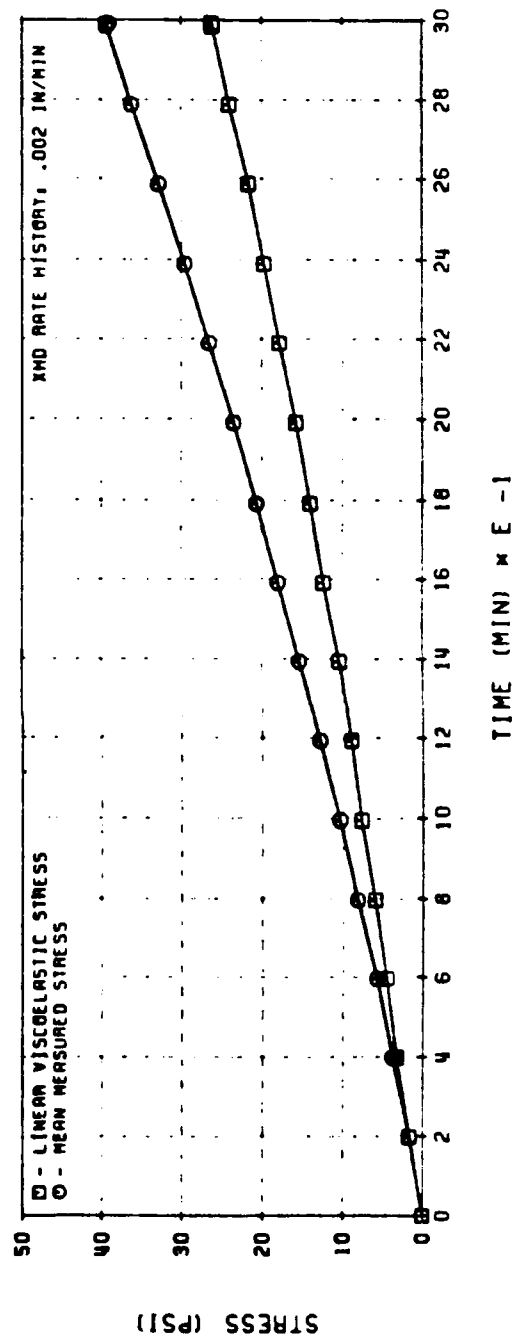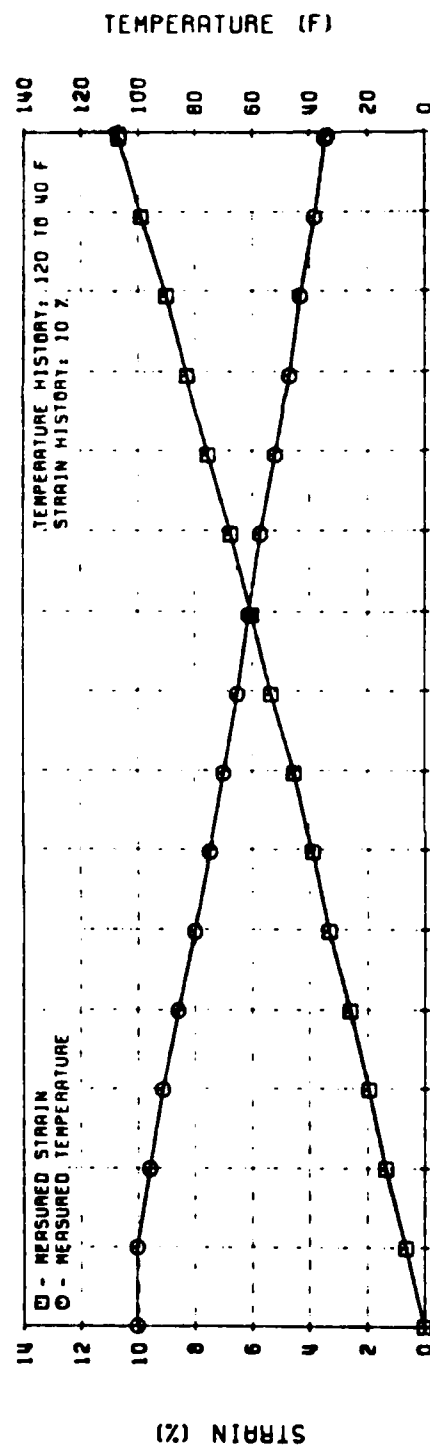
Figure 83. Linear Viscoelastic Stress Predictions for UTP-19,360B-400/1777 6-in. Bar Straining - Cooling (Test No. 18)

31080

135
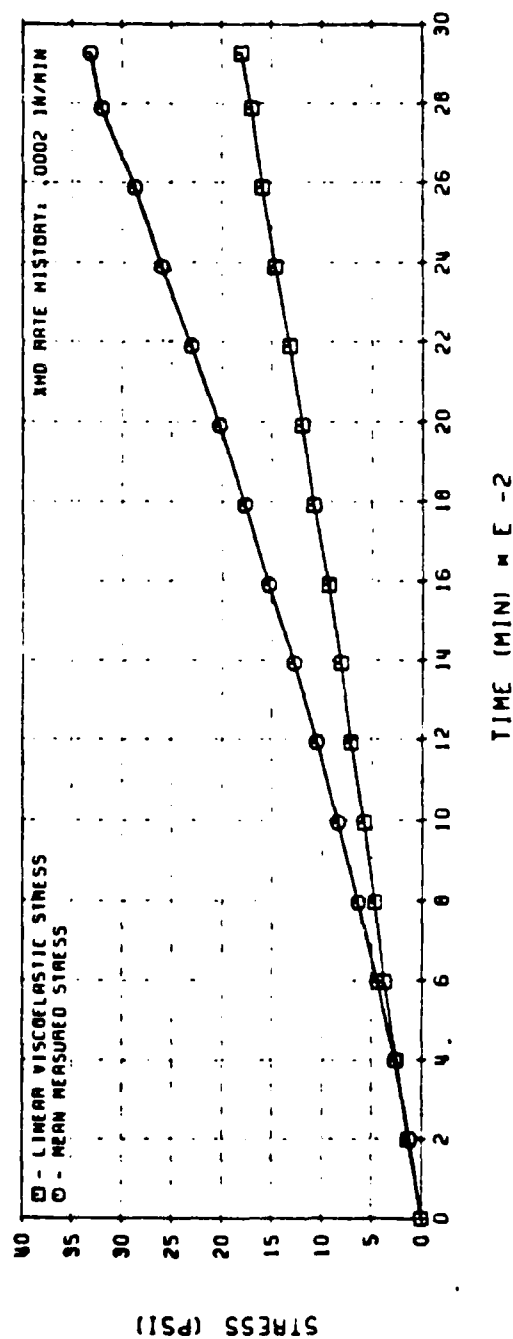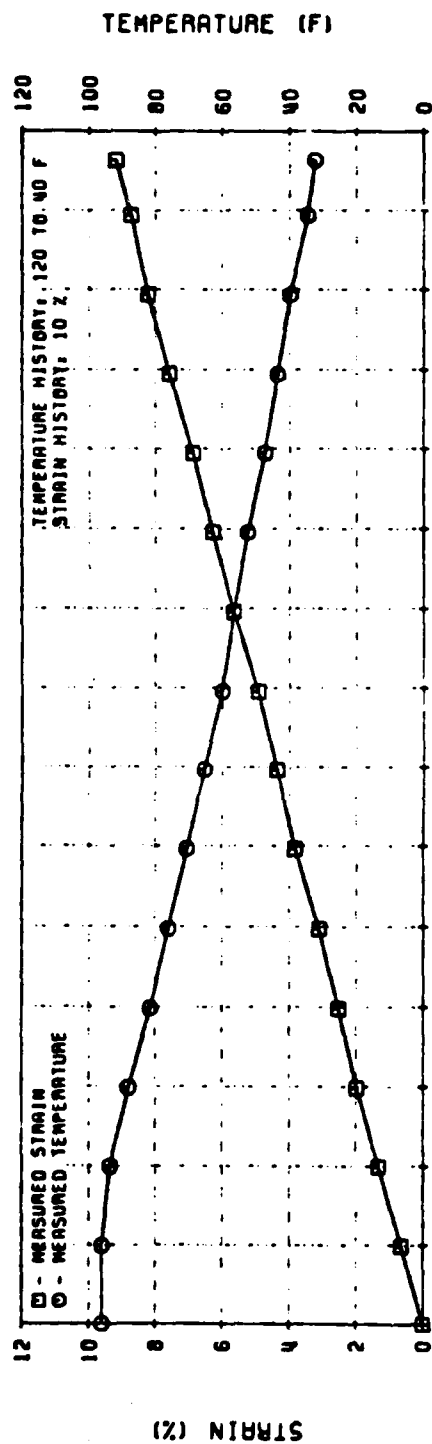
Figure 84. Linear Viscoelastic Stress Predictions for UTP-19,360B-400/1777 6-in. Bar Straining - Cooling (Test No. 18)

136
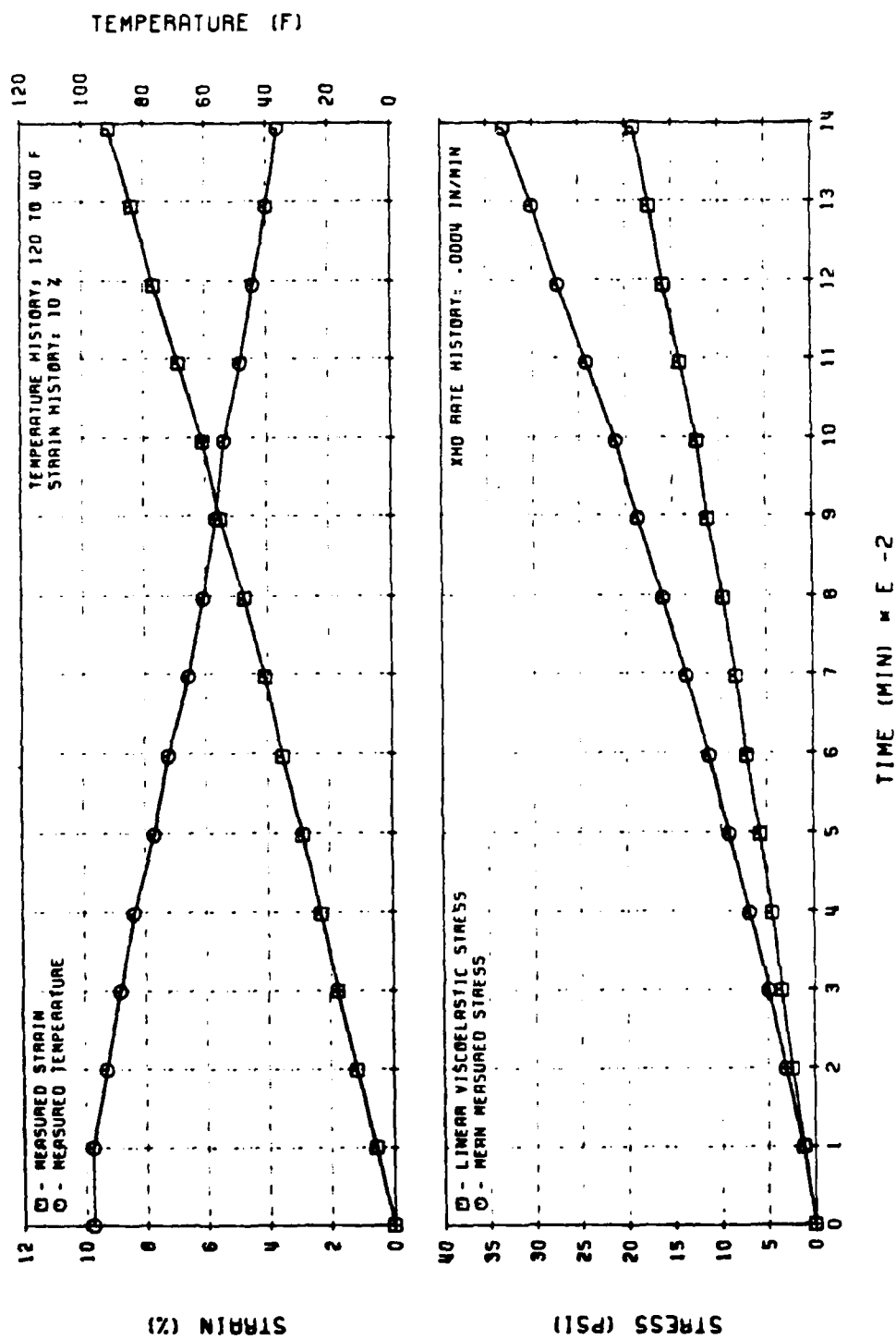
Figure 85. Linear Viscoelastic Stress Predictions for UTP-19,360B-400/1777
6-in. Bar Straining - Cooling (Test No. 18)
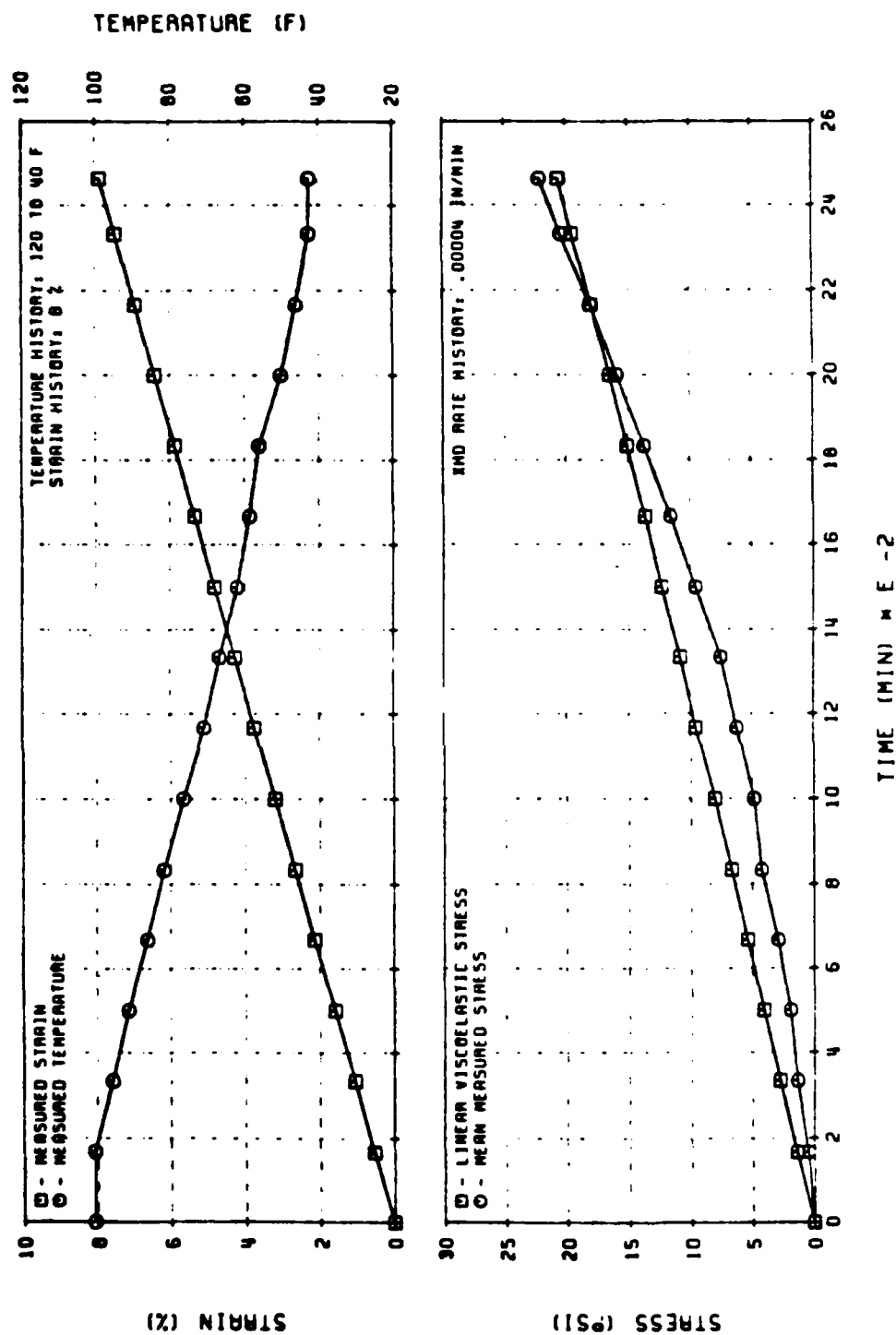
Figure 86. Linear Viscoelastic Stress Predictions for UTP-19,360B-400/1777 Biaxial Straining - Cooling (Test No. 15)
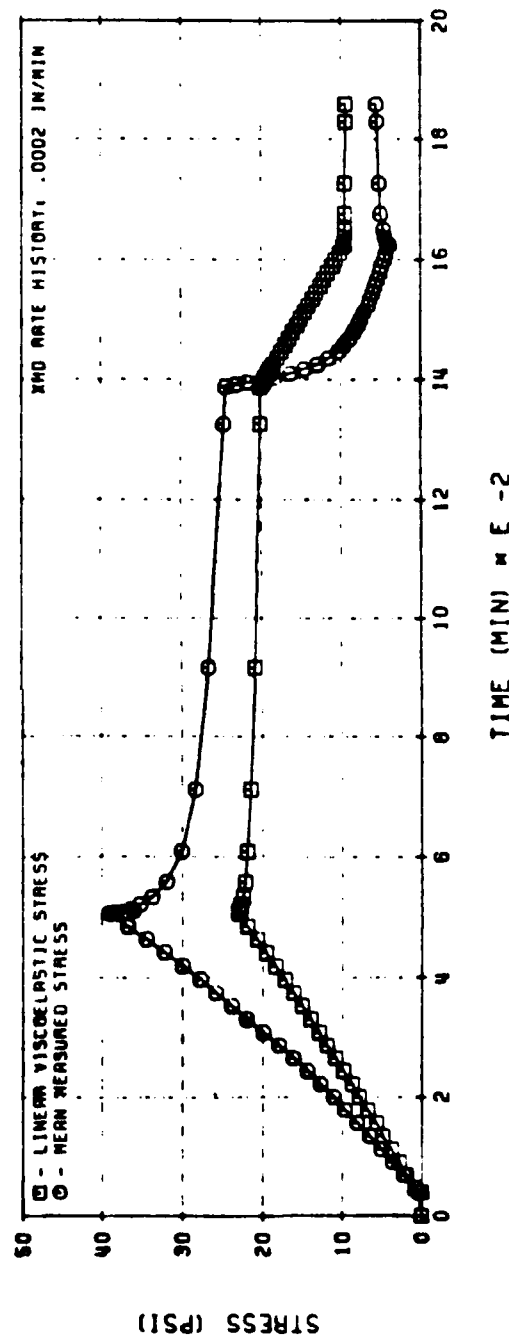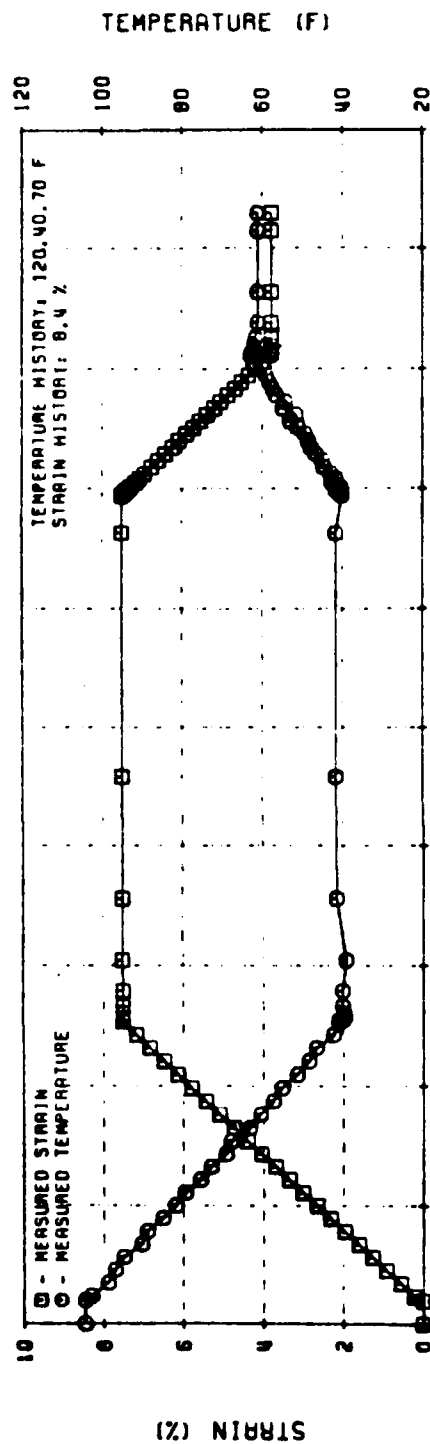
Figure 87. Linear Viscoelastic Stress Predictions for UTP-19,360B-400/1777 Biaxial Ramp-Relxation-Ramp (Test No. 21)

139
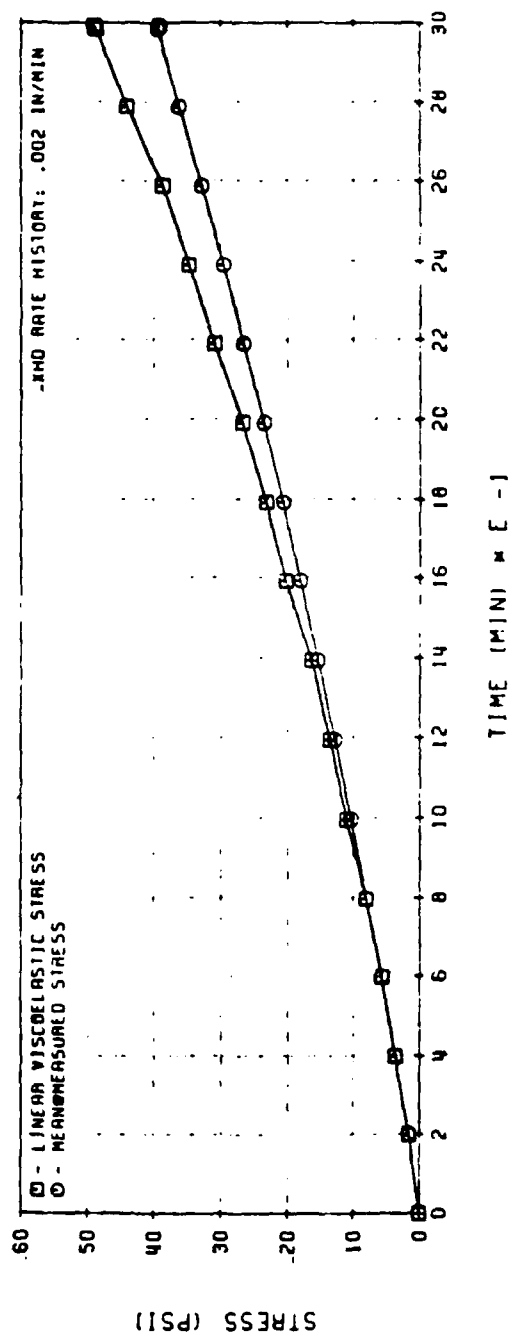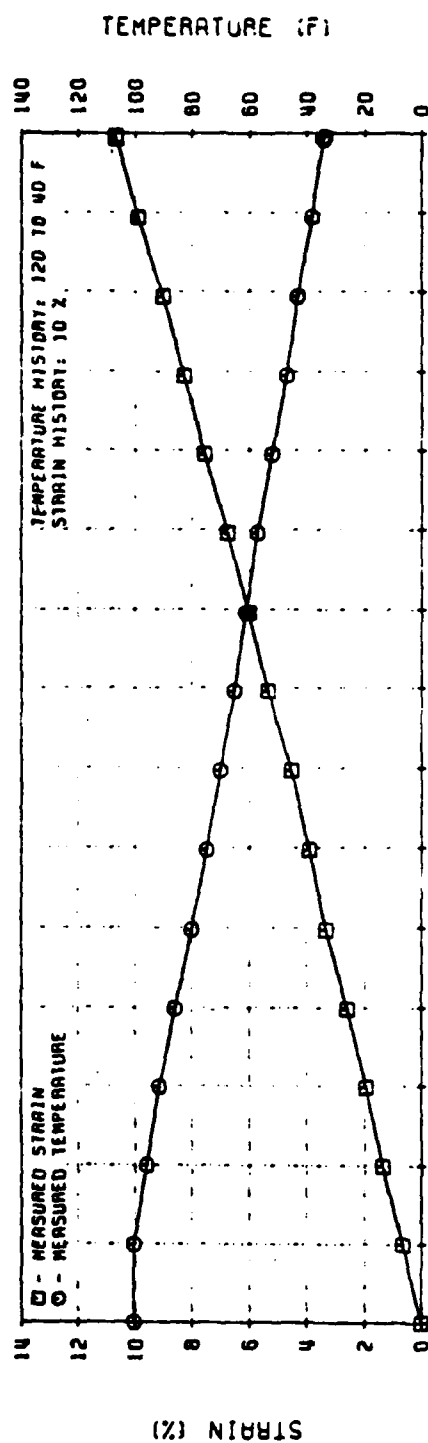
Figure 88. Linear Viscoelastic Stress Predictions for UTP-19,360B-400/1777 6-in. Bar Straining-Cooling (Test No. 18)

31085

140

TEMPERATURE (F)

TEMPERATURE HISTORY: 120 TO 40 F
STRAIN HISTORY: 10 %

XHD RATE HISTORY: .0004 IN/MIN

☐ —MEASURED STRAIN
⊙ —MEASURED TEMPERATURE

☐ —LINEAR VISCOELASTIC STRESS
⊙ —MEAN MEASURED STRESS

STRAIN (%)

STRESS (PSI)

TIME (MIN) × E -2
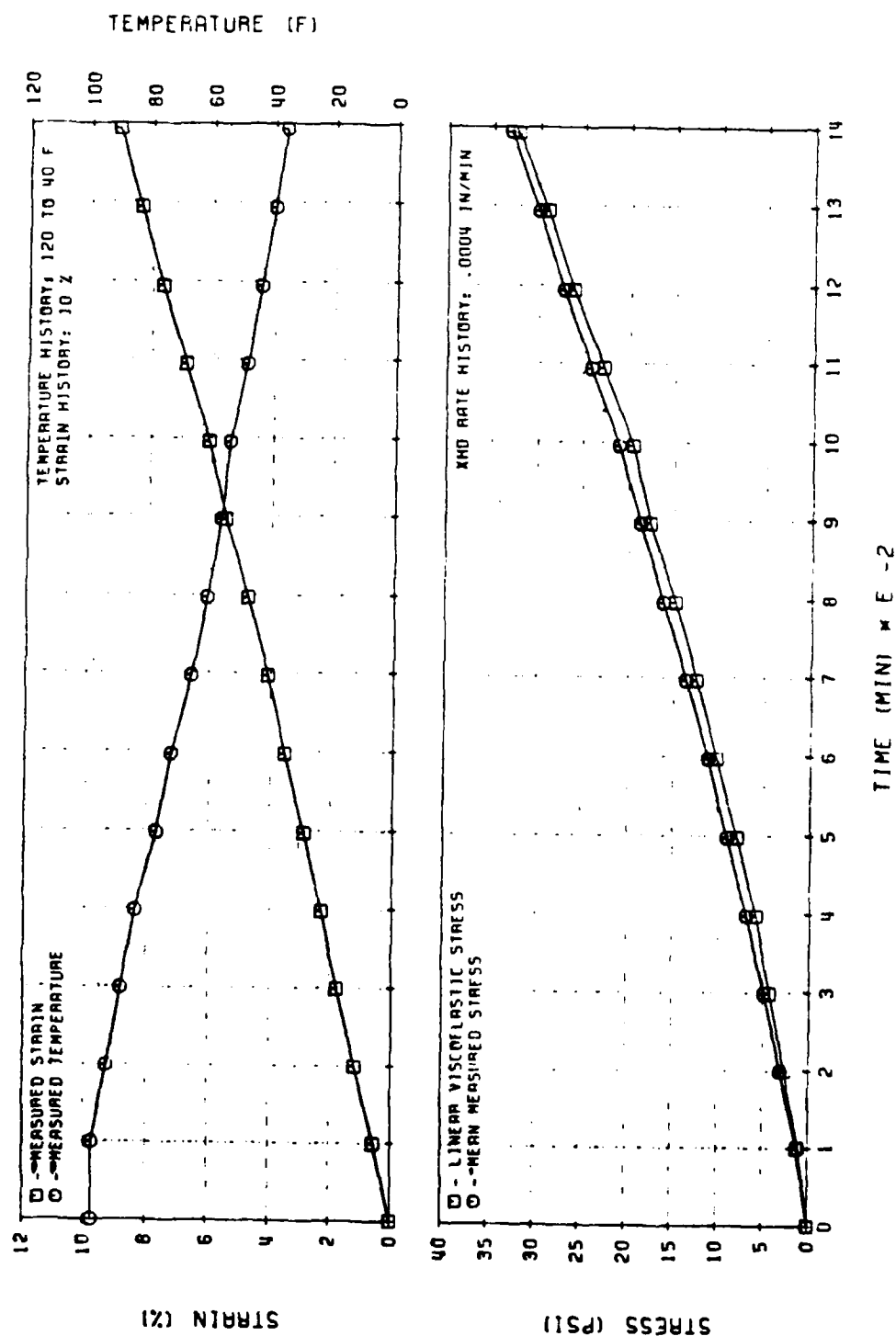
Figure 89. Linear Viscoelastic Stress Predictions for UTP-19,360B-400/1777 6-in. Bar Straining-Cooling (Test No. 18)

141
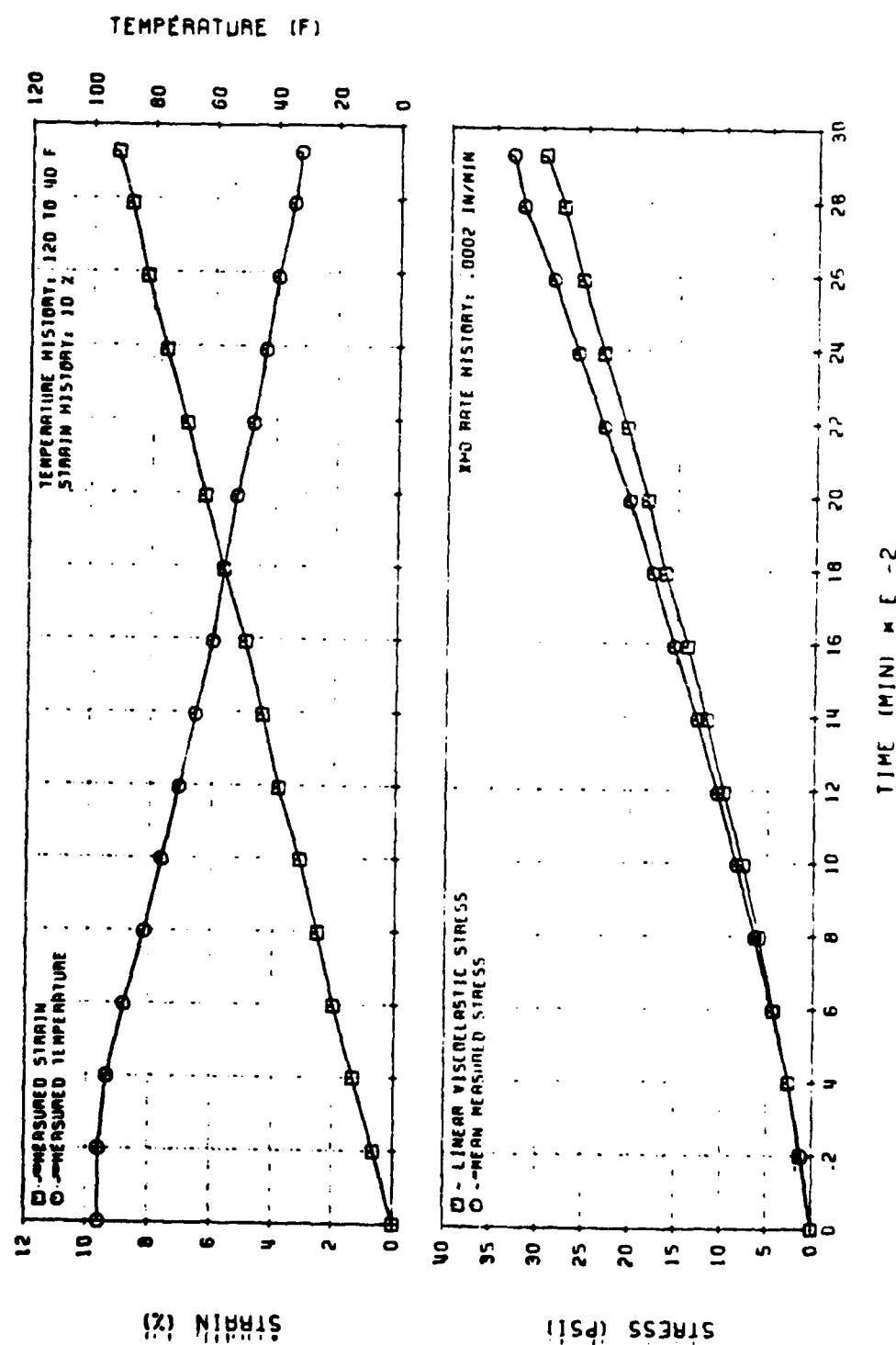
Figure 90. Linear Viscoelastic Stress Predictions for UTP-19,360B-400/1777 6-in. Bar Straining-Cooling (Test No. 18)

142
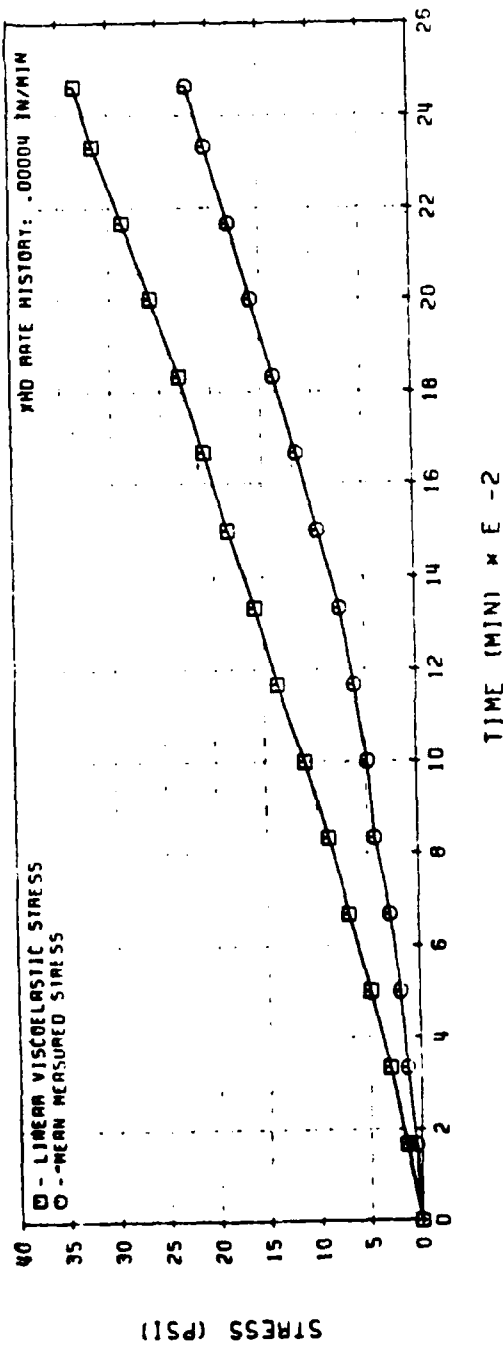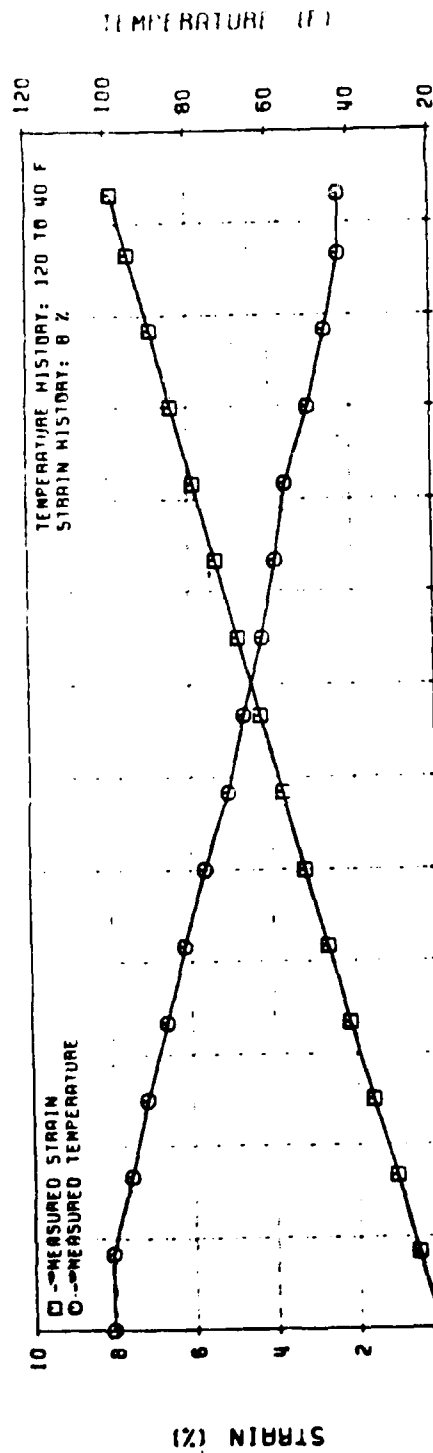
Figure 91. Linear Viscoelastic Stress Predictions for UTP-19,360B-400/1777 Biaxial Straining - Cooling (Test No. 15)

143
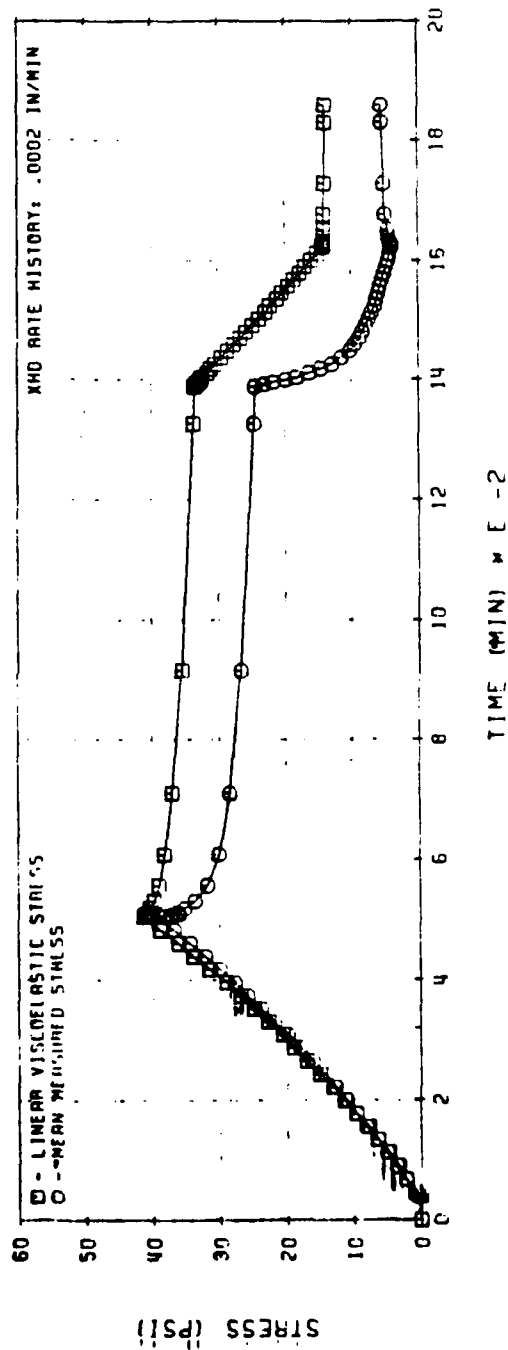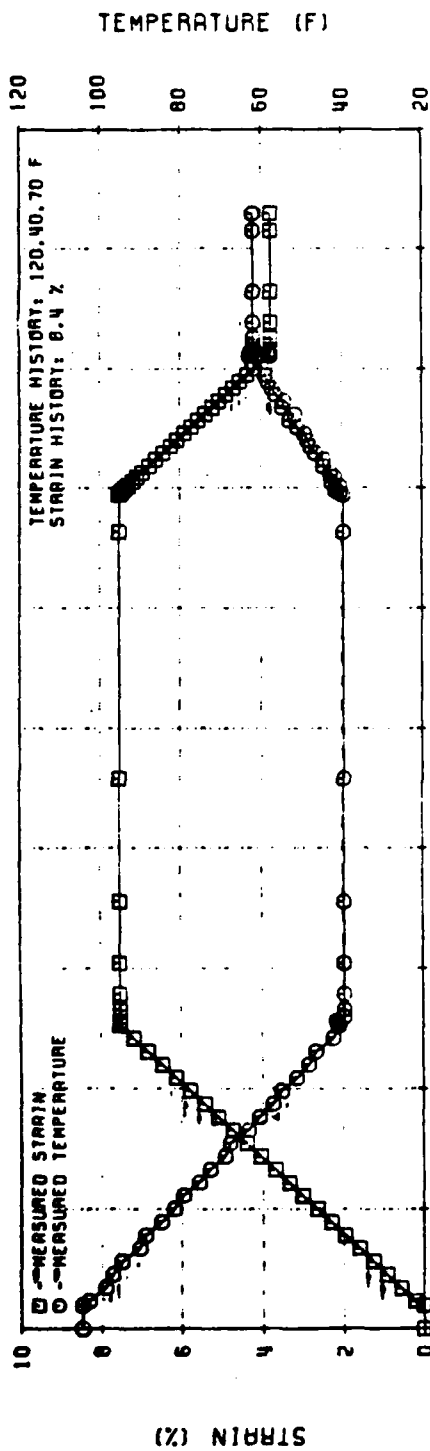
Figure 92. Linear Viscoelastic Stress Predictions for UTP-19,360B-400/1777
Biaxial Ramp-Relaxation-Ramp (Test No. 21)

31089

144

are induced by a deformation process. His constitutive model then took the form:

$$\sigma = \sigma_f + \sigma_b \tag{27}$$

in which:

σ = current stress

σ_f = fading-memory type stress

σ_b = stress correction due to change in the state of bonding.

Motivated to some extent by reaction-rate theory, Quinlan modeled the evolution of the bonding state through the following ordinary differential equation:

$$\dot{\pi} = \alpha \left\{ \dot{\phi} - \mu \left[1 - e^{\nu (\phi - \pi)} \right] \right\} \tag{28}$$

subject to the initial condition:

$$\pi(0) = 1 \tag{29}$$

in which π represents the state of bonding; α, μ, and ν are material parameters, and

$$\varphi = 1 + \epsilon \tag{30}$$

is the stretch ratio; with ϵ, the strain.

The unique solution of equation (27) may be readily obtained for piecewise linear stretch histories.[4]

Taking a linear viscoelastic relation for σ_f, and considering the stress correction term, σ_b, as proportional to the state of bonding, Quinlan arrived at the following stress-strain law:

145

$$\sigma(t) = \int_0^t G(t - \tau)\, \dot{\phi}(\tau)\, d\tau + B_o\, \dot{\pi}(t) \tag{31}$$

with:

$$G(t) = E_o\, t^{-n} \tag{32}$$

$$\dot{\pi}(t) = \alpha \left\{ \dot{\phi} - \mu \left[1 - e^{\nu(\phi - \pi)} \right] \right\} \tag{33}$$

and

$$\pi(t = 0) = 1 \tag{34}$$

The six parameters (E_o, n, B_o, α, μ and ν) needed in this theory to characterize a propellant may be obtained by fitting the model to the observed response of the material when subjected to a saw-tooth strain history that has increasing peak strains and sufficiently long rest periods between cycles. Alternatively, the studies reported in the literature on the effects of employing different data bases for characterization show that the test history should primarily include the maximum expected strain level, the expected range of strain rates, as well as rest and relaxation periods.

The model was used to predict the response of TP-H1011 under several loading histories, and it reproduced, somewhat accurately, the general trend of observed solid propellant behavior. CSD developed a computer code to automate Quinlan's constitutive equations.

The parameters entering Qunilan's law were determined by the code through minimization of the root-mean-square (rms) error between the observed stresses and those predicted via the foregoing equations. This procedure may be formally stated as follows:

Determine E, n, B, α, μ, ν so that

$$F = \left\{ \sum_{i=1}^{N} (\sigma_i - \sigma_{ci})^2 \right\}^{1/2} ; \tag{35}$$

acquire a minimum value, subject to

E, B, α, μ, $\nu > 0$; and $-1 < n < 0$

where N, σ_i, and σ_{ci} stand, respectively, for the number of data points, the ith measured stress, and the corresponding stress computed from the proposed law.

Such an optimization process is performed in the code with the Powell-BOTM sequential-search algorithm.

4.3.1.1 Verification of Published Experiment

In reproducing Dr. Quinlan's experiment, CSD took as a basic data set the reported values of time, measured stress, and stretch rate. The corresponding saw-tooth stretch history was internally built by the computer code. This approach introduced a difference in the degree of accuracy of representation between the values contained in Dr. Quinlan's report and those used by CSD (Table 11). Thus, small discrepancies were observed in verifying Quinlan's work. An overall measure of such deviations is given by the rms error per cycle. While Dr. Quinlan's reported value is 2.7 psi, that obtained at CSD was 2.98 psi.

4.3.1.2 Verification of Uniqueness of Solution

Establishing the uniqueness of parameter values for use with the nonlinear law is of capital importance. To this end, test history number 4 of Table 12 was
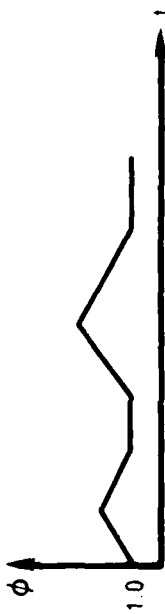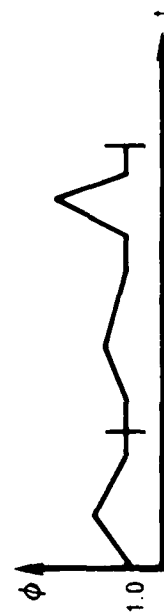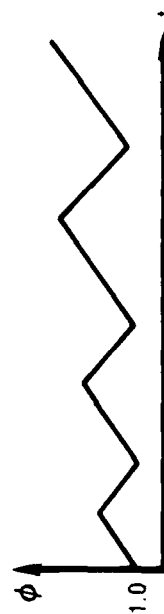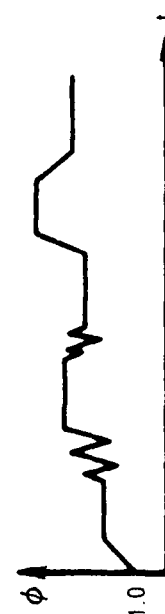
TABLE 11. SUMMARY OF QUINLAN'S AND CSD'S DATA

Cycle*	e, %	$\dot{e}$	Quinlan Computations $(\sigma_{comp} - \sigma_{meas})/$ peak	CSD Calculations Using Quinlan Parameters, $(\sigma_{comp} - \sigma_{meas})/$ peak	CSD First Two Cycles $(\sigma_{comp} - \sigma_{meas})/$ peak	Peak σ_{meas}
1	2.7	$\epsilon_0 = 0.34$ in./in./min	-6.8 psi	-6.3	-3.1	28.1
2	3.8	$\epsilon_0 = 0.34$ in./in./min	+2.3	+3.5	-1.8	28.1
3	4.5	$\epsilon_0 = 0.34$ in./in./min	+4.7	+5.7	-1.2	28.1
4	5.5	$\epsilon_0 = 0.34$ in./in./min	+6.4	+7.1	-3.6	28.1
5	6.6	$\epsilon_0 = 0.34$ in./in./min	+2.0	+2.8	-6.8	28.1
6	7.6	$\epsilon_0 = 0.34$ in./in./min	-2.7	-2.0	-10.1	28.1
7	6.9	$\epsilon_0 = 0.34$ in./in./min	-9.3	-9.1	+9.7	49.5
8	6.9	$\epsilon_0 \times 0.5$	-7.0	-6.7	+2.8	49.5
9	6.5	$\epsilon_0 \times 2.0$	-1.5	-2.2	+36.0	49.5
10	5.7	$\epsilon_0 \times 0.2$	-0.3	-0.9	+10.3	49.5
11	6.9	$\epsilon_0 \times 4.0$	+8.6	+5.2	+62.8	63.2
12	6.2	$\epsilon_0 \times 0.1$	-1.6	-0.1	+7.7	63.2
Root mean square			2.7	2.98	12.0	63.2
Computed coefficients:						
E			495	495	582	—
n			-0.103	-0.103	-0.053	—
B			7679	7679	3926	—
α			0.047	0.047	0.178	—
μ			0.00013	0.00013	0.00029	—
σ			195	195	159	—

* ~12-min rest at zero strain between each cycle

148

TABLE 12. TEST HISTORIES

30992

History Identification	Sketch	Features
1. Quinlan's first two cycles		One stretch rate only; relaxations at zero strain after each cycle
2. Quinlan's complete test		Six stretch rates; relaxations at zero strain between cycles
3. CSD's F-cycle sawtooth		One stretch rate only; no rest period between cycles; no negative stress upon unloading
4. First four cycles of CSD's similitude test		Two different rates; relaxation before and after high-rate cycles
5. CSD's similitude test		Two different rates; relaxation before and after high-rate cycles, and after last slow-rate unloading

149

employed as the basic input data for CSD's optimization and stress prediction code, with two distinct sets of initial guesses for the parameters. As shown in Table 13, the end results of both computer runs are essentially the same.

4.3.1.3 Modifications to Damage Equation

Under the hypothesis of a piecewise linear stretch history, say,

$$\phi(t) = \phi(t_0) + R(t-t_0); \quad t_0 < t < t_f \tag{36}$$

the damage-evolution equation provides the solution:

$$e^{\nu(\phi - \pi)} = c \left\{ 1 - e^{-\gamma(t-t_0)} \left[1 - ce^{-\nu\xi(t_0)} \right] \right\}^{-1}; \tag{37}$$

or: $\quad e^{\nu(\phi - \pi)} = \left\{ \alpha \mu \nu (t-t_0) + e^{-\nu\xi(t_0)} \right\}^{-1};$ whenever $c = 0$

for $t_0 < t \leq t_f$, where the following auxiliary parameters have been used:

$$c \equiv 1 + \frac{(1 - \alpha)}{\alpha \mu} \dot{\phi};$$

$$\gamma = \alpha\mu\nu c; \tag{38}$$

$$\xi(t_0) \equiv \phi(t_0) - \pi\left[(t_0) \right]$$

Now, continuous piecewise linear stretch histories have discontinuous stretch-rate histories, as schematically shown in Figure 93. It does make a difference whether the right- or the left-hand derivative stretch is employed in computing the evolution of damage. If the right-hand derivative is used, a jump discontinuity in the response is obtained which propagates through the cycle because $\dot{\phi}$ also affects the value of $e^{\nu}(\phi - \pi)$ through the auxiliary parameter c. If, on the other hand, the left-hand derivative is consistently used, no jump phenomenon is observed. Additionally, since in solving the damage-evolution equation, the values of ϕ and π at the end of the previous ramp constitute

TABLE 13. UNIQUENESS-OF-SOLUTION TEST

Parameters	Initial Guesses		Convergence Values	
	First Set	Second Set	First Set	Second Set
E	1249	400	878.4	878.3
n	-0.152	-0.8	-0.08293	-0.08291
B	4281	1000	5767	5768
α	0.00377	0.08	0.05757	0.05757
μ	0.1146	0.01	0.01196	0.01196
ν	402	1000	244.24	244.18
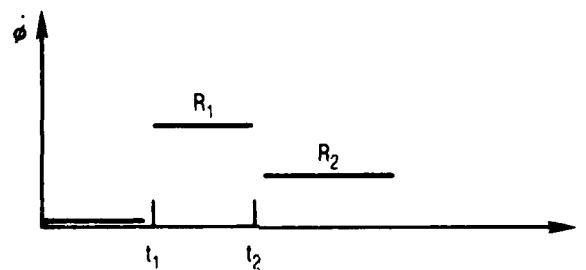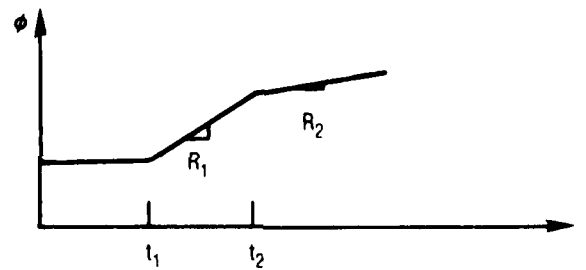
Figure 93. Piecewise Linear Stretch History

30965

the initial condition for the present ramp, another interpretation is yet possible of the $\dot{\phi}$ value to be used, namely, to compute $\xi(t_o)$ with the left-hand derivative of the stretch (i.e., this corresponds to the final value of the previous ramp), and evaluate $\dot{\pi}(t_o)$ using the right-hand derivative of the stretch. This alternative yields a jump only at the start of a cycle and nowhere else.

From the foregoing discussion it is apparent that the damage evolution equation may be unambiguously defined as:

$$\dot{\pi}(\phi_t) = \alpha \left\{ \dot{\phi}^{(-)} - \mu \left[1 - e^{\nu(\phi-\pi)} \right] \right\} \tag{39}$$

where $\dot{\phi}^{(-)}$ represents the left-hand derivative.

CSD proposed a modified version of the damage-evolution equation in the form

$$\dot{\pi}(\phi_t) = \alpha \left\{ (\phi - 1) - \mu \left[1 - e^{\nu(\phi-\pi)} \right] \right\} \tag{40}$$

which would allegedly recover the equilibrium component of the response and at the same time would eliminate the jump phenomenon. The reduced equation (in terms of $\xi = \phi - \pi$) corresponding to this version constitutes a differential equation with variable coefficients which may be numerically solved. The required subroutines to accomplish this have already been developed at CSD and the performance of the modified damage equation (either explicitly, as in equation (39), or implicitly through ϕ, as in equation (40)) was tested modifying the damage equation according to:

$$\dot{\pi} = \alpha^* \left[e^{\nu(\phi-\pi)} - 1 \right] \tag{41}$$

Use of equation (41) seriously affected time to convergence; furthermore, stress predictions based on this equation yielded larger errors than those based on equation (39).

Finally, it is interesting to note that even when an inconsistent form of equation (40) was used, whereby $\dot{\pi}$ was computed from equation (40) but π itself was determined from equations (37) and (38), better stress predictions were obtained than with Quinlan's original form. In this case, the first two cycles of Quinlan's experiment were fitted with these two approaches starting with the same initial values for the parameters. After the second iteration of the optimization routine, the error corresponding to the inconsistent form was always smaller than that for Quinlan's original equation.

The previous comments seem to indicate that equation (40) constitutes an appropriate definition of the damage evolution. It must be tested, however, under different types of stretch histories before it can be either accepted or discarded.

4.3.1.4 Effect of Data Base

Employing the stretch histories listed in Table 12, a preliminary evaluation was carried out of the features a test should include to properly characterize the material response. The tests described below were performed to gain some insight into the effects of data base on stress predictions and are by no means exhaustive for the purpose of completely ascertaining such effects.

4.3.1.5 Reducing the Data Base

History No. 1 (H.1) of Table 12 was curve-fitted and the corresponding parameters were used to predict material response under H.2. Errors in the predicted response seem to depend on whether or not the stretch maximum and/or the stretch rates are included in the data base used to determine the constitutive parameters. Typical plots of these results appear in Figures 94 to 97.

Based on the above observations, H.4 was next used to determine the parameters, and the response to H.5 was then predicted with virtually the same rms error per cycle. It is pointed out here that the base history (H.4)
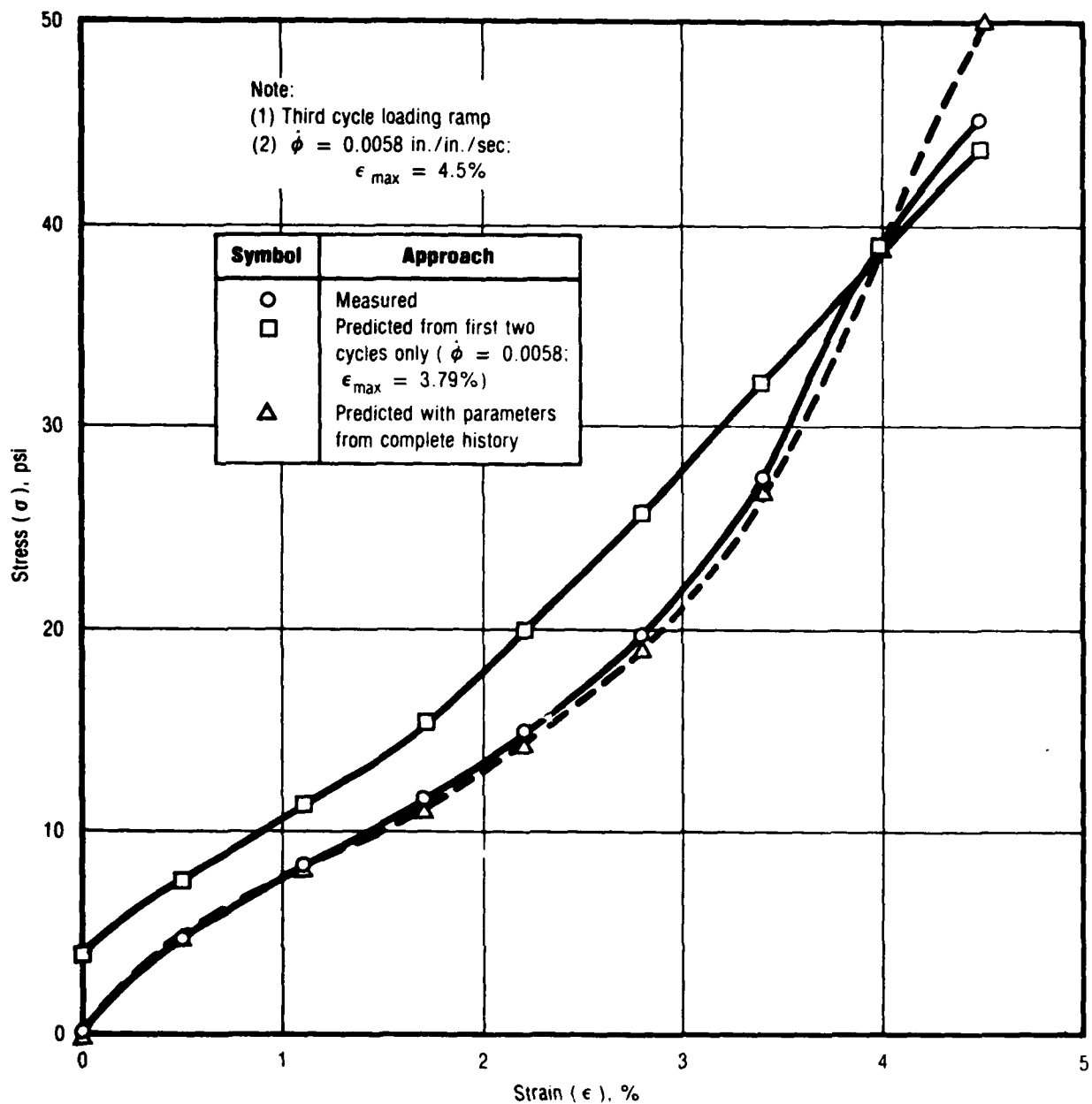
Figure 94. Effect of Jump and Strain Maximum

30966

included all the stretch rates of the history employed for stress predictions
(H.5), but did not contain the stretch maximum. The last fact introduced sig-
nificant errors in the response prediction along the ramp leading to the maximum
stretch, as shown in Figure 98.

154
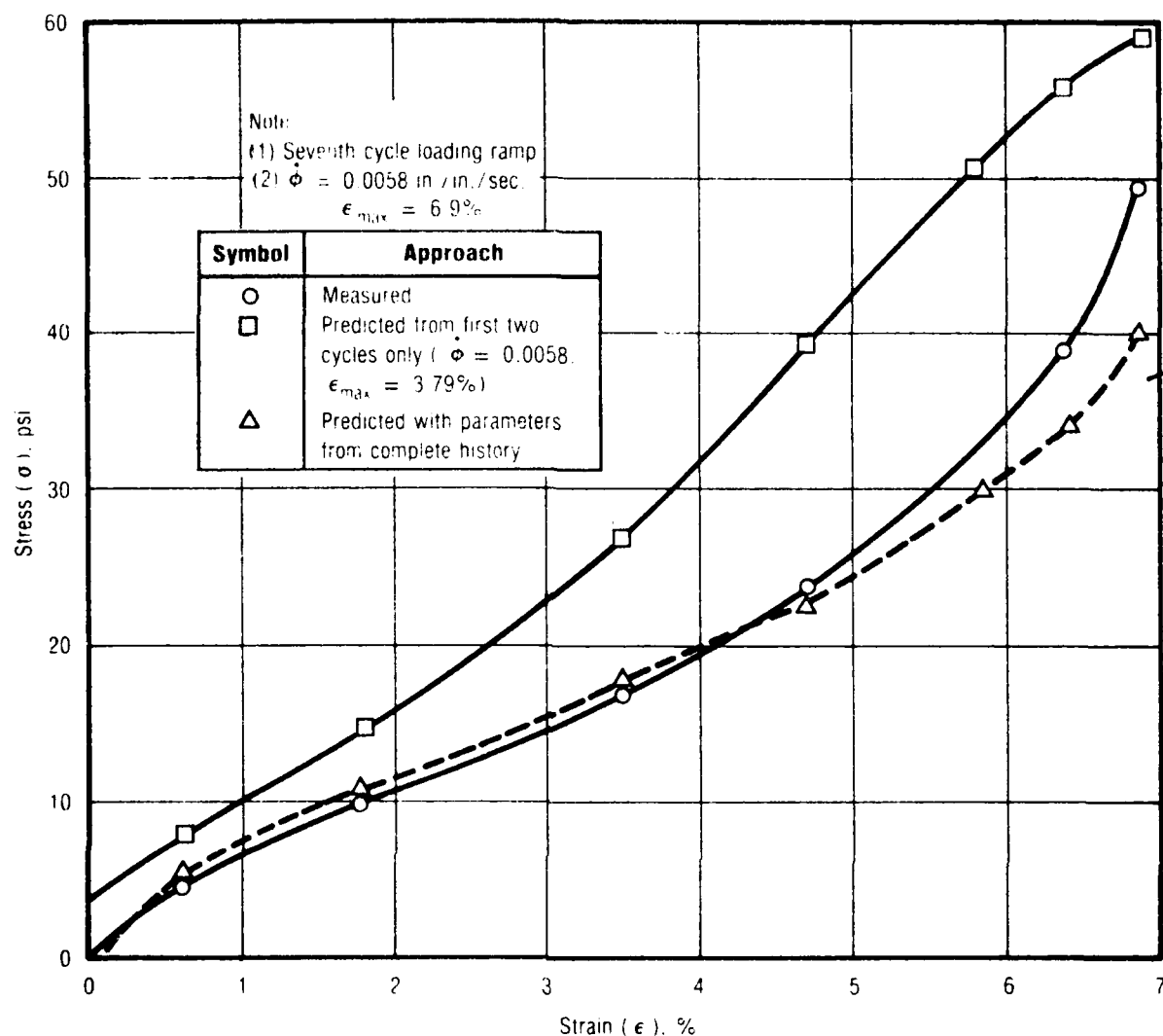
Figure 95.   Effect of Jump and Strain Maximum

30967

It is interesting to note that the measured response during the third stretch plateau of H.5 corresponds to a damaged recovery relaxation; and even though the base history ends before this phenomenon takes place, the predicted response to H.5 actually reproduces this type of behavior, as depicted in Figure 99.

4.3.1.6 Extrapolating to a Different Test

History No. 2 (Table 12), with Quinlan's reported values for the parameters, was used to predict response to H.3 without success. Material aging and/or differences in stretch maxima as well as in stretch rates might have been responsible for these bad predictions.

155
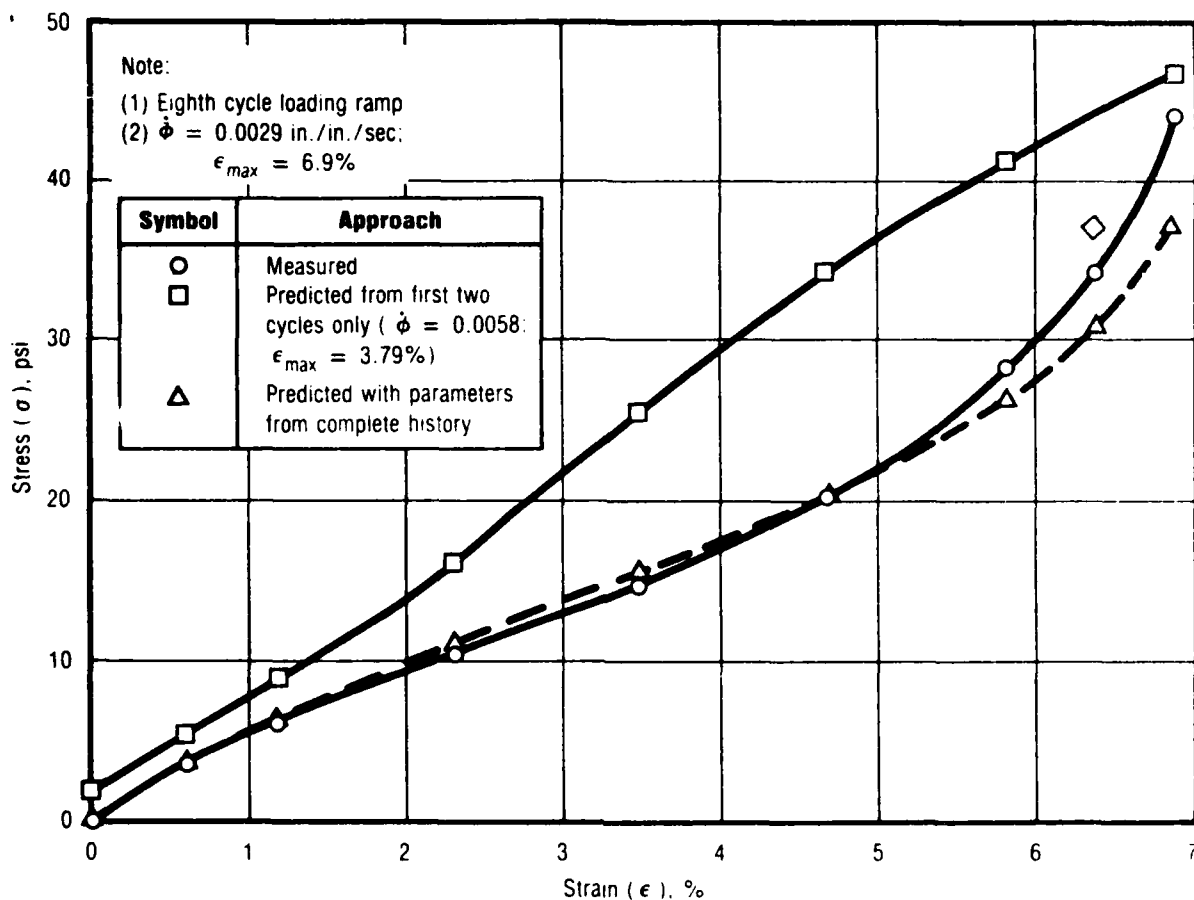
Figure 96. Effect of Strain Maximum and Strain Rate ($\dot{\phi} = 0.0029$)

30968

Next, the parameters corresponding to H.4 were used to predict response under H.3; the samples used in both tests came from the same propellant batch. The rms error per cycle of the predicted response to H.3 with parameters corresponding to H.4 was approximately 13.75 psi, whereas that obtained with parameters corresponding to H.3 was about 13.2.

Alternatively, when parameters obtained by curve-fitting H.3 were used to predict material response under H.5, large errors resulted. These errors may be attributed to differences in stretch maxima and stretch rates present in the two tests.

From these preliminary observations, it appears that parameters adequate for stress prediction purposes should be determined from tests which cover the expected range of stretches and stretch rates.

156
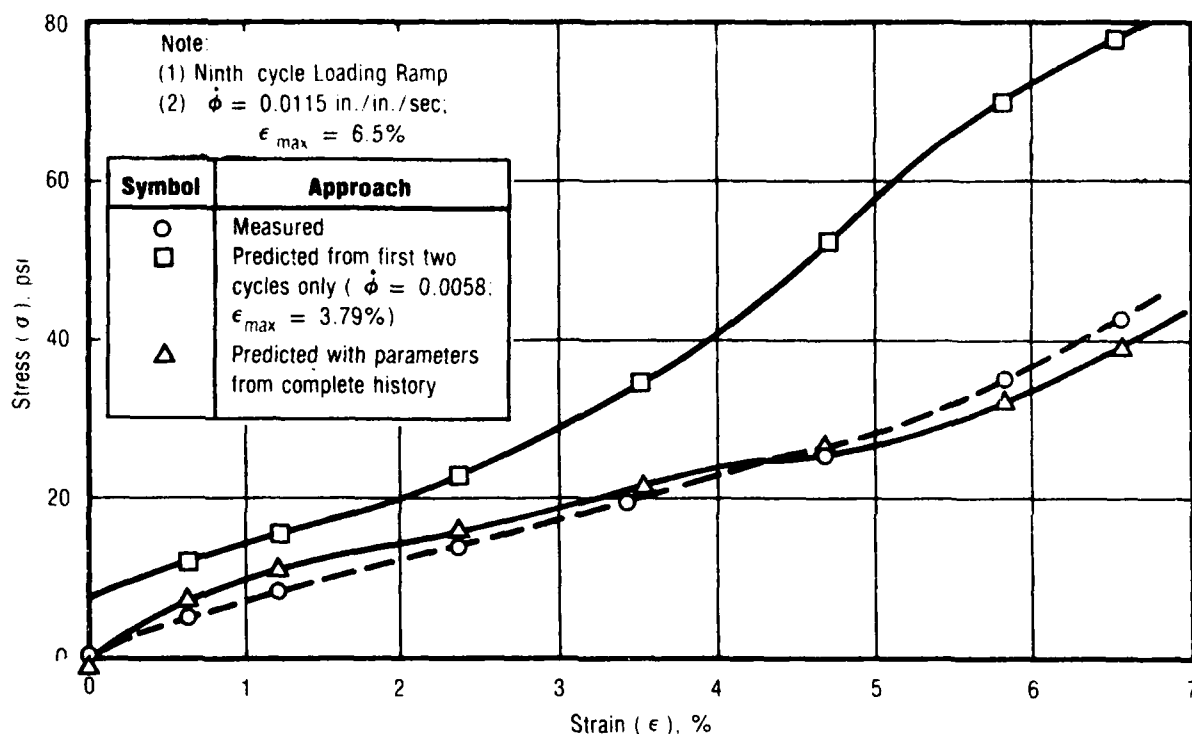
Figure 97. Effect of Strain Maximum and Strain Rate ($\dot{\phi}$ = 0.0115)

30969

4.3.1.7 Temperature Effects

As a first step to ascertaining the effect of temperature on the constitutive parameters entering Quinlan's constitutive law, isothermal tests were performed at three different temperatures. A saw-tooth strain history with successively higher peaks (2, 4, and 6% nominal strain) and without rest periods between cycles was used in the tests. The corresponding computer determined parameter values are summarized in Table 14.

These preliminary results seem to indicate monotonically decreasing behavior of the parameters with increasing temperature except for the coefficients α and μ, which appear to have, respectively, a bell-shaped and a monotonically increasing type of dependence on temperature.

Additional tests at different temperatures are needed to more precisely define the functional dependences previously referred to and to hopefully remove part of the hidden nature of the parameters involved.

157
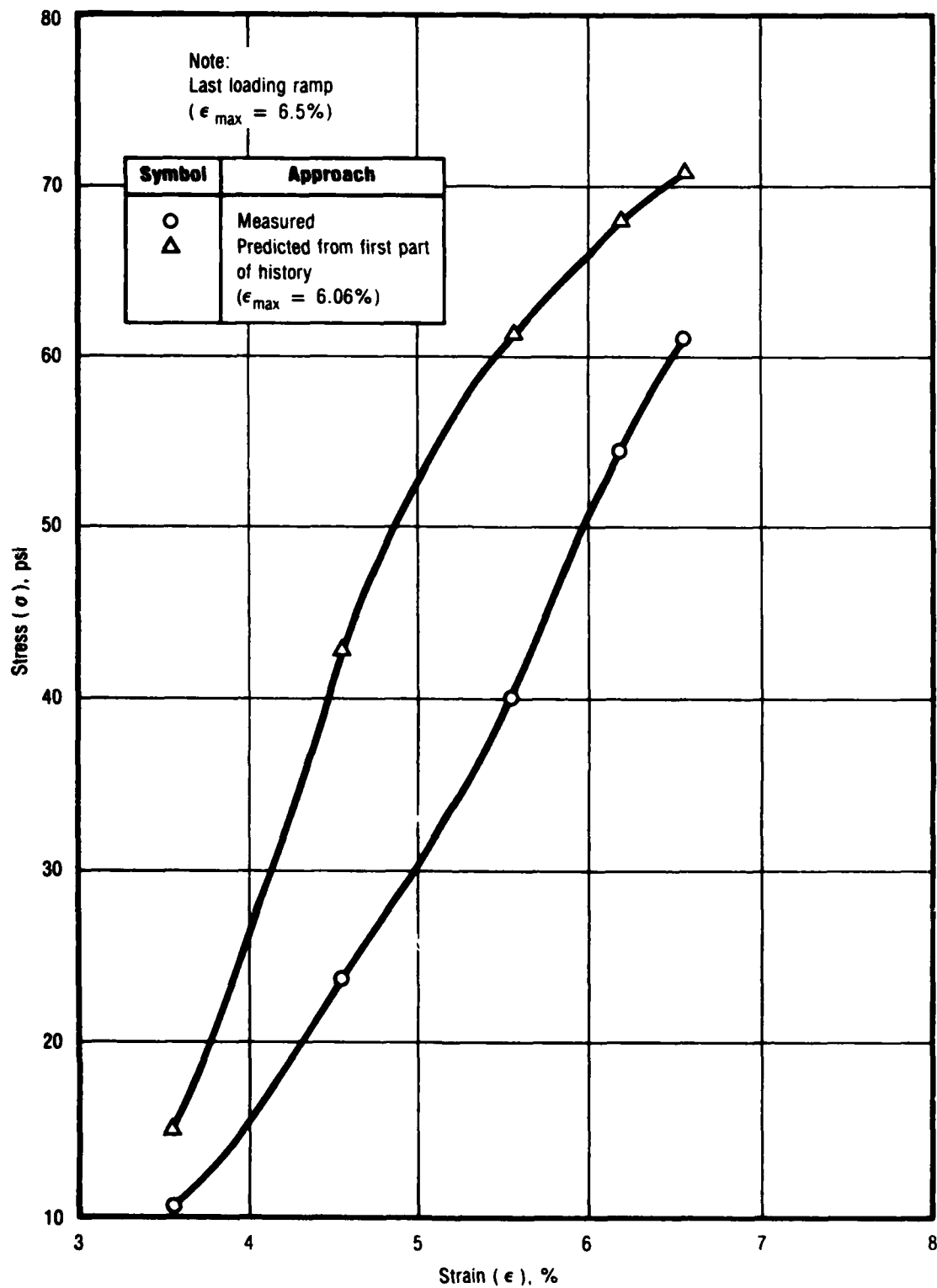
Figure 98. Effect of Strain Maximum (ϵ_{max} = 6.5%)

30970
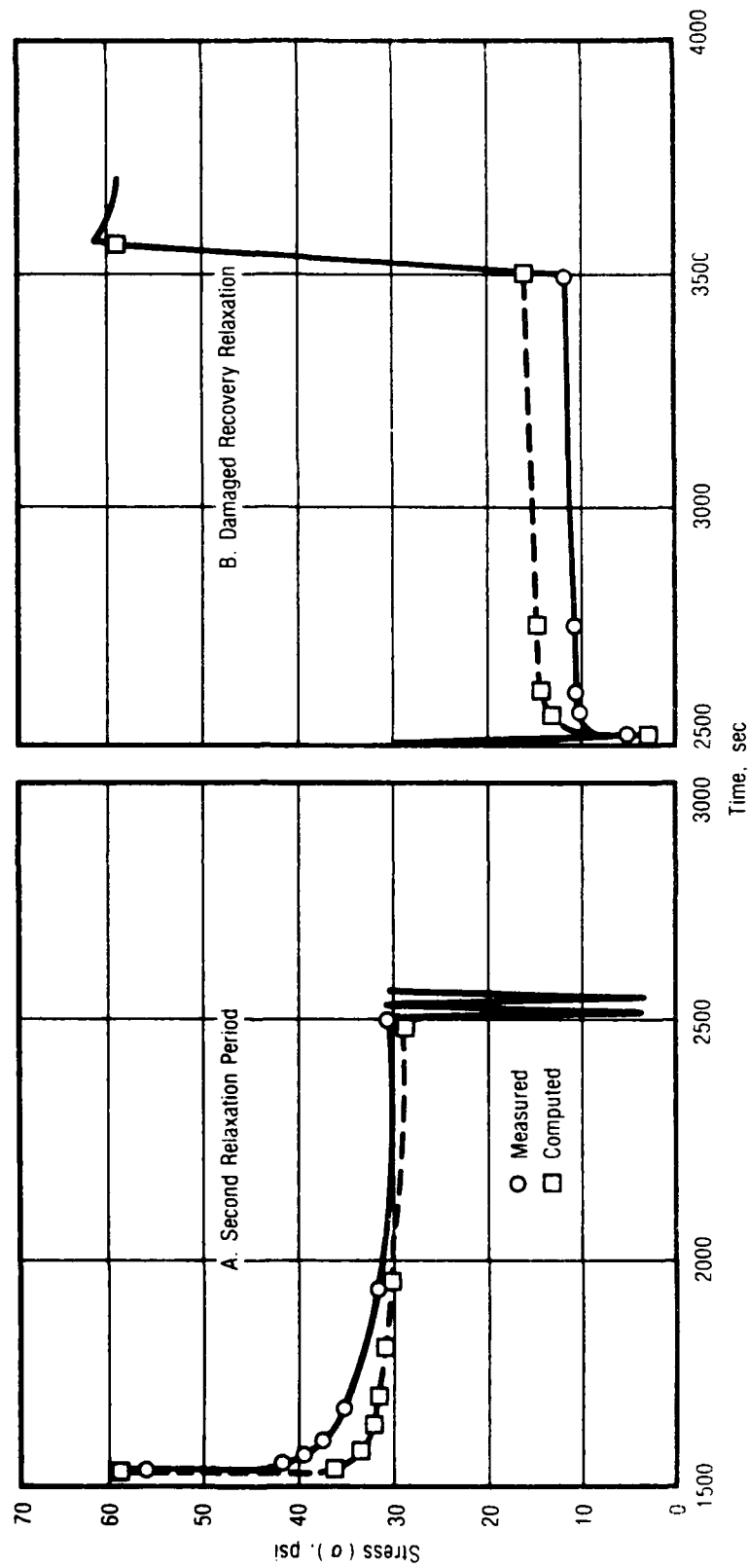
Figure 99. Reproduction of Modulus Recovery

159

30971

TABLE 14. EFFECT OF TEMPERATURE ON CONSTITUTIVE PARAMETERS

Parameters	Temperature, F		
	2	70	120
E	9019	1543	965
n	-0.327	-0.141	-0.142
B	547,250	40,210	15,458
α	0.00236	0.0675	0.00427
μ	0.229×10^{-5}	0.0735	1.415
ν	321	6.73	4.91
rms error/ cycle, psi	18.1	9.1	7.4

160

4.3.1.8 Desirable Test Features

Test data used to determine the constitutive parameters have a definite bearing on response predictions and may seriously limit the applicability of the corresponding results.

From a practical standpoint, the preliminary studies on data base effects for stress prediction purposes indicate that it is not imperative to duplicate the expected loading history; rather, the test history should primarily include the maximum expected strain level, the expected range of strain rates, and, if applicable, other characteristics such as rest, or relaxation periods. On the basis of these observations, it appears that a test may be so designed to include, within a reasonable time span, the minimum amount of information necessary to properly characterize the propellant for the intended use. Two possible stretch histories are shown in Figure 100.

4.3.2 Current Model

The theory developed by Quinlan has undergone several changes, mainly in the expression defining the evolution of damage. With the theory as developed, Quinlan has not been able to satisfactorily fit stress relaxation data. One
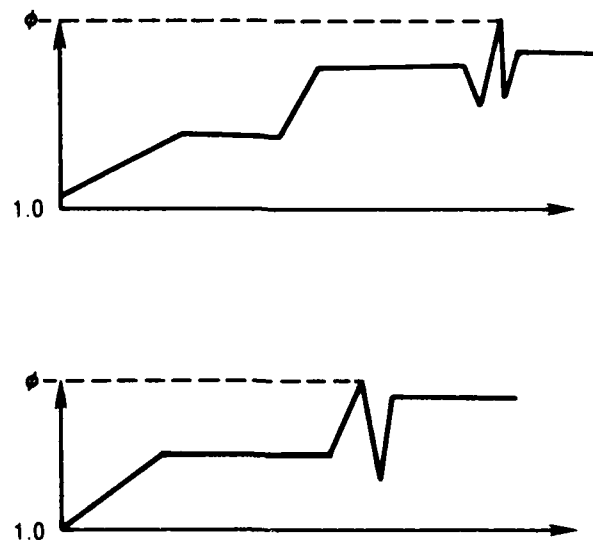
Figure 100. Stretch Histories

30972

possible modification here is to allow the relaxation modulus to depend on the damage parameter, π. This modification is reasonable, as tests generally show a lowering of modulus in stress relaxation. In particular, Figure 101 shows four stress-relaxation tests, each corresponding to a different prestrain. In the three upper curves, the initial strain in the test is greater than or equal to the prestrain; the three curves approximately coalesce. For the lower curve, however, the 3% strain is less than the 5% prestrain and there is considerable modulus reduction. This type of strain-sensitive damage phenomenon has been reported throughout the solid propellant literature.[10, 12, 33, 34]

The most effort however, has been spent on modifying the bonding law to reduce the jump phenomena, to improve the curve fit to data, and to include healing. The general form

$$\sigma(t) = \int_0^t H(t-\tau)\, \dot{\phi}(\tau)\, d\tau + C\dot{\pi}(t) \tag{42}$$

has been retained in all versions of Quinlan's theory, but the rate mechanism underlying damage

$$\dot{\pi} = P(\pi, \phi, \dot{\phi}) \tag{43}$$

for which

$$\pi(\phi = 1) = 1 \tag{44}$$

was assumed to contain a neutral rate, ζ, at which damage remain constant.

$$P(\pi, \phi, \zeta) = 0$$
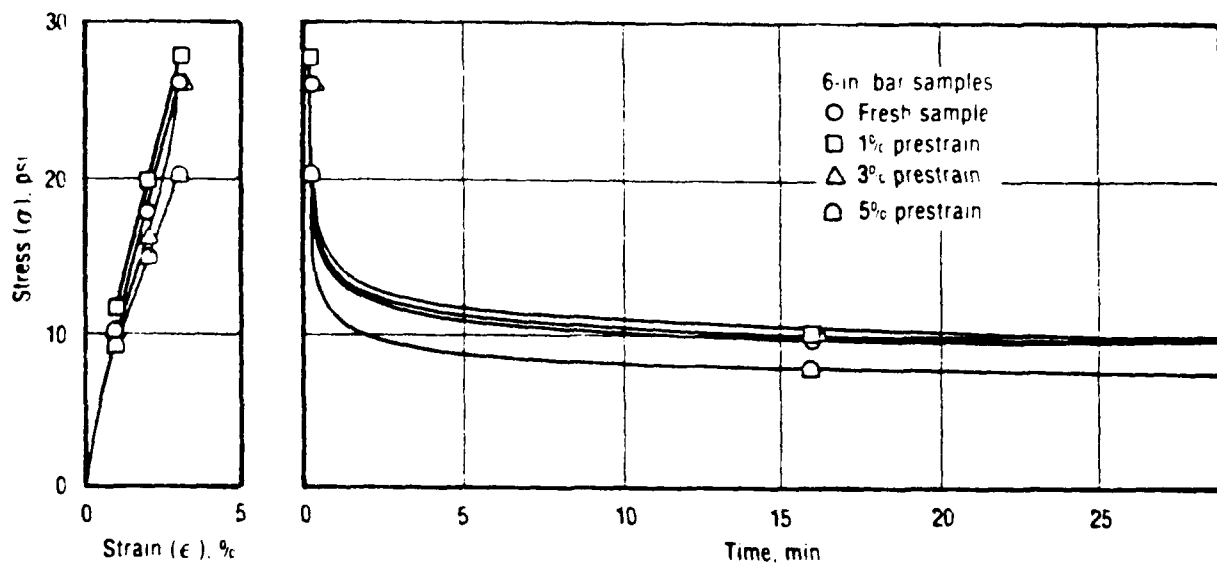
Figure 101. Typical Stress Relaxation Behavior for Undamaged
and Predamaged Samples

21967

This concept allows the concept that at rates higher than ζ, bond breakage would take place, while at rates slower than the neutral rate, bond formation would occur.

Equation (45) for the neutral rate, ζ, may be rewritten as:

$$\zeta = Q\ (\pi,\ \phi)$$

$$\zeta = 0 \text{ if and only if } \pi = \phi \tag{46}$$

which, upon expansion in Taylor series, becomes:

$$\zeta = Q\ (\pi,\ \pi\ -\ \phi)\Big|_{\phi\ =\ 0} + \frac{\partial Q\ (\pi,\ \pi\ -\ \phi)}{\partial (\pi\ -\ \phi)}\Big|_{\phi\ =\ 0} (\pi\ -\ \phi) + Q\ (|\pi\ -\ \phi|^2)$$

The first term on the right-hand side of this equation vanishes by virtue of equation (46), so that, neglecting the higher order terms, and defining:

163

$$\mu \stackrel{\text{def}}{=} \left. \frac{\partial Q (\pi, \pi - \phi)}{\partial(\pi - \phi)} \right|_{\phi = 0} \tag{47}$$

leads to the following first-order expression for the neutral rate:

$$\zeta = \mu(\pi - \phi) \tag{48}$$

where for bond breakage

$$\dot{\phi} - \zeta > 0 \tag{49}$$

while for bond formation

$$\dot{\phi} - \zeta < 0 \tag{50}$$

In addition, equation (43) may be cast in the following form:

$$\dot{\pi} = P(\pi, \phi, \dot{\phi}) = R(s, u) \tag{51}$$

where:

$$s = s(\pi, \phi) \tag{52}$$

and

$$u = \dot{\phi} - \zeta \tag{53}$$

with ζ given by equation (48).

Now, under the assumption that the process of bond formation is slower than that of bond breakage, the function R defining the evolution of damage must be of the form shown in the sketch below, in which the parameter α would represent the maximum rate of bond formation.
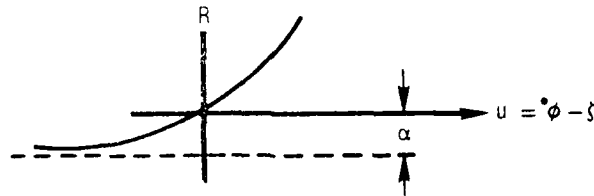
Hence, R may be defined through the following differential equation:

$$\frac{dR(s, u)}{du} = \nu \left[R(s, u) - \alpha \right] \tag{54}$$

where α and ν are positive constants.

Integration of equation (54) yields:

$$R(s, u) = \alpha(e^{\nu u} - 1) \tag{55}$$

Finally, putting equations (48), (53), and (55) into (51) results in:

$$\dot{\pi} = \alpha \left\{ \exp\left[\nu \dot{\phi} + \mu \nu (\phi - \pi) \right] - 1 \right\} \tag{56}$$

Equations (42) and (56) subject to (44) were used by Quinlan in several ways to characterize the response of UTP-19,360B. One such stress-strain law took the following form:

$$\sigma(t) = E_o \, \epsilon(t) + \left[E_1 + E_2 \, \epsilon(t) \right] \int_0^t (t - \tau)^{-n} \, \dot{\epsilon}(\tau) \, d\tau + C \dot{\pi} \tag{57}$$

in which E_o, E_1, E_2, n, and C are constants and ϵ is the strain. Although some aspects of propellant behavior were better modeled than with the original version of the theory, others were not, and further revisions were necessary. In the latest version of his constitutive law, Quinlan used a Prony series to represent the relaxation function and changed strain for stretch in the original equation of evolution for damage, so that, in summary, the current model looks as follows:

$$\sigma(t) = \sigma_v(t) + \sigma_b(t)$$

$$\sigma_v(t) = G_e \, \epsilon(t) + \int_c^t G(t - \tau) \, \dot{\epsilon}(\tau) \, d\tau$$

$$\tag{58}$$

$$G(t) = \sum_{i=1}^{n} C_i \, e^{-\tau_i t}$$

$$\sigma_b(t) = B e^{\gamma(\epsilon - \pi)} \epsilon(t)$$

$$\dot{\pi}(t) = \alpha \left\{ e^{\nu(\epsilon - \pi)} - 1 \right\} \quad ; \pi(o) = 0$$

This final version of the theory has been employed to characterize UTP-19,360B, but has not been used by Quinlan to predict the response of the propellant under any loading history other than a single characterization test. Its generalization to transient thermal loadings and two- and three-dimensional states is expected to require significant modifications, possibly including a complete reformulation.

166

4.4 R. SCHAPERY's NONLINEAR STRESS-STRAIN LAW

4.4.1 Original Model

Dr. R. Schapery used the constitutive theory advanced by him for viscoelastic materials with microcracking[17, 18] was taken by Dr. R. Schapery as the starting point for predicting the response of solid propellants under general loading conditions. The one-dimensional version of this law takes the following simple form:

$$\sigma = \frac{A_F}{\lambda} \sigma_\ell \tag{59}$$

where σ_ℓ is the linear viscoelastic stress for a thermorheologically simple material:

$$\sigma_\ell = \int_0^t E (\xi - \xi') \frac{d\epsilon_\sigma}{d\tau} \, d\tau \, , \tag{60}$$

with

$\epsilon_\sigma \equiv \epsilon - \alpha (T - T_0)$ = strain due to mechanically applied stress

$$\xi = \int_0^t dt'/A_T \left[T(t') \right]$$

$\xi' \equiv \xi (\tau)$

$E(\xi)$ = linear viscoelastic relaxation modulus

T_0 = temperature at $t = 0$

$A_F = A_F (T)$ = temperature-dependent material function

$\lambda = \lambda (S_\ell)$: softening function in which the damage parameter:

$$S_\ell = \int_0^\xi \left(\frac{\sigma_\ell A_F}{f} \right)^q d\hat{\xi} \tag{61}$$

167

depends only on the strain and temperature histories, and:

$$f = \begin{cases} 1 & \text{for } 0 \leqslant \epsilon < \epsilon_1 \\ (\epsilon/\epsilon_1)^\beta & \text{for } \epsilon_1 \leqslant \epsilon < \epsilon_2 \\ (\epsilon_2/\epsilon_1)^\beta & \text{for } \epsilon \geqslant \epsilon_2 \end{cases}$$

for constant threshold strains ϵ_1 and ϵ_2, with $\beta > 0$.

The function $F = F(\epsilon_\sigma)$ and the positive, constant exponent, q, originate with the equation for microcrack speed,

$$\frac{dA}{d\hat{\xi}} = M(K_I/f)^q \tag{62}$$

where M is a positive constant and

$$d\hat{\xi} = dt/A_c \tag{63}$$

in which $A_c = A_c(T)$ is the shift factor for microcrack growth rate.

The functional form of the softening function, $\lambda = \lambda(S_\ell)$, depends on the type of behavior that needs to be reproduced. The following special case was used:

$$\lambda = \left[1 + cS_\ell \right]^{p/q}$$

where c and p are positive constants. Note that when $S_\ell = 0$ or $c = 0$, a linear viscoelastic stress-strain equation is recovered from equation (59).

Taking $A_F \equiv 1$, several sets of numerical values for the constitutive parameters corresponding to TP-H1011 were tried without success. This theory was also used to predict the response of UTP-19,360 and UTP-3001. Having failed to perform better than linear viscoelasticity in many cases, it has undergone several changes since.

4.4.2 Current Model

The essential form of the modified uniaxial stress-strain relation is given by:

168

$$\sigma = f\left(\epsilon^O, \, \epsilon^O_m, \, S\right) \qquad (64)$$

where:

σ = engineering stress

ϵ^O_r = psuedo strain

$$\epsilon^O_r = \frac{1}{E_R} \int_0^t E(t - \tau) \frac{d\epsilon}{d\tau} d\tau \qquad (65)$$

ϵ^O_m = maximum value of $|\epsilon^O|$ up to the current time

S = damage parameter

$$S = \left(\int_0^t \left|\epsilon^O\right|^q \, dt \right)^{1/q} \qquad (66)$$

E_R = arbitrarily selected reference modulus,

$E(t)$ = linear viscoelastic relaxation modulus,

$$= E_e + E_2 \, t^{-n} \equiv E_2 \left(E_\tau + t^{-n}\right),$$

$$E_\tau = E_e/E_2, \qquad (67)$$

and

q = positive constant.

The functional form of f in equation (64) depends on the material considered. Studies on solid propellant to date indicate it may be taken as follows for some solid propellants:

$$f = Y_1 \, Y_2 \, Y_3 \, P_{15} \, \text{sign} \, (\epsilon^O) \qquad (68)$$

169

in which

$$\text{sign } (\epsilon^o) = \begin{cases} 1 & \text{if } \epsilon^o > 0 \\ 0 & \text{if } \epsilon^o = 0 \\ -1 & \text{if } \epsilon^o < 0 \end{cases}$$

and P_{15} is used to normalize function Y_3 to unity, at a reference point. The Y_i's are the following functions of damage and pseudo strain:

$$Y_1 = Y_1 (S) = \begin{cases} 1 + A_1 S + A_2 S^2 + A_3 S^3 & \text{for } S \leqslant S_o \\ A_4 \ S^{A_5} & \text{for } S > S_o \end{cases} \tag{69}$$

$$Y_2 = A_2 \ S^{0.63-Sx} \ (\epsilon_m^o)^{(0.463-M_x-L_x)} \ \left| \epsilon^o \right|^{L_x} \tag{70}$$

$$Y_3 = C_o + C_1 x + C_2 x^2 + C_3 x^3 + C_4 x^4 + C_5 x^5 \tag{71}$$

where:

$$x = x_r \left| \frac{\epsilon^o}{\epsilon_m^o} \right| \lambda \tag{72}$$

in which x_r is the only root of the equation:

$$\max(S_r) = Y_3 \ (x_r) \tag{73}$$

with max (S_r) representing the maximum value of S_r up to the current time, and:

$$S_r = \frac{S^{a_x} \left| \epsilon^0_m \right|^{M_x}}{P_{15}}$$

(74)

while λ is a factor that accounts for relatively small higher order effects possibly due to rehealing and particle interaction.

The constants entering the definitions of Y_1, Y_2, and Y_3 depend on the material. For UTP-19,360B they are:

$$\begin{aligned}
S_0 &= 42 \\
S_x &= 0.637 \\
M_x &= -0.387 \\
L_x &= 0.85
\end{aligned}$$

(75)

and the factor λ is given by:

$$\lambda = K_x \, C_{cm}^{-C_x}$$

(76)

The resulting form of equation (64) for UTP-19,360B is thus:

$$\sigma = P_{15} \, A_6 \, Y_1 \, Y_3 \, \left| \epsilon^0 \right|^{L_x} \text{sign} \, (\epsilon^0)$$

(77)

Clearly, if $L_x = 1$, equation (77) may be written as:

$$\sigma = A_F \int_0^t E \, (t - \tau) \, \frac{d\epsilon}{d\tau} \, d\tau$$

(78)

in which $A_F = A_F(\epsilon^0, \epsilon^0_m, S)$ plays the role of a softening function, remininscent of the Mullins-Tobin approach.

4.4.3 Stress Predictions

The current version of the nonlinear model developed by R. Schapery may be used to predict the response of solid propellants with a rather remarkable degree of accuracy, as may be seen in Figures 102 to 109, which are sample cases of the isothermal tests considered in the program. The first two plots (Figures 102 and 103) correspond to the highest and lowest constant rate tests (Test No. 1) available in the data for which the difference between theory and test is greatest. Figure 104 shows the saw-tooth test (Test No. 5) at constant rate with increasing strain peaks. Figures 105 and 106 pertain to the dual-rate tests (Test No. 3). Results for the short- and long-duration similitude tests (Test No. 12) are given in Figures 107 and 108, and Figure 109 includes a three-step relaxation test.

Finally, it is important to mention that a complete characterization of UTP-19,360B was also carried out using $L_x = 1$ (the value leading to equation (78)), and the ensuing response predictions were very close to those obtained with $L_x = 0.85$; only the low-to-high dual-rate test of Figure 8 was predicted somewhat better with $L_x = 0.85$.

4.4.4 Material Characterization

In evaluating the material constants and property functions, the following observations may be valuable:

- Y_i, its variation being brought about by vacuole formation, appears to be a decreasing and concave down function of damage, as presented in the following figure:

172
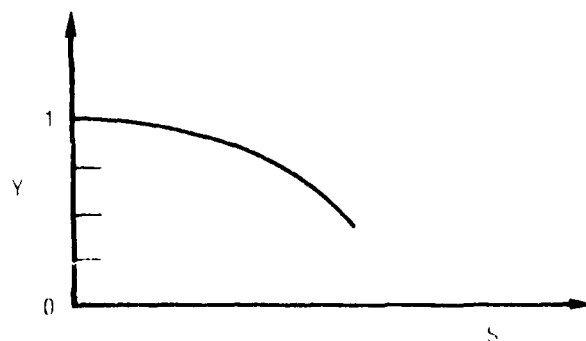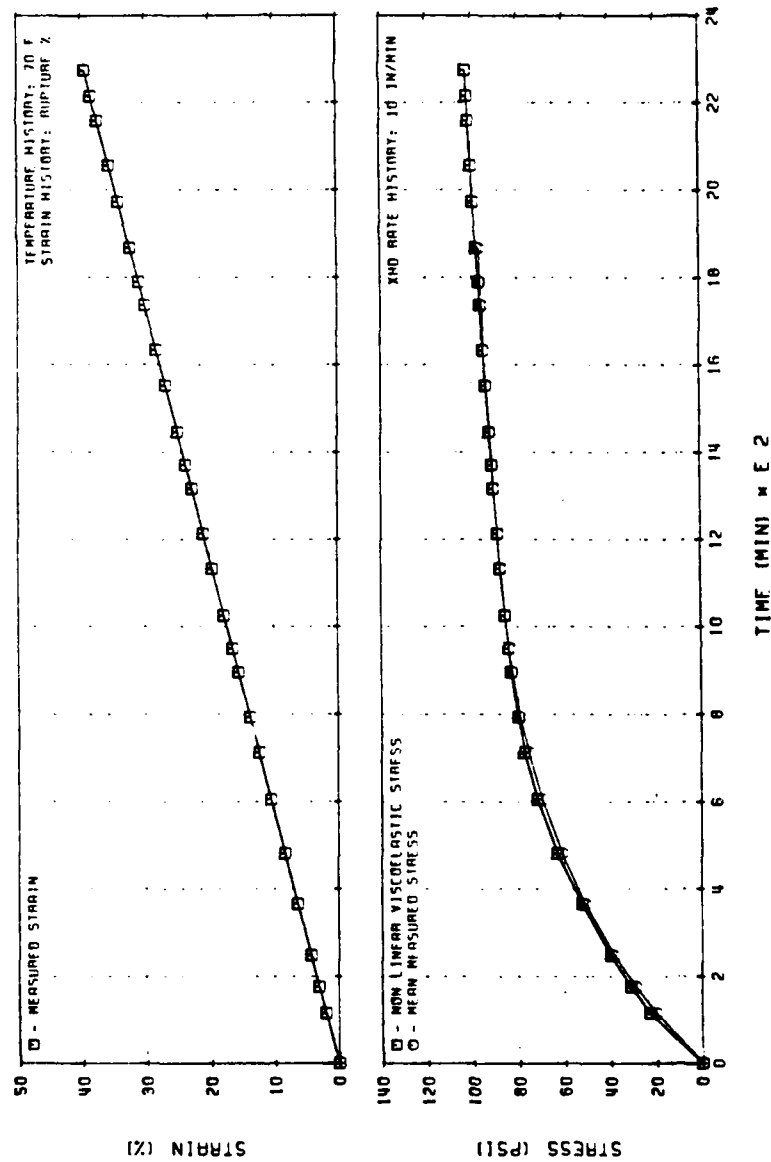
Figure 102. Dr. Schapery's Nonlinear Viscoelastic Stress Predictions for UTP-19,360B-400/1777 Constant-Rate Test Data (Code No. 1)

31021

173
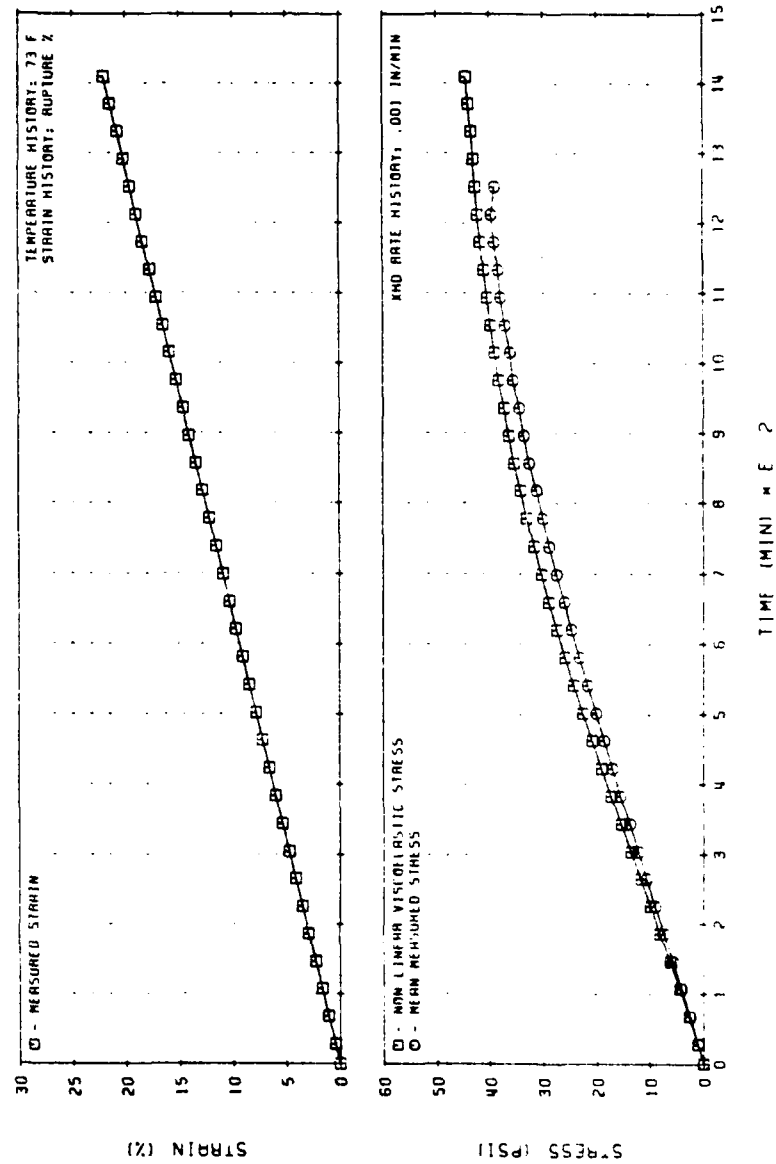
Figure 103. Dr. Schapery's Nonlinear Viscoelastic Stress Predictions for UTP-19,360B-400/1777 Constant-Rate Test Data (Code No. 1)

31022

174
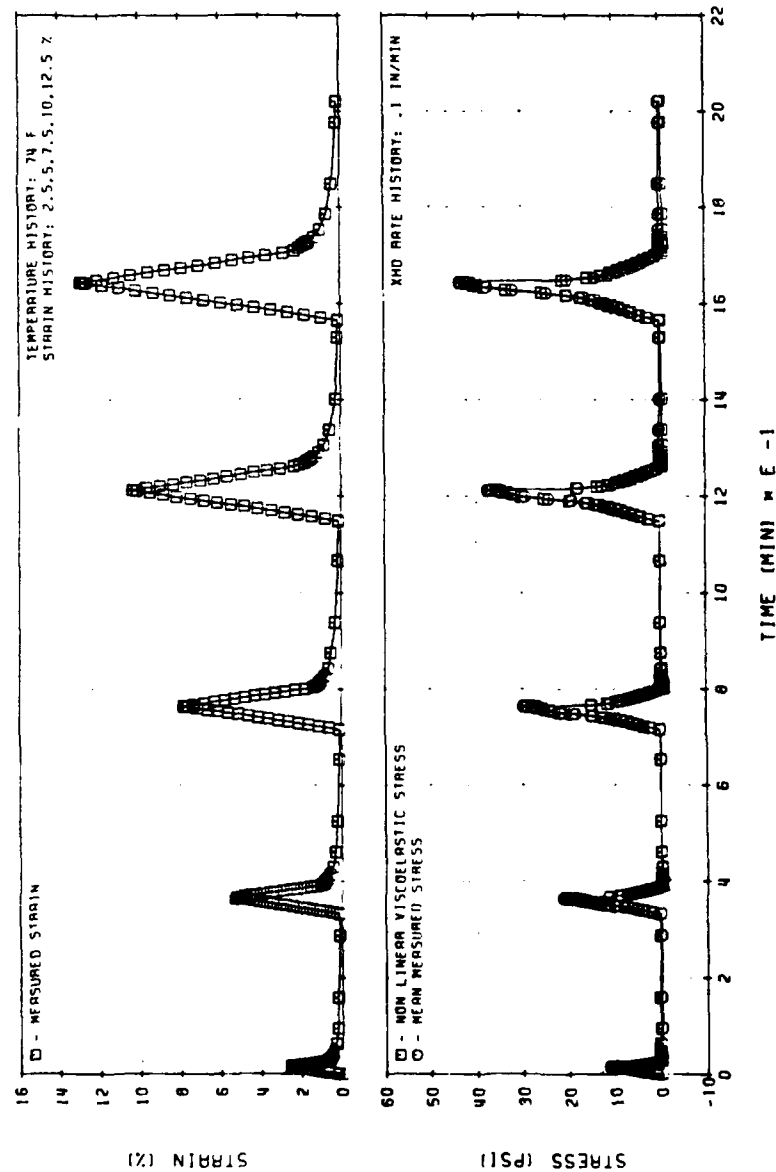
Figure 104. Dr. Schapery's Nonlinear Viscoelastic Stress Predictions for UTP-19,360B-400/1777 Multiple Loading Test History (Code No. 5)

31023

175
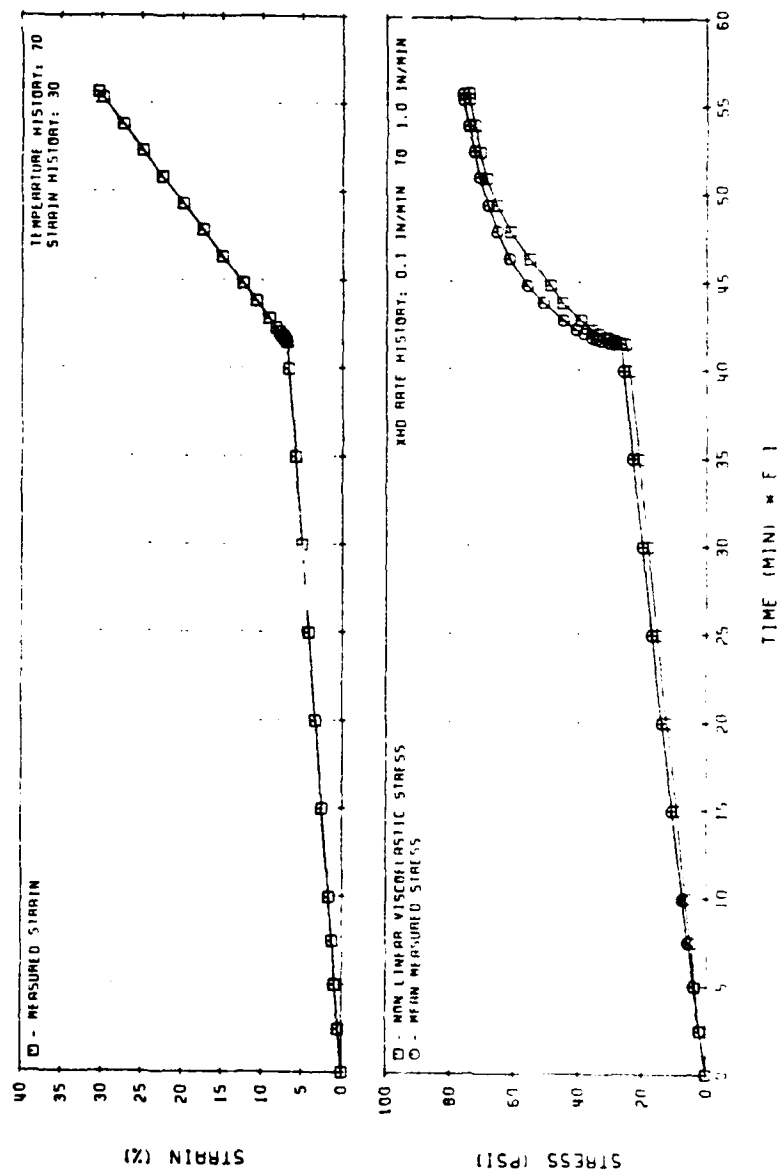
Figure 105. Dr. Schapery's Nonlinear Viscoelastic Stress Predictions for UTP-19,360B-400/1777 Two-Rate Test Data (Code No. 3)

31024
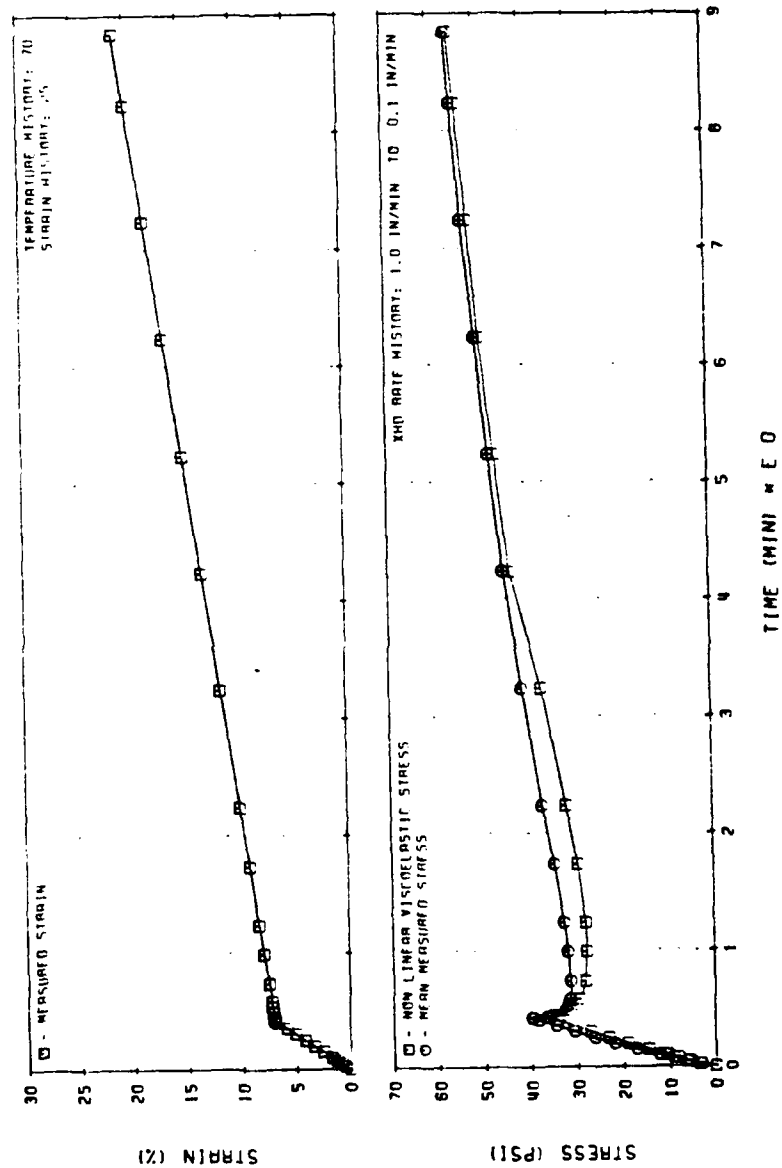
Figure 106. Dr. Schapery's Nonlinear Viscoelastic Stress Predictions for UTP-19,360B-400/1777 Two-Rate Test Data (Code No. 3)

31025
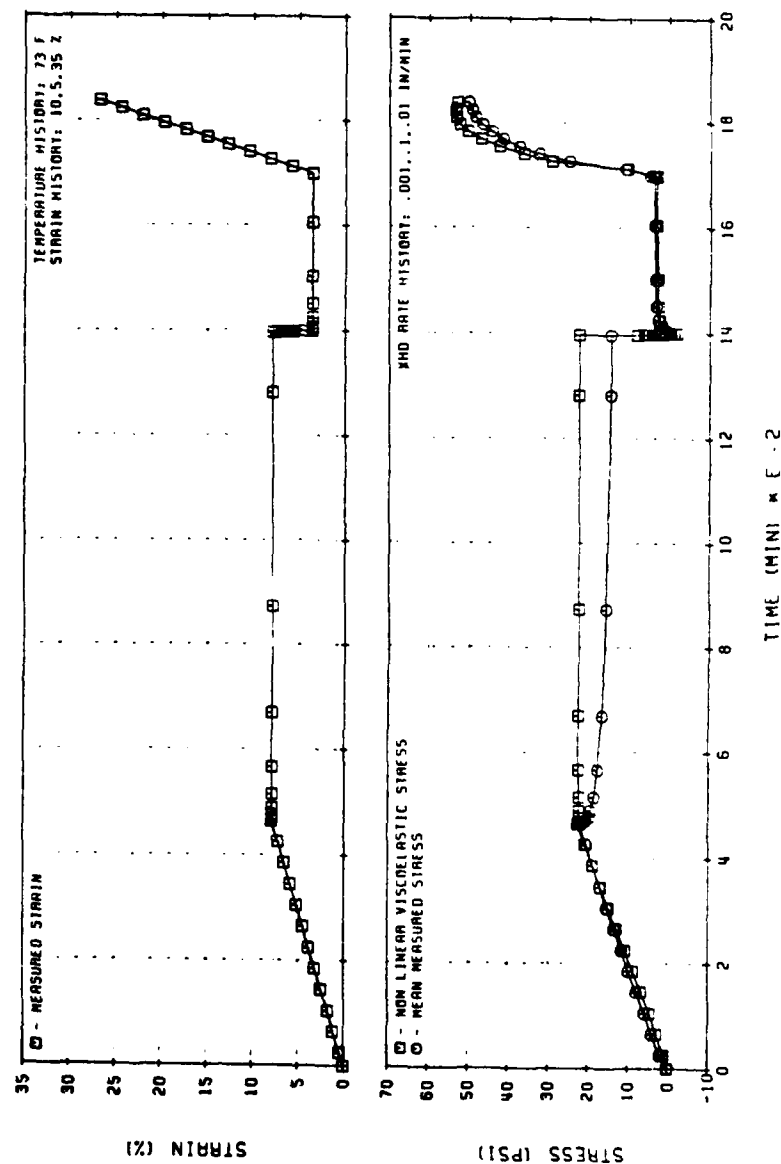
Figure 107. Dr. Schapery's Nonlinear Viscoelastic Stress Predictions for UTP-19,360B-400/1777 Similitude Test History Data (Code No. 12)

178
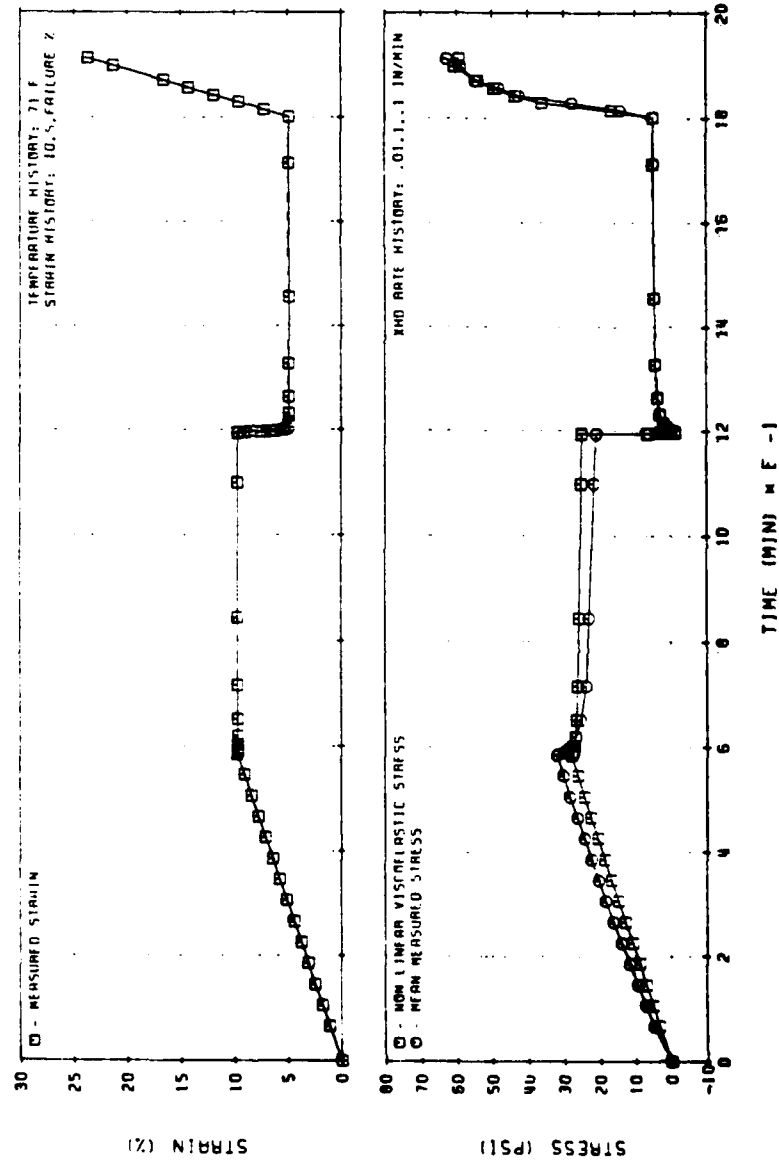
Figure 108. Dr. Schapery's Nonlinear Viscoelastic Stress Predictions for UTP-19,360B-400/1777 Similitude Test History Data (Code No. 12)

179
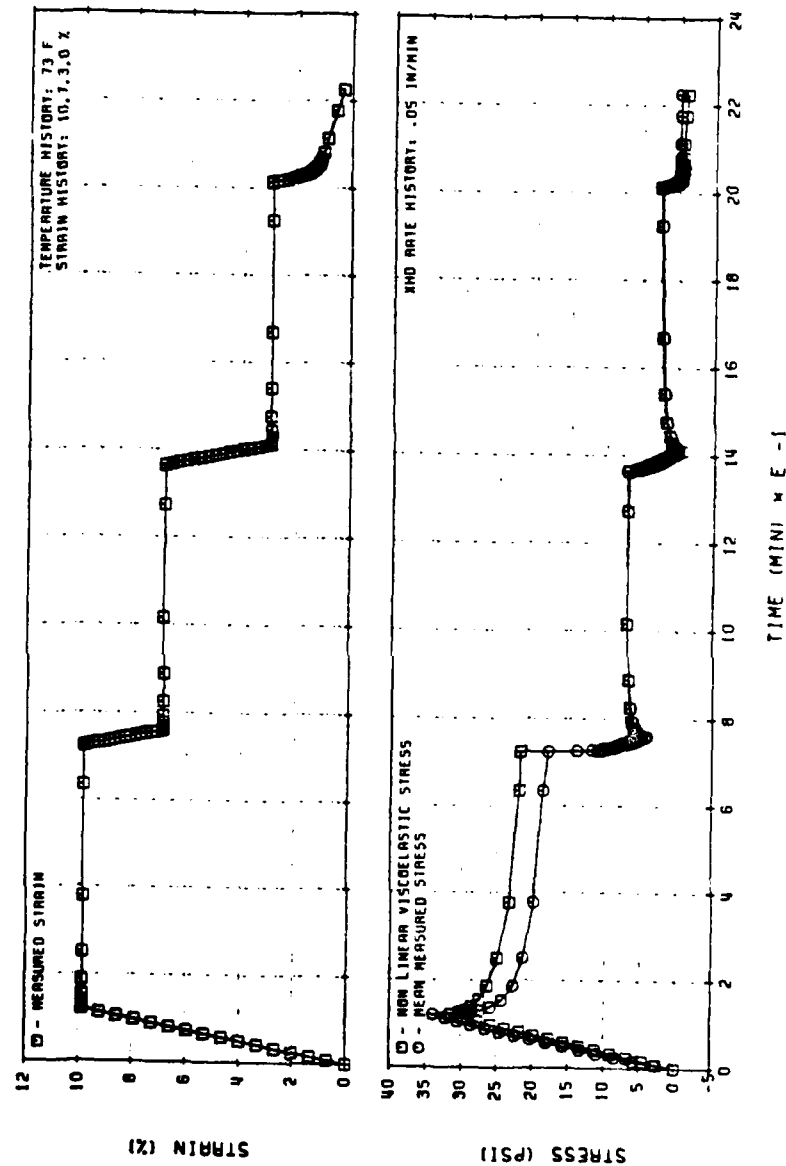
Figure 109. Dr. Schapery's Nonlinear Viscoelastic Stress Predictions for UTP-19,360B-400/1777 Three-Step Relaxation Test History (Code No. 13)

180

- The function S_r, which provides a certain measure of damage, increases as a direct result of a reduction in the number of polymer chains supporting the internal stresses; the larger the S_r, the higher the stress on each chain.

- For UTP-19,360B, the state of damage is essentially constant during unloading and reloading, and the shape of the so-called backbone curve resembles the stress-strain curve for rubber, which is of the form:

$$Y_3 \left| \epsilon^0 \right|^{0.85} \tag{79}$$

as shown in the sketch below, in which the steepness increased with increasing S_r.

(1) Loading portion
(2) Unloading and reloading portion
 (backbone curve)
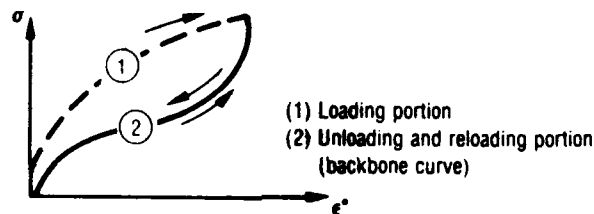
31459

- The selection of L_x can be made by plotting unloading data in the form suggested in the following diagram:

$L_x > 0.85$

$L_x = 0.85$

$\frac{\sigma}{(\epsilon^\cdot)}L_x$

Unloading from point on virgin curve
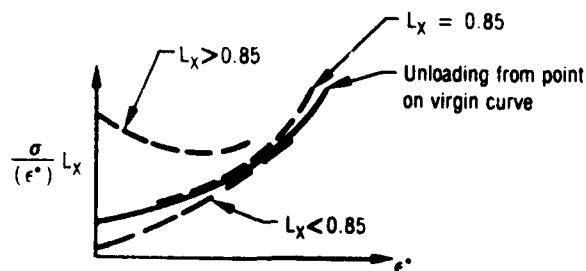
$L_x < 0.85$

31460

Noting that the quantity

$$\frac{\sigma}{(\epsilon^0)^{L_x}}$$

181

resembles a secant modulus and that, for most tests of UTP-19,360B L_x = 0.85 produced a finite limiting value as ϵ^o approached zero, it is suggested that L_x be found in this fashion for other propellants.

● For constant-rate tests, one has:

$$\epsilon^o = \epsilon^o_m$$
$$\lambda = 1$$

and thus, from equation (72):

$$X = X_r$$

Also

$$S_r = \max{(S_r)}$$

from which

$$Y_3 = S_r$$

Equation (77) then reduces to:

$$\sigma = 1.861 \ Y_1 \ S^{0.637} \ (\epsilon^o_m)^{0.463} \tag{80}$$

with $Y_1 = Y_1 \ (S)$ given by equation (69).

For very small damage:

$$Y_1 \ (S) = 1$$

182

so that equation (79) becomes:

$$\sigma \cong 1.861 \, S^{0.637} \, (\epsilon_m^{0})^{0.463} \tag{81}$$

in which the stress increases with damage, probably because of molecular chain stiffening due to an increase in stress per chain.

With the foregoing observations in mind, determination of the material properties can be accomplished as follows:

(1) The exponent, n, appearing in the relaxation function, is obtained from relaxation-modulus data.

(2) The normalized coefficient, E_r, entering the relaxation modulus, is determined to make unloading curve 2 in the figure above pass through the origin.

(3) The exponent, q (present in the definition of the damage parameter), is evaluated using equation (80) and two constant-rate tests at small values of damage.

(4) The function Y_1 is obtained by curve-fitting equation (79) to constant-rate tests over all strains out to failure.

(5) Experience to date indicates that the function Y_2 is independent of S and ϵ_m, and therefore equation (73) may be used instead of the more general form of equation (80).

(6) The backbone curve Y_3 is determined using unloading and reloading data like those available in a cyclic test whose first peak strain is the largest.

(7) Finally the correction factor, λ, can be ascertained from a relaxation test at a large strain level.

4.4.5 Multiaxial Generalization

A micromechanics model has been developed which predicts the form of equation (73), but its use was not pursued on this program.

4.5 M. GURTIN'S THEORIES FOR NONLINEAR VISCOELASTIC MATERIALS

Four essentially different approaches have been followed by M. Gurtin in trying to predict the response of solid propellants that exhibit damage. The stress-softening theory appears to be the most accurate of the four laws as will be pointed out.

4.5.1 Original Model

The one-dimensional stress-strain law for materials undergoing internal damage was based on the hypothesis that the state of damage at any time is completely characterized by the maximum strain, ϵ_m, that the material has experienced:

$$\epsilon_m (t) = \max_{0 \leq s \leq t} \epsilon(s) \tag{82}$$

The stress, σ, is given by a constitutive equation of the form:

$$\sigma(t) = g\left[\epsilon(t),\ \epsilon_m(t)\right] \tag{83}$$

and it depends only on the current values of strain and damage. Such an equation is, of course, rate-independent.

In this theory, if the maximum strain occurs at the present time, then

$$\epsilon_m (t) = \epsilon(t), \tag{84}$$

and equation (82) reduces to:

$$\sigma = G(\epsilon_m) = g(\epsilon_m,\ \epsilon_m) \tag{85}$$

184

The stress-strain curve

$$\sigma = G(\epsilon_m) \qquad (86)$$

is called the virgin curve and is traced out in an experiment with monotonically increasing strain.

Using the virgin curve, equation (83) may be rewritten in the form:

$$\sigma = F(\xi, \epsilon_m) \ G(\epsilon_m) \qquad (87)$$

with:

$$\xi = \frac{\epsilon}{\epsilon_m} \qquad (88)$$

the relative strain, and:

$$F(\xi, \epsilon_m) = \frac{g(\epsilon_m, \epsilon_m)}{G(\epsilon_m)} \qquad (89)$$

The function $F(\xi, \epsilon_m)$ is called the damage curve at the damage level ϵ_m, and is such that:

$$F(1, \epsilon_m) = 1 \qquad (90)$$

In some situations of interest $F(\xi, \epsilon_m)$ is independent of ϵ_m:

$$F(\xi, \epsilon_m) = F(\xi) \qquad (91)$$

185

When this is so, $F(\xi)$ is referred to as the master damage curve, and equation (87) reduces to

$$\sigma = F(\xi)G(\epsilon_m) \tag{92}$$

As pointed out previously, this is a rate-dependent theory, and as such, cannot be used for loading rates that differ much from that used to determine the damage function. This situation was remedied by changing the stress-strain law to the one described next.

4.5.2 Nonlinear Model Based on Stress Softening

To develop a simple theory of stress softening which allows for rate effects and which returns to Mullin's original ideas of using the past stress maximum as the damage parameter, two fundamental ingredients are considered. The first is the virgin stress, S, which represents the stress the material would experience in the absence of softening. This stress is assumed governed by a constitutive equation of the type encountered in linear viscoelasticity. The second ingredient is a damage function, F, which gives the true stress, σ, when the virgin stress, S, and its past maximum, S_m, are known.

The one-dimensional form of the constitutive law for a classical linear viscoelastic material is given by:

$$\sigma(t) = \int_{-\infty}^{t} G(t - \tau)\, \dot{\epsilon}(\tau)\, d\tau \tag{93}$$

in which $\sigma(t)$ is the stress; $\epsilon(t)$, the strain; and $G(t)$, the relaxation function. It is further assumed that $\epsilon(t) = 0$, prior to $t = 0$.

186

The generalization of equation (93) is begun by defining the quantity:

$$S(t) = \int_{-\tau}^{t} G(t - \tau)\, \dot{\varepsilon}(\tau)\, d\tau \qquad (94)$$

which is called the virgin stress and which represents the stress that would be present in the absence of softening. It is assumed that the extent of softening is governed by a constitutive equation giving the true stress, $\sigma(t)$, when $S(t)$ and its past maximum are known:

$$S_m(t) = \max_{0 \leqslant \tau \leqslant st} S(\tau) \qquad (95)$$

Without loss of generality, this constitutive equation is written in the form:

$$\sigma = S_m\, F\!\left(\frac{S}{S_m}\, ,\ S_m \right) \qquad (96)$$

and it is assumed that the damage function, F, satisfies the following conditions:

$$F(1,\ S_m) = 1$$
$$F(x,\ S_m) < x \quad \text{for } x < 1 \qquad (97)$$

These restrictions imply that:

$$(98)$$
$$\sigma(t) \leqslant S(t),$$

187

also that:

$$\sigma_m(t) = S_m(t), \tag{99}$$

and, that the following conditions are equivalent:

$$
\begin{array}{ll}
\text{i)} & \sigma(t) = S(t) \\
\text{ii)} & S(t) = S_m(t) \\
\text{iii)} & \sigma(t) = \sigma_m(t)
\end{array} \tag{100}
$$

where σ_m is the past stress maximum, defined analogically to S_m. The inequality equation (98) asserts that the material actually softens, while equation (99) indicates that this softening occurs when and only when $S(t) < S_m(t)$ (or equivalently $\sigma(t) < \sigma_m(t)$. The results of equation (98) and (99) show that one may equally well use the true stress, $\sigma(t)$, as the damage parameter.

Equation (97) and the fact that the first relation of equation (100) implies the third are direct consequences of the hypotheses laid down in equation (101). To verify equation (98), note that if the maximum of S on the interval $0 \leqslant T \leqslant t$, occurs at $\tau = \xi$, then:

$$S_m(t) = S(\xi) \tag{101}$$

Thus using equation (100) in (95), and recalling that equation (96):

$$\sigma(\xi) = S(\xi) \ F(1, S_m) \equiv S(\xi) \tag{102}$$

which, by virtue of (100) and the definition of S_m, implies that:

$$\sigma(\xi) = S(\xi) = S_m(t) \geqslant S(\lambda) \geqslant \sigma(\lambda); \quad 0 \leqslant \lambda \leqslant t \tag{103}$$

proving equations (97) and (98) and the first two equations of equation (100). To establish the third equation (100), note that if:

$$S_m(t) = S(t)$$

which implies that:

$$S_m(t) = \sigma(t)$$

because of equation (101); then, since:

$$S_m = \sigma_m \tag{104}$$

one would have that:

$$\sigma_m(t) = \sigma(t).$$

Conversely, if

$$\sigma(t) = \sigma_m(t),$$

then:

$$S(t) \geqslant \sigma(t) = \sigma_m(t) = S_m(t)$$

so that:

$$S(t) = S_m(t).$$

Returning to the constitutive equation (95), it is interesting to consider the special case in which the damage function depends only on S/S_m:

$$F\left(\frac{S}{S_m}, S_m\right) \equiv F\left(\frac{S}{S_m}\right); \tag{105}$$

which is a master damage curve of the type considered in the rate-independent model discussed previously.

When the virgin stress obeys an elastic stress-strain relation:

$$S = E\epsilon \tag{106}$$

then:

$$S_m = E\epsilon_m \tag{107}$$

in which ϵ_m is the past strain-maximum, and equation (95) yields:

$$\sigma = E\epsilon_m \, F\left(\frac{\epsilon}{\epsilon_m}, \, E\epsilon_m\right) \tag{108}$$

so that, defining:

$$F^*\left(\frac{\epsilon}{\epsilon_m}, \epsilon_m\right) \equiv F\left(\frac{\epsilon}{\epsilon_m}, \, E\epsilon_m\right) \tag{109}$$

leads to the starting assumption of Gurtin and Francis[26]:

$$\sigma = F^*\left(\frac{\epsilon}{\epsilon_m}, \, \epsilon_m\right) E\epsilon_m \tag{110}$$

presented earlier as the rate-independent model.

Although implicit in equation (95) is the assumption that the functional form of F would be the same for unloading conditions as for reloading, it was found experimentally that a different damage function is needed for each of these processes. Actually, there is more than one way of obtaining the same damage function. For TP-H1011, for instance, the following procedure was employed.

Considering the strain history shown in Figure 110, on the loading portion we have:

$$S(t) = \dot{\epsilon} \int_{o}^{t} G(\tau) \, d\tau \qquad \text{for } t \leqslant T \tag{111}$$

hence, S(t) increases monotonically and, by equation (98):

$$Sm(t) = S(t) = \sigma(t) \tag{112}$$

and, upon unloading, the past maximum of S is the true stress:

$$\sigma_{m} = \sigma(T), \qquad T \leqslant t < 2T \tag{113}$$
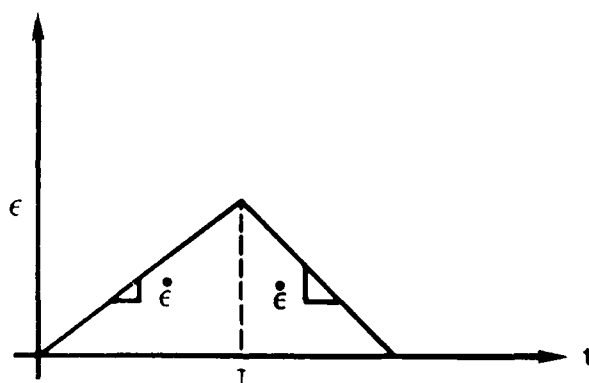
Figure 110. Strain History Used to Characterize the Damage Function

30973

191

Further, by equation (93):

$$S(t) = |\dot{\epsilon}| \left\{ \int\limits_{0}^{T} G(t - \tau) \, d\tau - \int\limits_{T}^{t} G(t - \tau) \, d\tau \right\} \qquad (114)$$

or, equivalently:

$$(115)$$

$$S(T + t) = G(t) - \sigma(t)$$

with:

$$G(t) \equiv |\dot{\epsilon}| \int\limits_{t}^{t + T} G(\tau) \, d\tau \qquad (116)$$

Letting $\sigma_1(t)$ and $\sigma_2(t)$ denote the true stress during loading and unloading, respectively, with t in $\sigma_2(t)$ measured from the time T at which unloading begins, equations (95) and (110) yield the simple formula:

$$\frac{\sigma_2(t)}{\sigma_m} = F \left[\frac{G(t) - \sigma_1(t)}{\sigma_m}, \sigma_m \right] \qquad (117)$$

Thus, summarizing, the stress-softening approach to damage is described through the following constitutive equation:

$$\sigma(t) = S_m F \left(\frac{S}{S_m}, S_m \right) \qquad (118)$$

where

$$S(t) = \int_{0}^{t} G(t - \tau) \frac{d\epsilon}{d\tau}(\tau) \, d\tau$$

and in which the damage function, F, may be determined from sawtooth tests with increasing peak strains and with sufficiently long rest periods between cycles. For conditions of reloading, F is given by:

$$\frac{\sigma_2}{\sigma_m} = F\left[\frac{\sigma_1(t)}{\sigma_m}, \, \sigma_m\right] \tag{119}$$

while for unloading the following form is employed:

$$\frac{\sigma_2}{\sigma_m} = F\left[\frac{G(t) - \sigma_1(t)}{\sigma_m}, \, \sigma_m\right] \tag{120}$$

Typical curves for unloading and reloading damage functions of TP-H1011 are included as Figures 111 and 112, respectively.

Finally, we point out that the use of this approach to predict the response of TP-H1011 yielded results that were far more accurate than those obtained with any of the other theories in their original form.

4.5.3 Nonlinear Models Based on Maximum Strain

A series of constitutive relations based on the past maximum strain have been proposed by M. Gurtin. The precursor of these relations took the form:

$$\sigma(t) = \int_{0}^{t} G(t - \tau) \frac{de}{d\tau}(\tau) \, d\tau \tag{121}$$
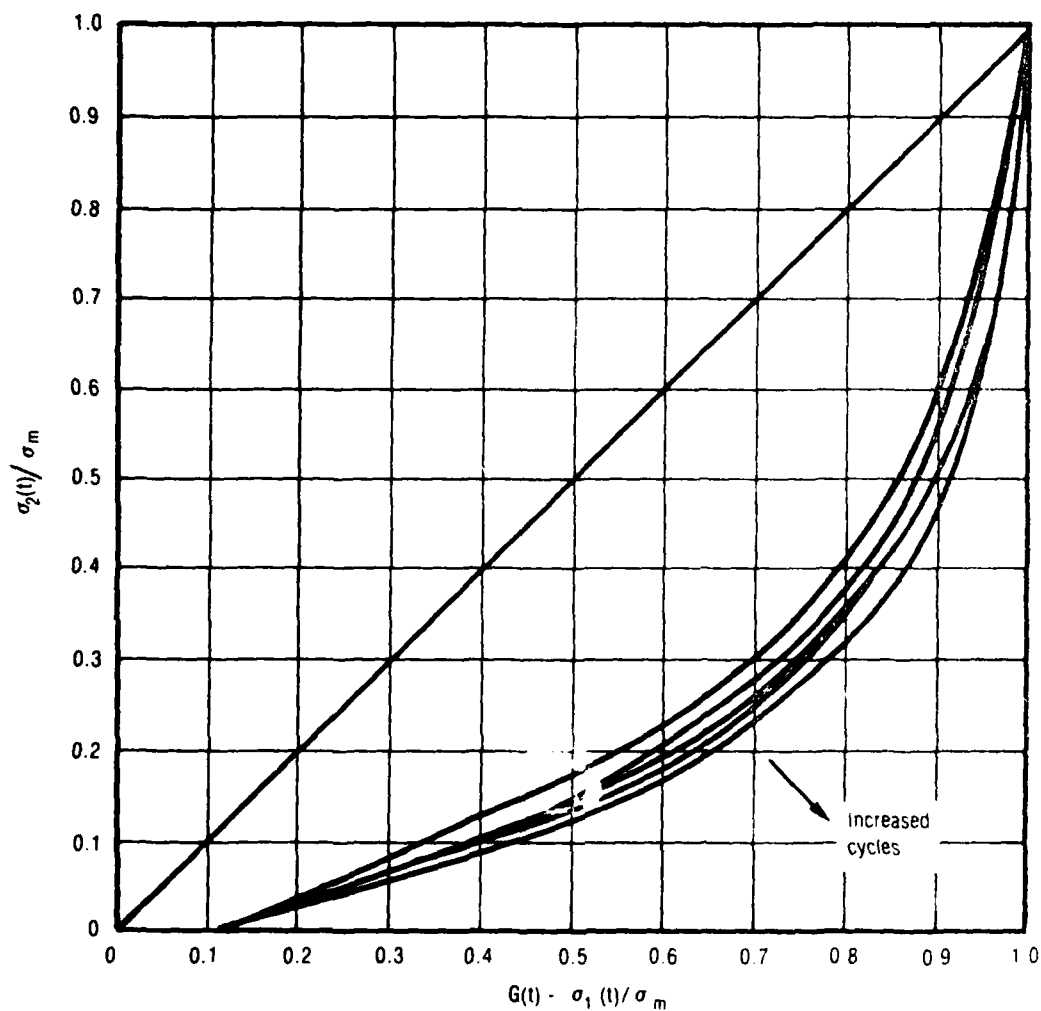
Figure 111. Damage Function for Unloading (TP-H1011)

where G represents the relaxation modulus, and the function e was expressed as a product of the reduced damage function, F, and the virgin-response function, g, in the following way:

$$e = F\left(\frac{\epsilon}{\epsilon_m} , \epsilon_m\right) g\ (\epsilon_m) \qquad (122)$$

with:

$$F(1, \epsilon_m) = 1 \qquad (123)$$

194
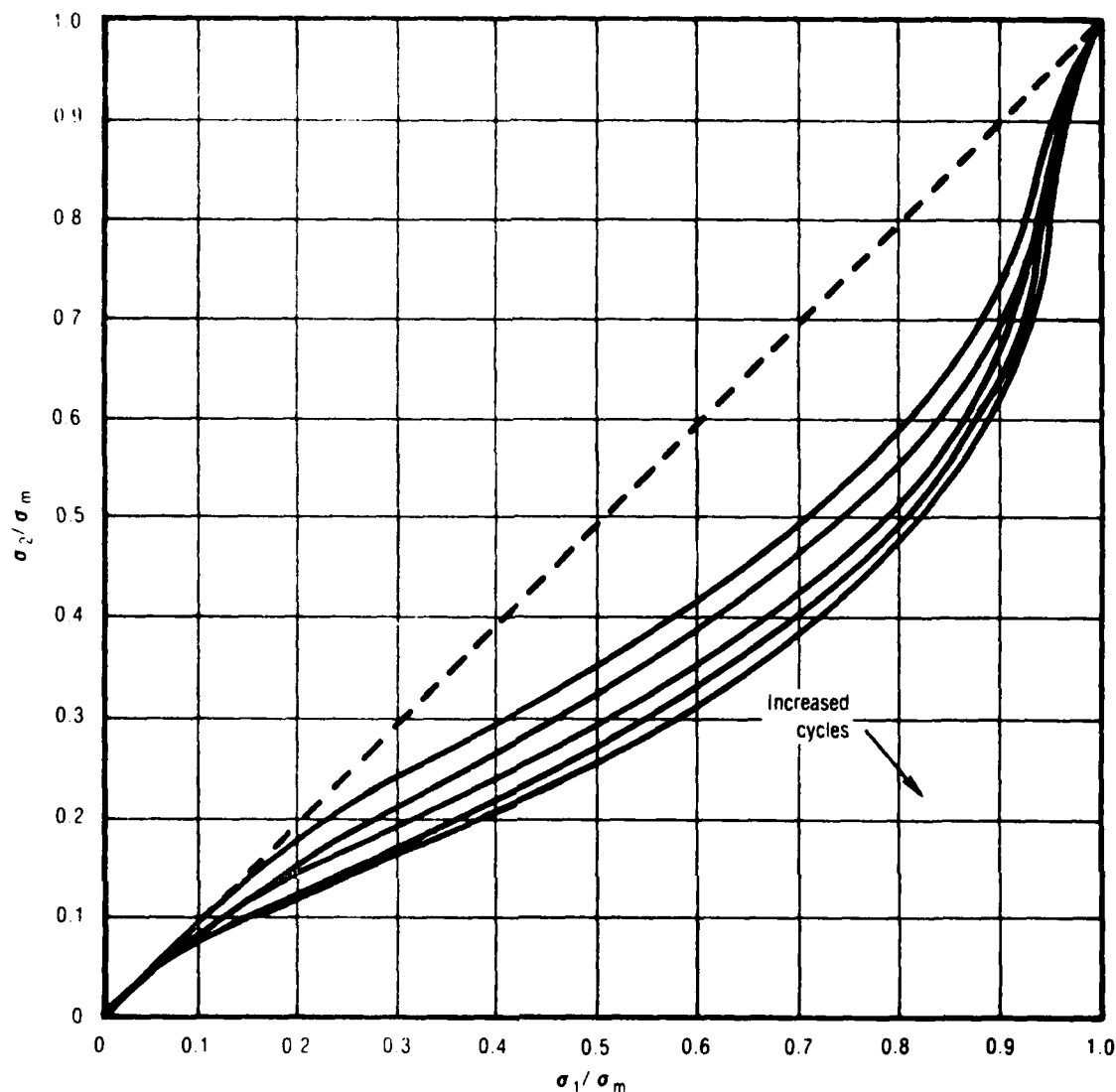
Figure 112.   Damage Function for Reloading (TP-H1011)

28892

and

$$\epsilon_m = \max_{0 \leq \tau \leq t} \epsilon(\tau) \tag{124}$$

so that, during virgin response, since:

$$\epsilon = \epsilon_m \tag{125}$$

195

one had:

$$\sigma(t) = \int_0^t G(t - \tau) \frac{dg(\epsilon)}{d\epsilon} \frac{d\epsilon(\tau)}{d\tau} d\tau \qquad (126)$$

and, by taking

$$g(\epsilon) = \sum_{k=1}^{k=K} A_k \epsilon^k \qquad (127)$$

the best values for the a_K's could be determined using least squares and the data of all constant-rate tests.

To characterize the reduced damage function, F, involved the determination of a creep function, J, solution of:

$$\int_0^t G(t-\tau) \frac{dJ(\tau)}{d\tau} d\tau = 1 \qquad (128)$$

and, such that:

$$e(t) = \int_0^t J(t-\tau) \frac{d\sigma(\tau)}{d\tau} d\tau \qquad (129)$$

Thus, taking the reduced damage function, F, in the form:

$$F(x, y) = F_1(x) F_2(x,y) \qquad (130)$$

$$F_1(x) = x^M + \sum_{m=1}^{M-1} d_m (x^m - x^M) \tag{131}$$

$$F_2(x,y) = 1 + \sum_{p=1}^{P} b_p \, y^p \left[x - x^Q + \sum_{q=2}^{Q-1} C_q (q - Q) \right] \tag{132}$$

and equating equations (114) and (118), the coefficients entering F were to be determined using least squares and all the saw-tooth data with increasing strain peaks.

When this constitutive law was applied to UTP-19,360B data, it was deemed necessary to change the form of the function e, because of the large errors observed in the predicted response.

The last of a sequence of modifications yielded the following stress-strain law:

$$\sigma(t) = \int_{0}^{t} G(t - \tau) \left\{ K\left(\epsilon_m, \dot{\epsilon}_m \frac{d}{d\tau} \left[F\left(\frac{\epsilon}{\epsilon_m}, \epsilon_m \right) \epsilon_m \right] \right) \right\} d\tau \tag{133}$$

where, as before, G was the relaxation modulus, and:

$$F(1, \epsilon_m) = 1 \tag{134}$$

197

with:

$$\epsilon_m = \max_{0 \leqslant \tau \leqslant t} \epsilon(\tau) \qquad (135)$$

In the present case, the virgin response was given by:

$$\sigma(t) = \int_0^t G(t - \tau) \, K(\epsilon_m, \dot{\epsilon}_m) \, \frac{d\epsilon_m}{d\tau} \, d\tau \qquad (136)$$

while, the damage response, for which ϵ_m remains constant, took the form:

$$\sigma(t) = K(\epsilon_m, 0) \int_0^t G(t - \tau) \frac{\partial F}{\partial x}(x, y) \, d\tau \qquad (137)$$

in which

$$K(\epsilon, \dot{\epsilon}) = 1 + A_1(\epsilon - \epsilon_0) + A_2(\epsilon - \epsilon_0)^2 + A_3(\epsilon - \epsilon_0)^3 + \qquad (138)$$
$$+ \dot{\epsilon}(B_1 \epsilon + B_2 \epsilon^2 + B_3 \epsilon^3)$$

$$F(x, y) = \alpha(x) \left[1 + (D_5 y + D_7 y^2) \left\{ x - x^3 + D_6(x^2 - x^3) \right\} \right] \qquad (139)$$

$$\alpha(x) \equiv x^5 + \sum_{m=1}^{4} D_m(x^m - x^5) \qquad (140)$$

198

with:

$$x \equiv \epsilon/\epsilon_m \tag{141}$$

and

$$y \equiv \epsilon_m \tag{142}$$

A set of stress predictions obtained for UTP-19,360B, with the resulting version of the theory, is included in Figures 113 through 119. Figure 113 is for the high-to-low dual rate test, Figures 114 through 116 are segments of the long-duration similitude test, and Figures 117 through 119 are segments of the three step relaxation test.

Since the dependence of the function K on the strain rate was felt to be artificial, the treatment of damage was revised in the manner explained next.

4.5.4 Current Model

The latest version of M. Gurtin's nonlinear stress-strain law is based on a strain-dependent relaxation function and has the form:

$$\sigma(t) = \int_0^t G\left[\epsilon(\tau), \tau\right]\dot{\epsilon}(t - \tau)\, d\tau \tag{143}$$

where

$$G(\epsilon, t) = G_r(t) + G_c(\epsilon, t) \tag{144}$$
$$\tag{145}$$

$$G = \text{relaxation modulus} \tag{146}$$

$$G_c = \text{correction modulus, defined as:}$$

199

$$G_c(\epsilon, t) = \sum_{n=1}^{N} A_n(\epsilon)(e)^{-t/\tau_n}$$

$$A_n(\epsilon) = \sum_{p=1}^{P} A_{np} \, \epsilon^p$$

For this material, the virgin curve ($\epsilon = \epsilon_m = \epsilon$) is:

$$\sigma = \sigma_r + \sigma_c \tag{147}$$

with σ_r, the linear viscoelastic stress

$$\sigma_r(t) = \int_0^t G_T(\tau) \, \dot{\epsilon}(t - \tau) \, d\tau \tag{148}$$

and the correction stress, σ_c, given by:

$$\sigma_c(t) = \int_0^t G_c\left[\epsilon(\tau), \tau\right] \dot{\epsilon}(t - \tau) \, d\tau \tag{149}$$

Hence, to characterize the virgin response, only constant rate tests need be employed. In this instance, σ and σ_r are known, so that form equation (131), σ_c may be computed, and equated to equation (133) using the fact that $\dot{\epsilon}$ is a constant; i.e.:

$$\sigma(t) - \sigma_r(t) = \sigma_c(t) \equiv \int_0^t G\left|\epsilon(\lambda), \lambda\right| d\lambda \tag{150}$$
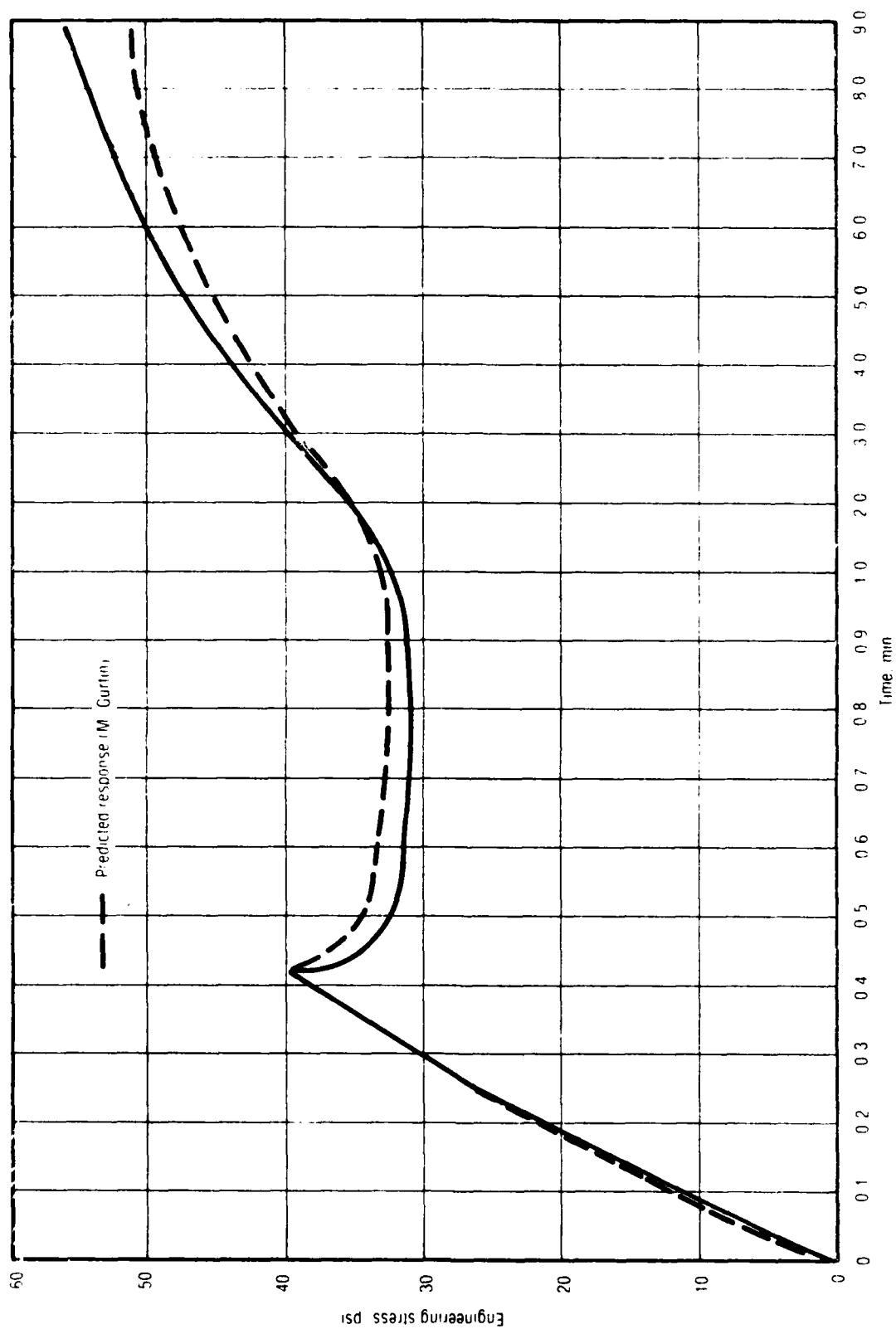
Figure 113. Two-Rate Loading (1 in./min to 0.1 in./min) of UTP-19,360B-400/1777

28006

201
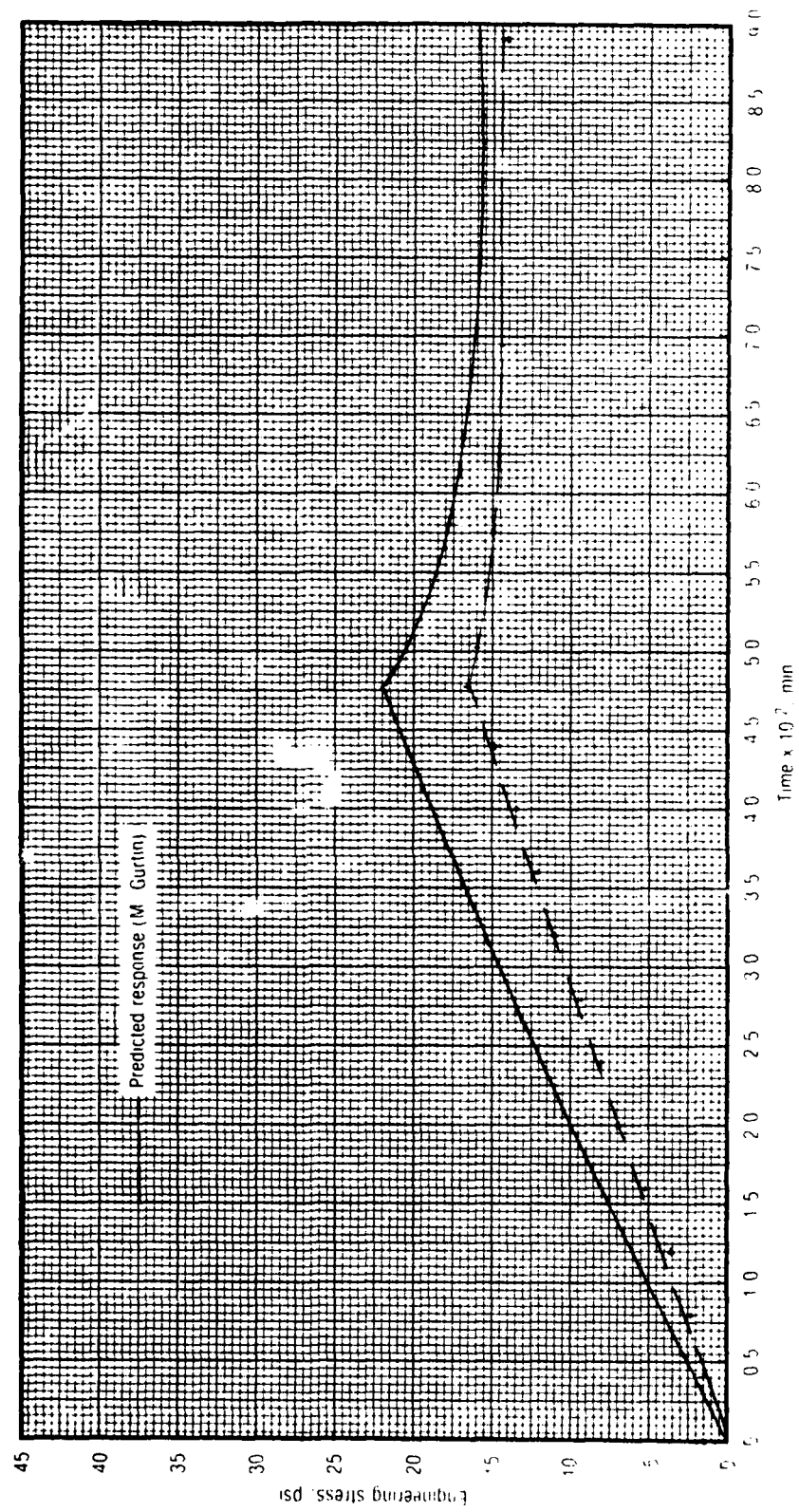
Figure 114. Relaxation-Unload-Reload of 6-in. Bar of UTP-19,360B-400/1777

28847
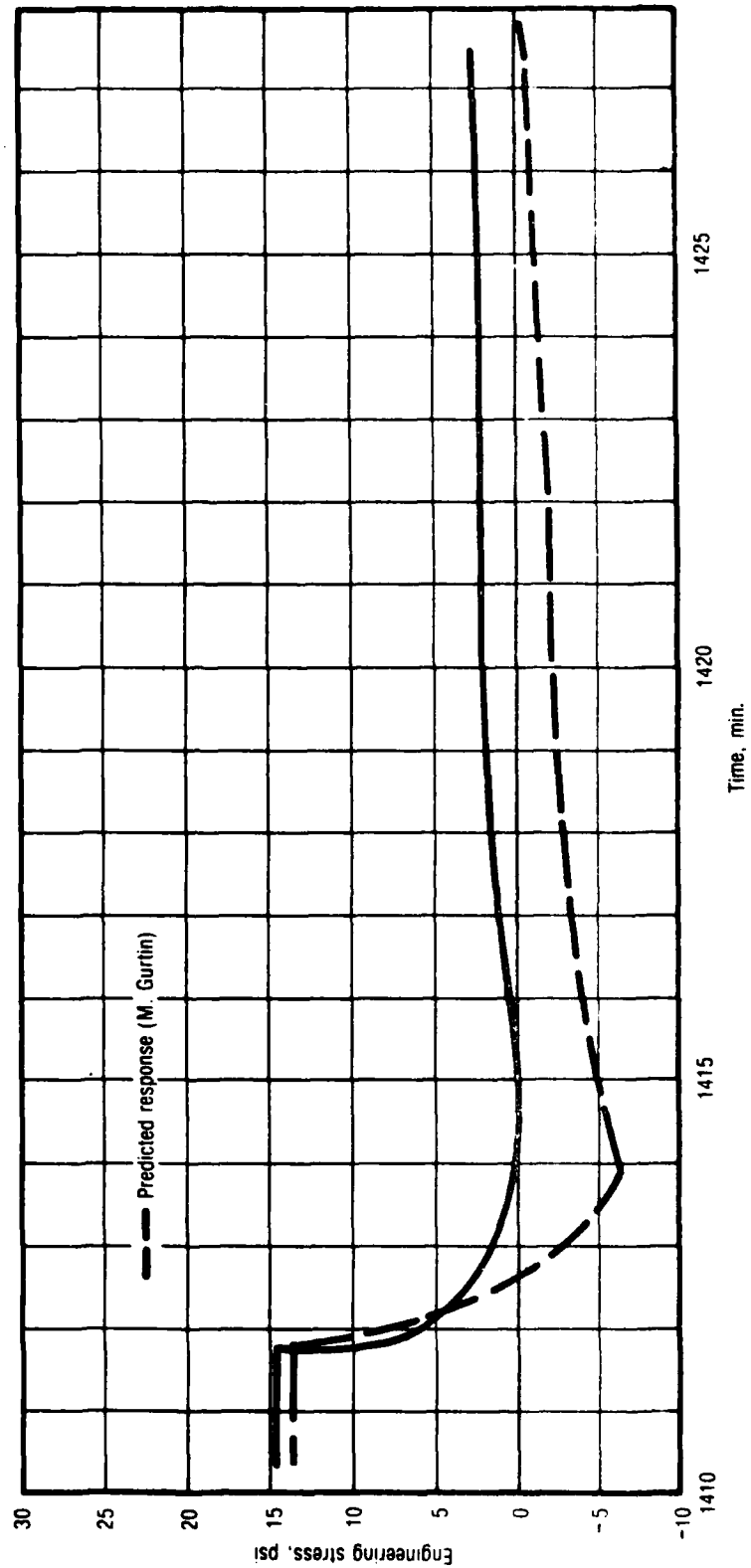
Figure 115. Relaxation-Unload-Reload of 6-in. Bar of UTP-19,360B-400/1777

28848
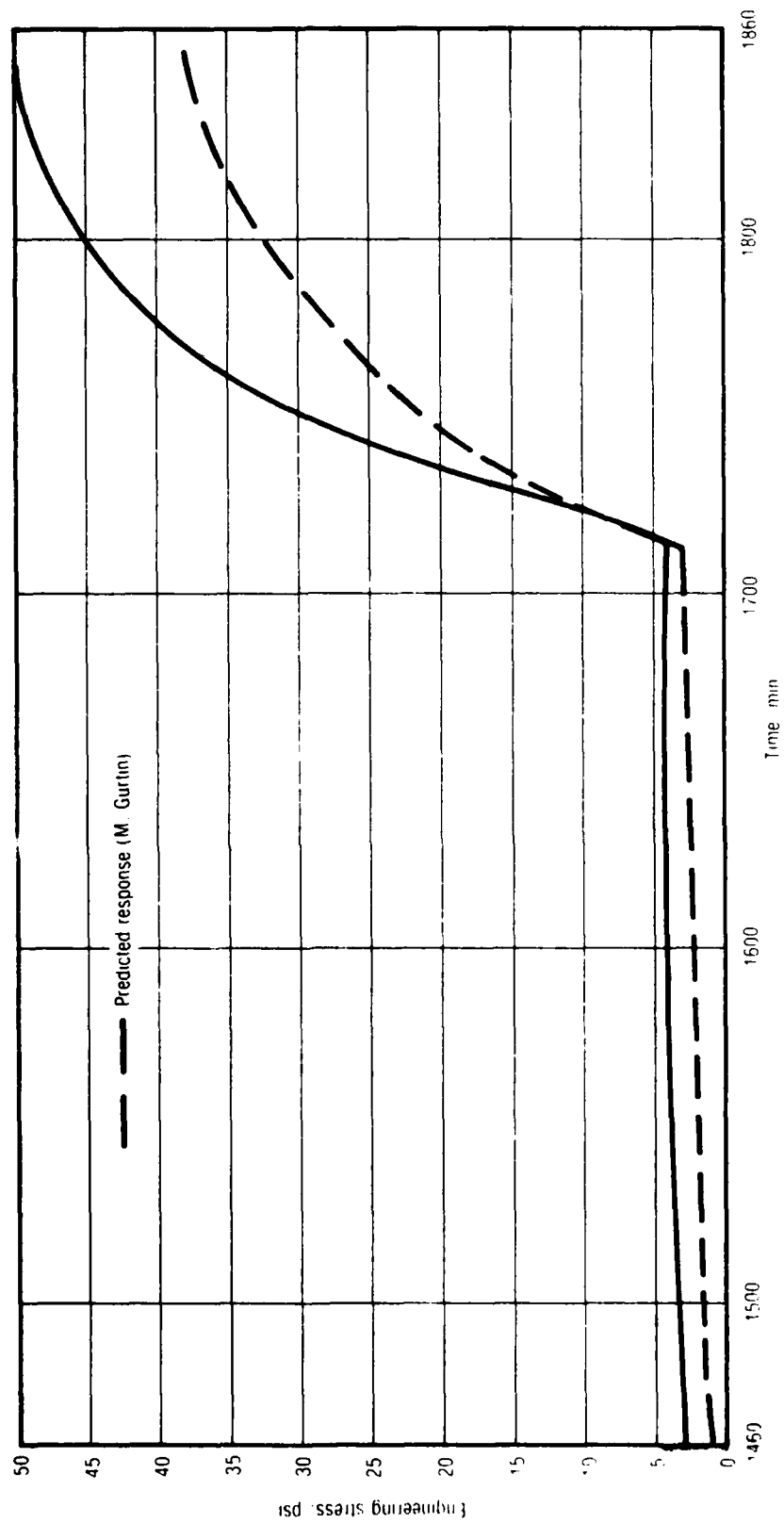
Figure 116. Relaxation-Unload-Reload of 6-in. Bar of UTP-19,360B-400/1777

28849

204
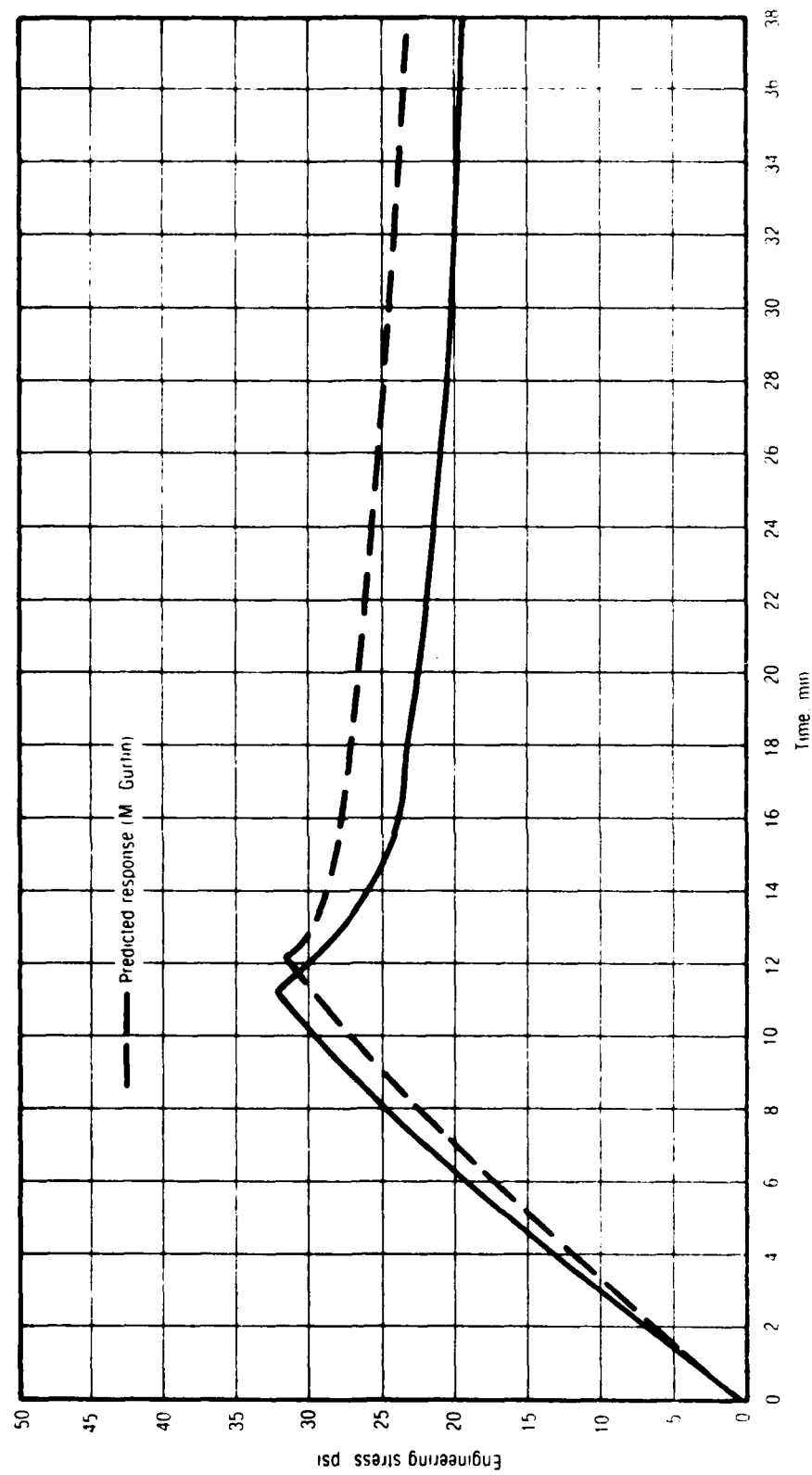
Figure 117. Three-Step Relaxation of 6-in. Bar of UTP-19,360B-400/1777

28850
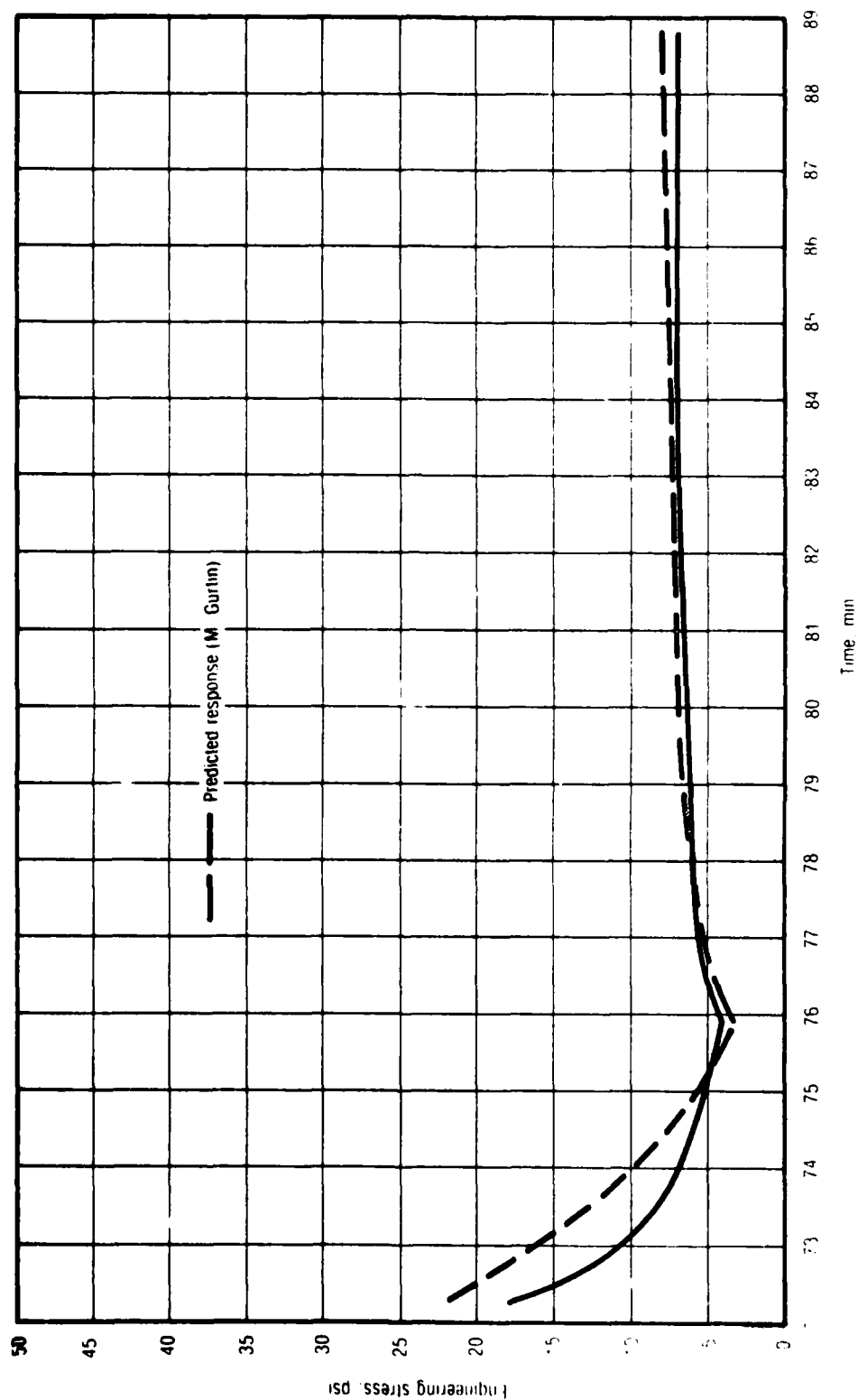
Figure 118. Three-Step Relaxation of 6-in. Bar of UTP-19,360B-400/1777

28899
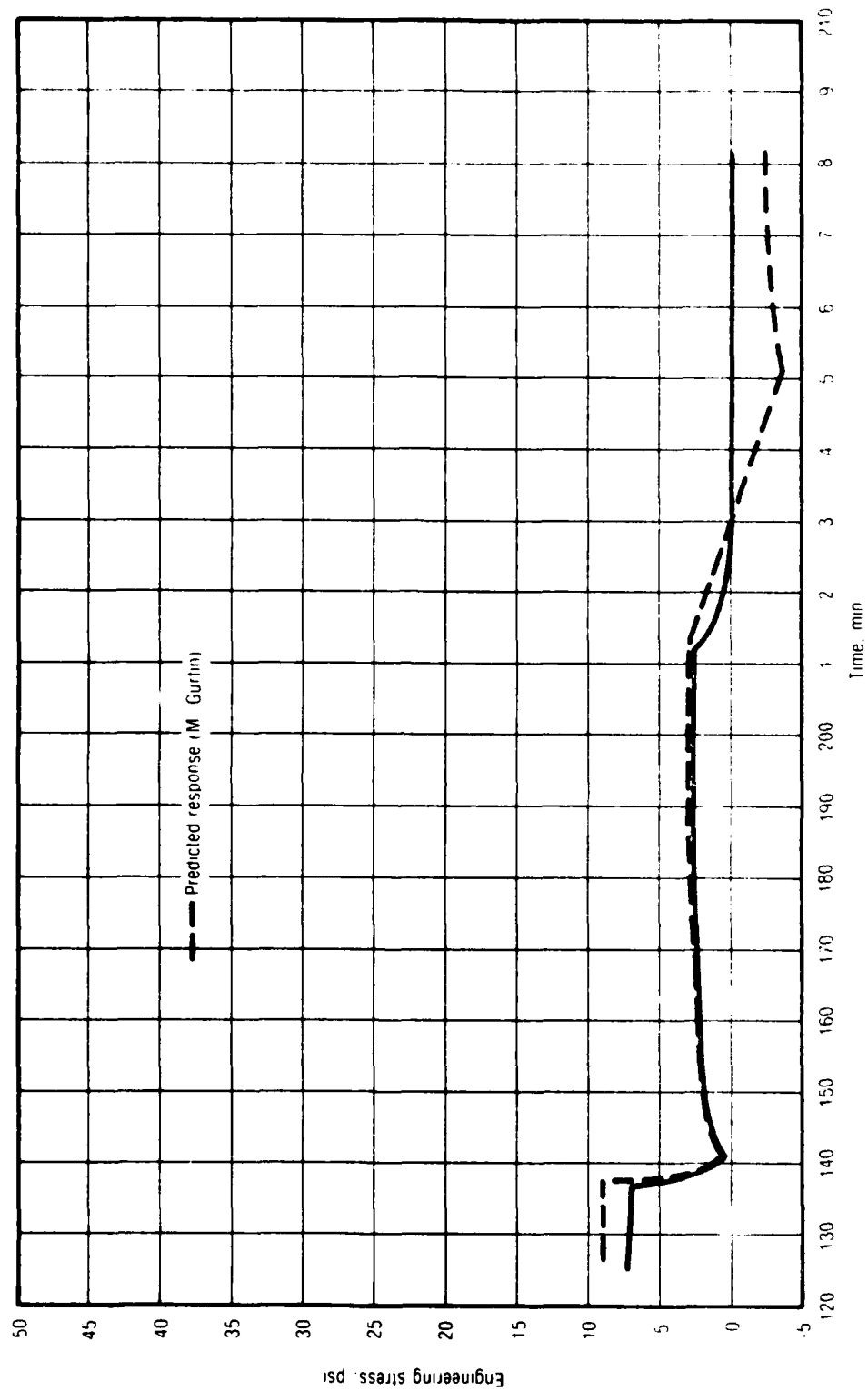
Figure 119. Three-Step Relaxation of 6-in. Bar of UTP-19,360B-400/1777

28900

207

which, upon recalling equations (134) and (135) becomes:

$$\sigma(t) - \sigma_r(t) = \sum_{n=1}^{N} \psi_n(t) \tag{151}$$

where:

$$\psi_n(t) = \sum_{p=1}^{P} A_{np} \dot{\epsilon} \int_o^t \epsilon^p(\lambda) \, e^{-\lambda/\tau_n} \, d\lambda \tag{152}$$

Furthermore, since for a constant-rate test

$$\epsilon(\lambda) = \dot{\epsilon}\lambda \tag{153}$$

it follows that:

$$\Psi_n(t) = \sum_{p=1}^{P} A_{np} \dot{\epsilon}^{p+1} \int_o^t \lambda^p \, e^{-\lambda/\tau_n} \, d\lambda \tag{154}$$

and after integrating by parts:

$$\Psi_n(t) = \sum_{p=1}^{P} A_{np} \dot{\epsilon}^{p+1} \tau_n^{p+1} f_p(t/\tau_n) \tag{155}$$

with

$$f_o (x) = 1 - e^{-x} \tag{156}$$

$$f_p (x) = -x^R e^{-x} + pf_{p-1} (x) \ ; \ p = 1, \ \ldots P$$

Clearly, equations (132) and (135) to (137) may be used to determine the coefficients a_{np} appearing in the definition of the correction modulus. The procedure suggested by M. Gurtin to accomplish this is as follows:

1. Take N tests with constant rates $\dot{\epsilon}_1, \dot{\epsilon}_2, \ldots \dot{\epsilon}_N$; and set:

$$\tau_i = \frac{1}{\dot{\epsilon}_i} \ ; \ i = 1, \ \ldots, \ N \tag{157}$$

2. Select the degree, P, of the series expansion of the correction modulus, as it appears in equation (130).

3. Use the $\dot{\epsilon}_1$ test and the approximation:

$$\sigma_c (t) = \Psi_1 (\dot{\epsilon}_1, \ t) \tag{158}$$

to find the a_{1p}.

4. Use the $\dot{\epsilon}_2$ test and the approximation

$$\sigma_c (t) - \Psi_1 (\dot{\epsilon}_2, \ t) = \Psi_2 (\dot{\epsilon}_1, \ t) \tag{159}$$

to find the a_{2p}.

5. Use the $\dot{\epsilon}_3$ test and the approximation

$$\sigma_c(t) - \Psi_1 (\dot{\epsilon}_3, \ t) - \Psi_2 (\dot{\epsilon}_3, \ t) = \Psi_3 (\dot{\epsilon}_3, \ t) \tag{160}$$

to find the a_{3p}, and so on for the $a_{4p} \ldots a_{np}$

209

6. Iterate this procedure if necessary; that is, define

$$\overline{\Psi}(\dot{\epsilon}, t) = \sum_{n = 1}^{N} \Psi_n (\dot{\epsilon}, t) \qquad (161)$$

so that Ψ is known. For each ramp test, define

$$\overline{\sigma}_c = \sigma_c - \overline{\Psi} \qquad (162)$$

and repeat the above procedure using $\overline{\sigma}_c$ to find constants $\overline{a_{np}}$. The new values of the a_{np} are

$$(a_{np})_{new} = a_{np} + \overline{a_{np}} \qquad (163)$$

7. Repeat the process if nec￢ary.

It is important to point out here that numerical difficulties may be encountered in applying this technique to characterizing the virgin response of solid propellants. In fact, some convergence problems were faced in connection with the UTP-19,360B data. Moreover, characterization of the damaged response calls for a large number of cyclic tests over a wide range of rates. This increases the convergence difficulties. The model was employed with the constant-rate tests only for this reason. Figures 120 to 123 show the results of the stress predictions obtained with the current version of the model. The first two plots correspond, respectively, to the lowest and highest rates available at ambient temperature.

So far in the program, none of the models developed by Gurtin have taken into account the effects of temperature on propellant response. However, the time-temperature superposition principle was tested with the current version of the theory. The results appear in Figures 122 and 123 for the thermal tests at 123 and 40 F, respectively. The use of the superposition principle breaks down at
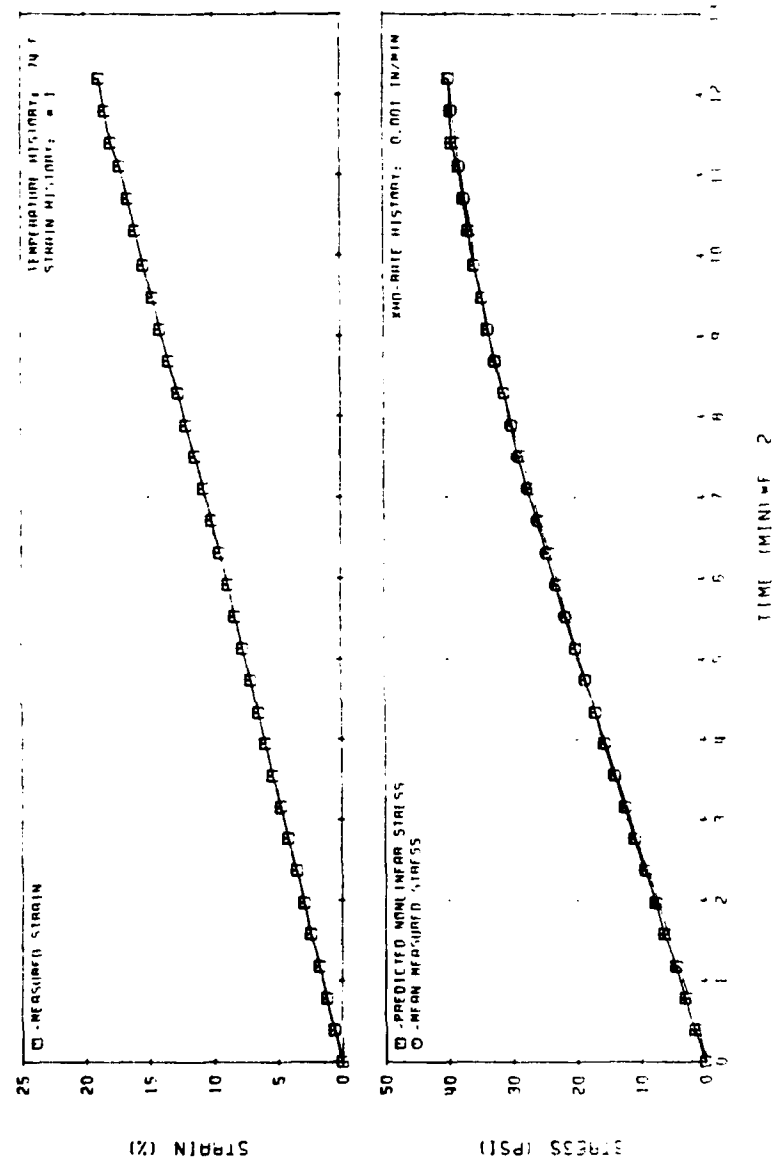
Figure 120. Nonlinear Viscoelastic Stress Predictions for UTP-19,360B-400/1777 at 0.001 in./min and 74 F (M. Gurtin's Theory)

31029
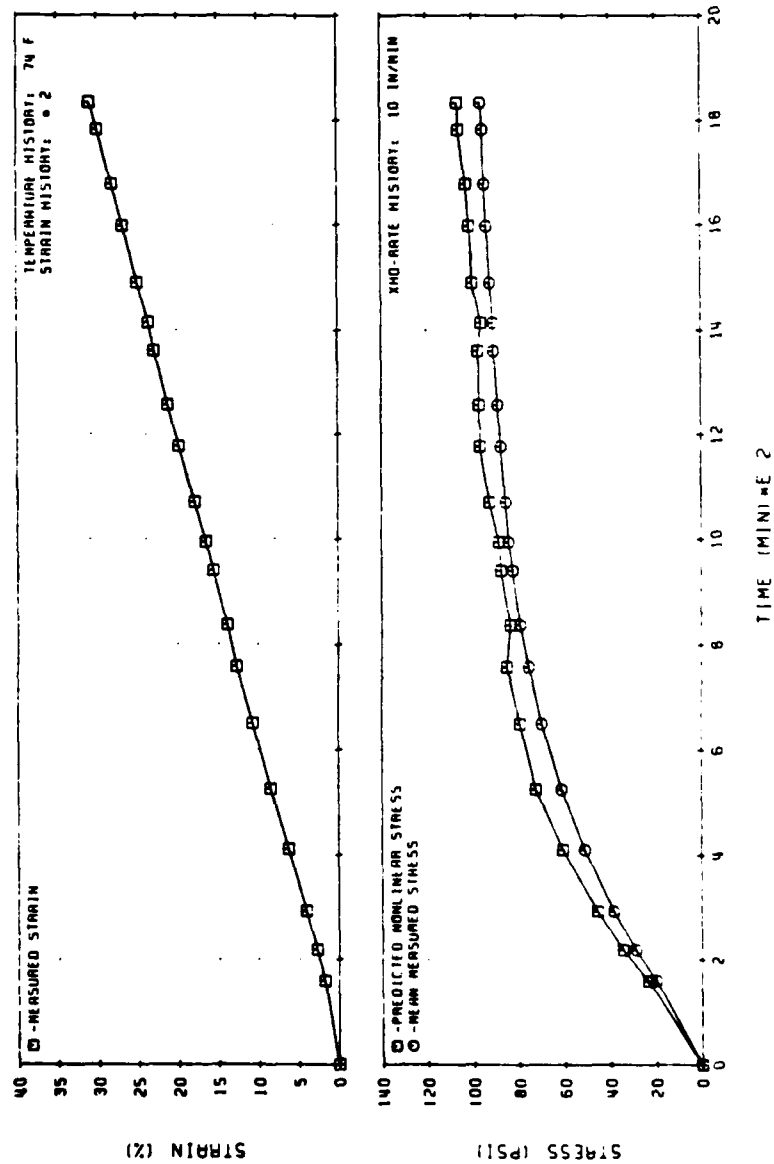
Figure 121. Nonlinear Viscoelastic Stress Predictions for UTP-19,360B-400/1777 at 70 F (M. Gurtin's Theory)

31030

212
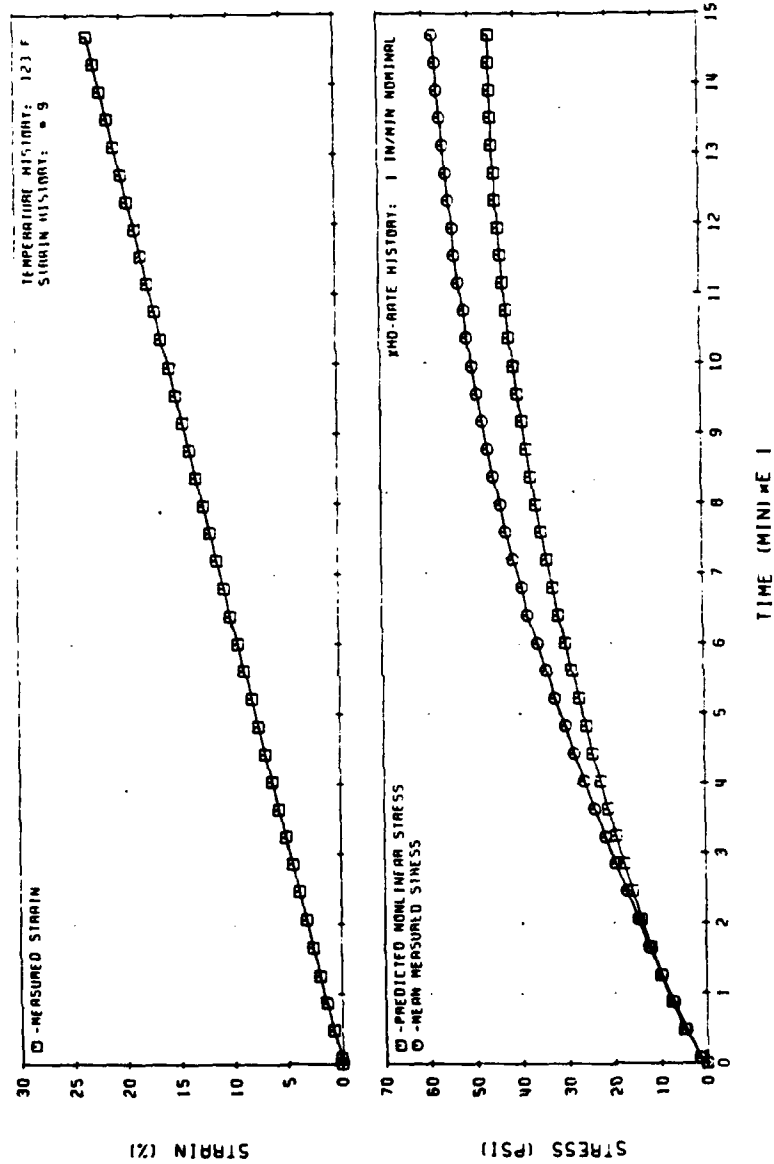
Figure 122. Nonlinear Viscoelastic Stress Predictions for UTP-19,360B-400/1777 at 123 F (M. Gurtin's Theory)

31031

213
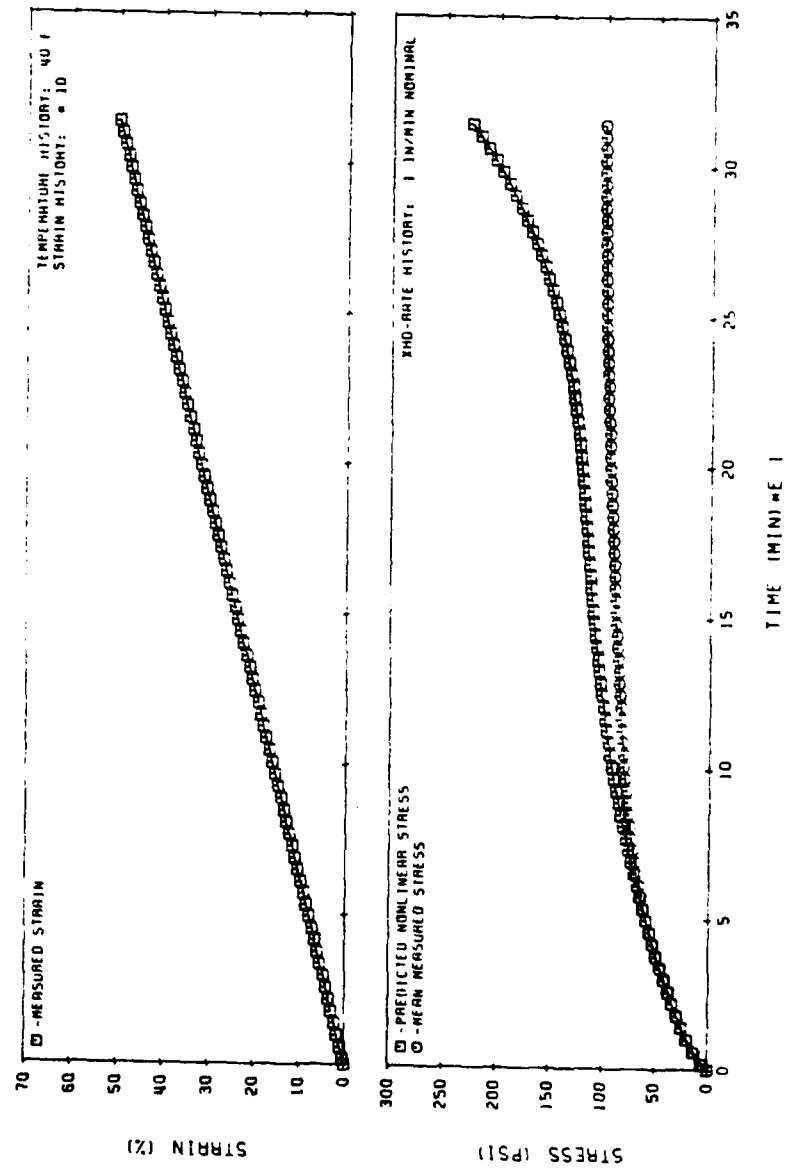
Figure 123. Nonlinear Viscoelastic Stress Predictions for UTP-19,360B-400/1777 at 40 F (M. Gurtin's Theory)

214

a strain of about 39%. This was apparently due to the ambient temperature data base being limited to a low strain level. Also, it might be necessary to allow the relaxation function (G_c) to depend on the glass transition temperature (T_g)

$$G_c = G_c \ (\epsilon, \ T_g, \ t)$$

4.6 RUSSIAN APPROACH TO PHYSICALLY NONLINEAR VISCOELASTIC SOLIDS

The Russians have explored two approaches for characterizing damage effects in solid propellants.[7, 8] They are a general functional approach and a kinetic equation of evolution for damage. Both approaches are based on internalvariable concepts, and either approach appears general enough to also incorporate cumulative damage and propellant response under multiaxial stress states. However, the general functional approach may be of little practical engineering value because a very extensive testing program may be required to evaluate material parameters. This approach requires introduction of damage measures which should reflect microstructural damage mechanisms, and a damage functional which characterizes the accumulation of damage or defects. The damage functional is then expanded into a series of multiple integrals in an analogous fashion to that followed by Green and Rivlin for nonlinear materials with fading memory. Herein lies the difficulty. Even assuming isotropy, four to six different types of multi-axial tests are required to evaluate the required material property functions for a first-order theory. Although the approach has theoretical merit and may even have some practical application in the future, its pursuit was abandoned in favor of the kinetic approach.

The essential feature of the kinetic approach is to introduce the degree of damage into the constitutive equations as a reduced-time parameter in the same way that temperature is introduced as a reduced-time parameter for the thermorheologically simple materials in linear thermoviscoelasticity. Damage is then defined in terms of some strength parameter of the material, and the degree of damage is characterized through an equation for damage, as explained subsequently.

4.6.1 Original Model

The one-dimensional constitutive equation, taken from the Russian literature by W. L. Hufferd as a means of predicting the response of physically nonlinear viscoelastic materials, may be expressed by:

$$\sigma(t) = \int_0^t E(t' - \tau') \frac{d\epsilon}{d\tau}(\tau) \, d\tau \qquad (164)$$

where

σ = stress

ϵ = strain due to mechanically applied stress

$E(t)$ = relaxation modulus

$E(t) = E_e + E_2 t^{-n}$

and

$$t' - \tau' = \int^t \frac{d\epsilon}{a_\eta \left[\eta \ (\xi) \right]} \qquad (165)$$

represents the damage-reduced time, which is arrived at in the manner described next.

First, a normalized damage function $\omega = \omega(t)$ is introduced through the following kinetic equation of evolution

$$\frac{d\omega}{dt}(t) = h(\omega) \ f(t) \qquad (166)$$

in which it is further assumed that:

$$f(t) = \int_0^t F(t - \tau) \ \phi \left| \sigma_0(\tau) \right| d\tau \qquad (167)$$

216

together with the conditions:

$$\omega(o) = 0 \tag{168}$$
$$\omega(t^*) = 1$$

indicating that no damage exists at the initial state, and that failure occurs at time t^*.

Next, equation (166) is integrated with $\omega(o) = 0$, leading to

$$\int_o^\omega \frac{d\omega}{h(\omega)} = \int_o^t f(\tau) \, d\tau \tag{169}$$

Setting $t = t^*$, so that $(t^*) = 1$, and substituting equation (167) for $f(\tau)$, it is obtained that

$$\frac{\displaystyle\int_o^{t^*} d\xi \int_o^\xi F(\xi - \tau) \, \phi \left| \sigma_o(\tau) \right| d\tau}{\displaystyle\int_o^1 \frac{d\omega}{h(\omega)}} = 1 \tag{170}$$

If now the function $F(t)$ is assumed to have a power-law representation

$$F(t) = F_o \, t^m \tag{171}$$

217

Equation (170) can be written in the form

$$\frac{\displaystyle\int_0^{t^*} d\xi \int_0^{\xi} F_0(\xi - \tau)^m \phi\left|\sigma_0(\tau)\right| d\tau}{\displaystyle\int_0^1 \frac{d\omega}{h(\omega)}} = 1 \qquad (172)$$

and integrating with respect to ξ, assuming that the order of integration may be interchanged, one arrives at

$$\frac{\displaystyle\frac{F_0}{1 + m} \int_0^{t^*} (t^* - \tau)^{1+m} \phi\left|\sigma_0(\tau)\right| d\tau}{\displaystyle\int_0^1 \frac{d\omega}{h(\omega)}} = 1 \qquad (173)$$

which, for the case where σ_0 and $\phi\left[\sigma_0\right] = \phi[\sigma_0]$ are constant, becomes

$$\frac{F_0 \phi_0(\sigma_0)}{(1 + m)(2 + m)} \frac{(t_0^*)^{2+m}}{\displaystyle\int_0^1 \frac{d\omega}{h(\omega)}} = 1 \qquad (174)$$

where t_0^* is the time to failure under the constant stress σ_0. Thus equation (173), in this case, may be written as:

218

$$(2 + m) \int_0^{t^*} (t^* - \tau)^{1 + m} \frac{d\tau}{(t_o^*)^{2+m}} = 1 \qquad (175)$$

If the time to failure under a constant stress, σ_o, has the power-law representation

$$\sigma_o^{\alpha} \, t_o^* = \text{constant} = \beta \qquad (176)$$

then equation (175) can be put in the form:

$$\int_0^{t^*} (t^* - \tau)^{1+m} \, \sigma_o^{\alpha(2+m)} \, d\tau = \frac{\beta^{2+m}}{2+m} \qquad (177)$$

so that, motivated by equations (175) and (177), the degree of damage accumulation may be introduced through the expression

$$\eta(t) = (2 + m) \int_0^{t} (t - \tau)^{1 + m} \frac{d\tau}{(t_o)^{2+m}} \qquad (178)$$

in which

$$\eta(o) = 0$$
$$\eta(1) = 1 \qquad (179)$$

The function $\eta(t)$ can be related to the damage function, ω, by

$$\eta = \frac{\displaystyle\int_o^\omega \frac{d\omega}{h(\omega)}}{\displaystyle\int_o^1 \frac{d\omega}{h(\omega)}} \tag{180}$$

This means that η represents the relative damage in the load history for the power-law representation of t^*_o. From equations (176) and (177), equation (178) may be written as:

$$\eta(t) = \frac{2 + m}{\rho^{2+m}} \int_o^t (t - \tau)^{1 + m} \, \sigma_o^{\alpha(2 + m)} \, d\tau \tag{181}$$

and finally, the influence of damage is treated as a reduced variable by introducing the modified time, t', defined by:

$$dt' = \frac{dt}{a_\eta \left| \eta(t) \right|} \tag{182}$$

on which equation (165) is based and where the shift function due to damage, a_η, depends on the material at hand.

4.6.2 Hufferd's Modification to Il'yushin Theory

One revised version of the Russian stress-strain law takes the form:

$$\sigma(t) = \int_o^t E\left(\frac{t - \tau}{a_\eta^*}\right) \frac{d\epsilon}{d\tau}(\tau) \, d\tau \tag{183}$$

220

where a_η^* is a damage-related shift function, assumed to depend only on the current state of strain; specifically:

$$a_\eta^* = a_\eta^* \left[\epsilon(t), \ \dot{\epsilon}(t) \right] \tag{184}$$

Clearly, if:

$$E(t) = E_e + E_2 t^{-n} \tag{185}$$

then equation (156) becomes:

$$\sigma(t) = E_e \ \epsilon(t) + (a_\eta^*)^n E_2 \int_0^t (t - \tau)^{-n} \frac{d\epsilon}{d\tau}(\tau) \ d\tau \tag{186}$$

which resembles the classical approach of the softening function used as a stress-correction factor.

Another revised version of the Russian approach consists of retaining most aspects of the original law, but constant strain-rate data are employed to express the time to failure as

$$t_o^* = \left(\frac{\beta}{\dot{\epsilon}} \right)^\alpha \tag{187}$$

and equation (178) is changed to

$$\eta(t) = \frac{(2 + m)}{\dot{\epsilon} t_o^*} \int_0^t (t - \tau)^{1+m} \phi(\tau) \ d\tau \tag{188}$$

221

where

$$\phi(t) = \epsilon(t) = \dot{\epsilon} t$$

and

$$\eta(t^*) = 1$$

Thus, evaluation of equation (188) at $t = t^*$ yields

$$\frac{(2 + m)}{\epsilon t_o^*} \int_0^{t^*} (t^* - \tau)^{1+m} \phi(\tau) d\tau = 1 \qquad (189)$$

which, through a change of variables and after some algebraic manipulations, may be integrated to

$$(190)$$

$$(t_o^*)^{2+m} = 3 + m$$

The solution for m, as a function of strain rate, is easy to obtain using equations (187) and (190) (as presented in Figure 124 for UTP-300).

In much the same way, integration of equation (188) for the relative damage function, $\eta(t)$, leads to

$$\eta(t) = \left(\frac{t}{t_o^*}\right)^{3 + m} \qquad (191)$$

222
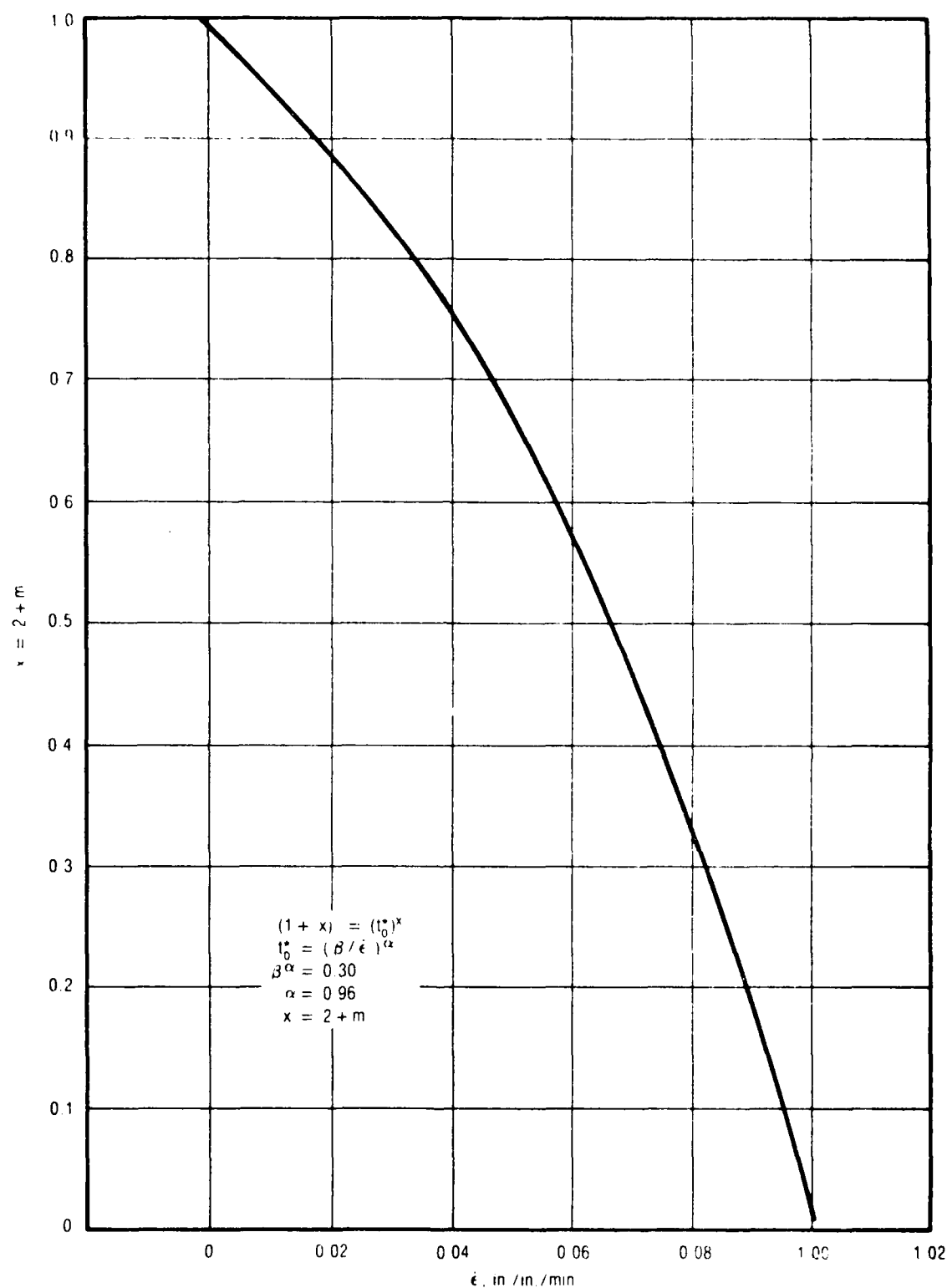
Figure 124. Solution for m as a Function of Strain Rate

28893

Hence, using constant strain-rate data to express the time to failure does simplify things, but a major assumption would still be needed regarding the form of the damage shift function as it was in the original set of equations. In this context, it is important to note that the linear expression

$$a_\eta = 1 - \eta \tag{192}$$

and the exponential form

$$a_\eta = e^{-\eta} \tag{193}$$

were used for the damage shift function without success. For this reason, the modified version used to run the stress predictions included in this report, corresponds to equation (186).

4.6.3 Stress Predictions

Figures 125 to 129 show the comparison between the observed response and that calculated using the present theory. As may be seen, the predicted response is quite accurate in all cases considered, which include constant- and dual-rate tests as well as a short-duration similitude loading.

4.6.4 Material Characterization

As may be gathered from equation (186), the simplest version of this theory requires the knowledge of only two material-property functions, to wit:

1. The relaxation modulus, and
2. The damage shift function:

$$(a_\eta^*) \overset{def}{=} \dot{a}_\eta = a_\eta \left| \epsilon(t), \dot{\epsilon}(t) \right| \tag{194}$$

which is determined in the following ways:
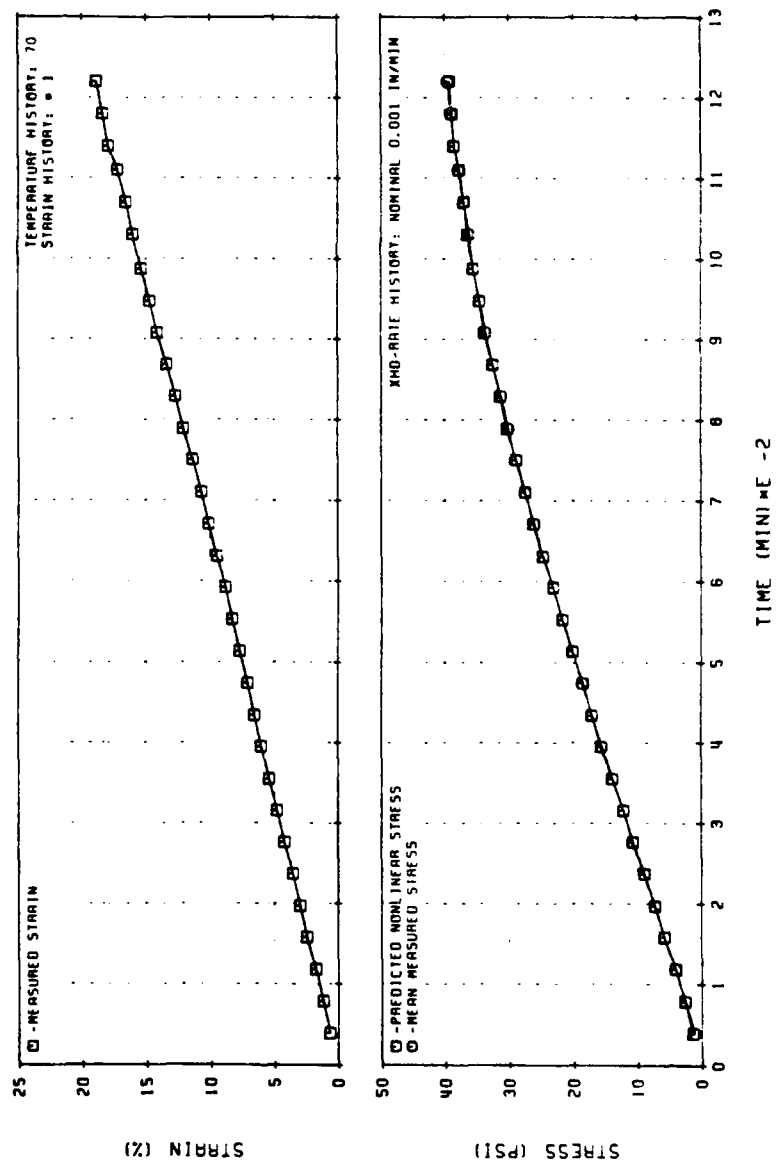
Figure 125. Nonlinear Viscoelastic Stress Predictions for UTP-19,360B-400/1777

31033
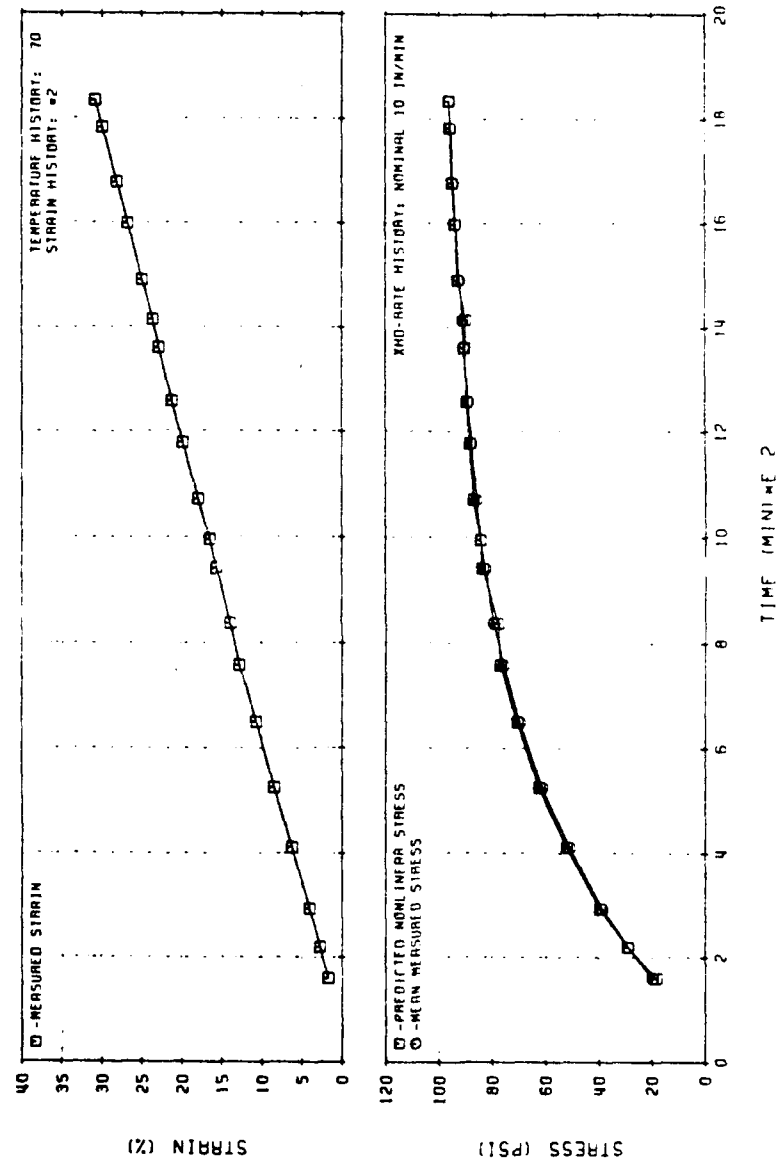
Figure 125. Nonlinear Viscoelastic Stress Predictions for UTP-19,360B-400/1777

31034

226
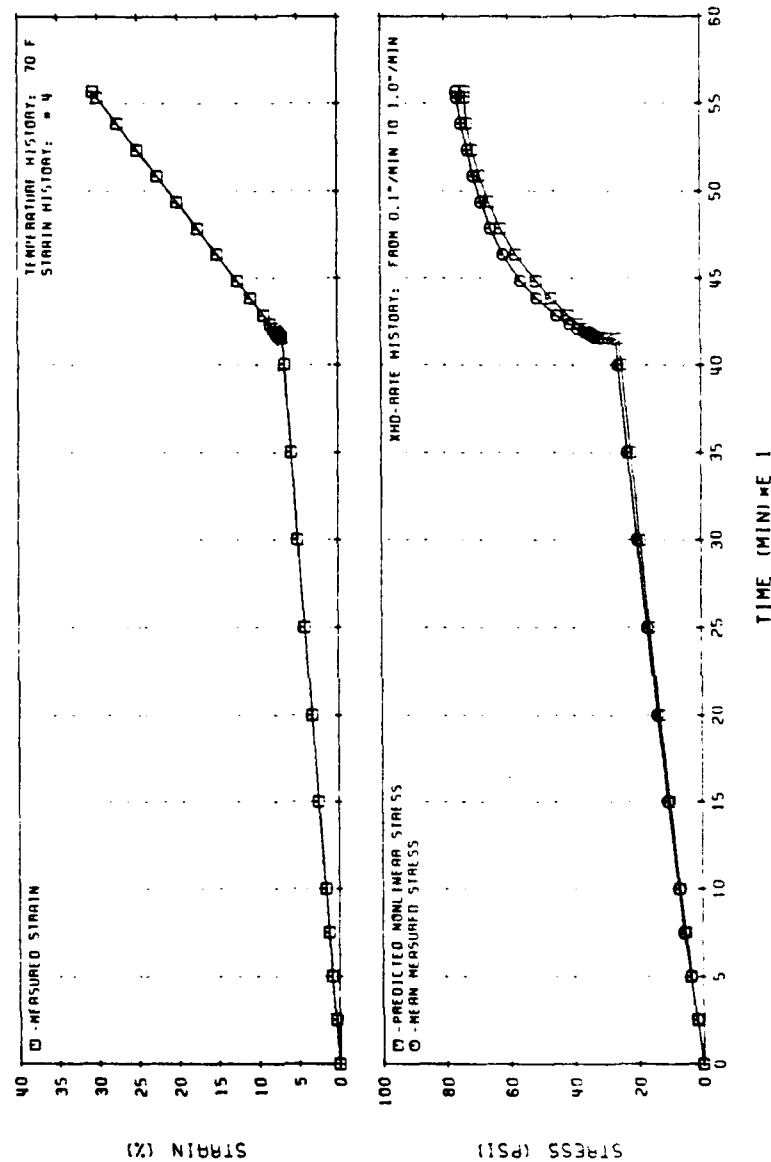
Figure 127. Nonlinear Viscoelastic Stress Predictions for Two-Rate Test (UTP-19,360B-400/1777)

31035

227
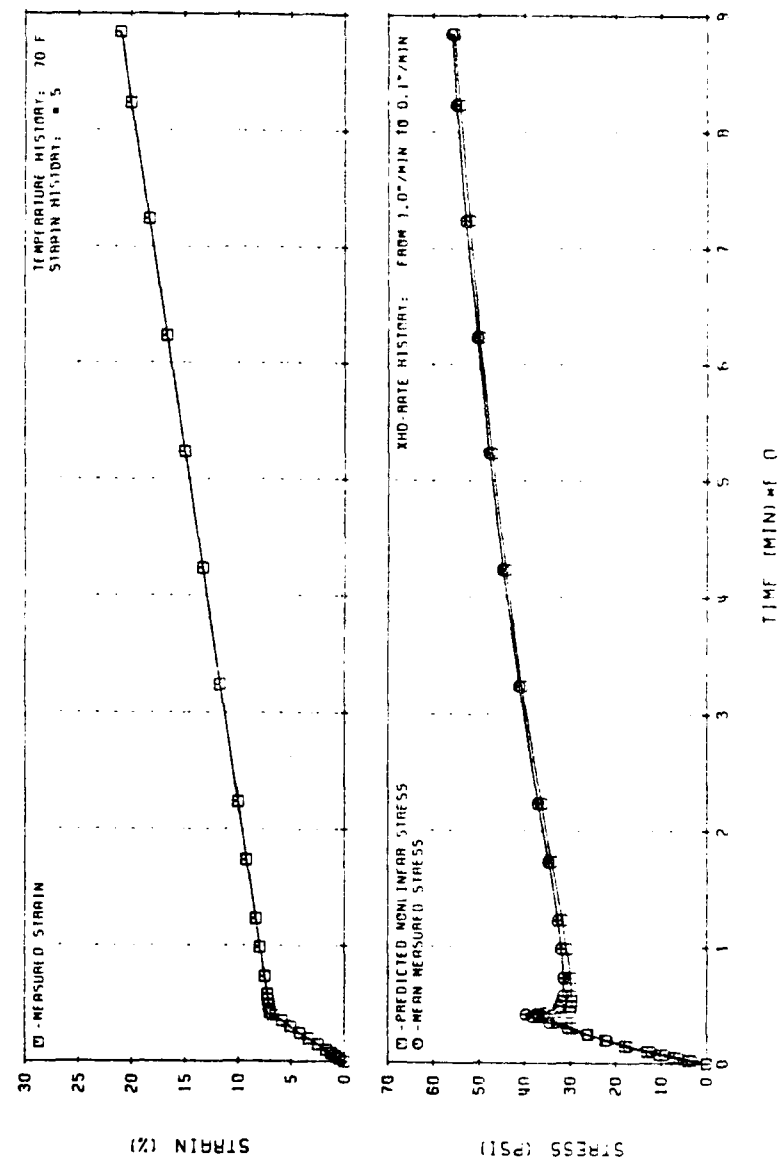
Figure 128. Nonlinear Viscoelastic Stress Predictions for Two-Rate Test (UTP-19,360B-400/1777)

31037

228
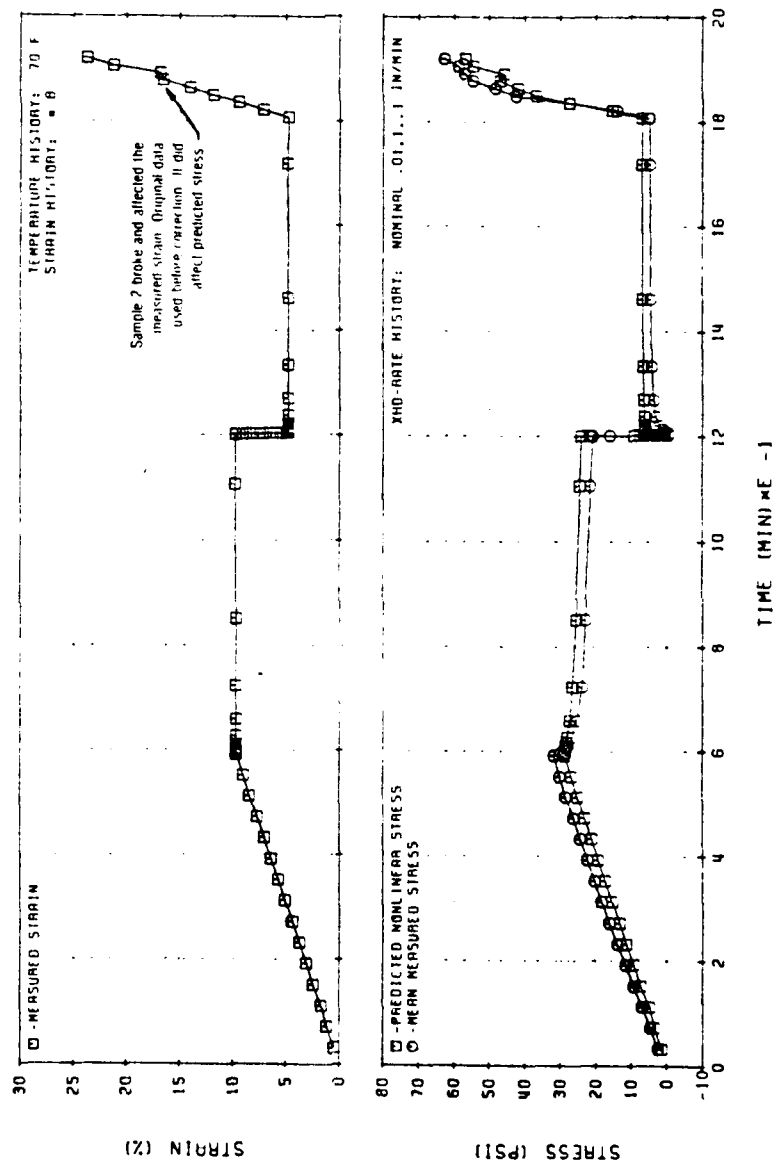
Figure 129. Nonlinear Viscoelastic Stress Predictions for Short Similitude Test (UTP-19,360B-400/1777)
(W. L. Hufferd's Theory)

a. From constant strain-rate tests, to correct the stress response during loading;

b. From a relaxation test at a large strain level, to account for healing; and

c. From a constant strain-rate cycle carried out to a large strain level, to more adequately reproduce the hysteretic behavior of the propellant.

The damage shift functions corresponding to UTP-19,360B are shown in Figures 130 to 134. The first three of these plots represent typical curves of a for low, intermediate and high strain-rate tests, while Figures 133 and 134 give the correction curves for relaxation and unloading, respectively.

4.6.5 Multiaxial Formulation

The previous forms of the constitutive equation were specialized from a three-dimensional theory. Returning now to this consideration and continuing to treat the influence of damage as a reduced variable by introducing the modified time t', where

$$dt' = \frac{dt}{a_\eta[\eta(t)]} \text{ and } t' = \int_o^t \frac{d\xi}{a_\eta[\eta(\xi)]}$$

(195)

The constitutive equations may then be written in the form

$$E(t) = I(t) \int_o^t J_1(t' - \tau', T) \frac{\partial}{\partial \tau} (\text{tr } S') \, d\tau \tag{196}$$

$$+ \int_o^t J_2(t' - \tau', T) \frac{\partial}{\partial \tau} S(\tau) \, d\tau$$

or

$$S(t) = I(t) \int_o^t E_1(t' - \tau', T) \frac{\partial}{\partial \tau} E(\tau) \, d\tau \tag{197}$$

$$+ \int_o^t E_2(t' - \tau', T) \frac{\partial}{\partial \tau} E(\tau) \, d\tau$$
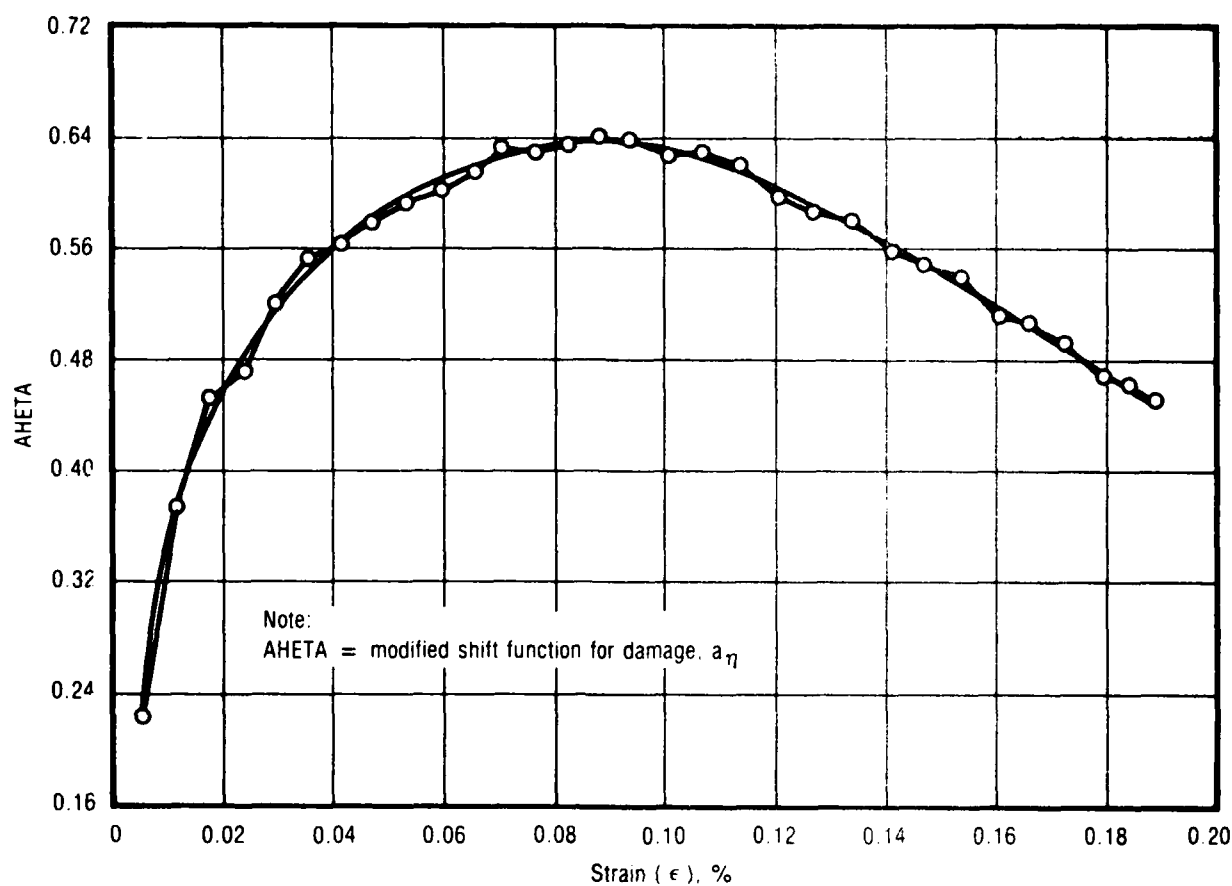
Figure 130. Constant-Rate Test (0.001 in./min)

30974

In equations (196) and (197), J_1 and E_1 are, respectively, the creep and relaxation functions in bulk and J_2 and E_2 the creep and relaxation functions in shear.

Assuming, for example, that a_η (η) has the exponential representation

$$a_\eta(\eta) = e^{-\alpha\eta} \tag{198}$$

then

$$t' = \frac{1}{\alpha_0} (e^{\alpha_0 t} - 1) \tag{199}$$

231
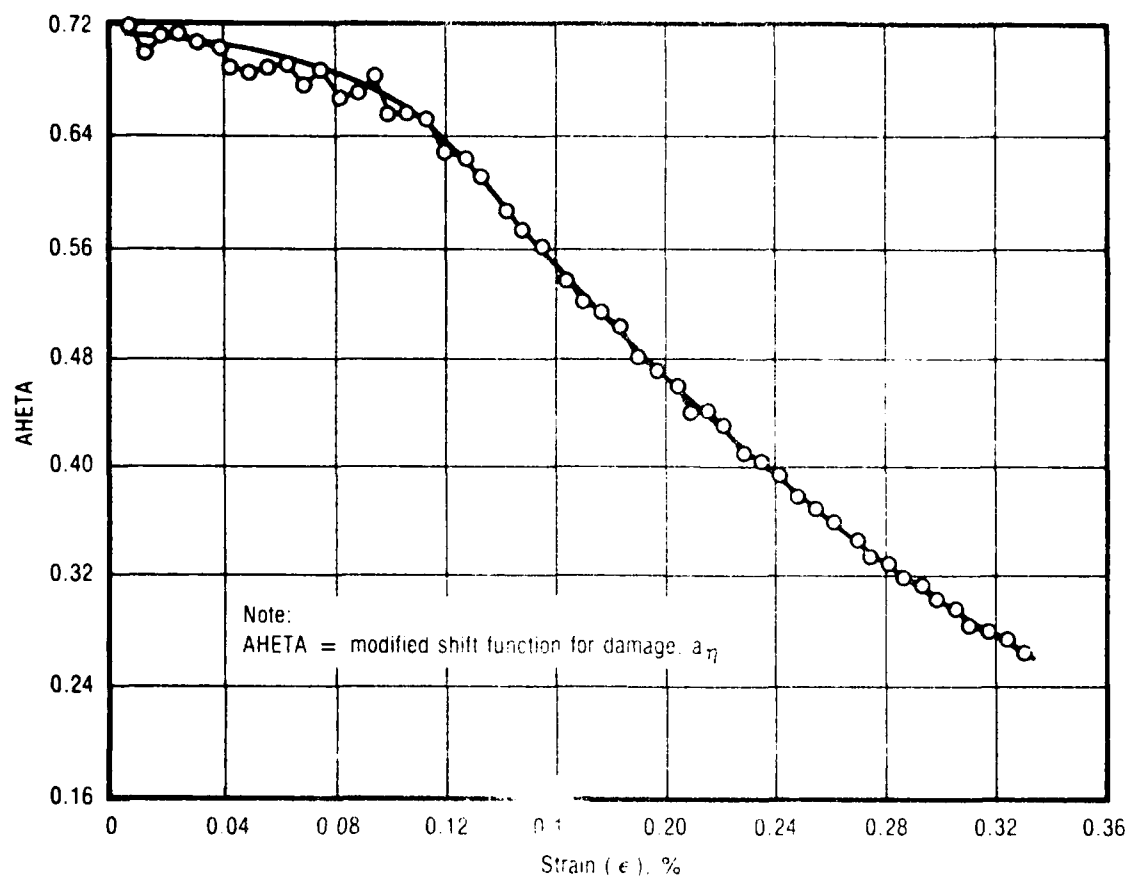
Figure 131. Constant-Rate Test (0.1 in./min)

where

$$\alpha_o = \frac{\alpha}{t_o(S^o)} \qquad (200)$$

If we make the further assumption that the bulk response is time independent and choose a power law representative for $J(t)$:

$$J(t) = A_o + B_o\, t^{\beta} \qquad (201)$$

equation (196) may be rewritten in the form

$$tr\, E(t) = J_1(T)\, tr\, S(t) \qquad (202)$$

236
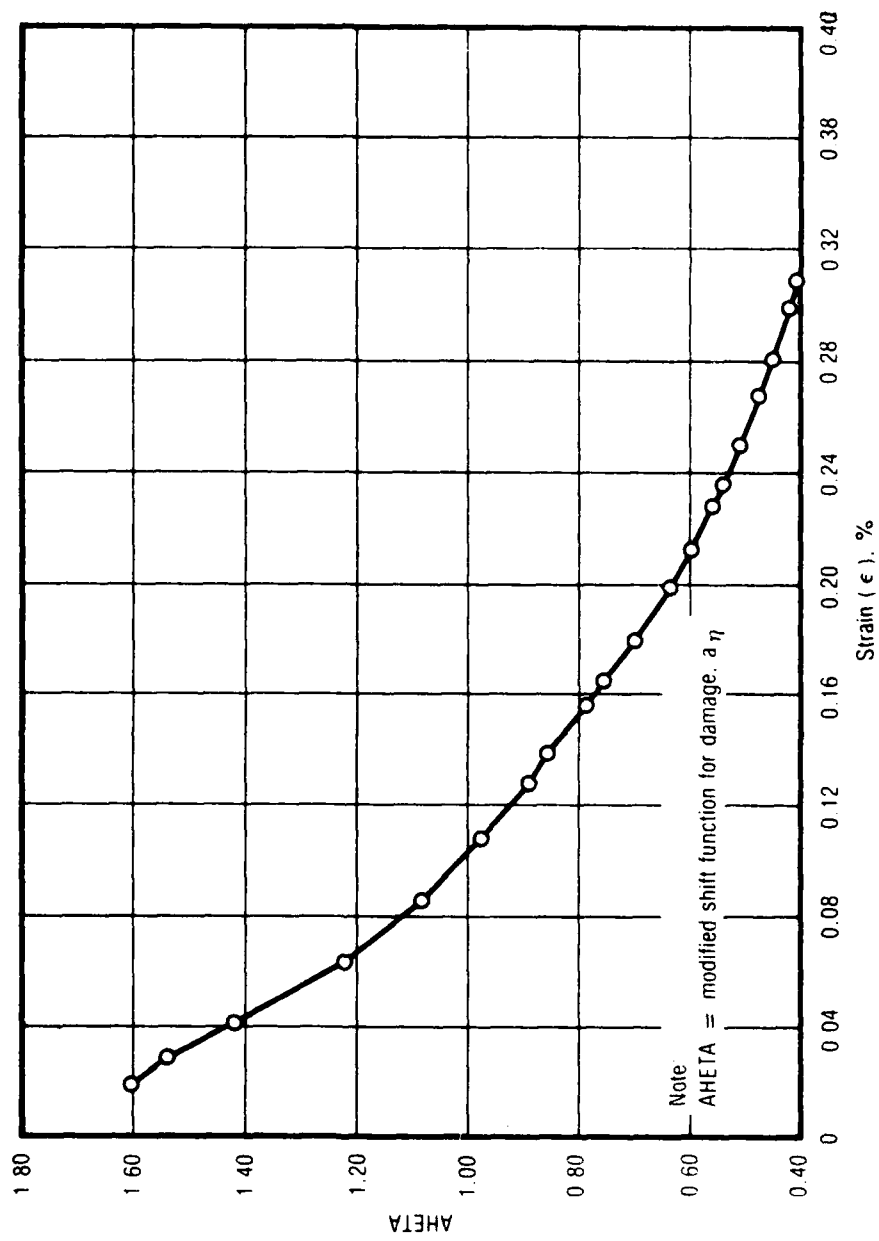
Figure 132. Constant-Rate Test (10 in./min)

30976

233
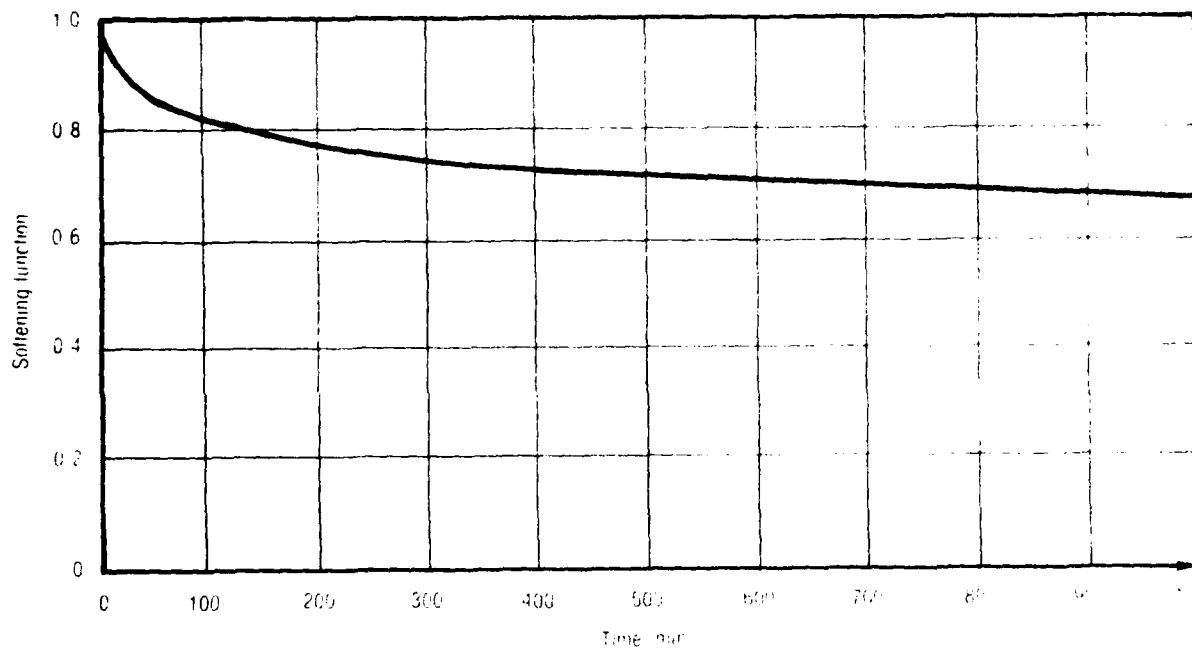
Figure 133. Softening Function During Relaxation

28894
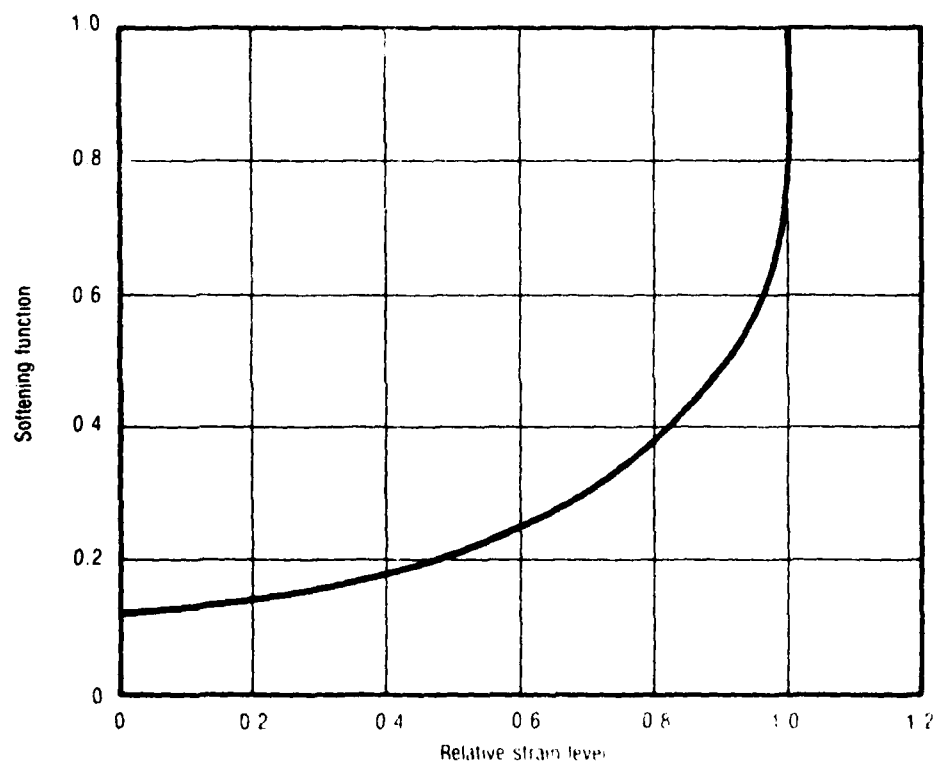
Figure 134. Softening Function During Unloading

28895

234

$$E_{ij}(t) = A_0 \, S_{ij}(t) + B_0 \int_0^t (t' - \tau')^\beta \frac{\partial}{\partial \tau} S_{ij}(\tau) \, d\tau \qquad (203)$$

To characterize the dependence on the magnitude of the previous loading, and to simplify the previous representations, stress and strain intensities defined by

$$S_e = \left({}^3/_2 \, S : S \right)^{1/2} \qquad\qquad (204)$$

$$E_e = \left({}^2/_3 \, E : E \right)^{1/2}$$

are introduced. Equation (196) may then be written in the form:

$$\varphi_1(E_e, \, trE) \, E_{ij} = f\,(S_e, \, trS) \, S_{ij}(t) \qquad (205)$$

$$+ \int_0^t T(t' - \tau') \, f_1(S_e, \, trS) \, S_{ij}(\tau) \, d\tau$$

and

$$\phi_2(trE, \, E_e) \, trE = f_2(S_e, \, trS) \, trS$$

$$\qquad\qquad\qquad\qquad (206)$$

$$+ \int_0^t U(t' - \tau') \, f_2(S_e, \, trS) \, trS(\tau) \, d\tau$$

Equations (205) and (206) now include coupling between deviatoric and dilatational behavior as well as time-dependent bulk response. Under certain conditions, it is possible to write equations (205) and (206) in the alternate form[5, 6]

$$f_1(S_e, \, trS) \, S_{ij} = \phi_1 \, (E_e, \, trE) \, E_{ij}$$

$$- \int_0^t R(t' - \tau') \, \phi_1 \left[E_e, \, trE \right] E_{ij}(\tau) \, d\tau \qquad (207)$$

and

$$f_2(S_e, trS) trS = \phi_2(E_e, trE) trE$$

$$- \int_0^t V(t' - \tau') \phi_2(E_e, trE) trE(\tau) d\tau \qquad (208)$$

The functions f_1, f_2, ϕ_1, and ϕ_2 may be represented by a Prony exponential series or the simple power law forms:

$$f_1(S_e, trS) = \sum_i A_i S_e^{\alpha - i} (trS)^i \quad (i = 0, 1, \ldots, m)$$

$$\phi_1(E_e, trE) = \sum_i B_i E_e^{\beta - i} (trE)^i \quad (i = 0, 1, \ldots, n)$$

$$f(S_e, trS) = \sum_i C_i (trS)^{\gamma - i} S_e^i \quad (i = 0, 1, \ldots, p)$$

$$\phi_2(E_e, trE) = \sum_i D_i (\ldots)^{\delta - i} E_e^i \quad (i = 0, 1, \ldots, q)$$

where A_i, B_i, C_i and D_i are constants and α, β, γ and δ are integers. Practically speaking, the first two or three terms should be sufficient to adequately characterize the damage response.

4.6.5.1 Evaluation of Damage Functions from Experimental Behavior

Characterization procedures for evaluating the damage functions described in the previous sections are discussed in the following paragraphs.

The simplest experiment is creep in pure shear. In this case there is only one non-zero component of stress (e.g. S_{12}) and one non-zero component of strain (E_{12}). The appropriate measures of stress and strain intensity from equation (204) are

236

$$S_e = \sqrt{3}\, S_{12}$$

and

$$E_e = \frac{2\, E_{12}}{\sqrt{3}} \tag{210}$$

Since $\text{tr}\, E = \text{tr}\, S = 0$, equation (206) is satisfied identically and only the non-vanishing equations of (208) by means of equation (209) has the form

$$B_0 \left(\frac{2\, E_{12}(t)}{\sqrt{3}} \right)^{\beta} E_{12}(t) = A_0 \left(\sqrt{3}\, S_{12} \right)^{\alpha} S_{12}\, \phi(t) \tag{211}$$

where

$$\phi(t) = 1 + \int_0^t T(t' - \tau')\, d\tau \tag{212}$$

If we normalize the response to the jth test, it follows that

$$\frac{E_{12}(t)}{\overset{(j)}{E_{12}}(t)} = \left(\frac{S_{12}}{\overset{(j)}{S_{12}}} \right)^{\frac{1+\alpha}{1+\beta}} \tag{213}$$

$$\phi(t)^{\frac{1}{1+\beta}} = \frac{2\, E_{12}^{(j)}(t)\, C^{\frac{1}{1+\beta}}}{\left(S_{12}^{(j)} \right)^{\frac{1+\alpha}{1+\beta}}} \tag{214}$$

and

$$C = 1/2\, \frac{B_0}{A_0}\, \frac{1}{3^{\frac{\alpha+\beta}{2}}} \tag{215}$$

237

The value of the ratio $(1 + \alpha)/(1 + \beta)$ can be determined from a cross plot of log creep strain versus log stress.

Consider next a constant strain rate test conducted under superimposed hydrostatic pressure. In this case,

$$S_{11} = S_o - P$$

$$S_{22} = S_{33} = -P$$

$$E_{11} = E_o - \frac{\text{tr } E}{3}$$

$$E_{22} = E_{33} = +\Delta v_p - \sqrt{E_o}$$

$$S_e = S_o$$

$$E_e = \frac{2}{3}(1 + \nu) E_o$$

$$\text{tr } S = -p + \frac{S_o}{3}$$

$$\text{tr } E = \Delta v_r + (1 - 2\nu) E_o$$

Here, E_o is the applied axial strain and S_o is the resultant stress; Δv_p is the (negative) volume change associated with applied pressure in the absence of applied deformations. Assuming elastic volumetric response and a constant strain rate test, $E_o = \dot{E}_o t$, it follows that

$$S_o^{(1 + \nu)}(E_o) \sum_k A_k \left(\frac{1}{3} - \frac{P}{S_o}\right)^k$$

$$= (1 + \nu) E_o^{1+\beta} \sum_k \left[\frac{2}{3}(1 + \nu)\right]^{\beta - k} \left(1 - 2\nu + \frac{\Delta v_p}{E_o}\right)^k$$

$$- (1 + \nu) \dot{E}_o^{1 + \beta} \sum_k B_k \left[\frac{2}{3}(1 + \nu)\right]^{\beta - k} \left\{ \int_o^t R(t' - \tau') \right.$$

$$\left. \times \left(1 - 2\nu + \frac{\Delta v_p}{\tau \dot{E}_o}\right)^k \tau^{1 + \beta} d\tau \right\}^\pi$$

(216)

238

The function S_0 is determined experimentally for various strain rates and pressures. The functions $R(t)$ may be determined from simple relaxation tests.

Equation (216) then represents a system of linear equations for determining the coefficients A_k and B_k.

More generally, it is possible to evaluate the functions f_1 and ϕ_1 in equation (207) from other tests, assuming time-independent bulk response. If we let $S = \text{tr } S$ and $E = \text{tr } E$, a suitable representation may be taken in the form of the exponential

$$f_1(S_e, \bar{S}) = A \, S_e^\alpha \, e^{k_1 \bar{S}} \tag{217}$$

$$\phi_1(E_e, \bar{E}) = B \, E_e^\beta \, e^{k_2 \bar{E}} \tag{218}$$

$$\bar{S} = K(E_e) \, \bar{E} = \frac{k_0}{1 + \gamma E_e} \, \bar{E} \tag{219}$$

where a, B, ..., k_0, k_1 and k_2 are determined experimentally. For example, assuming linear behavior at sufficiently small strains, then $B/A = 2G$ (i.e., twice the instantaneous shear modulus). The functions $R(t)$ and $V(t)$ represent the creep and relaxation functions in shear.

For a creep test under constant stress S_0, then equation (207) gives

$$3G\left[\frac{2}{3}(1+\nu)\right]^{1+\beta} E_0(t)^{1+\beta} \, e^{k_2 E_0 (t)(1-2\nu)} = S_0^{1+\alpha} \, e^{k_1 S_0/3} \phi(t) \tag{220}$$

when $\nu = $ constant, and for two arbitrary stresses S_0 and S_0^1,

$$\left(\frac{E_0(t)}{E_0^1(t)}\right)^{1+\beta} e^{k_2(1-2\nu)(E_0(t) - E_0^1(t))} = \left(\frac{S_0}{S_0^1}\right)^{1+\alpha} e^{(k_1/3)(S_0 - S_0^1)} \tag{221}$$

239

or

$$\log_e \frac{E_o(t)}{E_o^1(t)} + \frac{k_2}{1+\beta} (1 - 2\nu) (E_o(t) - E_o^1(t)) \qquad (222)$$

$$= \left(\frac{1+\alpha}{1+\beta}\right) \log_e \left(\frac{S_o}{S_o^1}\right) + \frac{k_1 \left(S_o - S_o^1\right)}{3(1+\beta)}$$

Now, as noted previously, the ratio $(1+\alpha)/(1+\beta)$ may be determined from tests in pure shear. Then, from equation (120), $k_2(1 + 2\tau)/(1+\beta)$ and $k_1/(1+\beta)$ may be determined from a log-log plot of $E_o(t)/E_o(t)$ versus S_o/S_o^1 for several values of creep stress and strain. Finally, the function $\phi(t)$ may be evaluated from equation (221).

The constants k_o and γ should be determined from pressurized tests for various effective strain levels, E_e.

4.6.6 Non-Isothermal Characterization

For the situation of transient temperature loadings, e.g., simultaneous cooling and straining, the uniaxial constitutive equation was written

$$\sigma(t) = \int_0^t E(\xi - \xi') \frac{\partial[\epsilon(\tau) - \alpha\Delta T(\tau)]}{\partial\tau} \, d\tau \qquad (223)$$

with

$$\xi - \xi' = \int_\tau^t \frac{d\,u}{A_\eta[\eta(u)]\, A_T[T(u)]\, A_F[T(u), \epsilon(u), \dot{\epsilon}(u)]} \qquad (224)$$

The "damage" shift function was determined from uniaxial tests, and A_T was determined from uniaxial tests at different temperatures. The possibility of the requirement of a thermomechanical coupling coefficient is permitted through the shift function, A_f. In practice, A_f and A_η can be determined as a single coefficient from simultaneous cooling and straining tests.

A determination of A_f was not made, since the computer code used to make predictions was not modified to preform the integration of equation (223) for transient temperature loadings.

240

4.7 THE SWANSON NONLINEAR CONSTITUTIVE LAW

4.7.1 Original Model

The framework for this theory was established by taking into account some typical behavior aspects of high-elongation propellants. The principal features considered were: (1) the usual viscoelastic dependence of the response on the strain rate, (2) the ability of the solid propellant to sustain large strains, (3) the marked deviation of the solid-propellant response from that associated with Linear Viscoelasticity, as evidenced by the large hysteresis exhibited under cyclic loading of many solid propellants, even at small strains, and (4) the dependence of the stress-strain response on superimposed pressure.

Although it is not essential to have done it this way, the capability of handling large strains was incorporated into the constitutive equations by using the cauchy-stress tensor (σ) as a measure of the state of stress at a point. Its conjugate, the left Cauchy-Green deformation tensor (B) was used as the measure of straining. The Cauchy stresses, defined in terms of force per unit deformed area, are also called "true" stresses. In a principal coordinate system B takes on the diagonal form:

$$B = \begin{bmatrix} \lambda_1^2 & 0 & 0 \\ 0 & \lambda_2^2 & 0 \\ 0 & 0 & \lambda_3^2 \end{bmatrix} \tag{225}$$

in which the λ_i's are simply the extension ratios in the principal directions.

The remaining aspects of the observed response of solid propellant were modeled through the use of a softening function as a stress correction factor. The major constitutive assumption in this theory relates the invariants of the deviatoric stress and deformation tensors through the form:

$$\sqrt{II_{\sigma'}} = (f)(g) \tag{226}$$

This separable form has been used previously[11,29] and is motivated by the fact that the constant strain rate tensile curves are roughly similar.

In equation (224), f is the following viscoelastic function:

$$f = \int_0^t G(t - \tau) \frac{d\sqrt{II_B'}}{d\tau} d\tau \qquad (227)$$

with G being the relaxation modulus in shear, taken in this theory as one third the tensile relaxation modulus, and

g = softening function

$\sigma_{ij}' = \sigma_{ij}' - (\sigma_{kk}/3) \delta_{ij}$ = deviatoric stress tensor

$B_{ij}' = B_{ij} - (B_{kk}/3)\delta_{ij}$ = deviatoric deformation tensor $\qquad$ (228)

$$II_\alpha \equiv \left| -\left[\alpha_{11} \alpha_{22} + \alpha_{22} \alpha_{33} + \alpha_{33} \alpha_{11}\right] + \alpha_{12}^2 + \alpha_{23}^2 + \alpha_{31}^2 \right|^{1/2}$$

Second invariant of tensor $\alpha = \sigma,\ B$

Now, g is a function of deformation and pressure (mean stress) and can be considered to be primarily a strain-softening function. It is defined as that function of the invariant $\sqrt{II_B'}$ that will force the viscoelastic Cauchy stress to coincide with the experimental results; thus, unloading hystersis as well as the effects of pressure may be readily incorporated into this theory, simply by obtaining the corresponding forms of the softening function under such conditions.

The softening function corresponding to virgin loading is obtained by fitting the model to uniaxial tensile tests at constant crosshead speed. Under these conditions, the deviatoric stress invariant reduces to

$$\sqrt{II_{\sigma'}} = \frac{\sigma_{11}}{\sqrt{3}} \qquad (229)$$

where, again σ_{11} is Cauchy stress.

Assuming incompressibility

$$\lambda_1 \lambda_2 \lambda_3 = 1 \qquad (230)$$

and noting that

$$\lambda_2 = \lambda_3 \qquad (231)$$

the deformation invariant becomes

$$\sqrt{II_{B'}} = \frac{1}{\sqrt{3}}\left(\lambda_1^2 - \frac{1}{\lambda_1}\right) \qquad (232)$$

Taking the rate of change of the invariant as being approximately constant results in

$$f = \sqrt{3}\,\dot{\lambda} \int_0^t G(t - \tau)\,d\tau \qquad (233)$$

so that, from equations (227), (230), and (232) the following is obtained:

$$\frac{\sigma_{11}}{\sqrt{3}} = g\,\sqrt{3}\,\dot{\lambda} \int_0^t G(t - \tau)\,d\tau \qquad (234)$$

from which the softening function, g, may be obtained. The assumption leading to equation (232), that the time-rate of change of $\sqrt{II_B{'}}$ is approximately constant, need be guarded against conditions of changing strain rate. For example, as in dual-rate tests, where viscoelasticity does not predict as fast a response to the rate change as is experimentally observed.

The modification to linear viscoelasticity necessary to accommodate this behavior is as follows. The response of the function f in equation (235) to a constant time rate of change of the deformation invariant is defined as f_c. It can be expressed as

$$f_c = \dot{\overline{\sqrt{II_B{'}}}} \int_0^\xi G_{rel}(\xi - \tau) \, d\tau$$

$$\text{where } \xi = \sqrt{II_B{'}} / \sqrt{\dot{II_B}}$$

(235)

The modification to the f function is done in an incremental manner through

$$\dot{f}_{modified} = \dot{f} + \beta \left[f_c - f \right] \sqrt{\dot{II_B{'}}}$$

(236)

and the following incremental relationship is used:

$$f \bigg|_{t + dt} = f \bigg|_t + \frac{df_{mod}}{dt} dt$$

(237)

The parameter β governs the response of the f function under changing strain rates. As $\beta > 0$, the response is analogous to linear viscoelasticity.

The algorithm developed by Herrman and Peterson[30] has been used to implement the calculation of the convolution integral for f. In brief, let the shear relaxation modulus be represented by a Prony series as

$$G(t) = \sum_{i=1}^{m} G_i e^{-\alpha_i t} \qquad (238)$$

The let the f function at time t_n be given by:

$$f(t_n) = \int_{0}^{t_n} \sum_{i} G_i e^{-\alpha_i (t_n - \tau)} \, \partial \sqrt{\frac{II_{B'}}{\partial \tau}} \, d\tau \qquad (239)$$

A recursion relation can be easily developed to compute $f(t_n)$[30]. Let

$$f(t_n) = \sum_{i=1}^{m} I_{n,i} \qquad (240)$$

and

$$I_{n,i} \equiv \int_{0}^{t_n} G_i e^{-\alpha_i(t_n - \tau)} \, \partial \sqrt{\frac{II_{B'}}{\partial \tau}} \, d\tau \qquad (241)$$

then

$$I_{n,i} = e^{-\alpha_i \Delta t_n} \, I_{n-1,i} + \sqrt{II_{\dot{B}_n'}} \, \frac{G_i}{\alpha_i} \left[1 - e^{-\alpha_i \Delta t_n} \right] \qquad (242)$$

giving for the change in these terms:

$$\Delta I_{n,i} = \sqrt{II_{\dot{B}_n'}} \left\{ \frac{G_i}{\alpha_i} \left[1 - e^{-\alpha_i \Delta t_n} \right] + I_{n-1,i} + \left[e^{-\alpha_i t_n} - 1 \right] \right\} \qquad (243)$$

which is directly analogous to linear viscoelasticity. The modification proposed above can then be implemented as

$$(\Delta I_{n,i})_{modified} = \Delta I_{n,i} + \beta \left[I_{cn,i} - I_{n,i} \right] \Delta \sqrt{II_B'} \qquad (244)$$

and the I terms can be incremented according to

$$I_{n,i} = I_{n-1,i} + (\Delta I_{n,i})_{modified} \qquad (245)$$

This has the effect of changing each term of the series so that it approaches the value it would have been if it was always at the new strain rate. Note again that (as discussed in Reference 30) varying temperatures can be incorporated into the time scale as usual.

Unloading tests required a further refinement of the model. For lack of more detailed information, the parameter β may be taken as zero for unloading states (i.e., states in which $\sqrt{II_B'}$ is decreasing). The large amount of hysteresis seen in load-unload cycles is then modeled in part by the hysteresis inherent within linear viscoelasticity primarily through the g function. This is accomplished by giving g a different value when the deformation invariant $\sqrt{II_B'}$ is less than its maximum previously achieved during the loading history. If $\sqrt{II_B'}_{max}$ is the current maximum value, the function

$$g = g(\sqrt{II\,B'_{max}}) \left\{ 1 - C_1 \left[1 - \sqrt{II\,B'} / \sqrt{II_{B'_{max}}} \right] \right\} \qquad (246)$$

provides plasticity-like behavior.

The behavior of the g function for unloading and reloading conditions is illustrated in Figure 135 (taken from Reference 9).

The Swanson approach[9] was used with an only limited degree of success to predict the stress response of TP-H1011 and UTP-19,360B under several strain histories.

246
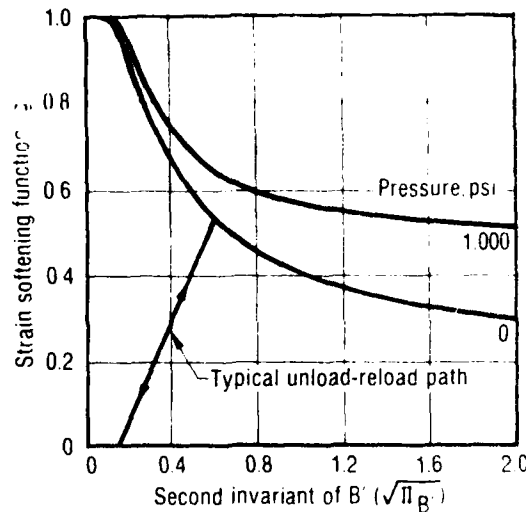
Figure 135. Effect of Deformation and Pressure on the Strain
Softening Function

22059

In the case of TP-H1011, the errors in the predictions were believed to be
due to uncertainties in the value of the changing-rate coefficient (β). There
was no data available to determined β directly for this propellant.

It was possible to characterize UTP-19,360B in a complete fashion. The
corresponding predictions were not any better than those obtained for TP-H1011.
This led to changing the law as discussed below.

4.7.2 Current Model

Analysis of the stress predictions, carried out for UTP-19,360B with the
original Swanson theory, revealed the importance of several inadequacies and
oversimplifications listed below.

1. The softening function (g) should depend not only on the strain and
    pressure but also on the strain rate.
2. The softening function, as defined by equations (227) and (235), should
    be different for unloading than for reloading.
3. The softening function for unloading or for reloading should never
    become zero for conditions of tensile straining only. A zero value
    could occur with the softening function defined by equation (246).

247

4. The healing process observed during relaxation in solid propellants like UTP-19,360B was not taken into consideration by the original Swanson theory.

5. The reverse-recovery observed in solid propellants during relaxation or rest periods that follow an unloading process, only poorly modeled by classical viscoelasticity, is not considered in the approach by Swanson.

6. The changing-rate coefficient (β) is more a mathematical device than it is a material property. If the softening function is made to depend on the strain rate then β need not be used.

7. The use of a softening function as a stress correction factor eliminates the need of using the Cauchy stress (σ) and the nonlinear measure of stretching (B).

All these observations were incorporated into the original stress-strain law but the general form of the corresponding equations remained the same, namely

$$\sigma_{11} = \sqrt{3}\,(g) \int_{0}^{t} \ddot{u}\,(s_t - s_\tau)\,\partial\sqrt{II_{B'}}\,\,\frac{}{\partial\tau}\,d\tau \tag{247}$$

valid for one-dimensional loading, with:

$$s_t - s_\tau = \int_{\tau}^{t} \frac{d\xi}{A_T\left|\tau(\xi)\right|} \tag{248}$$

representing temperature-reduced time; and where the time-temperature shift function was taken in the power-law form

$$A_T = \left(\frac{T_R - T_a}{T - T_a}\right)^m \tag{249}$$

248

in which T_R is the shift reference temperature, T_a and m are material parameters, and T is the current temperature.

The modified version of the Swanson theory was most successfully used to predict the response of UTP-19,360B, as explained next.

4.7.3 Stress Predictions

The degree of accuracy of the predictions made with the current version of the Swanson approach may be realized by examining Figures 136 through 148. The first two figures correspond to the lowest and highest constant-rate tests available. Figures 138 and 139 present the results for the dual-rate tests while Figure 140 pertains to the saw-tooth test at constant rate and increasing peak strains. Figures 141 to 145 show the predictions corresponding to complex multiple loading, twenty-four hour relaxation, long-duration similitude, three-step relaxation, and predamage relaxation. Finally, figures 146 to 148 show the results obtained for comparable constant rate tests at 70 F, 123 F, and 40 F.

They testify to the fact that the time-temperature superimposition principal may be used without sacrificing more accuracy than is already lost in fitting equation (185) to the very limited time-temperature shift data.

4.7.4 Material Characterization

According to this theory, only the following listed properties are needed to characterize a solid propellant completely:

1. The relaxation function, G, as defined:

$$G(t) = \frac{E_{rel}(t)}{3} \qquad (250)$$

where $E_{rel}(t)$ is the linear viscoelastic relaxation modulus.
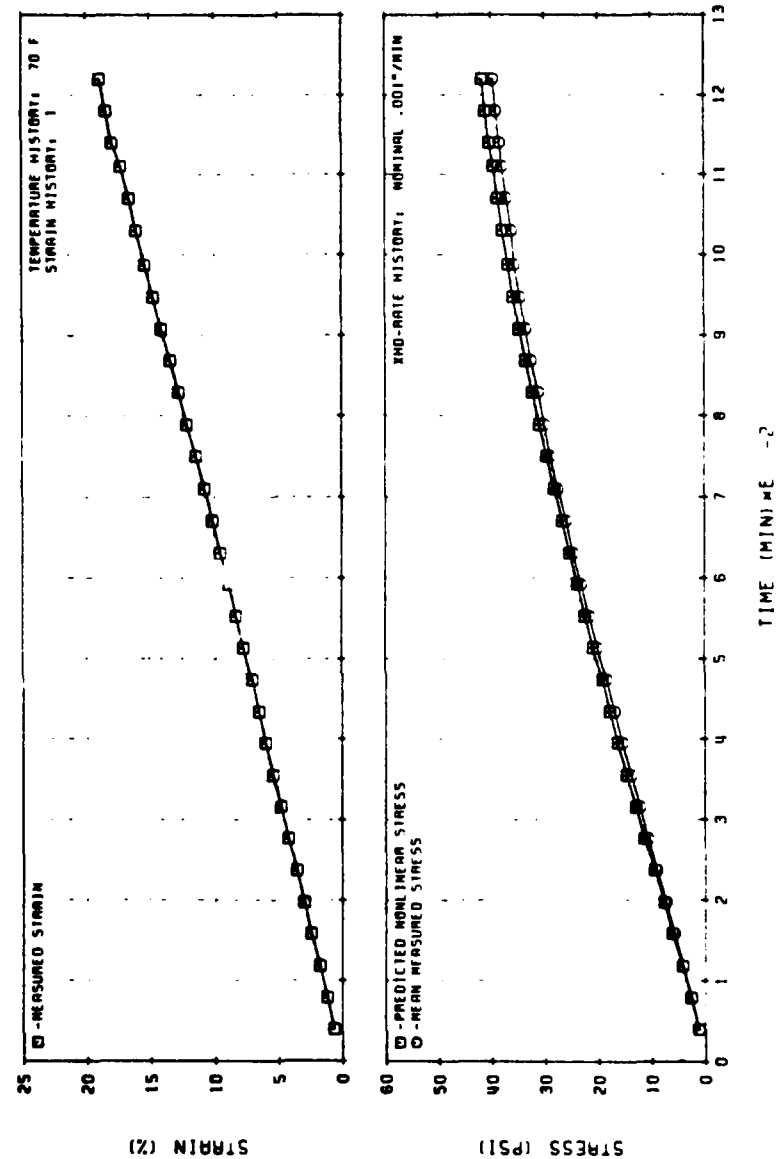
Figure 136. Nonlinear Viscoelastic Stress Predictions for Constant-Rate Test (UTP-19,360B-400/1777)

250
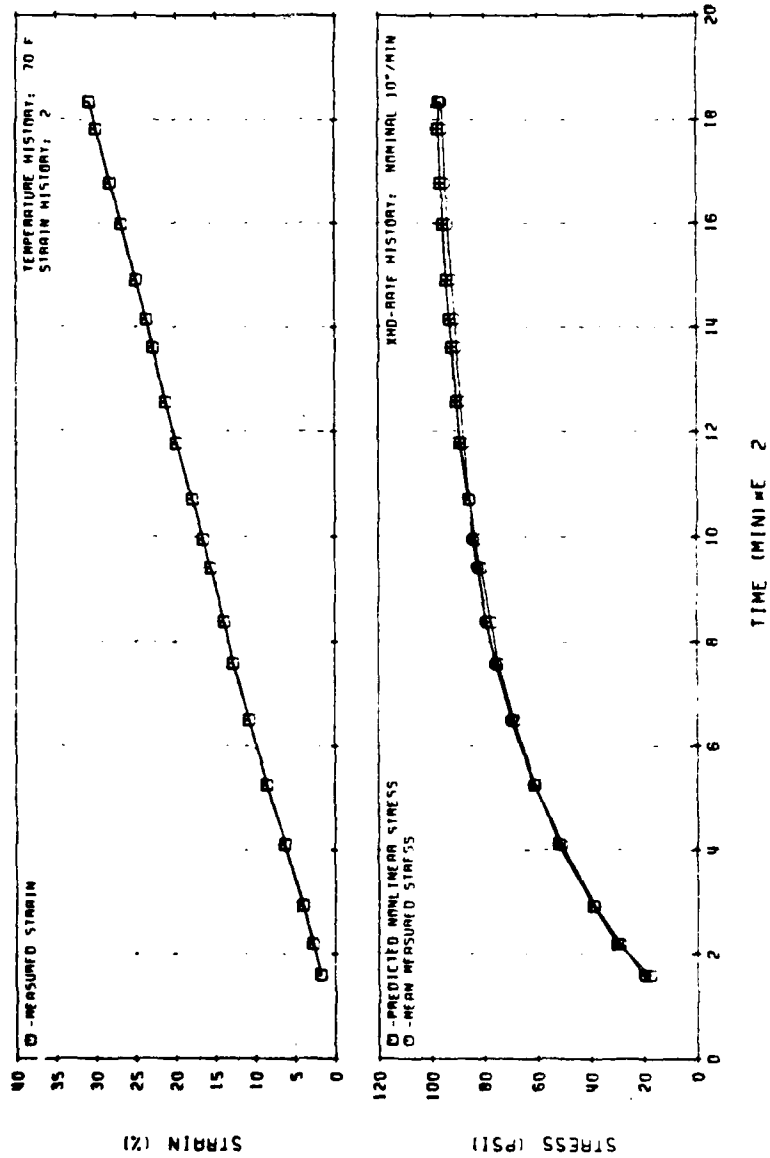
Figure 137. Nonlinear Viscoelastic Stress Predictions for Contstant-Rate Test
(UTP-19,360B-400/1777)
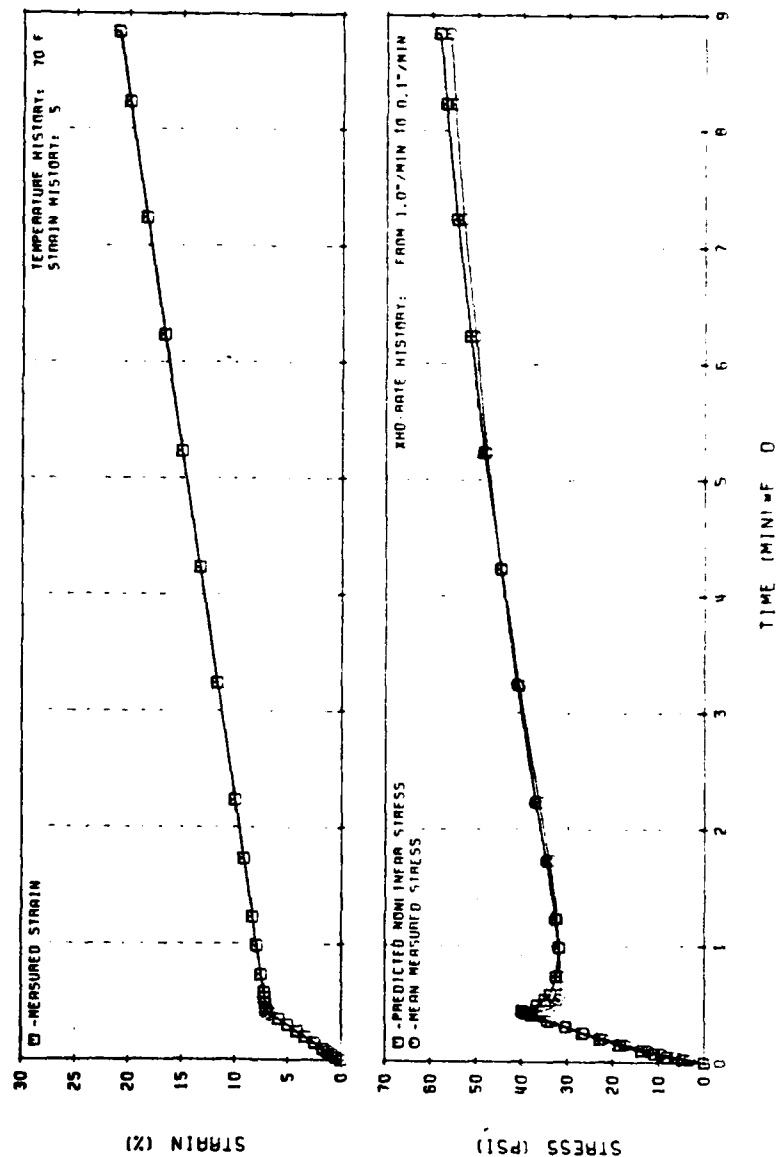
Figure 138. Nonlinear Viscoelastic Stress Predictions for Two-Rate Test (UTP-19,360B-400/1777)

252
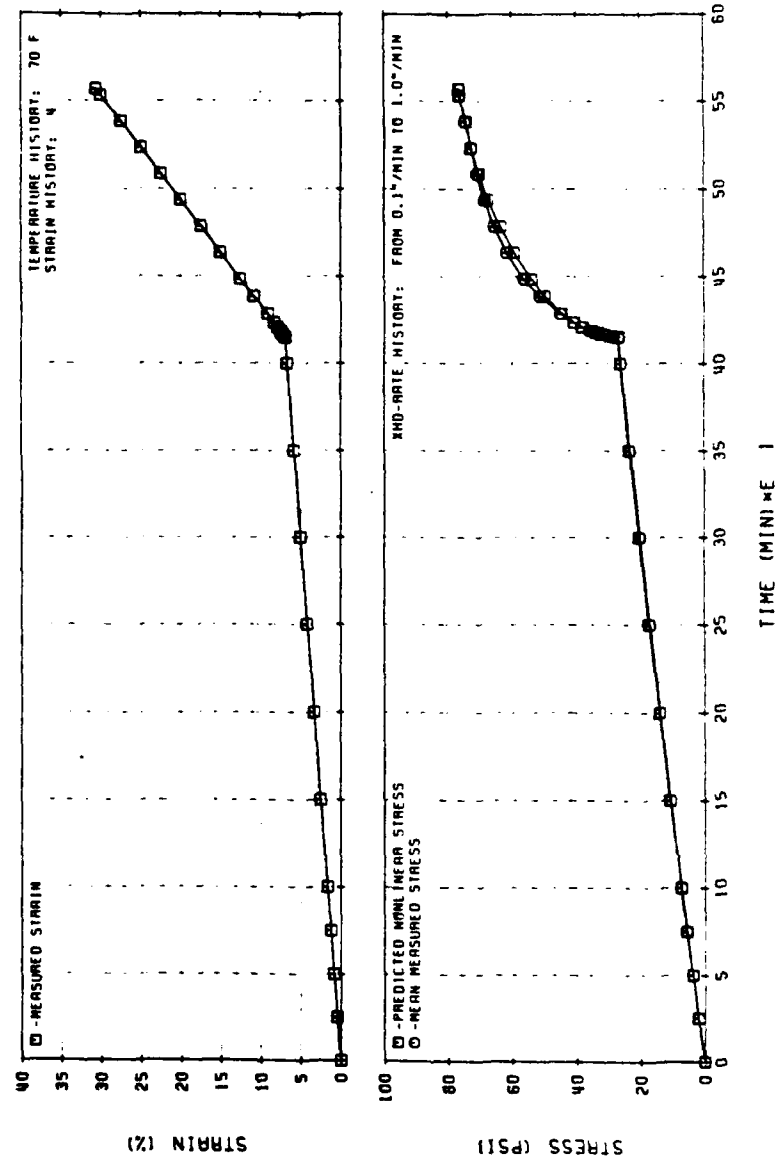
Figure 139. Nonlinear Viscoelastic Stress Predictions for Two-Rate Test (UTP-19,360B-400/1777)

253
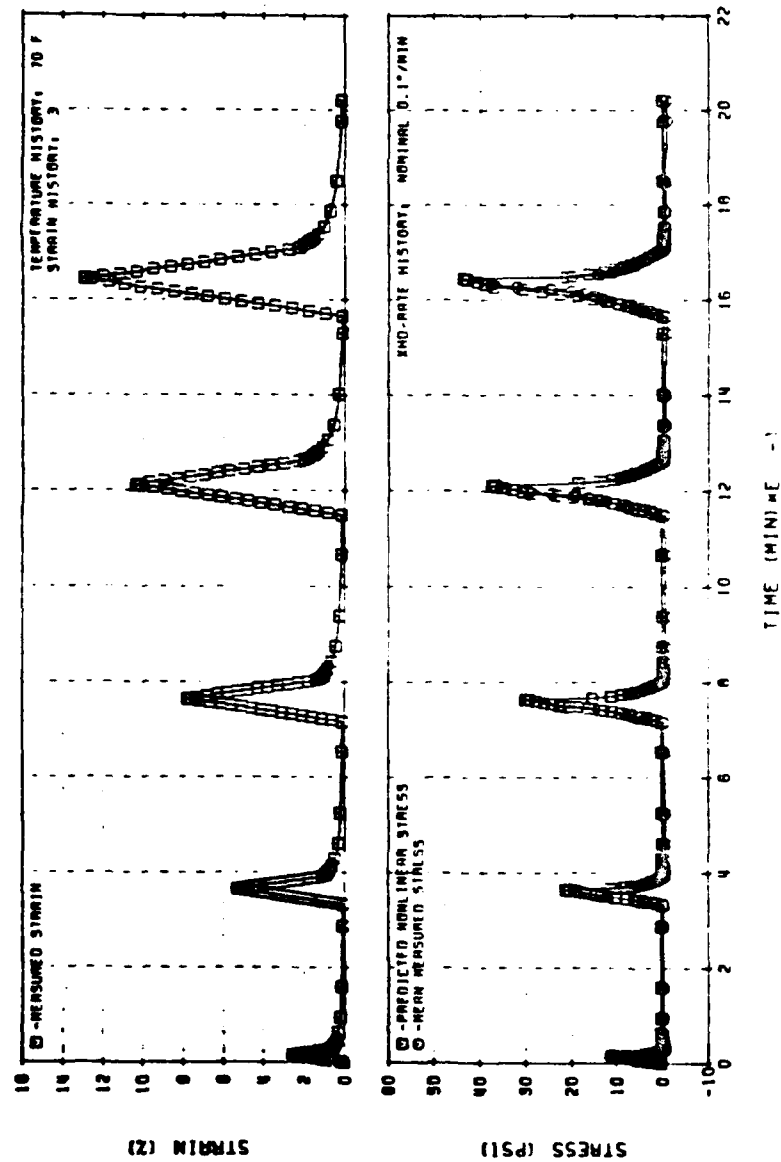
Figure 140. Nonlinear Viscoelastic Stress Prediction for the Saw-Tooth Test
(UTP-19,360B-400/1777)
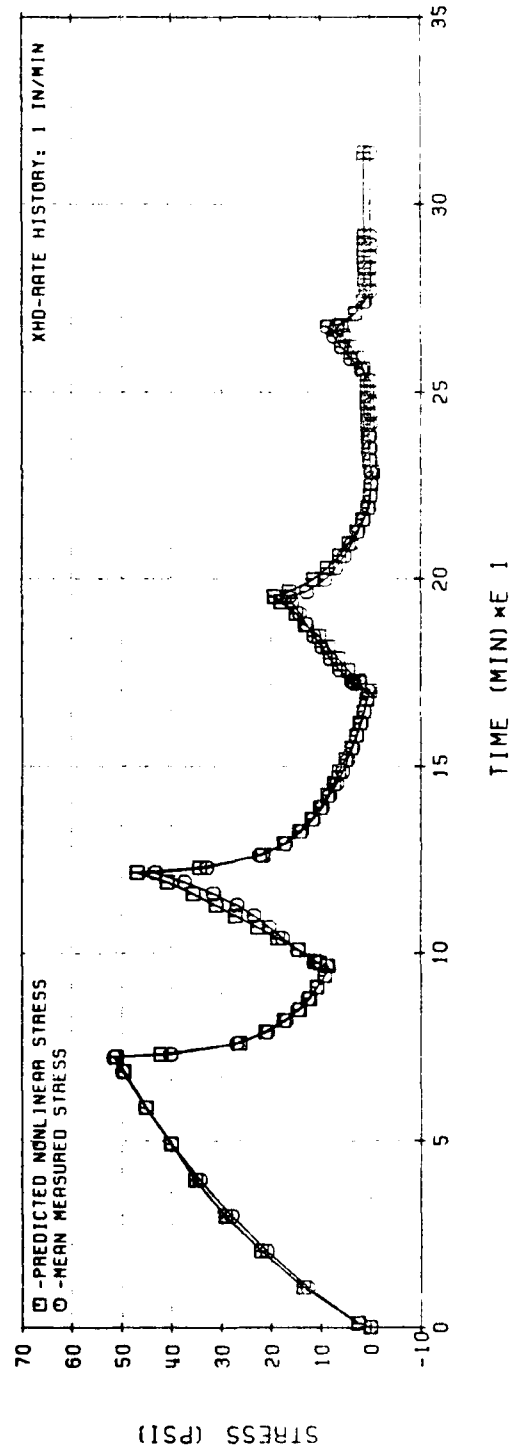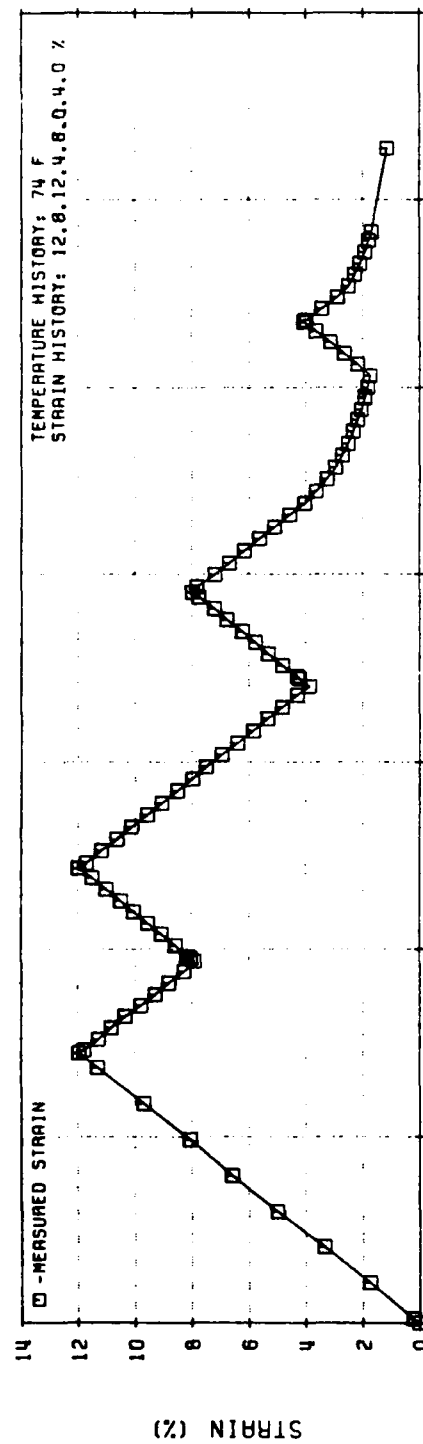
Figure 141. Swanson Theory Stress Predictions for the UTP-19,360B-400/1777 Complex Multiple Loading (Test No. 10)

31044

255
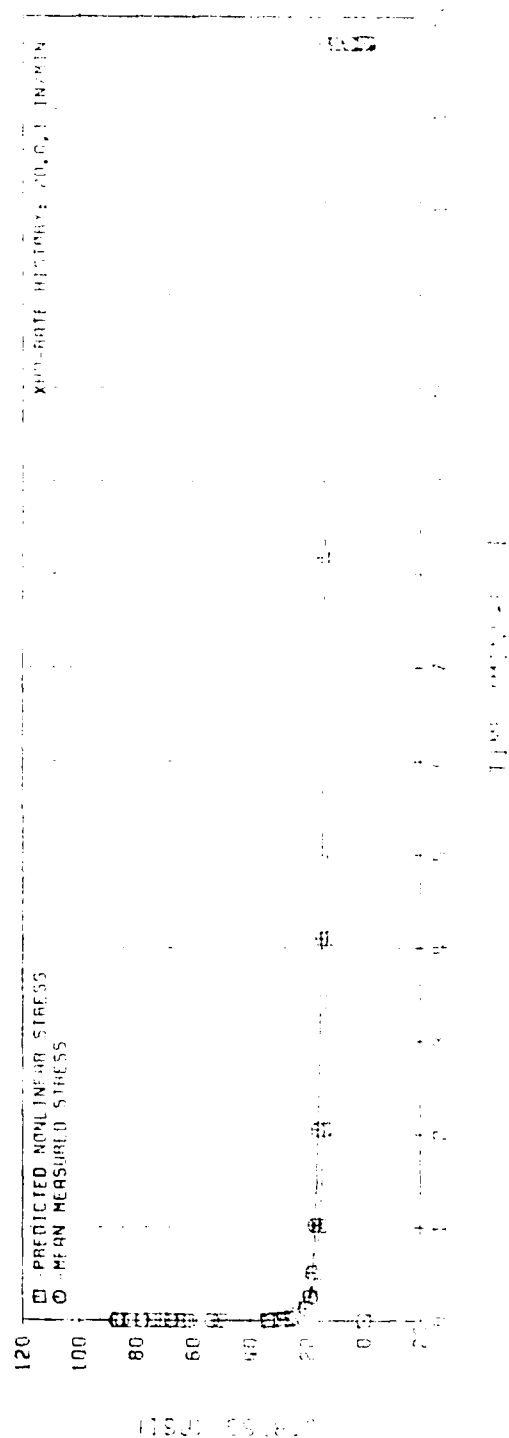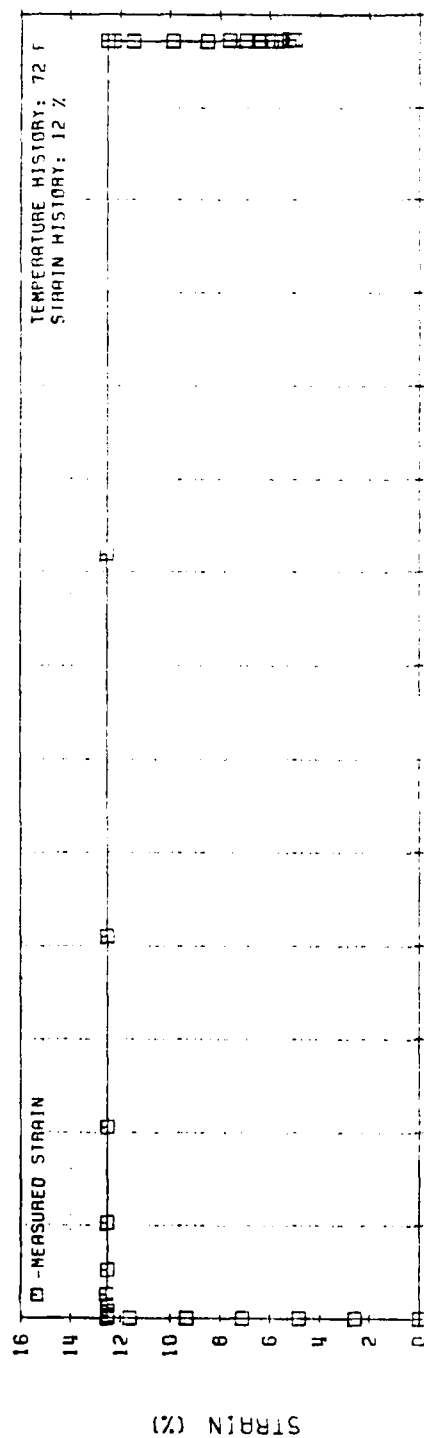
Figure 142. Swanson Theory Stress Predictions for UTP-19, P6.0R-H09 — Step Relaxation
(Test No. 8)
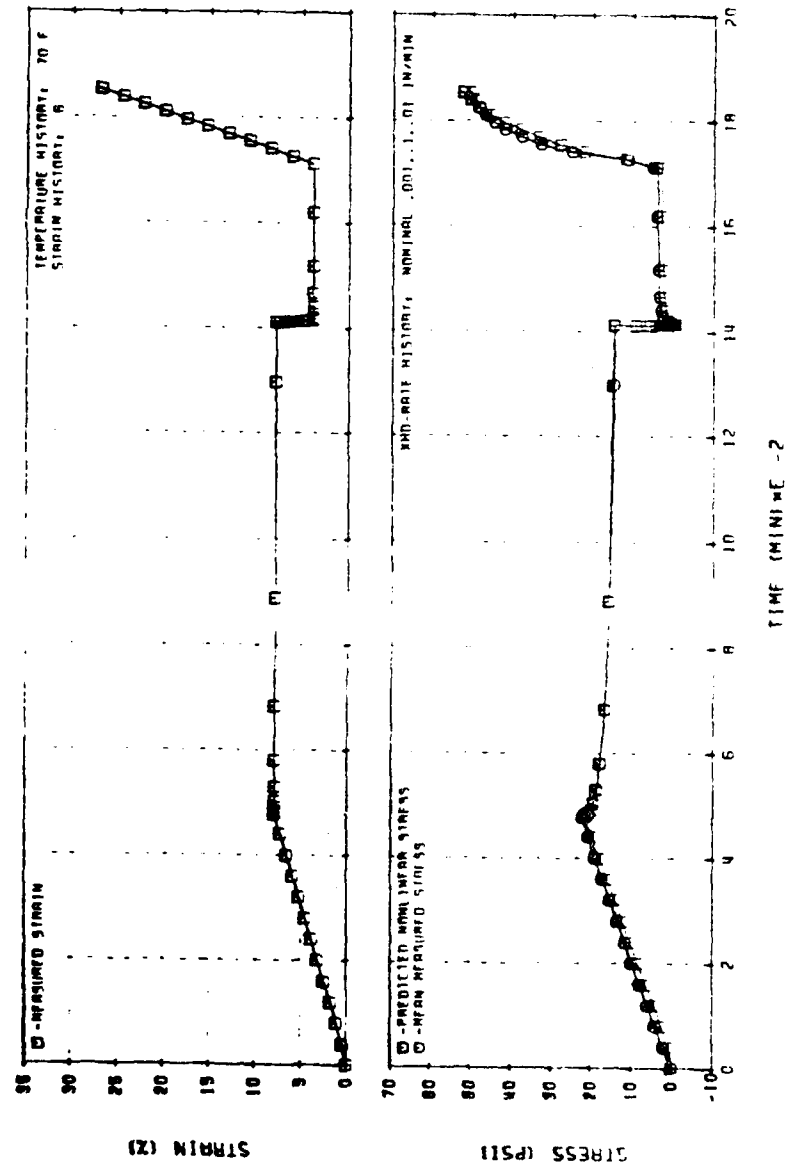
Figure 143.   Nonlinear Viscoelastic Stress Predictions for Long Similitude Test
(UTP-19,360B-400/1777)

31046

257
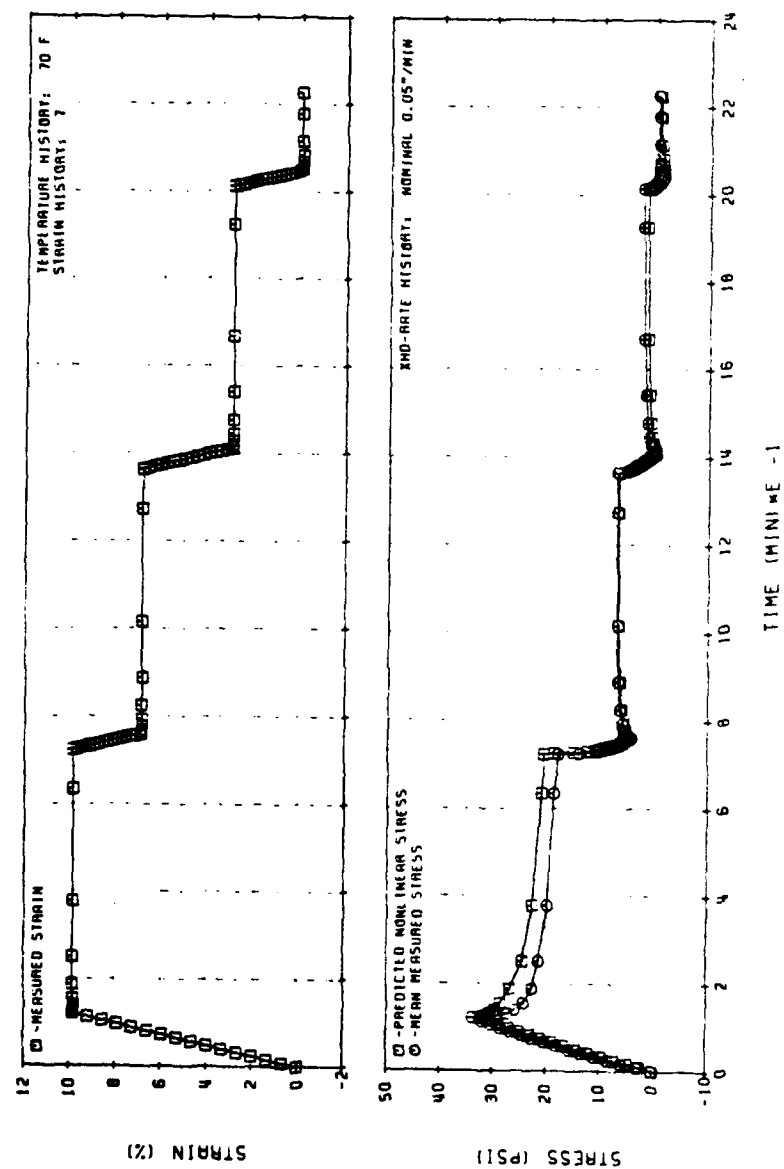
Figure 144. Nonlinear Viscoelastic Stress Predictions for Three-Step Relaxation
(UTP-19,360B-400/1777)

258
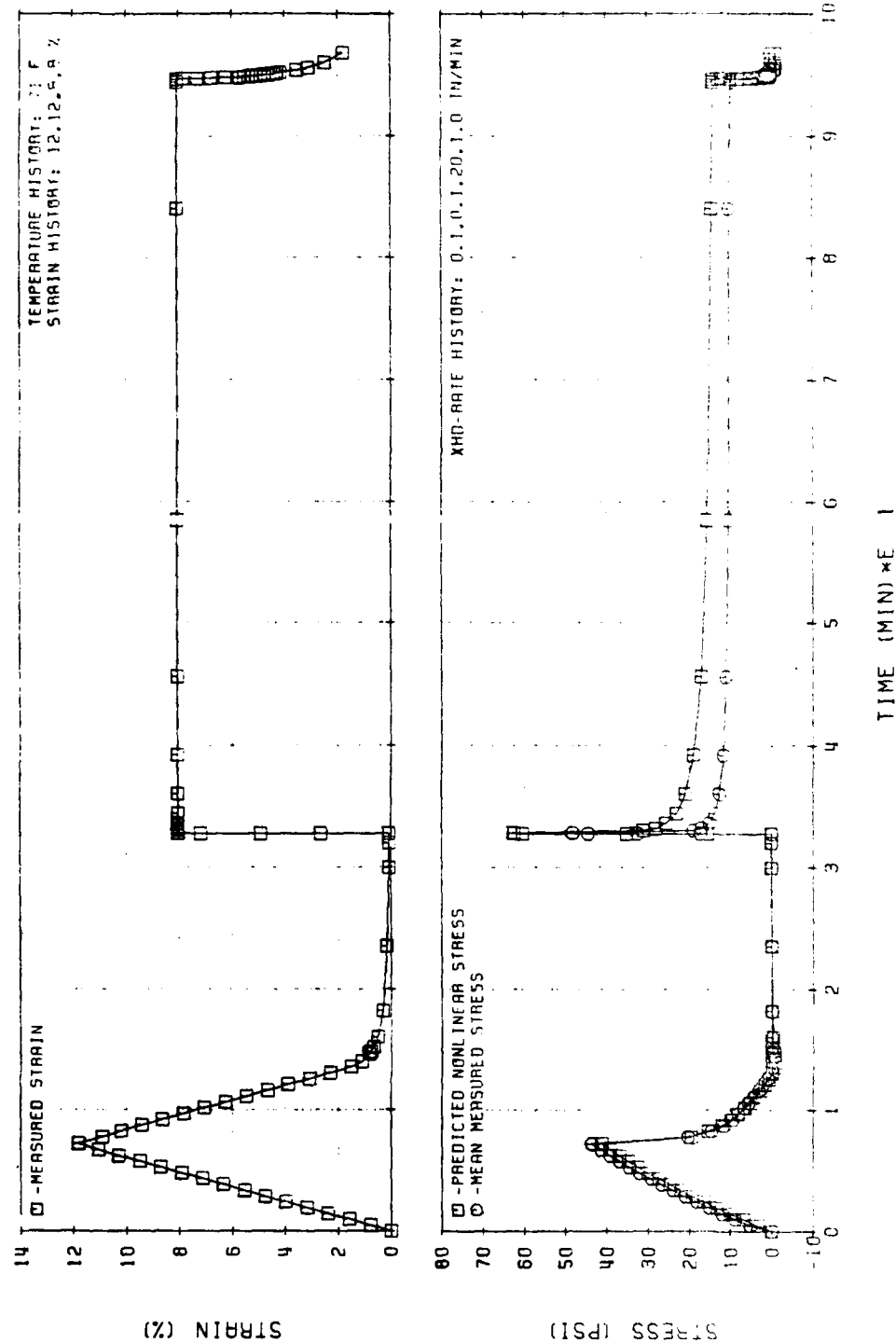
Figure 145. Swanson Theory Stress Predictions for UTP-19,360B-400/1777 Predamaged Relaxation (Test No. 9)

31048

259
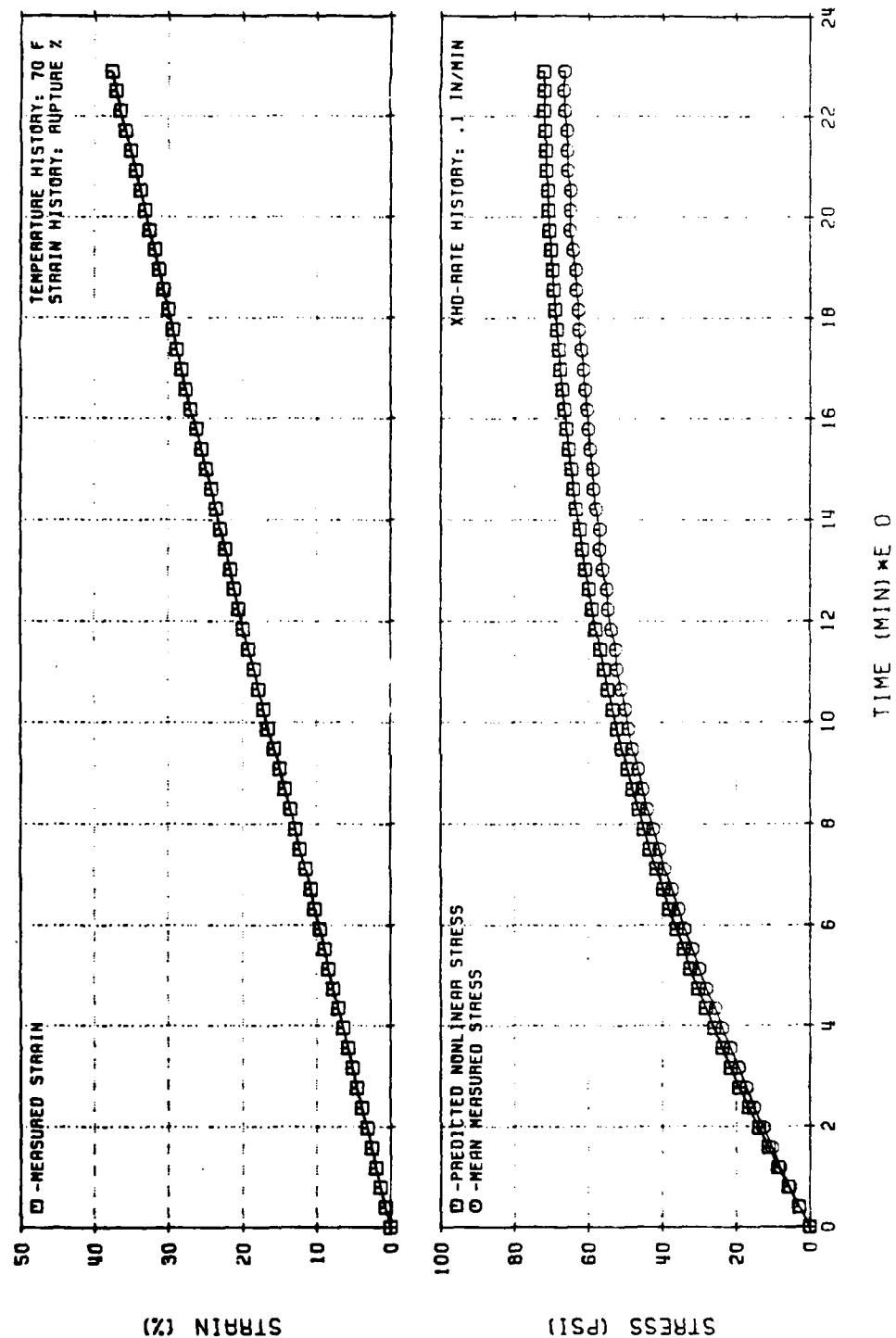
Figure 146. Swanson Theory Stress Predictions for UTP-19,360B-400/1777
Constant Strain Rate

31049

260
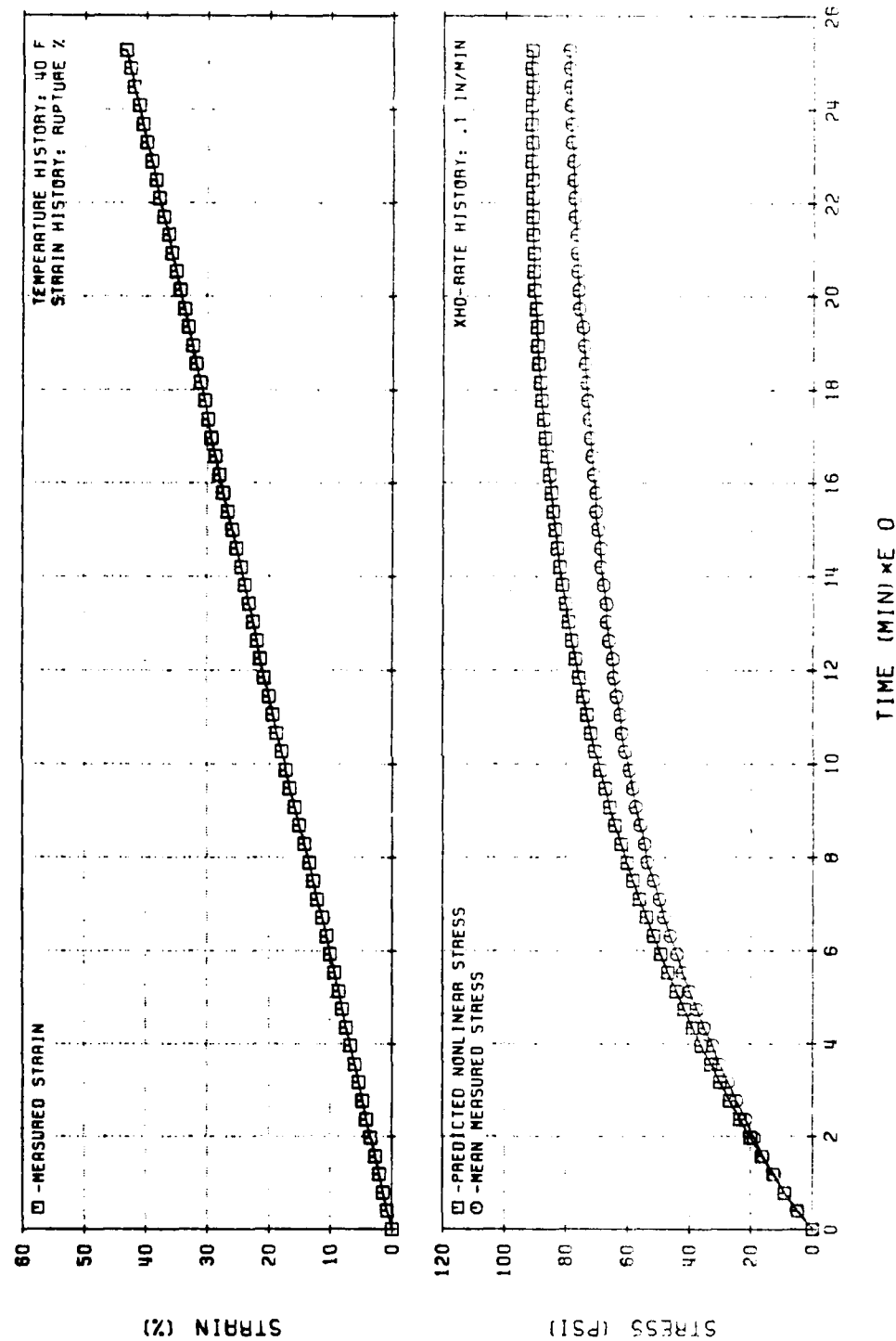
Figure 147. Swanson Theory Stress Predictions for UTP-19,360B-400/1777 Constant Strain Rate

31050
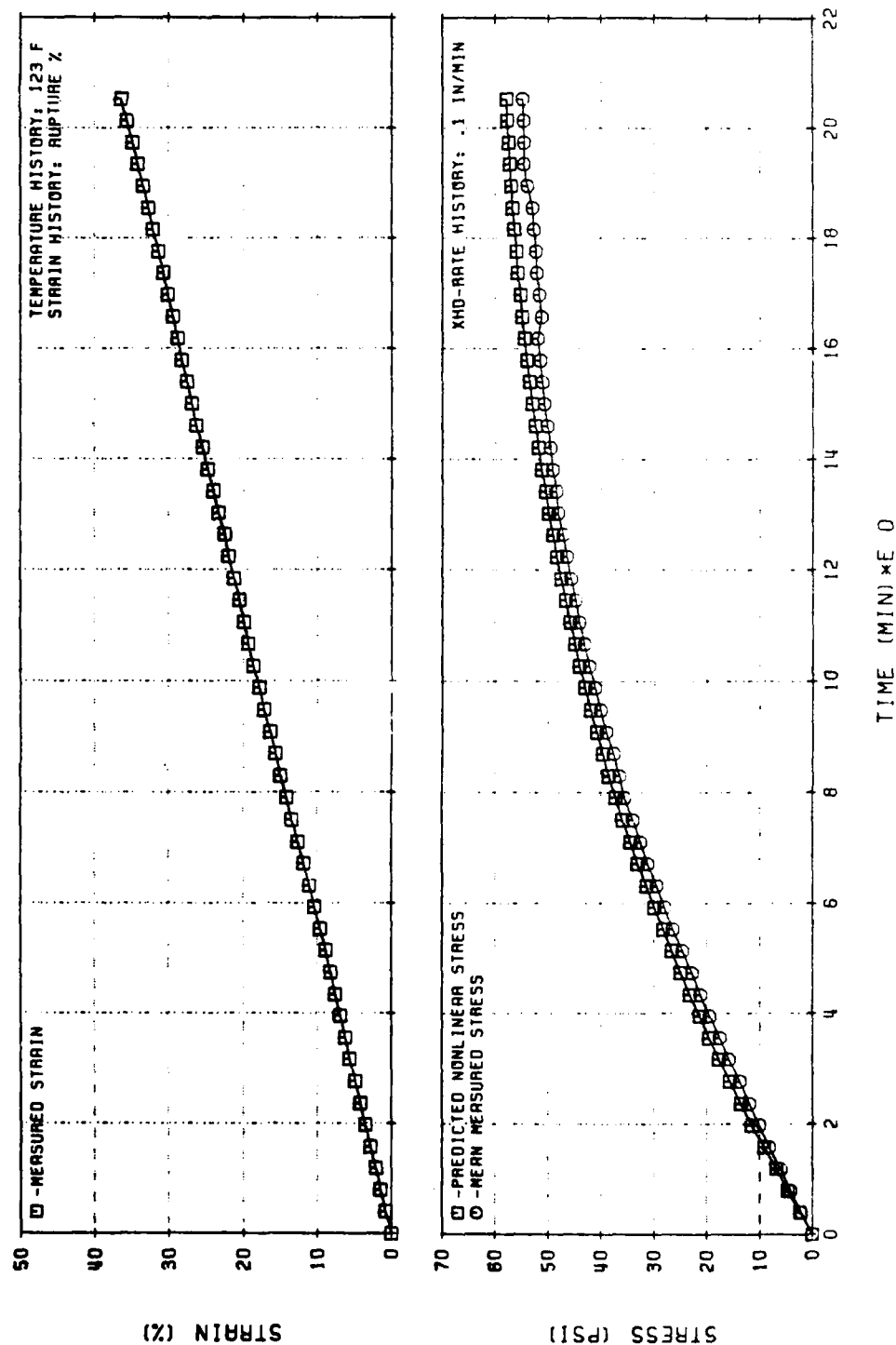
Figure 148. Swanson Theory Stress Predictions for UTP-19,360B-400/1777 Constant Strain Rate

31051

7. The softening function, g, defined and obtained as follows:

    a. For loading conditions:

$$g_L = g \; (\epsilon \; , \; \dot{\epsilon}) \tag{251}$$

and it is obtained from a sequence of constant rate tests with at least three different rates that span the range expected in the applications.

    b. For unloading conditions:

$$g_u = g \; (\epsilon / \epsilon_{max}) \tag{252}$$

where ϵ_{max} represents the maximum strain previously achieved during the loading history. The g is determined from the unloading portion of a loading-unloading cycle carried up to an intermediate strain level.

    c. For relaxation conditions:

$$g_r = g_r \; (t - t_o) \tag{253}$$

in which t_o is the time at which the relaxation process begins and g is evaluated from a relaxation test at an intermediate strain level.

In addition, for relaxation after partial unloading or during rest periods starting at $t = t_o$:

$$\hat{g}_r = \frac{1}{g_r \; (t - t_o)} \tag{254}$$

Also, the stress-correction function for reloading is taken as a linear function of the relative strain. It is a straight line from the point where reloading starts to the point of maximum loading over the past history.

4.7.5 Three-Dimensional Version of the Model

The (general) constitutive assumption used to relate the deviatoric components of the stress and deformation tensors, takes the following form:

$$\frac{\sigma'_{ij}}{\sqrt{II_{\sigma'}}} = \frac{B'_{ij}}{\sqrt{II_{B'}}}; \quad i, j = 1, 2, 3 \tag{255}$$

together with

$$\sqrt{II_{\sigma'}} = (g)(f) \tag{256}$$

or, equivalently

$$\sqrt{II_{\sigma'}} = (g) \int_{o}^{t} \tilde{\jmath}(t - \tau) \frac{\partial \sqrt{II_{B'}}}{\partial \tau} d\tau \tag{257}$$

where

σ'_{ij} = i-j component of the deviatoric Cauchy stress tensor

B'_{ij} = i-j component of the deviatoric Left Cauchy-Green deformation tensor

$II_{\sigma'}$, $II_{B'}$, = second invariants of the deviatoric stress and deformation tensors

with

$$\sigma'_{ij} = \sigma_{ij} + \frac{1}{3}(\sigma_{11} + \sigma_{22} + \sigma_{33})\delta_{ij}; \quad i, j = 1, 2, 3 \tag{258}$$

$$II_{\sigma'} \overset{def}{=} \left| -\left[\sigma'_{11}\sigma'_{22} + \sigma'_{11}\sigma'_{33} + \sigma'_{22}\sigma'_{33}\right] + (\sigma'_{12})^2 + (\sigma'_{13})^2 + (\sigma'_{23})^2 \right| \tag{259}$$

264

and similarly for B_{ij}' and II_B'; and in which

$$\delta_{ij} \overset{\text{def}}{=} \begin{cases} 1 \text{ for } i = j \\ 0 \text{ for } i \neq j \end{cases} \tag{260}$$

also

g = softening function that depends primarily on the strain level, the strain rate, and the applied pressure.

and

$$G(t) \overset{\text{def}}{=} E(t)/3 \tag{261}$$

where $E(t)$ represents the tensile relaxation modulus at a small strain.

According to the constitutive assumptions (255) and (257), the distortional behavior of the material is completely characterized through the softening function, g, and the relaxation function, G, which may be evaluated from one-dimensional tests, as explained in the previous section. Indeed, the stress-strain relations set forth in equation (255) and (257) reduce, as they should, to those employed in the one-dimensional version of the model.

To complete the theory, an assumption is still needed about volumetric behavior; and although time-dependent bulk response may be important in some applications, the elastic relation

265

$$\frac{1}{3}(\sigma_{11} + \sigma_{22} + \sigma_{33}) = K\left(|\lambda_1 \lambda_2 \lambda_3| - 1\right) \tag{262}$$

may be employed; in which K is the bulk modulus and the λ_i's are the stretch ratios.

For an incompressible material (and solid propellants are nearly incompressible)

$$\lambda_1 \lambda_2 \lambda_3 = 1 \tag{263}$$

so that equation (262) breaks down, and the stress tensor has to be considered a function of the mean pressure $(\sigma_{11} + \sigma_{22} + \sigma_{33})/3$, as well as of the deformation tensor, leading, eventually, to a stress-strain law of the form given in equation (255).

4.7.6 Application of the Model to Two-Dimensional Problems

In order to use the stress-strain law presented in the foregoing section, one must have available the deformation tensor at each point of the continuum where the stresses are desired. This solution in terms of deformation may be arrived at numerically or analytically through finite elements.

The accuracy with which the present constitutive theory may predict the two-dimensional response of solid propellants may be seen in Figures 149 to 154, which correspond to constant strain-rate tests of strip-biaxial samples of UTP-19,360B. The first three figures belong to tests performed at a nominal crosshead displacement rate of 0.02 in./min at 40 F, 70 F, and 120 F, respectively; while Figures 150 to 154 show the results for a crosshead displacement rate of 0.2 in./min at the same low, intermediate, and high temperatures of 40, 70, and 120 F. The plotted data refer to the direction of applied loading, which
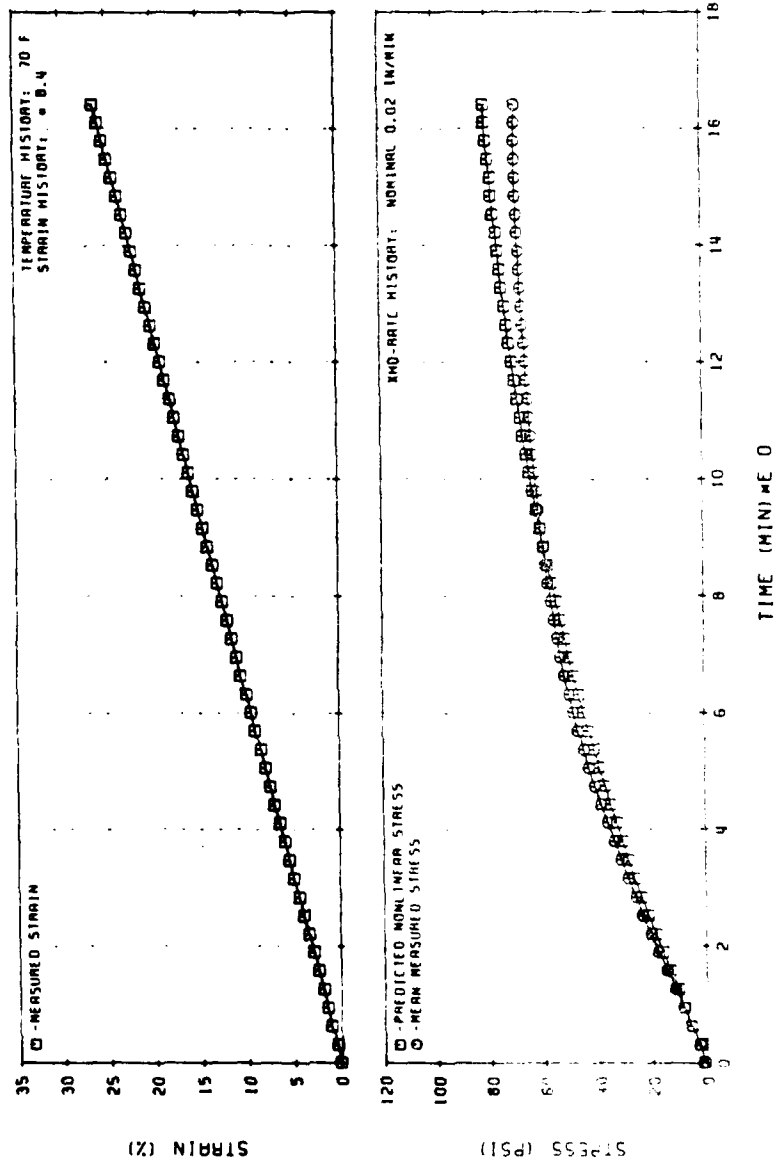
Figure 149. Nonlinear Viscoelastic Stress Predictions for UTP-19,360B-400/1777 (Biaxial Sample) Hercules Theory

267
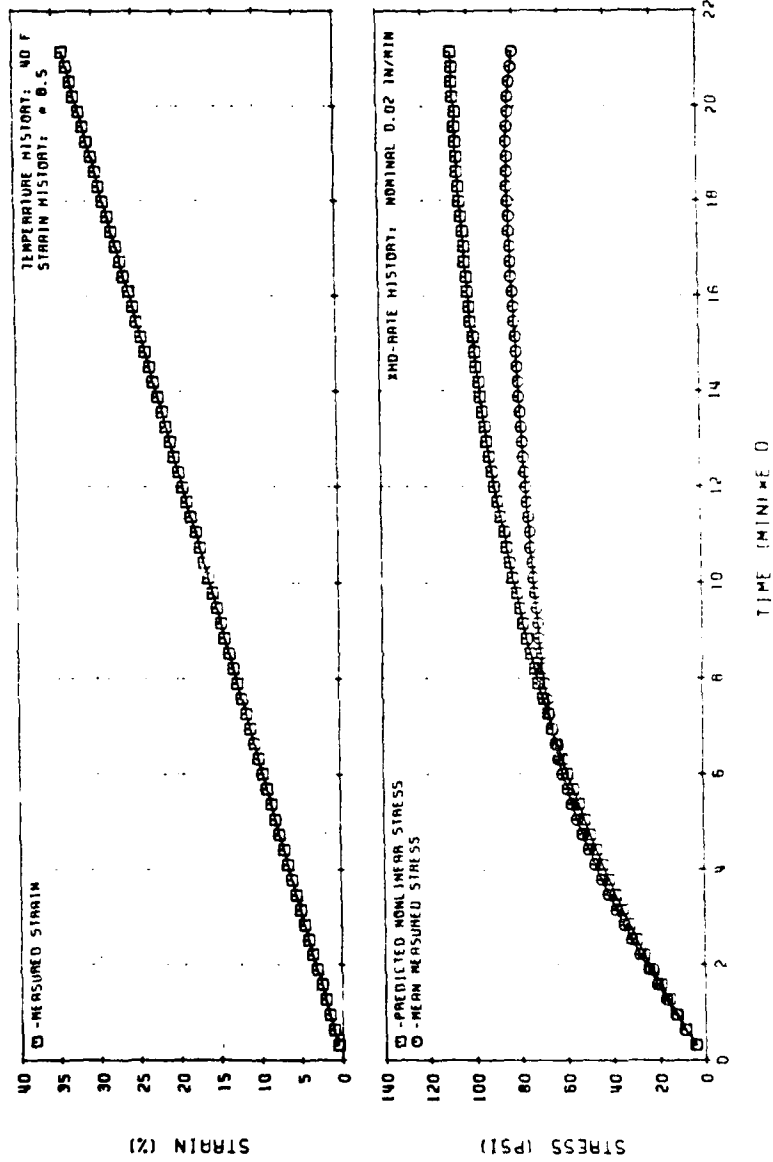
Figure 156. Nonlinear Viscoelastic Stress Predictions for UTP-19,360B-400/1777 (Biaxial Sample) Hercules Theory

31053
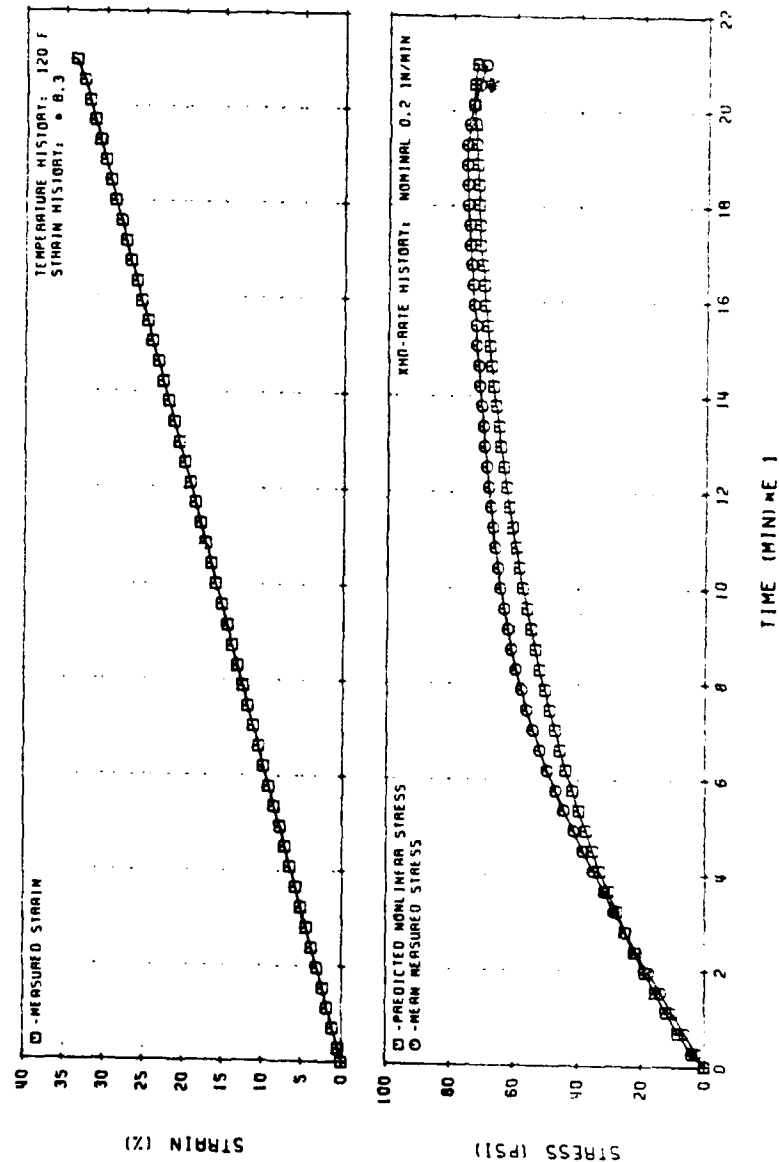
Figure 151. Nonlinear Viscoelastic Stress Predictions for UTP-19,360B-400/1777 (Biaxial Sample) Hercules Theory
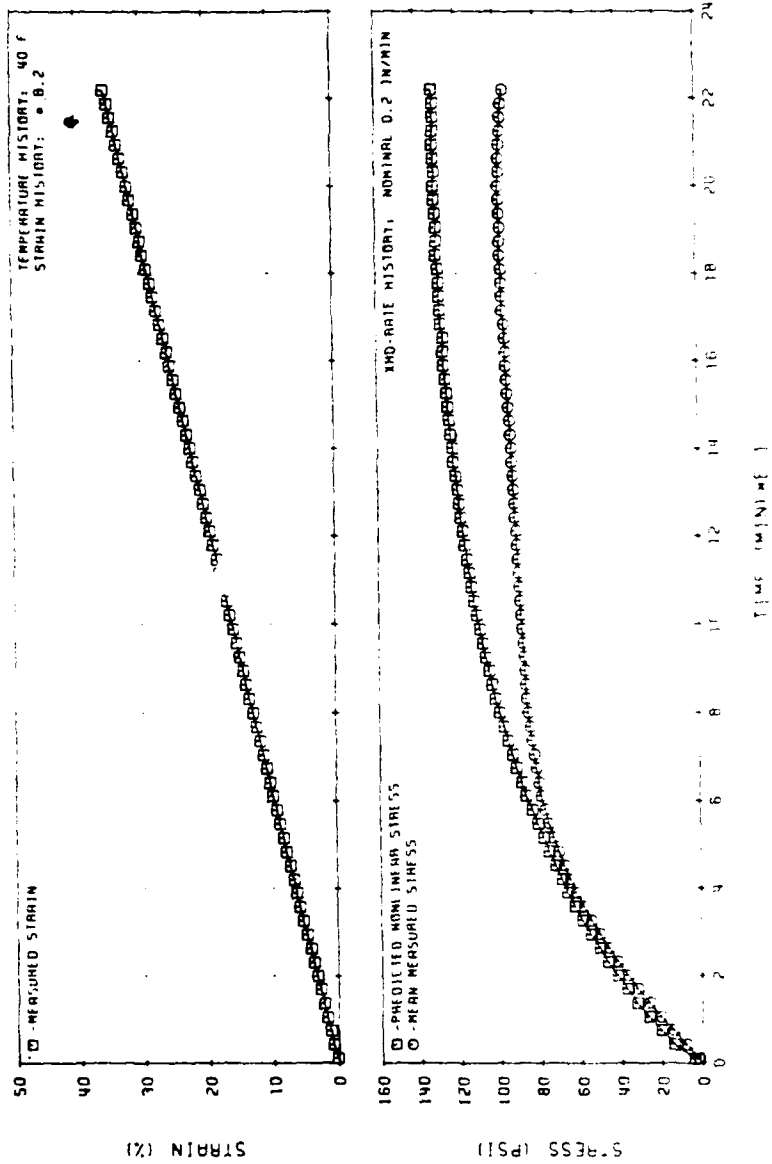
Figure 152. Nonlinear Viscoelastic Stress Predictions for UTP-19,360B-400/1777 (Biaxial Sample) Hercules Theory

31055
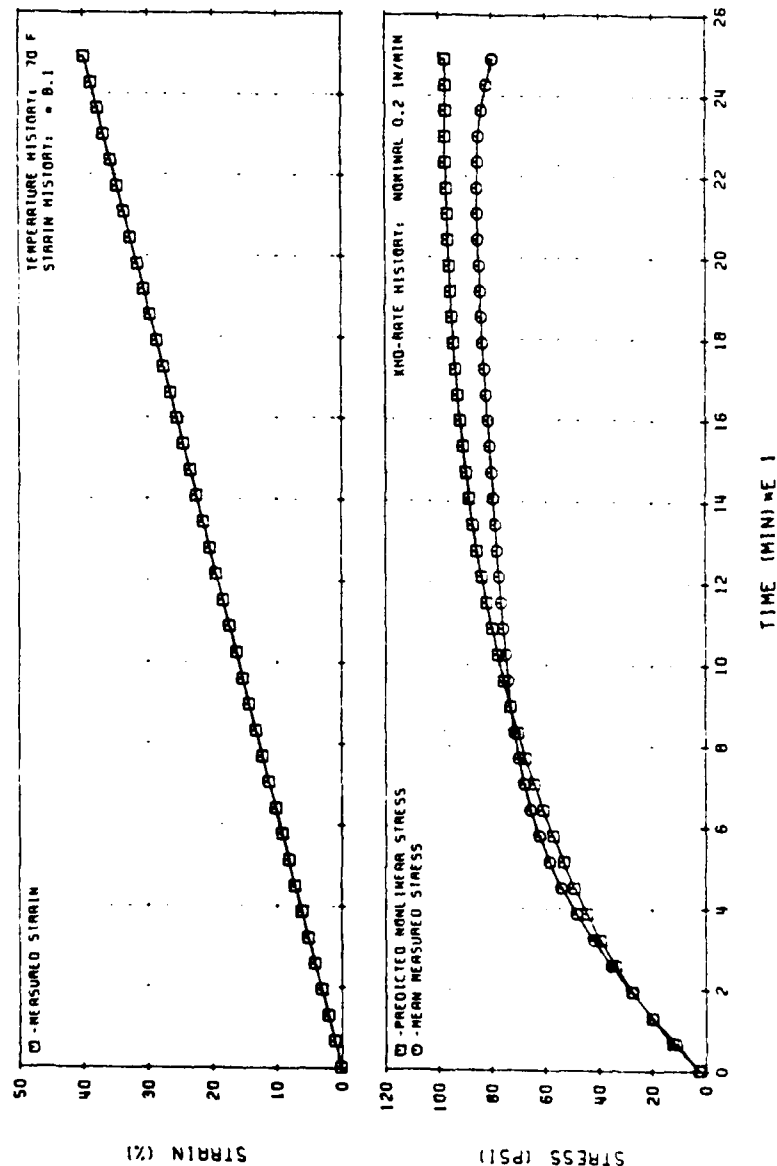
Figure 153. Nonlinear Viscoelastic Stress Predictions for UTP-19,360B-400/1777 (Biaxial Sample) Hercules Theory

31056
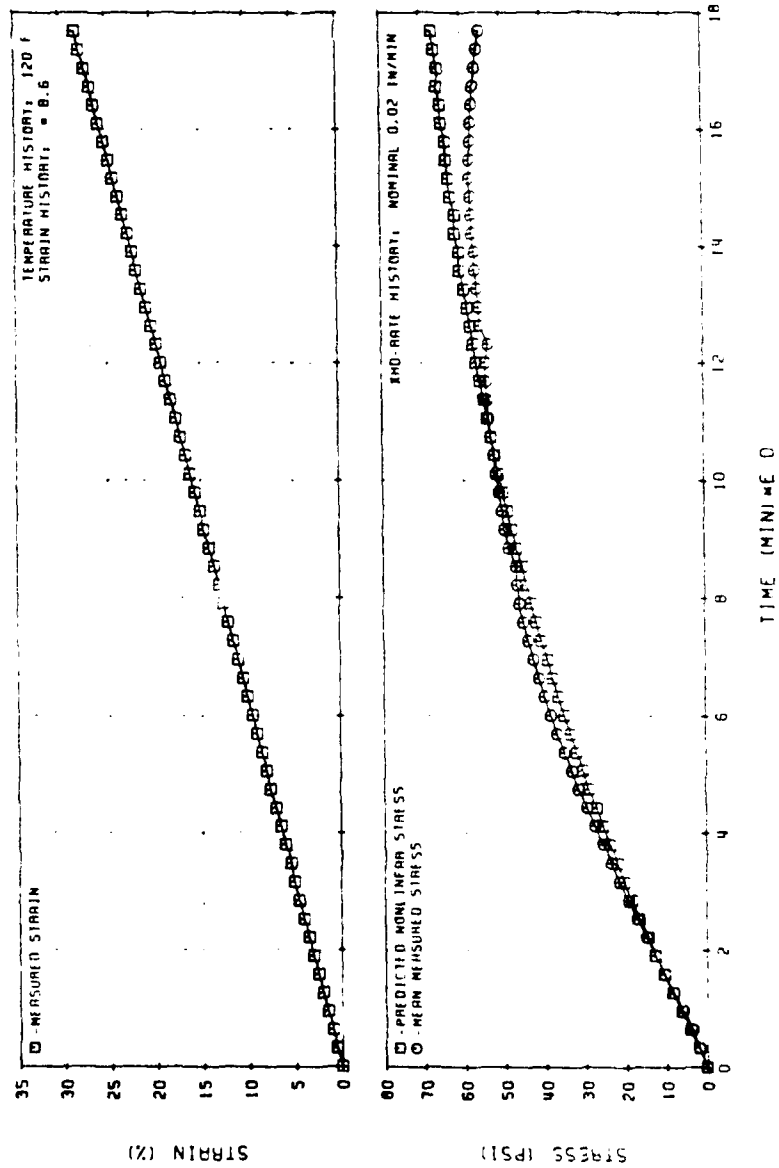
Figure 154. Nonlinear Viscoelastic Stress Predictions for UTP-19,360B-400/1777 (Biaxial Samples) Hercules Theory

272

is also the direction of maximum principal stress and strain. The **geometry of** the strip-biaxial sample used is as presented in the following sketch:
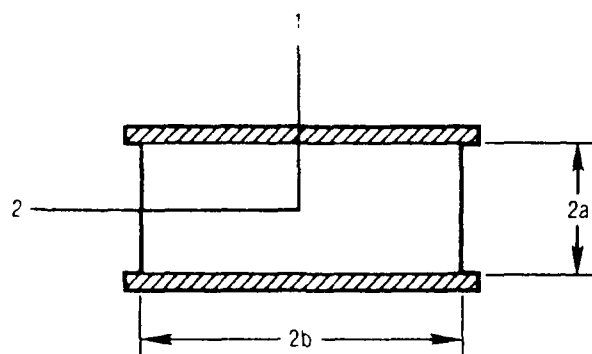
$$a/b = 1.25/6 \doteq 4.8 \qquad (264)$$

$$\sigma_{22}/\sigma_{11} \equiv \phi_\sigma \doteq 0.481$$

$$\epsilon_{22}/\epsilon_{11} \equiv \phi_\epsilon \doteq 0.025$$

The stress- and strain-axiality factors, ϕ_σ and ϕ_ϵ were taken from **Reference** 31, and are valid at the center of the sample for small strains only.

The constitutive relations given in (255) and (257) yield:

$$\sigma'_{ij} = (g)\frac{B'_{ij}}{\sqrt{II_{B'}}} \int_0^t G(t-\tau)\, \frac{\partial \sqrt{II_{B'}}}{\partial \tau}\, d\tau \qquad (265)$$

where

$$\frac{\partial \sqrt{II_{B'}}}{\partial t} = \frac{\partial \sqrt{II_{B'}}}{\partial B'_{ij}}\, \frac{\partial B'_{ij}}{\partial t}; \quad i, j = 1, 2, 3 \qquad (266)$$

with summation implied over repeated indices.

Now, under conditions of plane stress of an incompressible material, and along the principal directions, one has

273

$$\left[\sigma'_{ij}\right] = \frac{1}{3}\begin{bmatrix} (2\sigma_1 - \sigma_2) & 0 & 0 \\ 0 & (2\sigma_2 - \sigma_1) & 0 \\ 0 & 0 & -(\sigma_1 + \sigma_2) \end{bmatrix} \qquad (267)$$

$$\left[B'_{ij}\right] = \frac{1}{3}\begin{bmatrix} (2\lambda_1^2 - \lambda_2^2 - \lambda_3^2) & 0 & 0 \\ 0 & (2\lambda_2^2 - \lambda_3^2 - \lambda_1^2) & 0 \\ 0 & 0 & (2\lambda_3^2 - \lambda_1^2 - \lambda_2^2) \end{bmatrix} \qquad (268)$$

$$II_{B'} = -B'_{11} B'_{22} - B'_{11} B'_{33} - B'_{22} B'_{33} \qquad (269)$$

To evaluate (266), we first write it in unabridged notation, noting that in this case, if $i \neq j$ then $B_{ij} = 0$; thus:

$$\frac{\partial\sqrt{II_{B'}}}{\partial t} = \frac{\partial\sqrt{II_{B'}}}{\partial B'_{11}} \frac{\partial B'_{11}}{\partial t} + \frac{\partial\sqrt{II_{B'}}}{\partial B'_{22}} \frac{\partial B'_{22}}{\partial t} + \frac{\partial\sqrt{II_{B'}}}{\partial B'_{33}} \frac{\partial B'_{33}}{\partial t} \qquad (270)$$

and using (269):

$$\frac{\partial\sqrt{II_{B'}}}{\partial t} = \frac{1}{2\sqrt{II_{B'}}}\left[(-B'_{22} + B_{33}) \frac{\partial B'_{ij}}{\partial t} + (-B'_{33} - B'_{11}) \frac{\partial B'_{22}}{\partial t} + \right.$$
$$\left. + (-B'_{11} - B'_{22}) \frac{\partial B'_{33}}{\partial t} \right] \qquad (271)$$

where, from (268) one has, for instance, that

$$\frac{\partial B'_{11}}{\partial t} = \frac{2}{3}\left(2\lambda_1 \frac{d\lambda_1}{dt} - \lambda_2 \frac{d\lambda_2}{dt} - \lambda_3 \frac{d\lambda_3}{dt} \right) \qquad (272)$$

and similarly for the derivatives of B_{22} and B_{33}.

274

In the previous derivations, the stretch ratios are computed as

$$\lambda_1 = 1 + \epsilon_1(t) \tag{273}$$

$$\lambda_2 = 1 + \epsilon_2(t) \doteq 1 + \phi_\epsilon \epsilon_1(t)$$

$$\lambda_3 = 1/(\lambda_1\lambda_2)$$

in which $\epsilon_1(t)$ is the strain history imposed on the sample along coordinate 1, and the last expression of (273) follows from the incompressibility condition, equation (263).

Hence, the first component-equation of the constitutive relation (265) yields:

$$\sigma_{11}' \equiv \frac{1}{3}(2\sigma_1 - \sigma_2) = (g)\frac{B_{11}'}{\sqrt{II_{B'}}} \int\limits_0^t G(t - \tau) \frac{\partial\sqrt{II_{B'}}}{\partial\tau} d\tau$$

or, in view of (264)

$$\sigma_1 \frac{(2 - \phi_\sigma)}{3} = (g)\frac{B_{11}'}{\sqrt{II_{B'}}} \int\limits_0^t G(t - \tau) \frac{\partial\sqrt{II_{B'}}}{\partial\tau} d\tau$$

and finally:

$$\sigma_1 = \frac{3}{(2 - \phi_\sigma)}(g)\frac{B_{11}'}{\sqrt{II_{B'}}} \int\limits_0^t G(t - \tau) \frac{\partial\sqrt{II_{B'}}}{\partial\tau} d\tau \tag{274}$$

Using equations (264), (268), and (271) to (274), we obtained the response of the biaxial sample in the direction of the applied loading. The plots included in this report, show the engineering stress:

275

$$\sigma_1 = \sigma_1 / \lambda_1 \tag{275}$$

rather than the Cauchy stress, σ.

4.7.7 Application to Transient Temperature Loadings

The model in the previous section has been modified to the form

$$\sqrt{II}_{\sigma'} = A_F \ g(B, \overset{\circ}{B}) \int_0^t E_{rel} \ (\xi - \xi') \ \frac{\partial}{\partial \tau} \ \sqrt{II_B'} \ d\tau \tag{276}$$

where

$$\xi - \xi' = \int_\tau^t \ A_T \frac{du}{[T(u)]} \tag{277}$$

and the thermomechanical coupling coefficient, A_f, has been introduced for the transient straining and cooling loading history. The deformation gradient, F, and the Green strain tensor, B, incorporate the free thermal expansion, $\alpha \Delta T$.

Figure 155 shows that A_F, as determined from uniaxial straining and cooling tests, is nearly constant ($A_f = 1.27$) for this approach. Figures 156 through
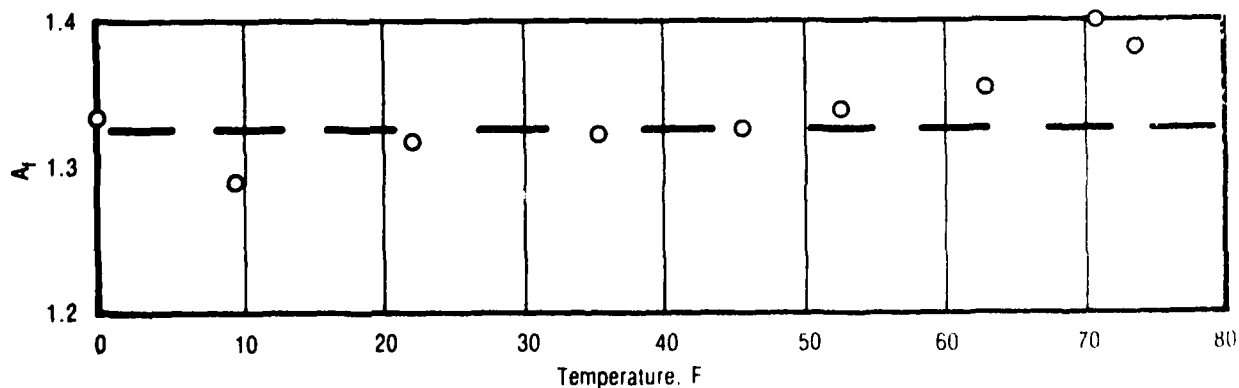
Figure 155. Swanson's Linear Viscoelastic Theory

30952

276

160 show the agreement with uniaxial and biaxial straining and cooling tests. The biaxial ramp-relaxation-ramp test was particularly well predicted by this approach; much better than by any other approach. The large disparity shown in Figure 160, in contrast to the good agreement in Figure 159, lends credence to our previous contention in section 4.2.3 that this is simply a bad test result.
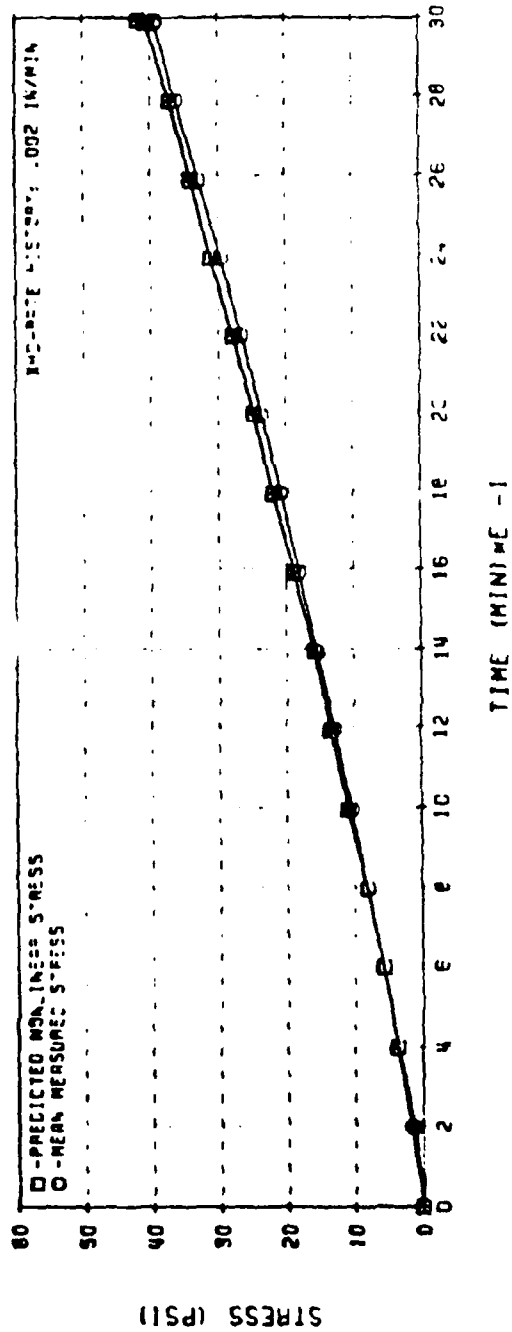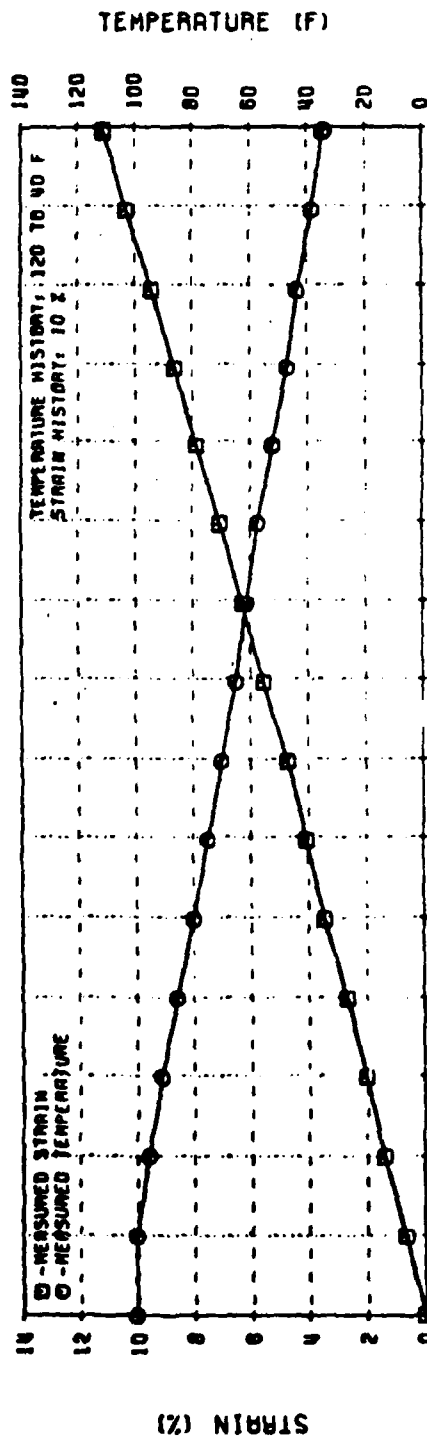
Figure 156. Swanson's Theory Stress Predictions for UTP-19,360B-400/1777 6-in. Bar Straining-Cooling (Test No. 18)

278
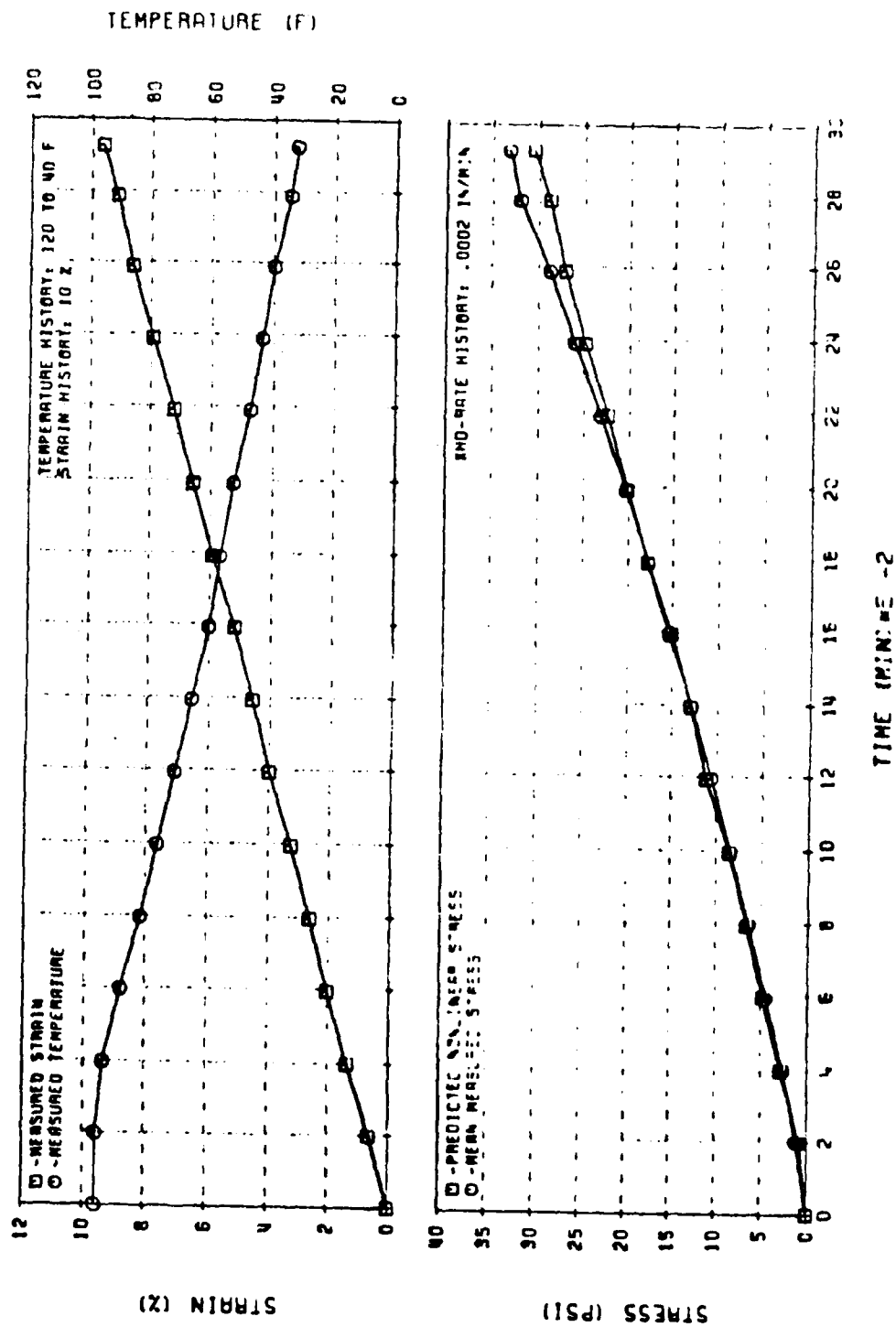
Figure 157. Swanson's Theory Stress Predictions for UTP-19,360B-400/1777 6-in. Bar Straining-Cooling (Test No. 18)

279

31059
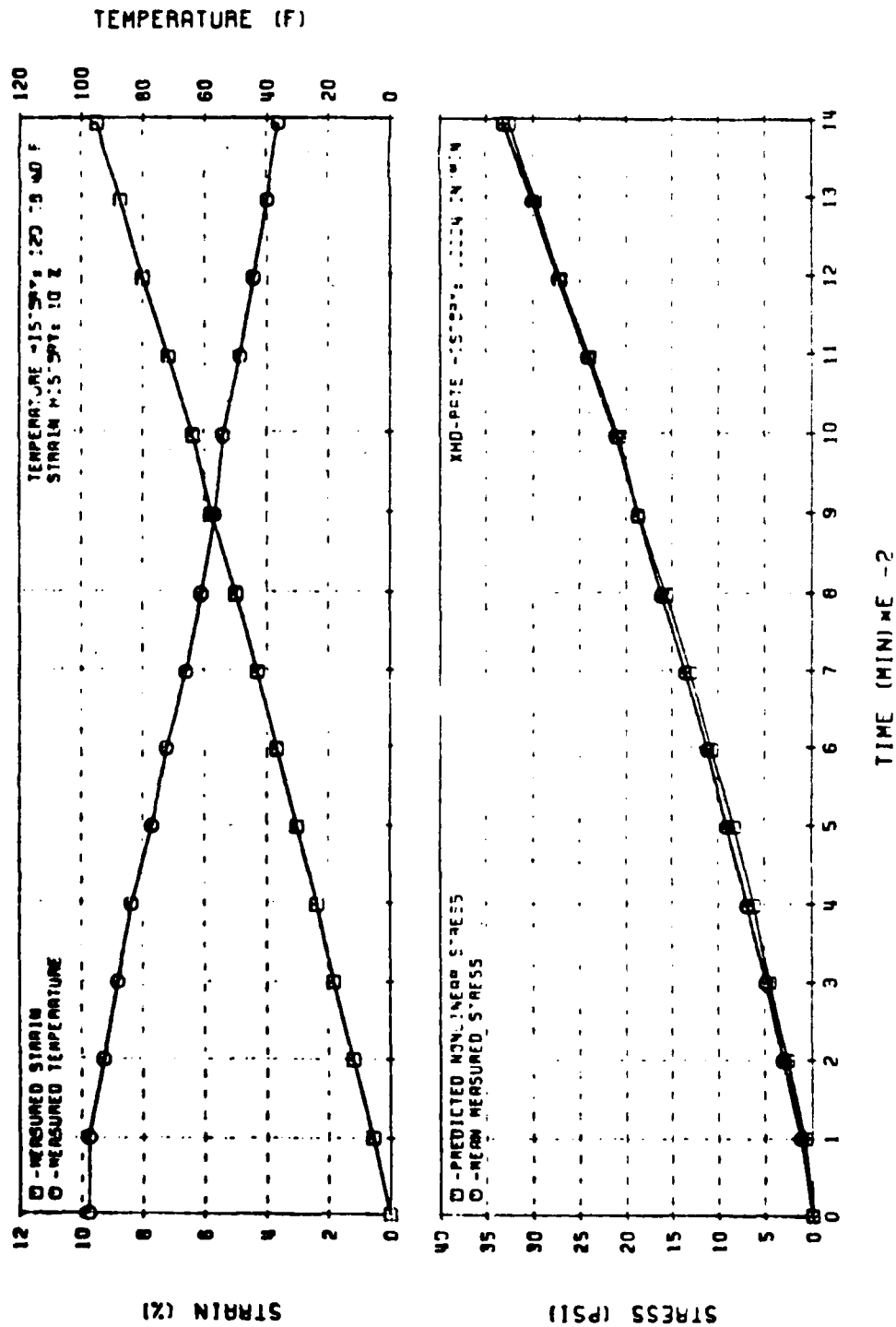
Figure 158. Swanson's Theory Stress Predictions for UTP-19,360B-400/1777 6-in. Bar Straining-Cooling (Test No. 18)

280
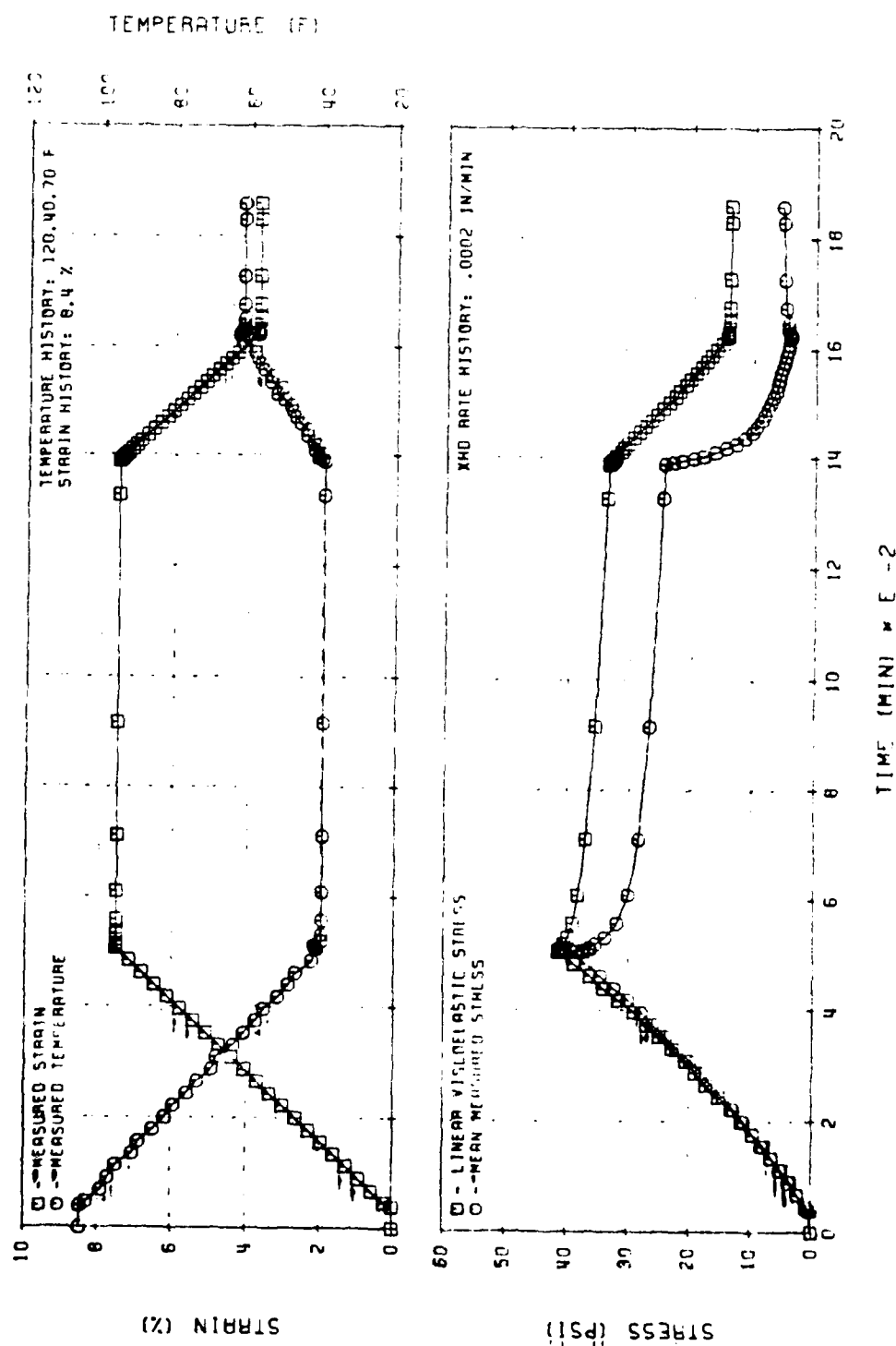
Figure 159. Swanson's Theory Stress Predictions for UTP-19,360B-400/1777 Biaxial Ramp-Relaxation-Ramp (Test No. 21)

281
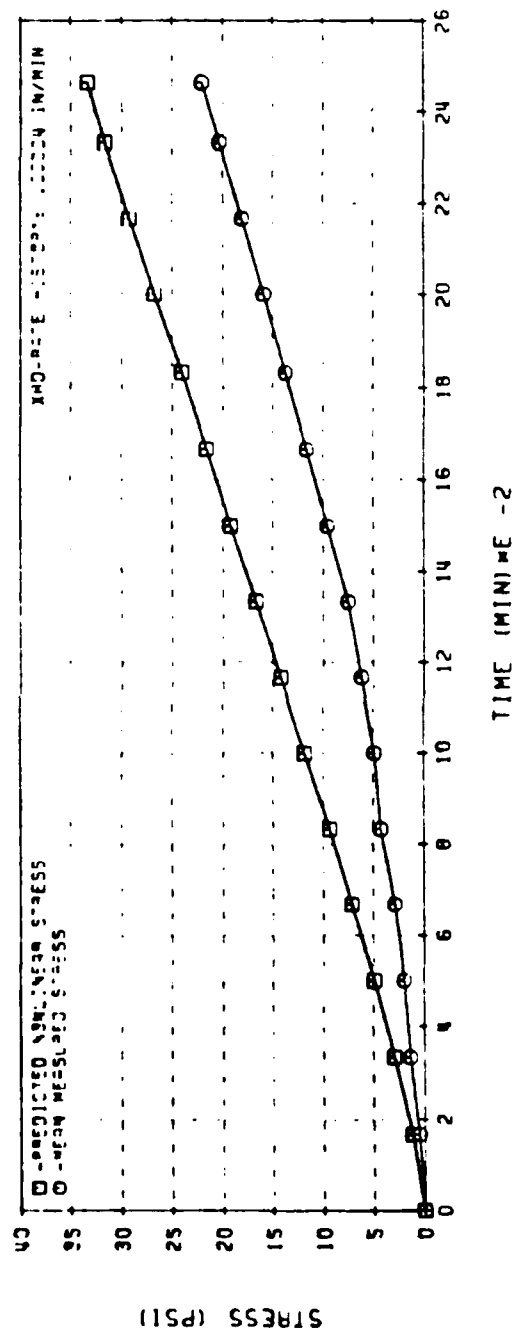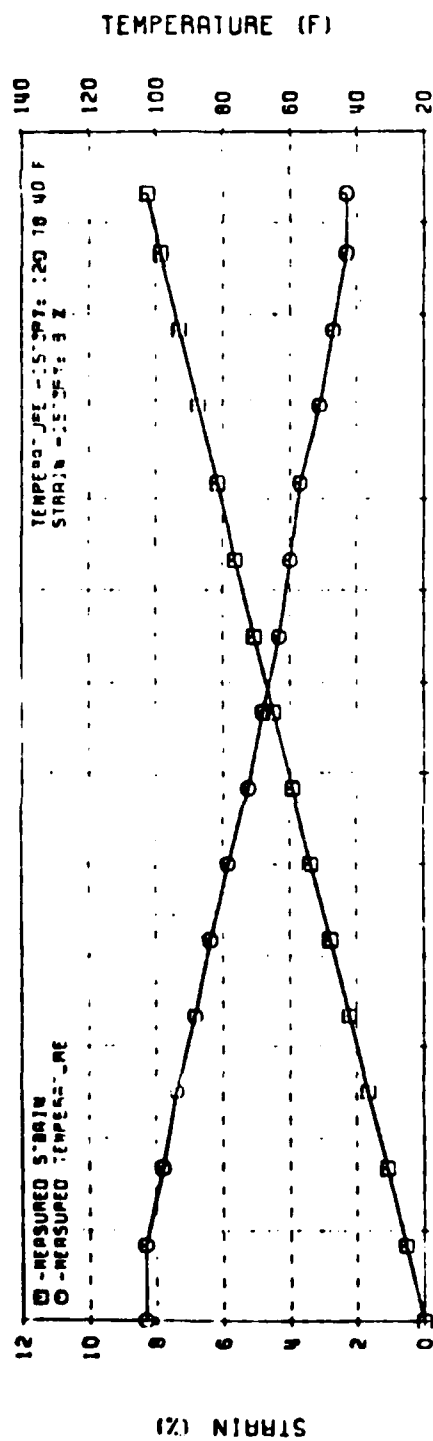
Figure 160. Swanson's Theory Stress Predictions for UTP-19,360B-400/1777 Biaxial Straining — Cooling (Test No. 15)

31062

282

5.0 SUBSCALE MOTOR ANALYSES AND STRESS PREDICTIONS

5.1 LINEAR ELASTIC ANALYSES

Linear elastic stress analyses, following commonly accepted handbook and industry practices, were performed to provide a basis for comparison with the nonlinear constitutive theory predictions and to illustrate the inadequacy of elasticity analyses for thermal cycling of solid rocket motors.

The linear elastic analyses consisted of:

1. Handbook Calculations/Design Curves
2. TEXGAP 2D Finite Element Analyses.

5.1.1 Handbook Calculations

The solid propellant structural integrity handbooks[34],[35] suggest the use of the equations

$$\sigma_{rr}(b) = (\lambda^2 - 1)\ \overline{P}_r\ E_p\ \alpha_R\ \Delta T \tag{278}$$

or

$$\frac{\sigma_{rr}\ (b)}{E_p\ \delta_p} = \frac{1.5 - 1.3\ \dfrac{\delta_c}{\delta_p}}{\dfrac{1.5}{\lambda^2-1} + 0.9\ \dfrac{bE_p}{hE_c}}\ \overline{P}_r \tag{279}$$

for the midplane case/grain interfacial pressure (i.e., radial bond stress), where:

λ = 2b/2a = grain OD/grain ID

E_p = propellant modulus

E_c = case modulus

α_R = $\alpha_p - 2/3\ (1 + \nu_c)\ \alpha_c$

α_p = propellant coefficient of linear thermal expansion

283

α_c = case coefficient of linear thermal expansion

h = case thickness

$\delta_c = \alpha_c \, \Delta T$

$\delta_p = \dfrac{\delta_s}{3} + \alpha_p \, \Delta T = \alpha_p \left\{ (T_o - T_c) + \Delta T \right\}$

T_o = stress free temperature

T_c = motor cure temperature

P_r = finite length correction factor.

Equations (278) and (279) are derived from the Lame equations for a composite cylinder assuming a thin elastic casing and an incompressible inner core. In equation (278), ΔT is referenced to the stress-free temperature, and in equation (279), ΔT is referenced to the motor cure temperature. For the situation where $bE_p/hE_c \ll 1$, equation (279) reduces to equation (278). Hence, equation (278) was used to make elasticity stress predictions for the subscale motors.

Figures 161 and 162 compare elastic stress predictions using equation (278) with measured radial stresses for the 0.75-in. subscale motor with UTP-19,360B-400/1777 propellant. In these calculations:

$\lambda = 5.37$

$\alpha_p = 5.3 \times 10^{-5}$ in./in./F

$\alpha_c = 6 \times 10^{-5}$ in./in./F

$E_p = 151.4$ psi

$\overline{P}_r = 0.83$

$\nu_c = 0.3$

Figure 161 shows stresses calculated from the measured strain-free temperature of 166.5 F, whereas Figure 162 is based on the measured stress-free temperature of 141 F. Not all the points are connected in these figures.

As expected, the linear elastic predictions underpredict stresses during transient conditions, but compare favorably with the longer term equilibrium behavior when the measured stress-free temperature is used in the calculations. The experimental results obtained here, as suggested in Reference 3, indicate that it is incorrect to assume stress and strain-free temperatures as identical, even at the completion of cure. Since the stiffness of the motor case is so
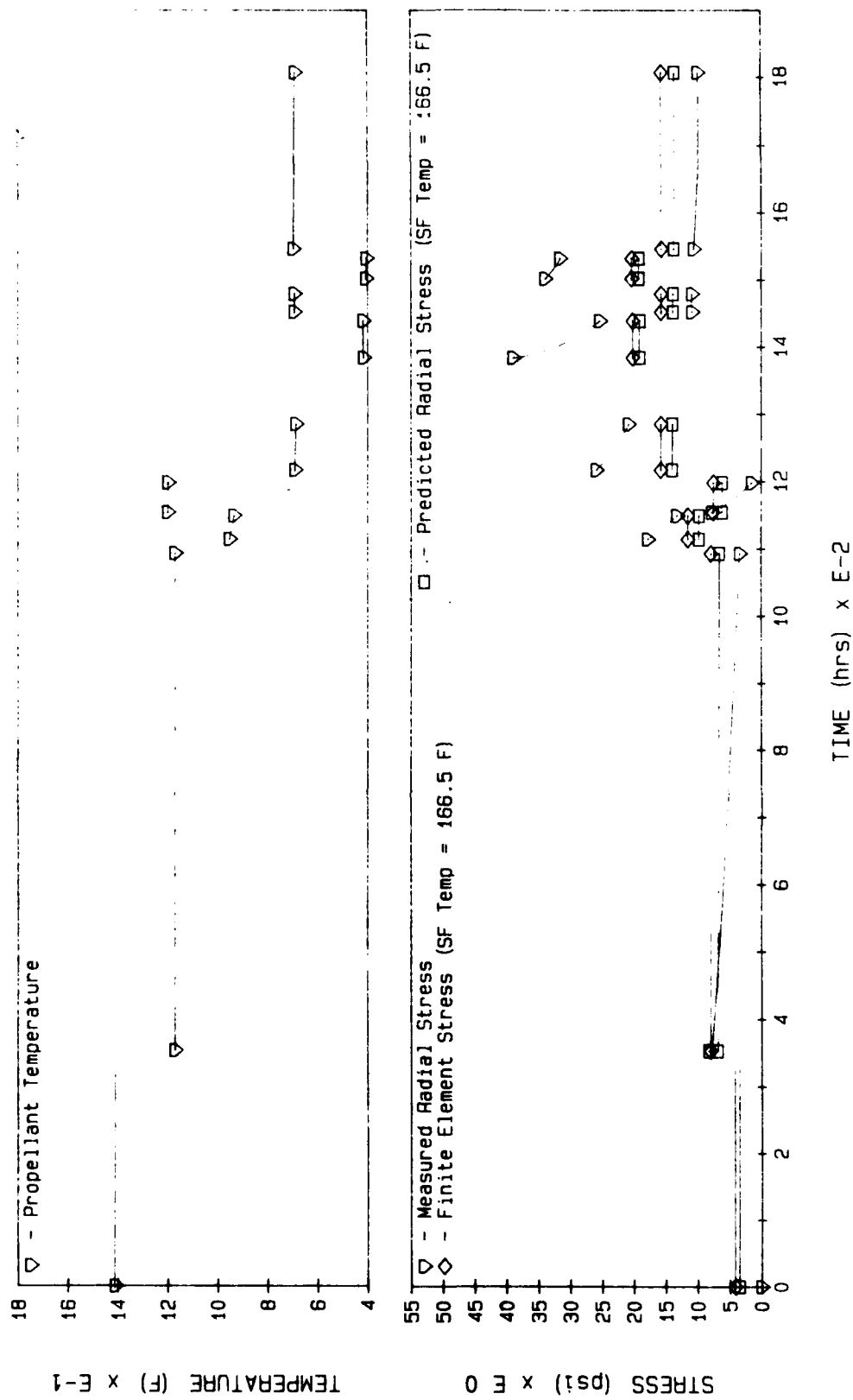
Figure 161. Elastic Stress Predictions for UTP-19,360B-400/1777

285

31063
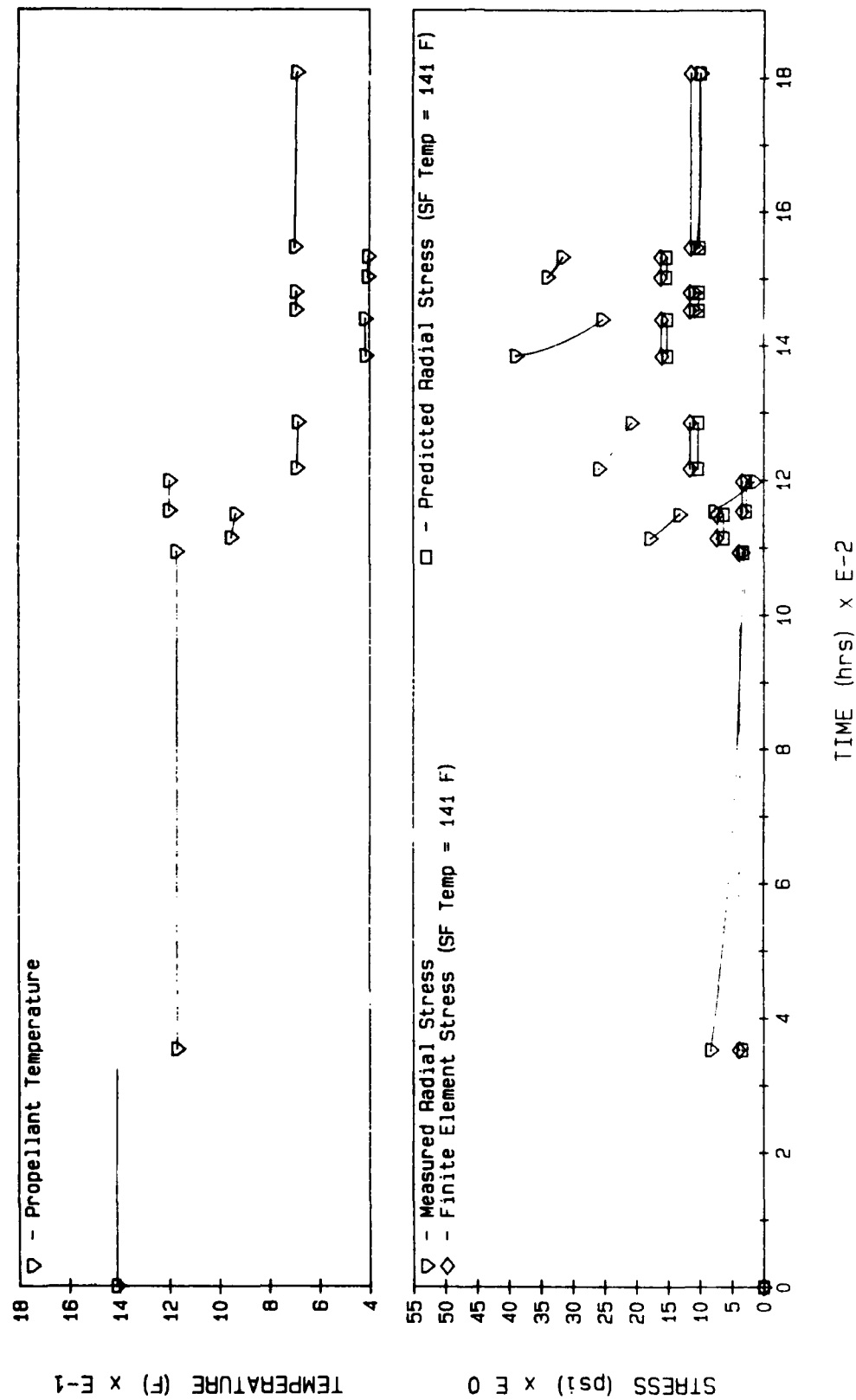
Figure 162. Elastic Stress Predictions for UTP-19,360B-400/1777

31064

than that of the propellant, the state of deformation in a propel-
largely independent of the propellant modulus. Thus, the strain-
temperature is determined by the original geometry. In contrast, stresses
are proportional to the propellant modulus, and there is no a priori justifica-
tion for assuming that the stress-free temperature and strain-free temperature
are the same. The difference is significant, and care should be exercised in
making motor stress and strain predictions.

It should be noted that the stress and strain-free temperatures can
generally only be defined for one components of stress or strain. It is
probably not possible to make all component of stress or strain vanish at the
same temperature. For example, the normal procedure for determining the strain-
free temperature in a circular port motor for example, is to make bore measure-
ments at the motor midplane at several temperatures near, below, and possibly
above the cure temperature, and then extrapolating to the temperature where the
bore strain ϵ_θ goes to zero. One generally finds that the entire mandrel
dimensions are not obtained at the so-called strain-free temperature. The
reasons for this are severalfold. For one thing, propellants are not truly
incompressible even though Poisson's ratio is very nearly equal to one-half.
Second, it is not always possible to eliminate or compensate for slump. Also,
the propellant is cured or polymerized under varying degrees of constraint,
depending upon the location within the motor.

With regard to the stress-free temperature, it is normally obtained in a
manner similar to that for the strain-free temperature determination only using
stress transducer data for the radial bond stress at the midplane of the motor.

Again only one component of stress is used, and the reasons for all components
of stress not vanishing are the same as those given in the previous paragraph
with regard to strain.

5.1.2 TEXGAP Finite Element Analyses
Linear elastic axisymmetric finite element analyses using TEXGAP 2D were also
performed on the subscale motors subjected to thermal testing. The geometry
analyzed is shown in Figure 163, and the undeformed grid is shown in Figure 164.
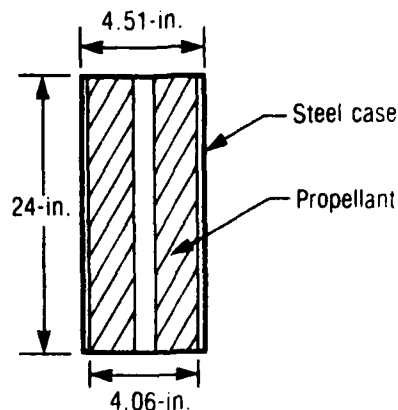
Figure 163. Circular Port Motor Geometry

The analyses considered a thermal load of 100 F and used the following material properties:

$$\nu_{propellant} = 0.499$$
$$\alpha_{propellant} = 5 \times 10^{-5} \text{ in./in./}^{\circ}F$$
$$E_{propellant} = 151.4 \text{ psi}$$
$$\nu_{case} = 0.31$$
$$\alpha_{case} = 6 \times 10^{-5} \text{ in./in./}F$$
$$E_{case} = 3 \times 10^{7} \text{ psi}$$

The radial component of the calculated mid plane bond stress is also shown in Figures 161 and 162. As expected, these stresses agree exactly with the handbook calculations.

5.2 APPROXIMATE VISCOELASTIC ANALYSES

Thermal stress analyses of solid propellant rocket motors are routinely conducted using an approximate (quasi-elastic) viscoelastic analysis. The procedure involves the use of an equivalent propellant modulus which approximates the true time and temperature behavior in conjunction with an elastic stress analysis. The immediate objectives of the motor analyses are to determine the sophistication and the extent of realism in the modulus approximation.
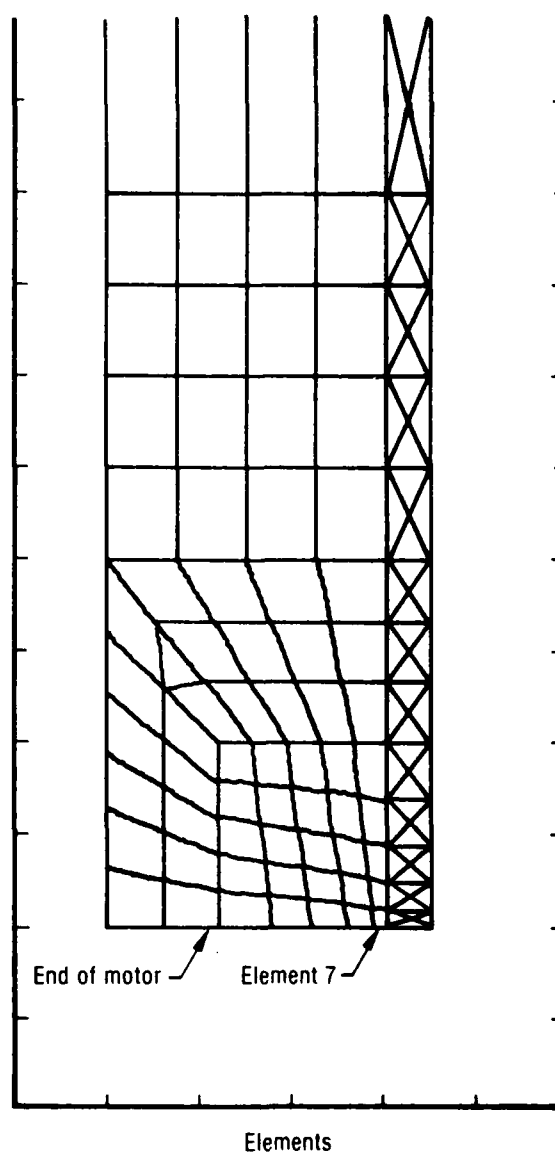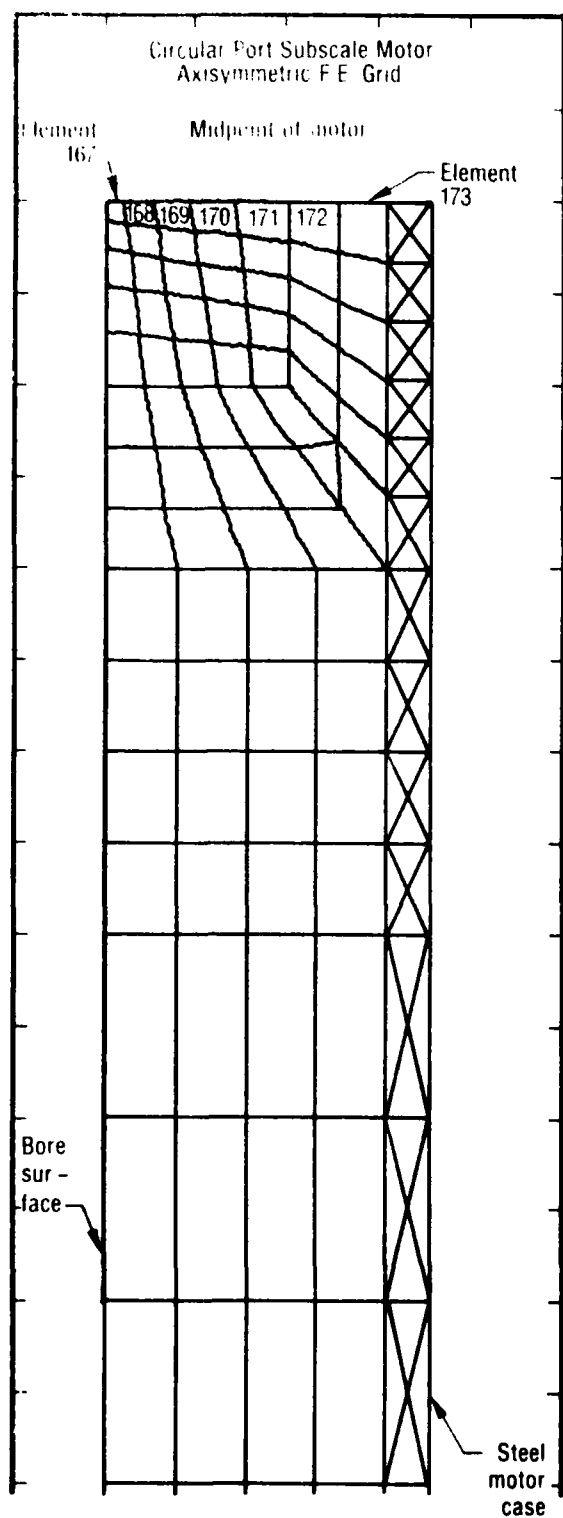
Figure 164. TEXGAP Finite Element Grid for Circular Port Subscale
Motor Analysis

21570

289

The effective modulus is determined assuming thermorheologically simple material (TSM) behavior or thermorheologically complex material (TCM) behavior. The decision to perform a TSM or TCM analysis is based on comparisons of predicted linear thermoviscoelastic stress response with the measured stress response during simultaneous straining and cooling tests of laboratory specimens conducted at strain rates, strain levels, and over temperature ranges representative of the anticipated motor environment. If the linear predictions agree with the measured stresses, then a TSM analysis is conducted; if they do not agree, then a thermochemical coupling coefficient is introduced and a TCM analysis is conducted.

The stress, $\sigma_{ij}(X_k,T)$, at any point x_k ($x_k = x,y,z$, or r, θ, z) in the propellant grain at time t are calculated by the quasi-elastic method using the formula

$$\sigma_{ij}(X_k, t) = K_{ij}(X_k) \frac{E_{eff}(t) \, \alpha_p \, \Delta T_\sigma(t)}{E_{FEM} \, \alpha_{FEM} \, \Delta T_{FEM}} \tag{280}$$

while the strains, $\epsilon_{ij}(x_k,t)$ are calculated from

$$\epsilon_{ij}(X_k, t) = K'_{ij}(X_k) \frac{\alpha_p \, \Delta T_\epsilon(t)}{\alpha_{FEM} \, \Delta T_{FEM}} \tag{281}$$

The subscripts FEM in equations (280) and (281) denote the values of modulus, E, linear coefficient of thermal expansion (LCTE), α, and temperature increment from the stress or strain-free temperature, ΔT, used in an elastic finite element analysis. The constants $K_{ij}(x_k)$ and $K'_{ij}(xk)$ are, respectively, the stresses and strains at the point x_k obtained from elastic finite element analysis using E_{FEM}, α_{FEM} and ΔT_{FEM} as input. The constants K_{ij} and K'_{ij} incorporate the effects of motor geometry and the material properties of the case, insulation, and liner. They also depend on the ratio of case to propellant modulus. These latter properties, if taken to be an average of the properties over the temperature range of interest, introduce only small

errors in equations (280) and (281) due to their own viscoelastic behavior. Also, to ensure the validity of equations (280) and (281), Poisson's ratio of the propellant, ν_p, must be time-independent; that is, the bulk response of the propellant must be nearly elastic, which is the typical assumption made in stress analysis of propellant grains. Equations (280) and (281) also assume that the propellant LCTE is a constant; however, they are equally valid if α_p is a function of temperature.

Four stress predictions were made for the 0.75-in. bore structural analog involving four different approximations to E_{eff}. The first involved simply replacing the elastic modulus by the relaxation modulus at the appropriate time and temperature; that is,

$$E \longrightarrow E_{rel} \; (t/A_T)$$

A comparison with measured stresses is shown in Figures 165 and 166 without all points connected. As in the case of the elastic analyses, the results agree well with the long term relaxation behavior, but are low by a factor of 2 to 3 during transient temperatures.

The next set of predictions were made using linear viscoelasticity theory:

$$E \longrightarrow E_{eff}(t) = E_e + \frac{1}{t}\int_0^t \Delta E(\xi - \xi') \; d\tau \qquad (282)$$

$$\xi - \xi' = \int_\tau^t \frac{dx}{A_T \; [T(x)]} \qquad (283)$$

Results for this prediction are shown in Figures 167 through 170. Again, the agreement is not too discouraging during relaxation periods, and the last temperature excursion but are low by a factor of two during the early transient thermal conditions. The agreement during the last cycling may be the
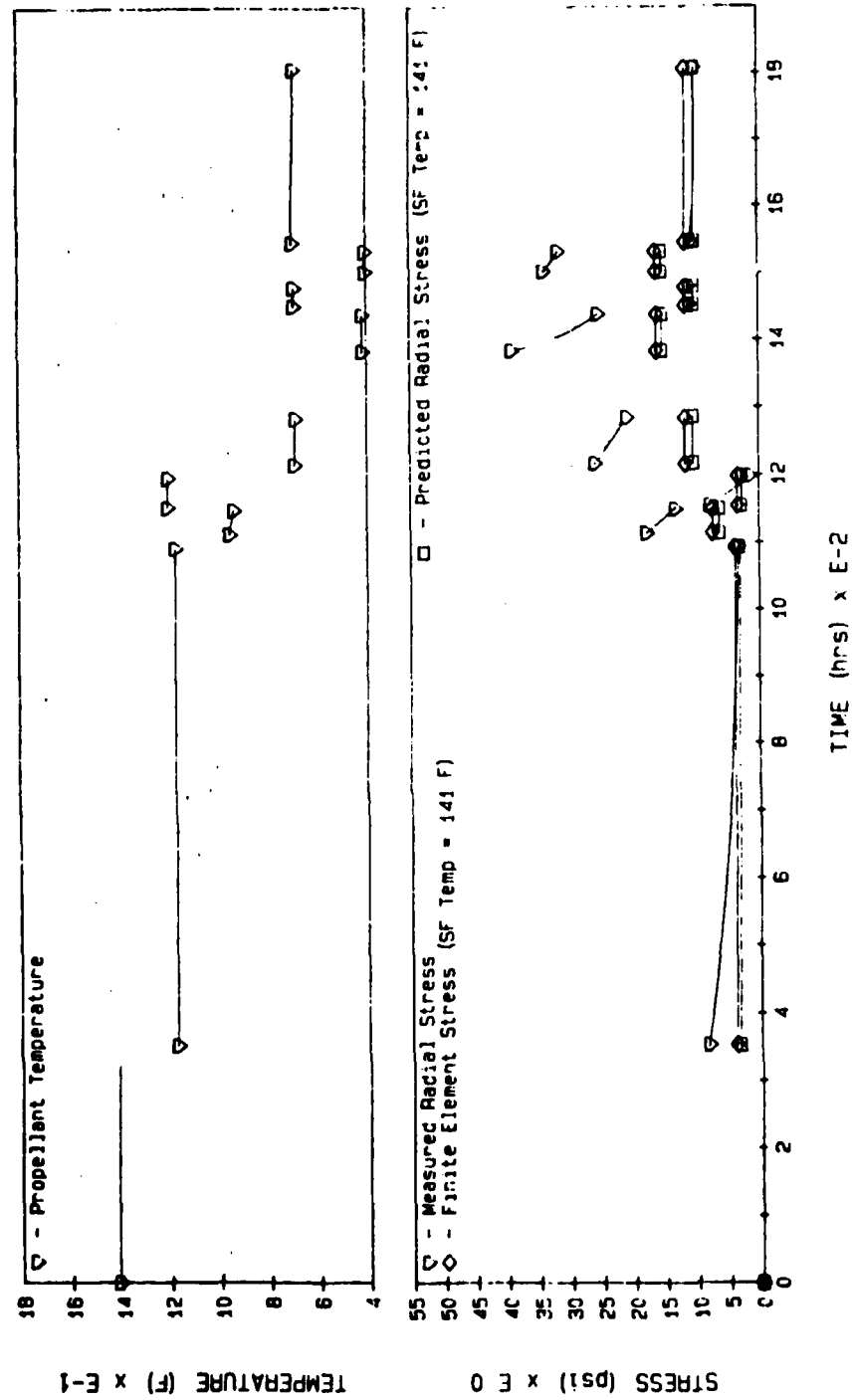
Figure 165. Viscoelastic Stress Predictions for UTP-19,360B-400/1777

31065
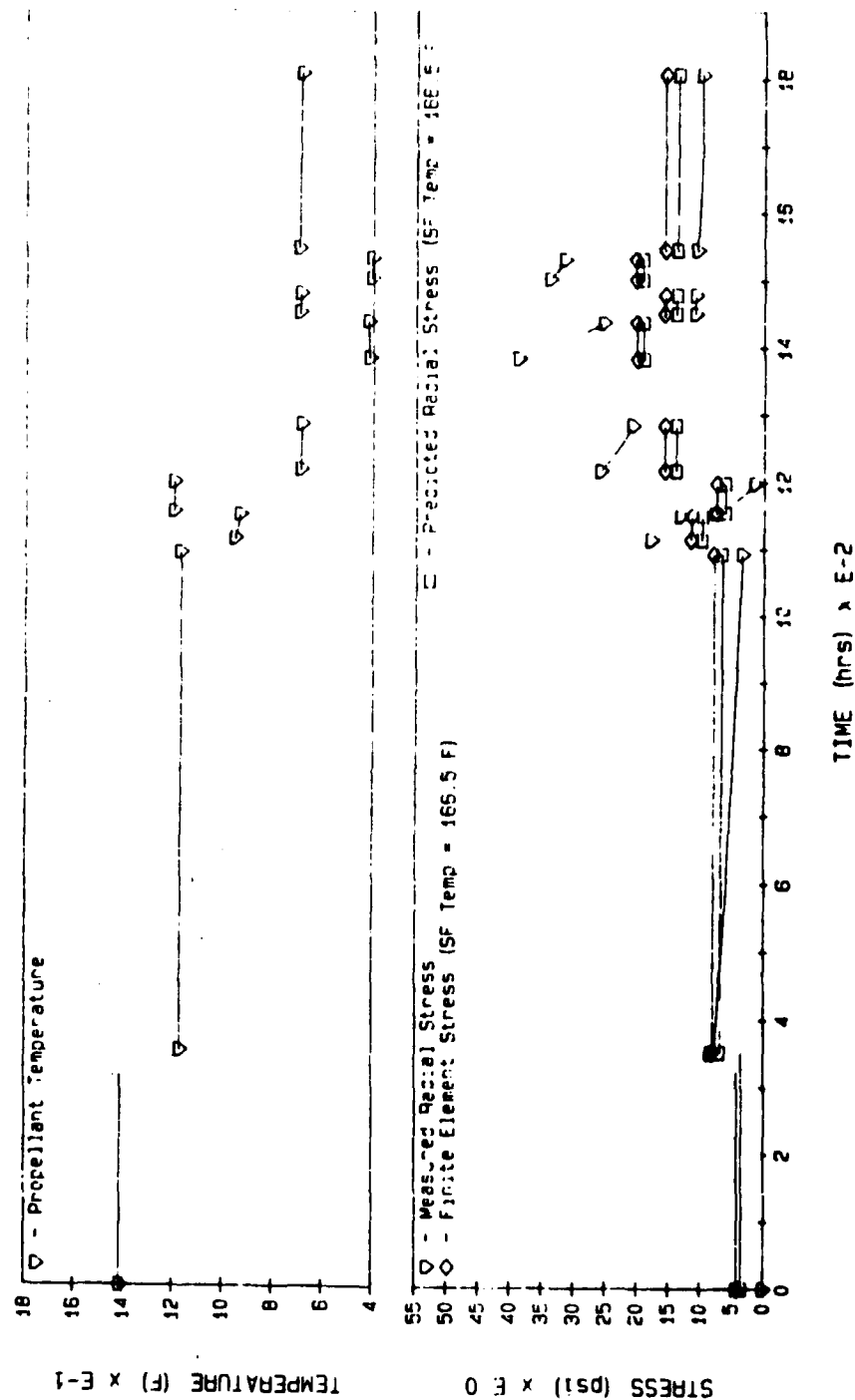
Figure 166. Viscoelastic Stress Predictions for UTP-19,360B-400/1777

31066

293
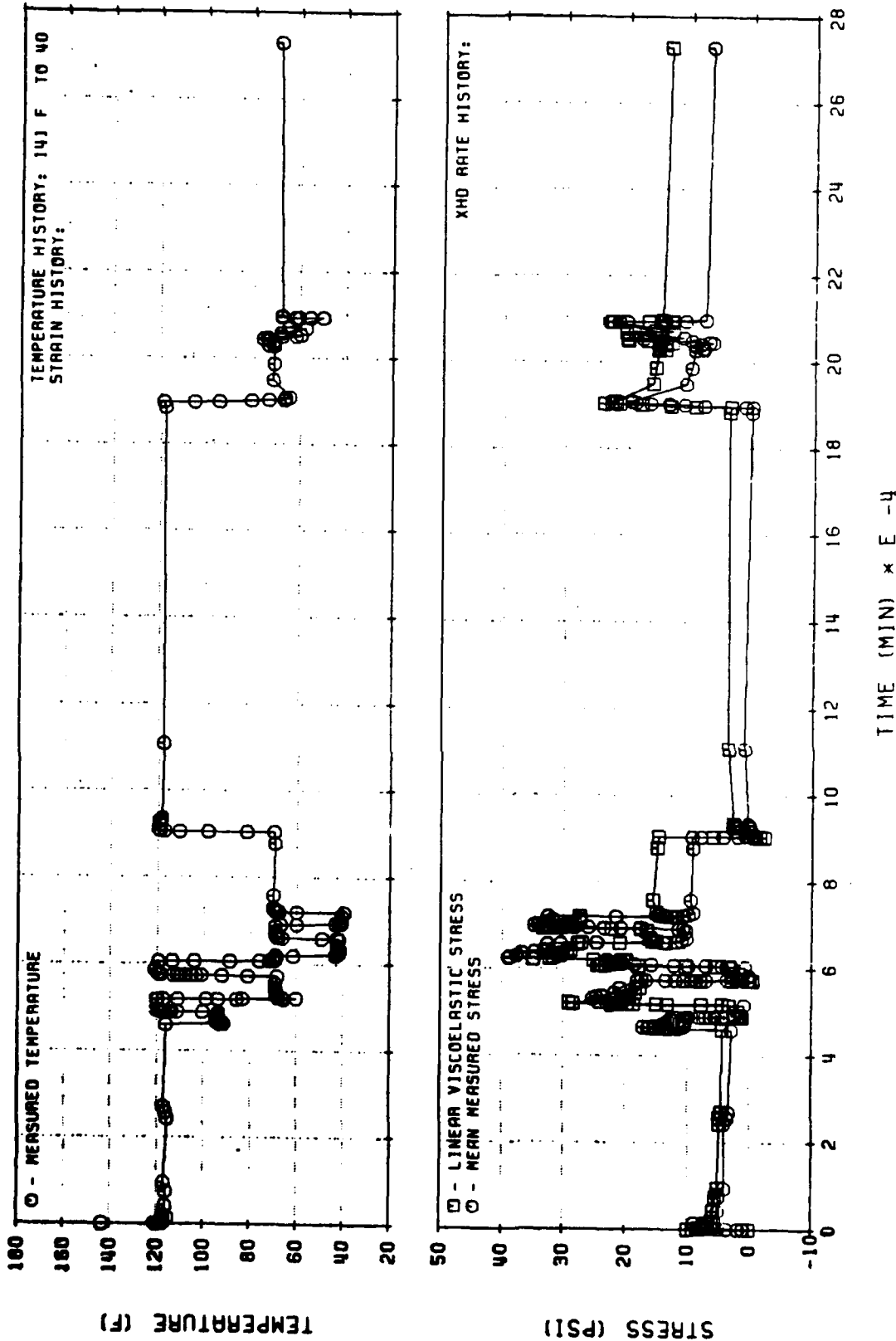
Figure 167. Linear Viscoelastic Stress Predictions for UTP-19,360B-400/1777 Subscale Motor Thermal Cycling (C-510)

294
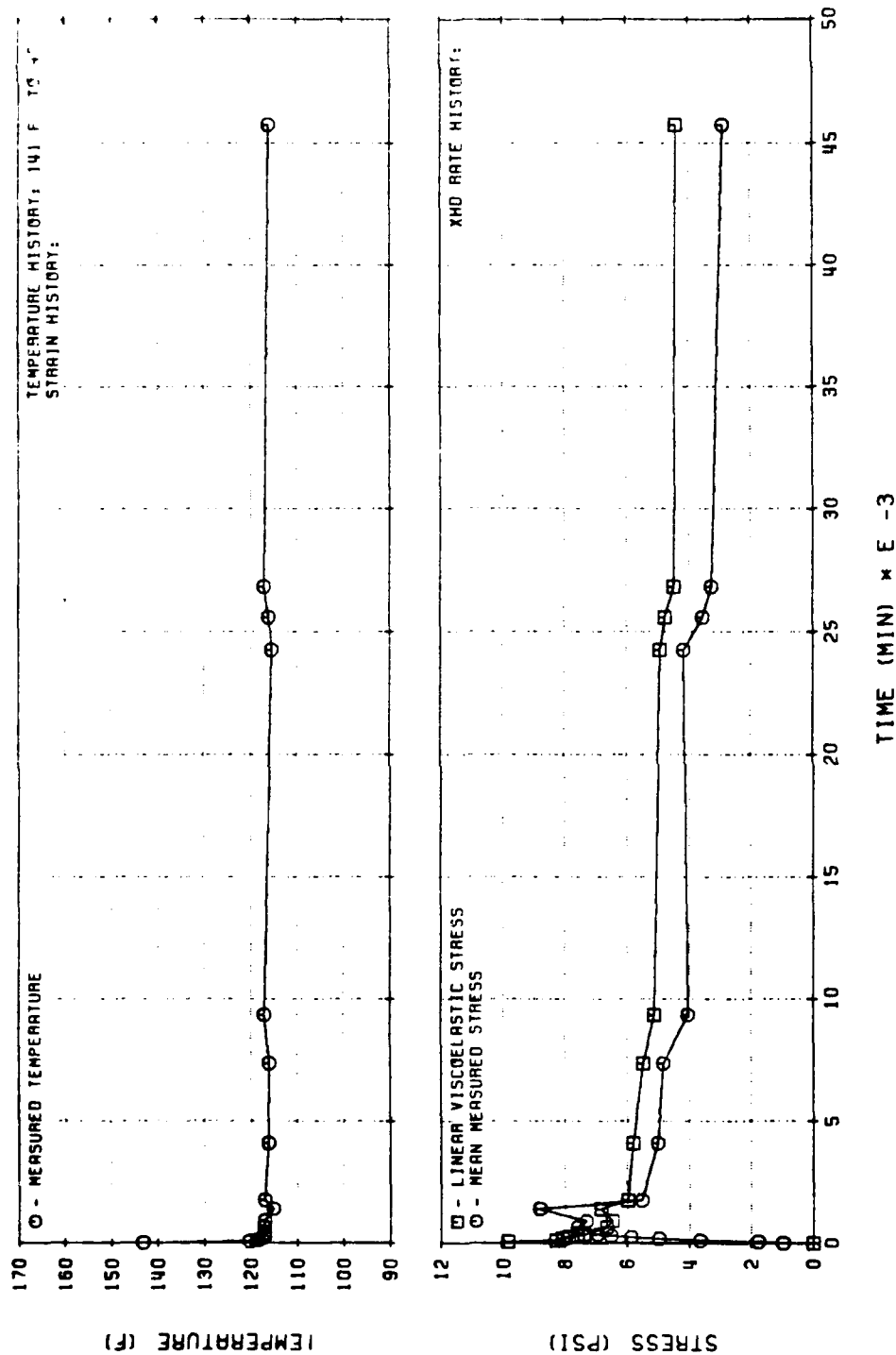
Figure 168. Linear Viscoelastic Stress Predictions for UTP-19,360B-400/1777 Subscale Motor Thermal Cycling (C-510)

295
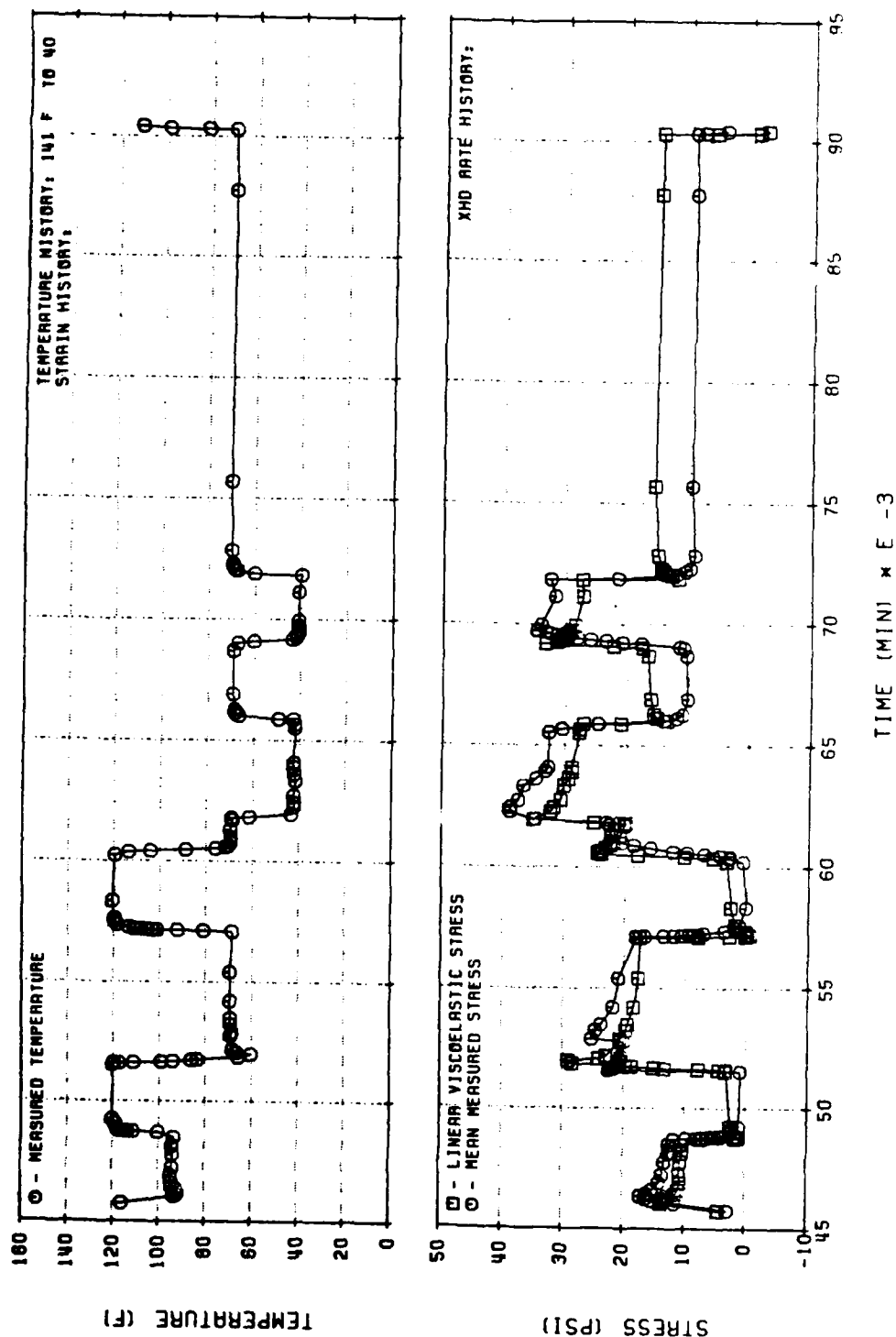
Figure 169.   Linear Viscoelastic Stress Predictions for UTP-19,360B-400/1777 Subscale Motor Thermal Cycling (C-510)

296
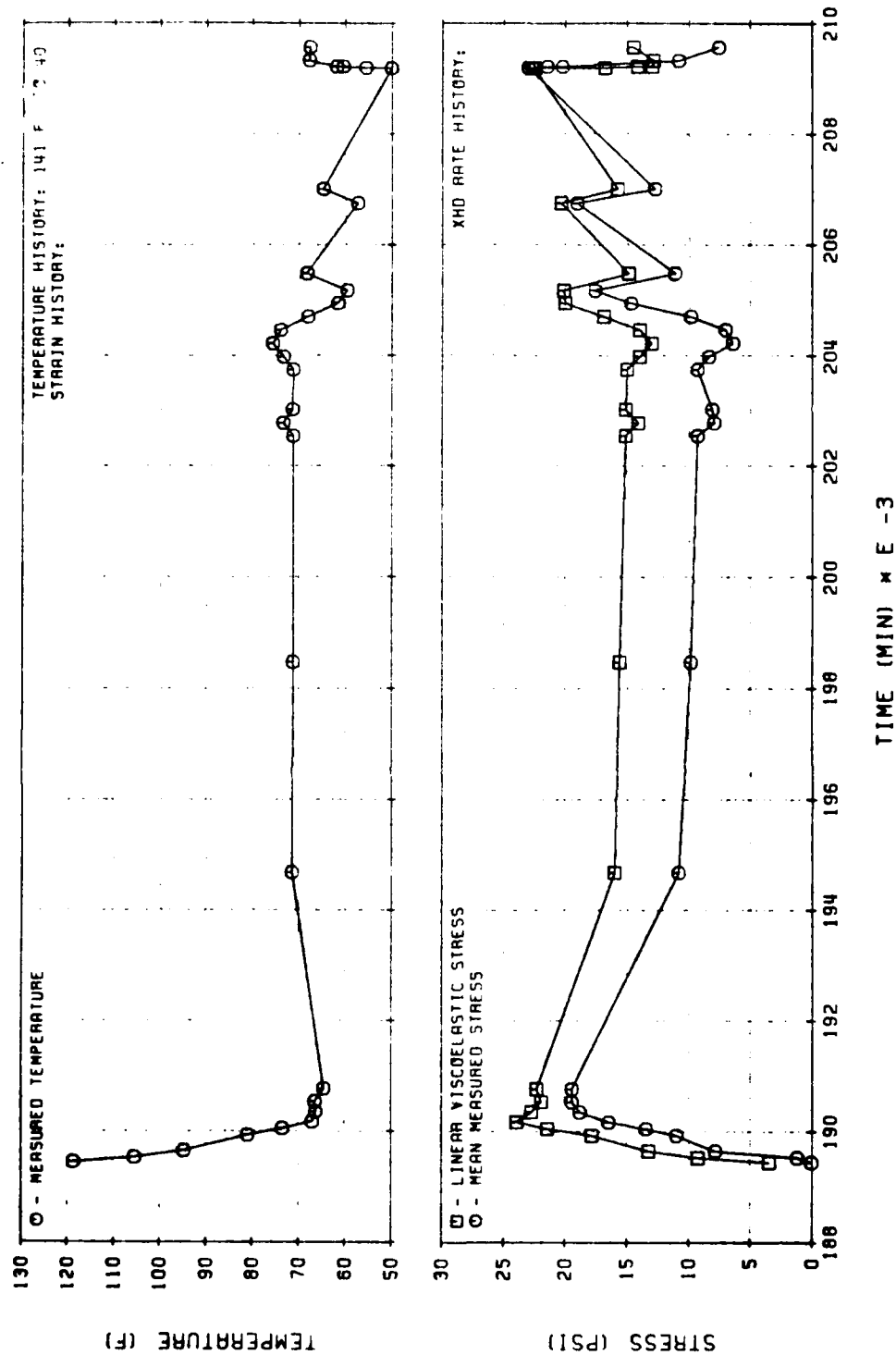
Figure 170. Linear Viscoelastic Stress Predictions for UTP-19,360B-400/1777 Subscale Motor Thermal Cycling (C-510)

31070

297

result of either one or a combination of two observations. First, the last temperature excursion was to approximately 40 F. The motor had previously been subjected to two temperature excursions below 40 F. Much industry work has shown that solid propellants, when reloaded to a lower strain level after being subjected to a prior loading history, display essentially linear viscoelastic responses. Hence, the propellant could be in a state of near-constant damage, and its behavior approximates that of a linear viscoelastic material. On the other hand, the agreement could be the fortuitous result of a shift in the stress-free temperature from 141 F to a temperature closer to 105 F. Immediately prior to the last temperature excursion, the analogs had been stored at 105 F for nearly 70 days. This time is sufficient to cause a shift in the stress-free temperature to the storage temperature. The result is that stresses would be lower on subsequent temperature excursions, but linear viscoelastic predictions would be incorrect since they are based on too high of a stress-free temperature. If one corrects this probable event, then the viscoelastic stress predictions are decreased by about 40%; which would then bring the error in line with the error for the previous thermal excursions.

Several predictions were made using the simple modification to linear viscoelasticity theory of incorporating a thermomechanical coupling coefficient (A_f) into the equations for linear viscoelasticity. The general procedure, as described in section 4.2.3 assumes that

$$A_f = A_f(t)$$

and

$$\sigma(t) = \int_0^t E_{rel}\ (\xi - \xi')\ \frac{\partial}{\partial \tau}\ \left\{ A_F\ (\epsilon - \alpha \Delta T) \right\}\ d\tau \qquad (284)$$

Under simplifying assumptions, however, assuming that A_f = constant, equation (284) can be written

$$\sigma(t) = E_e\ (\epsilon - \alpha \Delta \tau) + A_F \int_0^t \Delta E(\xi - \xi')\ \frac{\partial}{\partial \tau}\ (\epsilon - \alpha \Delta \tau)\ d\tau \qquad (285)$$

298

Based on the experimental results discussed in section 4.2.3 for the 0.004 in./min and 0.0002 in./min uniaxial straining and cooling tests, A_f varied between 2.0 and 3.1. A constant $A_f = 2.56$ was used for both the transient cooling-straining portion of the loading as well as the constant temperature relaxation. This led to the results shown in Figure 171. Although the transient behavior is predicted reasonably well, the relaxation behavior is over predicted by 50% or more. Thus, the attempt to use a constant A_f does not work well in this case.

5.3 LINEAR VISCOELASTICITY PREDICTION PROCEDURES

Linear viscoelastic stress predictions were made using the model given in equation (19) in section 4.2.1. The material characterization for uniaxial iso-thermal test history predictions involved fitting the master relaxation and time-temperature shift curves. The relaxation modulus curve was fit to the exponential series:

$$E(t) = G_{eq} + \sum_{i=1}^{m} G_i e^{-\alpha_i t} \tag{286}$$

where G_{eq} is the equilibrium modulus and G_i and α_i are curve fit constants. The equilibrium modulus and reduced time-modulus pairs were picked from the master relaxation modulus curve. The series exponents, α_i's, were chosen as

$$\alpha_i = 1/t_i \tag{287}$$

The constants, E_i were taken as the solution to the system of simultaneous linear equations

$$E(t_j) - G_{eq} = \sum_{i=1}^{m} G_i e^{-\alpha_i t_j}, \quad j = 1,m \tag{288}$$
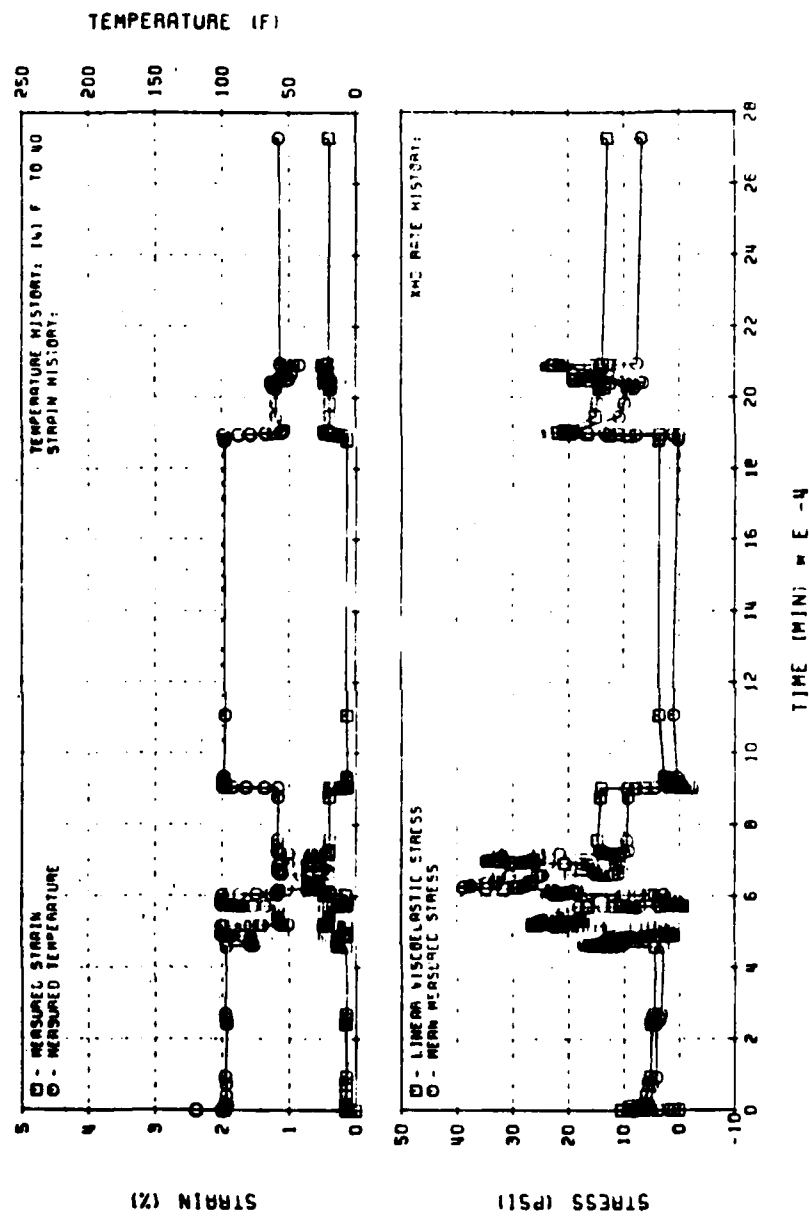
Figure 171. Linear Viscoelastic Stress Predictions for UTP-19,360B-400/1777
Subscale Motor Thermal Cycling (C-510)

300

The time-temperature shift function, A_T, was fit to

$$A_T = \left(\frac{T_R - T_a}{T - T_a} \right)^m \tag{289}$$

where T_R was the reference temperature and T_a and m were fit constants. From temperature ΔT pairs taken from the A_T curve, T_a and m were determined using Powell's algorithm which minimizes the error function

$$F(T) = \sum_{i=1}^{n} \left[A_{T_i} - \left(\frac{T_R - T_a}{T_i - T_a} \right)^m \right]^2 \tag{290}$$

Predictions for biaxial samples were done by applying a correction to the uniaxial modulus or utilizing the biaxial relaxation modulus. For UTP-19,360B propellant, the biaxial modulus was taken as

$$E(t)_{biaxial} = 4/3 * E(t)_{uniaxial} \tag{291}$$

where 4/3 is the ratio of the biaxial to uniaxial modulus. UTP-3001 propellant biaxial samples were predicted by fitting the master biaxial relaxation curve to the exponential series described above. In both cases the time-temperature shift function used was the same previously utilized for uniaxial predictions.

For predictions involving transient temperature test histories, the linear viscoelastic stress was expressed as

$$\sigma(t) = \int_{0}^{t} G_{eq} + A_f (\Delta T) \sum_{i=1}^{m} G_i e^{-\alpha_i(t'-T')} \frac{d\epsilon}{dT} \, dT \tag{292}$$

301

where A_f is the thermo-mechanical coupling factor. A_f was determined from uniaxial straining while cooling tests as

$$A_f (\Delta T) = \frac{\sigma_{meas}(t) - G_{eq} \epsilon (t)}{\int_0^t \sum_{i=1}^m G_i e^{-\alpha_i (t' - T')}} \tag{293}$$

The ΔT-A_f function was represented in a discreet point form, where values for A_f were determined by interpolation.

5.4 MOTOR STRESS PREDICTIONS WITH SWANSON CONSTITUTIVE THEORY

Equation (265) was applied to predicting the stress response of the 0.75-in. bore analog. Since equation (265) is formulated in terms of the second invariant of the deviatoric stress and strain tensors, and since only the radial component of the bond stress is measured, it is necessary to use analytical or finite element analysis results either to modify the measured stress or to solve the predicted deviatoric stress for the radial component of stress. In this case we have chosen to do the former.

The softening function g also requires special attention when determining it for the induced motor strain history. In this case, the procedure followed was to use a volume averaged deviatoric strain; that is,

$$\overline{B} = \frac{1}{V} \int_V^B dV \tag{294}$$

Since we treat propellant as nearly incompressible, and since the stress state at the case wall at the midplane of a motor is nearly equal triaxial tension, the principal components of the deviatoric strain tensor (i.e., B_{11}', B_{22}', B_{33}') are zero. II_B' is also zero. To apply the modified Swanson's theory correctly in this situation one must make use of a volumetric or bulk response constitutive relation. In this application, however, a simple ad hoc approach was used in an attempt to predict the radial bond stress in the analog motors.

302

Since the stress state at the bore surface is nearly a 2:1 biaxial stress state, II_R' was evaluated at the bore surface and used as the strain history input. The relationship between σ_r at the case wall and $II\sigma'$ at the bore surface was then used to calculate the predicted radial bond stress.

Predicted stresses are shown in Figures 172 and 173. While the procedures have many approximations, the resulting agreement is, perhaps, better than should be expected.

5.5 SWANSON THEORY PREDICTION TECHNIQUES

Swanson's constitutive theory stress predictions were made using the model given in equation (17). Characterization of the material involved defining the softening function and viscoelastic function parameters.

The softening function, $g(\epsilon, \dot{\epsilon})$, for virgin loading has the form:

$$g(\epsilon, \dot{\epsilon}) = A \left[\epsilon\right]^B e^{-C\epsilon} \tag{295}$$

where A, B, and C are fit constants. From constant strain rate uniaxial test data, the softening function curve for individual strain rates were determined as

$$g(\epsilon, \dot{\epsilon}) = \frac{\sigma_{meas}(t)}{f(t)} \tag{296}$$

For each curve, A, B, and C were determined using Powell's algorithm, which minimizes the error function

$$F(\epsilon, \dot{\epsilon}) = \sum_{i=1}^{n} \left[g(\epsilon_i, \epsilon) - A(\epsilon_i)^B e^{-C\epsilon_i} \right]^2 \tag{297}$$

303
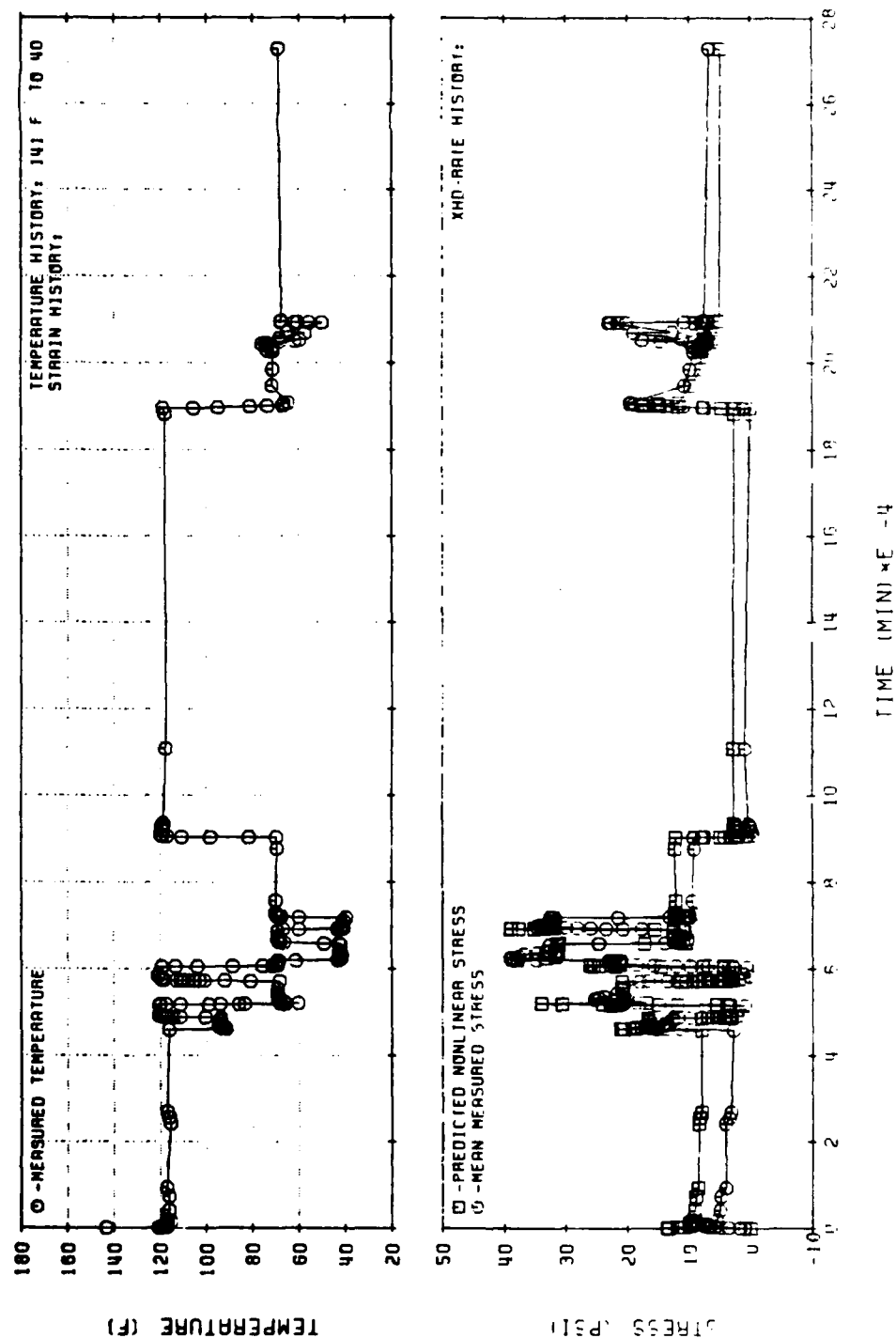
Figure 172. Swanson Theory Stress Predictions for UTP-19,360B-400/1777 Subscale Motor Thermal Cycling (C-510)

31072

304
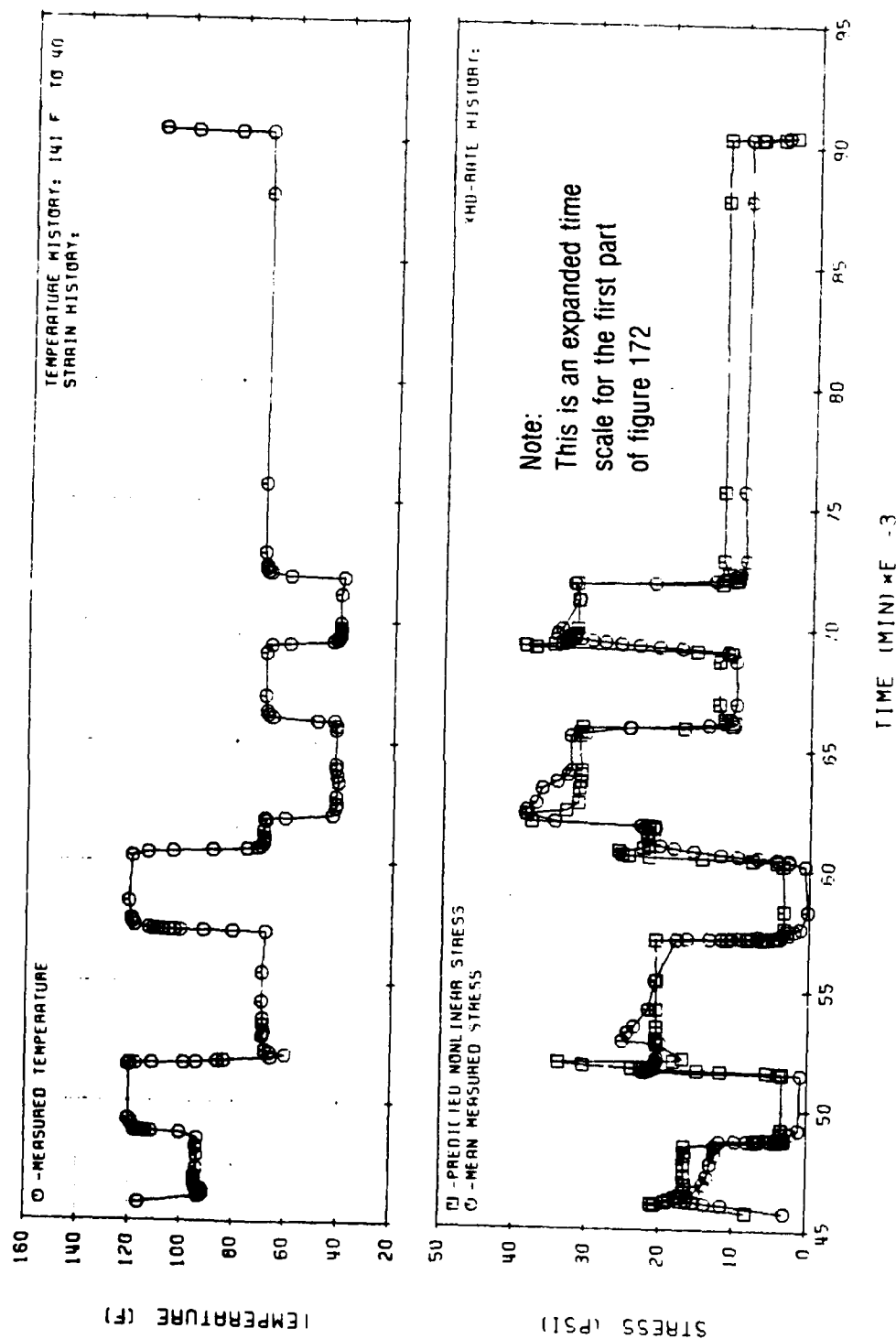
Figure 173. Swanson Theory Stress Predictions for UTP-19,360B-400/1777 Subscale Motor Thermal Cycling (C-510)

305

For predictions made at intermediate strain rates, values for A, B, and C were obtained by interpolation.

The softening functions for relaxation and unloading were expressed as

$$g(\epsilon, \dot{\epsilon}) = \gamma(\Delta t) \star \hat{g}(\epsilon(t_0), \dot{\epsilon}) \qquad (298)$$

and

$$g(\epsilon, \dot{\epsilon}) = \gamma(\epsilon_{rel}) \star \hat{g}(\epsilon(t_0), \dot{\epsilon}) \qquad (299)$$

respectively. $\hat{g}(\epsilon(t_0))$ is defined as the softening function value at the beginning of relaxation or unloading. Δt, and ϵ_{rel} are given by

$$\Delta t = t - t_0 \qquad (300)$$

and

$$\epsilon_{rel} = \epsilon(t)/\epsilon(t_0) \qquad (301)$$

The gamma functions curves were determined from load-relaxation and load-unload test histories as

$$\gamma = \frac{\sigma_{meas}(t)}{\hat{g}(\epsilon(t_0), \dot{\epsilon}) \star f(t)} \qquad (302)$$

The curves were expressed in a discrete point manner, where values were obtained by interpolation.

For relaxation after partial unloading or during rest periods, the softening function was expressed as

$$g(\epsilon, \dot{\epsilon}) = \frac{\hat{g}(\epsilon(t_0), \dot{\epsilon})}{\gamma(\Delta t)} \qquad (303)$$

The softening function for reloading was taken as a linear function of relative strain. The relative strain is given by

$$\epsilon_{rel} = \frac{\epsilon(t) - \epsilon_{min}}{\epsilon_{max} - \epsilon_{min}} \qquad (304)$$

where ϵ_{min} is the minimum strain of unloading and ϵ_{max} is the maximum strain of the previous loading. The softening function is expressed as

$$g(\epsilon, \overset{\circ}{\epsilon}) = \left[\gamma_{unload} + \left[\theta - \gamma_{unload} \right] * \epsilon_{rel} \right] \times \hat{g}(\epsilon(t_0)\dot{\epsilon}) \qquad (305)$$

where γ_{unload} is the gamma function at the end of unloading and θ is the ratio of reloaded to virgin stress.

The viscoelastic function is given by equation (292). The shear relaxation modulus, $G(t)$, is defined as

$$G(t) = E(t)/3 \qquad (306)$$

where $E(t)$ is the uniaxial relaxation modulus. The uniaxial relaxation modulus was expressed in the exponential series form described in section 5.3. The time-temperature shift function, A_T, was expressed and determined in the manner described in the same section.

307

Where stress predictions involved transient temperature test histories, the thermomechanical coupling factor, A_F, was used in equation (292) as

$$\sigma(t) = A_F (\Delta T) \cdot g(\epsilon, \dot{\epsilon}) \cdot f(t) \tag{307}$$

A_F was determined from uniaxial straining while cooling tests as

$$A_F (\Delta T) = \frac{\sigma_{meas}(t)}{g(\epsilon, \dot{\epsilon}) \cdot f(t)} \tag{308}$$

For UTP-19,360 propellant, A_F was found to be a constant equal to 2.26.

5.5.1 3D Analysis Evaluation

The only 3D application of the modified Swanson theory on this program was an instrumented test vehicle subjected to a complex thermal-mechanical load history. This test was selected because it represented the most difficult condition for predictive stress analysis. Other simpler 3D tests such as triaxial poker chips or tension-torsion of thin-walled tubes may have been easier to analytically model but would not provide a realistic check for rocket motor applications. The selected 3D applications highlighted some specific applications problems generated by the stress/strain axiality and amplitude variations between the bore and bond area and the corresponding variation in strain and strain rate history throughout the grain. These could be automatically accounted for in a nonlinear finite element code if the theory were incorporated. However, this application had to approximate these variations using an effective stress-strain axiality, stress-strain amplitude, and equivalent loading history to account for the material nonlinearities. Even with these approximations the modified Swanson theory followed all of the measured stress changes much better than linear viscoelasticity. The predicted peak stresses were above the measured peaks, but the predicted values were in agreement with motor stresses during the hold period.

The measured stresses also reflected the actual thermal gradients in the grain which had to be neglected in the predictive analysis. If the grains could have physically changed temperature more rapidly, then the measured peak stresses would be higher and in better agreement with the predictions. When the analytic approximations required for the analysis are considered, the predictive stresses are considered in reasonable agreement with the stress measurements. These analytical limitations would be eliminated if the modified Swanson theory were incorporated into a nonlinear viscoelastic finite element code.

REFERENCES

1. Solid Propellant Mechanical Behavior Manual, CPIA Publication No. 21, Section 4.3.2.

2. Jones, J., "Solid Propellant Structural Integrity Investigations: Dynamic Response and Failure Mechanisms in Solid Propellants," RPL-TDR-64-32, Vol. I, Lockheed Propulsion Co., February 1964.

3. Francis, E. C. et al., "Predictive Techniques for Failure Mechanisms in Solid Rocket Motors," AFRPL-TR-79-87, Chemical Systems Division, January 1980.

4. Quinlan, M. H., "An Application of the Theory of Materials with Variable Bonding to Solid Propellant," AFRPL-TR-78-37, Air Force Rocket Propulsion Laboratory, June 1979.

5. Farris, R. J., Hermann, L. R., Hutchinson, J. R., and Schapery, R. A., "Development of a Solid Rocket Propellant Nonlinear Viscoelastic Constitutive Theory," AFRPL-TR-75-20, Aerojet Solid Propulsion Co., May 1975.

6. Penny, D. N., "Further Investigations of Permanent Memory Materials," Ph.D. Thesis, University of Utah, June 1975.

7. Ilyushin, A. A., and Pobedrya, B. Ye., "Principles of the Mathematical Theory of Thermoviscoelasticity," FTD Translation FTD-MT-24-9A-71, February 1972.

8. Moskvitin, V. V., "The Strength of Viscoelastic Materials as Applied to Charges of Solid Propellant Rocket Engines," FTD Translation FTD-MT-24-714-73, October 1973.

9. Swanson, S. R., Christensen, L. W., and Christensen, R. J., "A Nonlinear Constitutive Law for High Elongation Propellant," CPIA Publication 331, December 1980, pp. 149-161.

10. Schapery, R. A., "Recent Developments in the Nonlinear Viscoelastic Characterization of Solid Propellant," Lead Article, Solid Rocket Structural Integrity Abstracts, Vol. 8, No. 2, University of Utah, April 1971

11. Quinlan, M. H., "Materials with Variable Bonding," Arch. Rational Mechanics and Analysis, 1978, Vol. 67, pp. 165-181.

12. Farris, R. J. and Fitzgerald, J. E., "Deficiencies of Viscoelastic Theories as Applied to Solid Propellants," Bulletin of the 8th JANNAF Mechanical Behavior Working Group Meeting, CPIA Publication No. 193, Vol. 1, The Johns Hopkins University, March 1970, pp. 163-192.

13. Lindsey, G. H. and Murch, S. A., "On the Mechanical Behavior of Dewettable Solids," Bulletin of the 8th JANNAF Mechanical Behavior Working Group Meeting, CPIA Publication No. 193, Vol. I, The Johns Hopkins University, March 1970, pp. 139-151.

14. Farris, R. J., "Homogeneous Constitutive Equations for Materials with Permanent Memory," Project Thesis Report AFOSR 70-1962TR, University of Utah, June 1970.

15. Fitzgerald, J. E. and Farris, R. J., "Characterization and Analysis Methods for Nonlinear Viscoelastic Materials," Project Thesis Report UTEC TH 70-204, University of Utah, November 1970.

16. Schapery, R. A., "On the Mechanical Behavior of Solid Propellant under Transient Temperatures," section in Texas A & M Report No. MM 3064-783, August 1978.

17. Schapery, R. A., "Application of Viscoelastic Fracture Mechanics to Nonlinear Behavior and Fracture of Solid Propellant," Report No. MM 2995-74-5, Texas A & M University, July 1974.

18. Schapery, R. A., "A Nonlinear Constitutive Theory for Particulate Composites Based on Viscoelastic Fracture Mechanics," Proc. 1974 Combined JANNAF Structures and Mechanical Behavior and Operational Serviceability Working Groups, CPIA Publication No. 253, The Johns Hopkins University, July 1974, pp. 345-355

19. Schapery, R. A., "Studies on the Nonlinear Viscoelastic Behavior of Solid Propellant," Report No. MM 2803-73-2, Texas A & M University, May 1973.

20. Farris, R. J., "The Stress Strain Behavior of Mechanically Degradable Polymers," in Polymer Networks: Structural and Mechanical Properties, edited by A. J. Chompft and S. Newman, Plenum Publishing Co., New York 1971, pp. 341-394.

21. Quinlan, M. H., "On the Theory of Materials with Permanent Memory," Ph.D. Thesis, University of Utah, June 1974.

22. Lee, T. Y., "Permanent Memory and Coupled Thermomechanical Effects in Filled Polymers," Ph.D. Thesis, University of Utah, June 1975.

23. Hufferd, W. L., Fitzgerald, J. E., and Sulijoadikusumo, A. U., "Permanent Memory Effects in Solid Propellants," UTEC CE 73-217, Proc. 1974 Combined JANNAF Structures and Mechanical Behavior and Operational Serviceability Working Groups, CPIA Publication, No. 253, The Johns Hopkins University, July 1974, pp. 371-384.

24. Lepie, A. H. and Adicoff, A., "Energy Balances and Internal Damage of Solid Propellants," Proc. 1974 Combined JANNAF Structures and Mechanical Behavior and Operational Serviceability Working Groups, CPIA Publication No. 253, The Johns Hopkins University, July 1974, pp. 371-384.

25. Blatz, P. J., "A New Theory of Solid Propellant Mechanical Behavior," Proc. 1974 Combined JANNAF Structures and Mechanical Behavior and Operational Serviceability Working Groups, CPIA Publication No. 253, July 1974, pp. 403-426.

26. Gurtin, M., and Francis, E. C., "On a Simple Rate-Independent Model for Damage," Preliminary Report, in CPIA Publication 331, Dec. 1980. pp. 127-133.

27. Mullins,"L. J. Effect of Stretching on the Properties of Rubber," J. Rub. Res., 16, 275-289, 1947.

28. Oberth, A. E., and Brenner, R. S., "Tear Phenomena Around Solid Inclusions In Castable Elastomers," Transaction of the Society of Rheology 912, pp. 165-185 (1965).

29. Farris, R. J., and R. A. Schapery, "Development of a Solid Rocket Propellant Nonlinear Viscoelastic Constitutive Theory," AFRPL-TR-73-50, June 1973.

30. Hermann, L. R., and Peterson, F. E., "A Numerical Procedure for Viscoelastic Stress Analysis," Proc. 7th Mtg. of ICRPG Mech. Beh. Working Group, CPIA Pub No. 177 (1968).

31. Cost, T. L. and Parr, C. H., "Analysis of the Biaxial Strip Test for Polymeric Materials," J. Materials J MLSA, Vol. 4, pp. 312-323, 1969.

32. Francis, E.C., Carlton, C.H., Thompson, R., Fisher, W. M., and D. Gutierrez-Lemini, "Propellant Nonlinear Constitutive Theory Extension: Preliminary Results," AFRPL-TR-83-034, January 1983.

33. Handbook for Engineering Structural Analysis of Solid Propellants, CPIA Publication No. 214, May 1971.

34. JANNAF Solid Propellant Structural Integrity Handbook, CPIA Publication No. 230, September 1972.

Appendix A

MULTISTATION AUTOMATED DATA REDUCTION

INTRODUCTION

Automated handling of multistation tester data is accomplished with a
system of interactive programs on the HP 9825 desk top computer (Figure A-176).
These programs include data acquisition, stress relaxation-master modulus,
straining while cooling or heating, straining to failure, and complex histories.
The acquisition of data and test control are functions of the data acquisition
program which supply data to the data reduction programs. The reduction
programs reduce and output data for a particular type of test history. In
addition, terminal emulating software for the HP 9825 provide a data link for
the transfer of data to the VAX-11 mainframe computer. This makes the data
directly available to the nonlinear constitutive theory programs.

SYSTEM INSTRUMENT CONFIGURATION

The multistation data acquisition instruments are configured to provide
load, crosshead position, temperature and elapsed time data to the data
acquisition program. The system consists of a Hewlett Packard 9825 desk top
computer, 3455 digital voltmeter, 3495 scanner, 98035 programmable clock, and
9885 flexable disk drive (Figure A-177).

The HP 9825 and data acquisition program act as the system controller. The
controller processes incoming test data and crosshead information and responds
by sending instructions to other instruments in the system over an HP-IB inter-
face. Output signals from the tester's load transducers, linear potentiometer,
and analog thermometers are input into the scanner's programmable relay cards.
The scanner's relays under command of the controller can be opened independently
to route output data signals individually to the digital voltmeter where they
are digitized and read by the program. Crosshead control information from
output lines connected to the tester's motor-clutch assembly, is supplied to the
program through the scanner in the same way as the data output signals. These

315

```
                        ┌──────────────┐
                        │    Tester    │
                        │     data     │
                        └──────┬───────┘
                               │
                        ┌──────▼───────┐
                        │Data acquisition│
                        │   program    │
                        └──────┬───────┘
                               │
                        ┌──────▼───────┐
                        │  Temporary   │
                        │   flexible   │
                        │     disk     │
                        │   storage    │
                        │     file     │
                        └──────┬───────┘
```
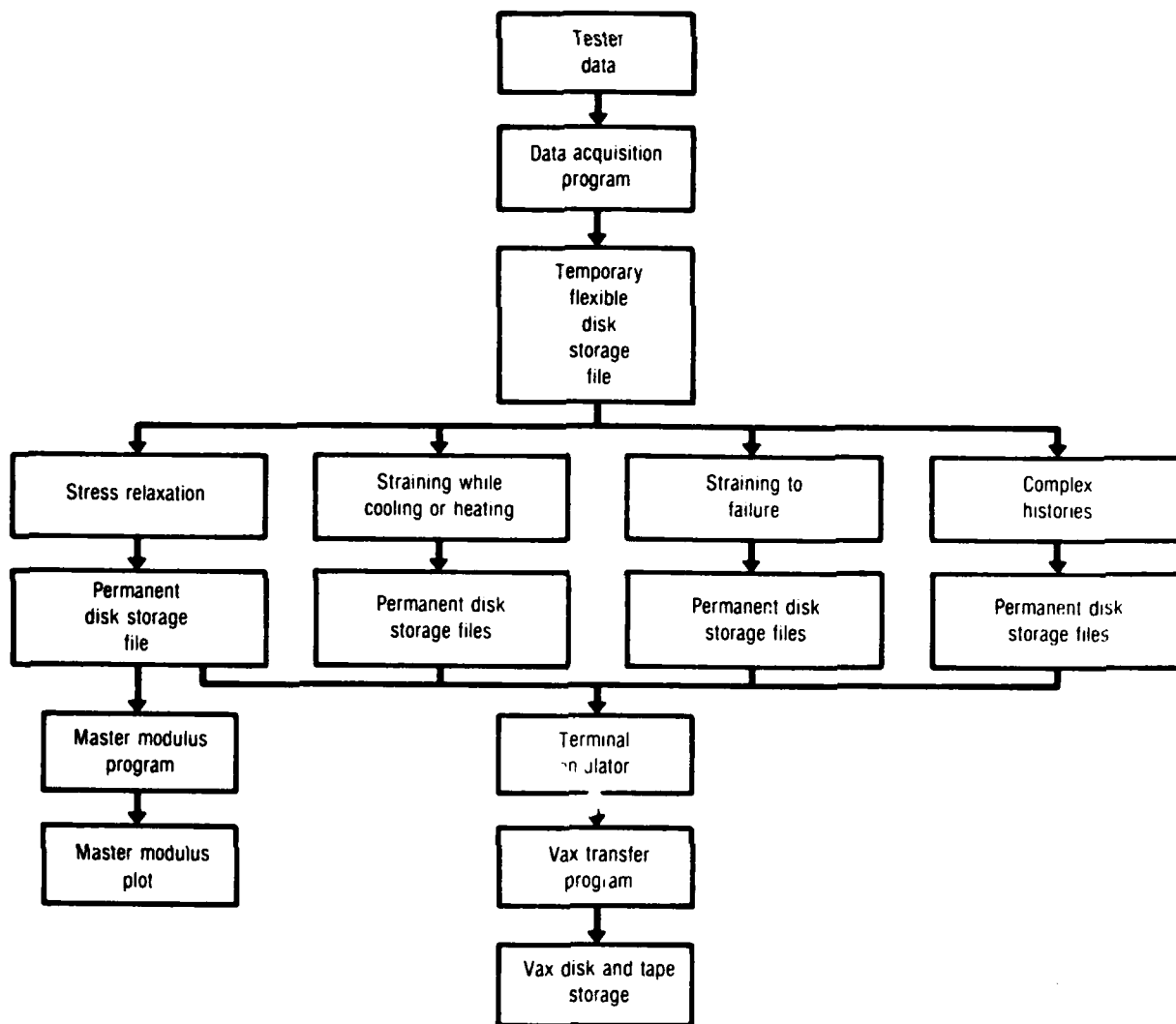
Figure A-176

28842

signals enable the controller to react to changes in crosshead movement and
direction without relying on operator intervention. The programmable clock
connects directly to one of the computer's I/O ports. It provides the program
with elapsed time data and a program interrupt capability for controlling the
rate at which data is taken. The flexible disk drive provides a mass storage
medium where data is stored during testing for latter access by one of the data
reduction programs.

316
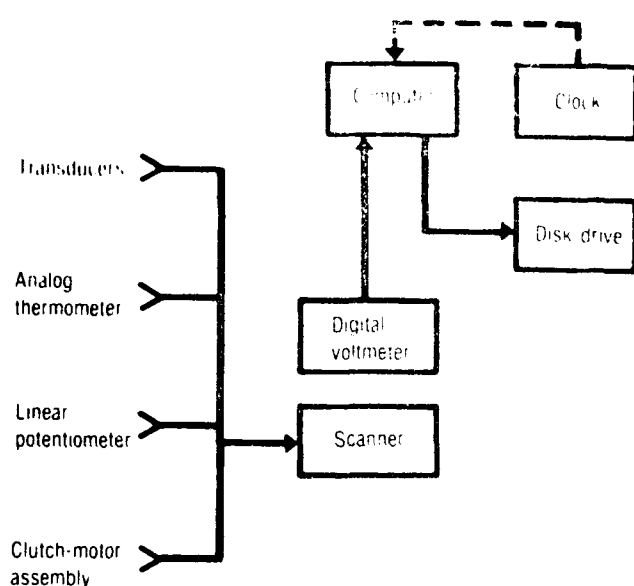
PROGRAMS

Data Acquisition:

As previously stated, the data acquisition program is used to collect data from the multistation tester. Operation of the program involves steps to initialize the program, calibrate the system, and collect and store test data.

Initialization of the program is accomplished by operator entered information used to identify the particular test and define samples being tested. In response to promps from the computer display, the operator inputs descriptions on test material, crosshead rates, strain levels, and temperature levels of the test history. Data input on the test samples include their number, gage length, and individual cross sectional areas, along with their channel locations. In addition, the operator enters pairs of crosshead rates and delta strains for each test interval used to compute sampling rates. The operator also determines how data is taken during relaxation cycles by specifying whether sampling is to be done in a fixed or log time interval.

Calibration of the system is done by an operator-interactive procedure to determine the tester's transducers and potentiometer sensitivities. This involves the operator queuing the program to take readings from the transducers at differing load conditions. By comparing the change in output signals for a known change in load, the lb/volt sensitivity of each transducer may be determined. Similarly, by moving the linear potentiometer probe a known distance its in./volt sensitivity is determined. The analog thermometers are not calibrated at the time of testing. These units output a 10 mv/F representation of the test chamber and internal sample temperature. Calibration on them is done periodically by the CSD electronics laboratory. For short time and isothermal tests, calibration is done once before testing begins. For tests

Figure A-177

28843

317

lasting over a long time period, a second calibration is done when testing is complete to enable compensation for drift in the tester's electronics. Since the load transducers are temperature sensitive, for thermal tests two calibrations must be performed at differing temperatures to determine the change in sensitivity per degree change in temperature.

When calibration is complete, the program stops operation until testing is ready to begin. On a queue from the operator, zero load and position data is taken and the system's instruments programmed to their initial conditions. The clock interupt period is set for a sampling rate determined from the initial crosshead rate and delta strain information. Scanner relays are also arranged to monitor the tester's break input voltage.

The program monitors the break voltage until detecting the break has disengaged which signifies crosshead motion. The clock's counter and interupt units are then started. Interupt signals are output by the clock at the set sampling rate until changed by the program at the end of the straining interval.

When interupt instructions are received from the clock, program operation branches to a data collection subroutine. The voltmeter and scanner are set to read output signals from each of the transducer, potentiometer, and thermometer channels. Fifty milliseconds are required to read each channel. Elapsed time, read from the clock counter, is taken as the mean time over which the data set was read. The test data is retained in a memory buffer until transferred to a disk storage file.

The program continues to monitor the crosshead break and clock information channels throughout the test. When a change in crosshead motion is detected, the clock interrupt is stopped. From the test description data corresponding to the test interval, a sampling rate is determined and the clock reset. For log time interval samplings, the clock interrupt unit is stopped after each reading and the rate doubled.

Up to 600 data sets may be retained in the computer's memory at one time. Data is transferred to the disk either between data set samplings, if time allows, or when testing is complete.

Data Reduction Programs:

The reduction programs reduce and output multistation data pertinent to particular types of test histories. The programs are stress relaxation-master modulus, straining while cooling or heating, straining to failure and complex histories. A description of the strain and temperature histories relevant to each is listed in Table A-15.

Test identification, calibration, load, sample extension, thermal, and time data are supplied to the programs from the acquisition data files or entered directly by the operator. In addition, relaxation cathetometer strain measurements and the thermal expansion coefficient may be optionally entered.

Each program reduces stress, strain, modulus, temperature, and elapsed time data when applicable. The method by which each is determined depends on the test history and amount of information available to the program.
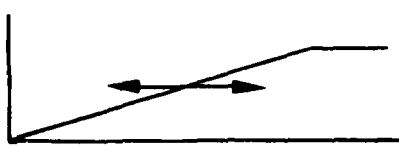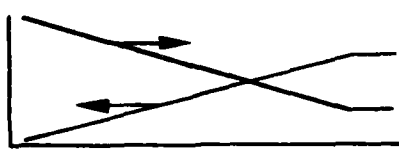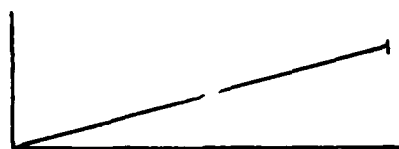
Calibration sensitivity (S) of the transducer and potentiometer are determined in general by

$$S = load/(load\ output-zero\ load\ output)$$

where load is the transducer calibration weight or potentiometer probe displacement. For tests where multiple calibrations were performed, the sensitivities at time t are corrected for electrical drift and thermal variations with the linear relationships

$$S(t) = S_{initial} + \frac{(S_{final} - S_{initial})}{X_{final} - X_{initial}} X\ (t)$$

319

TABLE A-15

Program	Test Strain History	Output
1. Stress relaxation		Tabular - time, modulus Graphic - modulus vs time
2. Straining while cooling or heating		Tabular - time, strain, temperature, stress Graphic - stress vs time and temperature
3. Straining to failure		Test History - Tabular - time, strain and stress Graphic - stress vs time and straining Mech Properties Tabular - initial modulus, maximum stress and strain - corrected stress and strain - rupture strain
4. Complex histories	Combination of straining, relaxation and temperature intervals	Tabular - time, strain temperature and stress Graphic - stress vs time and strain and temperature vs time

where X is time for isothermal and temperature for nonisothermal tests.
Temperature corrections are not made on the potentiometer sensitivity since it
is located outside the environmental test chamber.

Zero load outputs (ZO) for the transducers are also corrected for
electrical drift and thermal variation by the same method as the sensitivities.

320

Corrections on the zero position output of the potentiometer cannot be made
since the crosshead can't be accurately returned to its initial position.

Sample stresses (σ) at time t are calculated by

$$\sigma(t) = [\text{transducer output} - ZO\,(t)]\ S(t)/\text{cross-sectional area}$$

Sample strain (ϵ) at time t is determined by

$$\epsilon(t) = [\text{pot output} - ZO]\ S(t)/\text{gage length}$$

For nonisothermal tests a strain correction may be applied using the thermal
expansion coefficient (α). In this case, the total sample strain becomes

$$\epsilon(t) = \text{mechanical strain} + [T(t) - T_{initial}]\ \alpha/\text{gage length}$$

An additional correction for effective gage length may be made using cathe-
tometer measurements of actual sample strains. The correction factor is
determined as the ratio of the mean intervals in the test history. For
histories where multiple cathetometer measurements were made, the correction
factors are linearized to measured strain between them.

Relaxation and secant modulus (E) at time t is determined by

$$E(t) = \sigma(t)\ \ 1 + \epsilon(t)\ /\epsilon(t)$$

where $\epsilon(t)$ is held constant over relaxation test intervals.

Temperature is reduced from analog thermometer readings by converting the
millivolt output to volts.

Elapsed time is calculated as the difference between when the data was
taken and when initial loading occurred (t_o) since loading times may vary from
sample to sample, t_o is approximated by the time of initial straining.

Once data is reduced, a tabular and graphic summary of the test is output
by each program. A description of the outputs is listed in Table A-15. To

retain data for future reference and reuse, identification, calibration, and raw test data are stored on permanent diskette data files.

Terminal Emulator

The program is used to transfer data between the HP 9825 and VAX-11, desk top and mainframe computers.

A link is created between the computer types utilizing the VAX-11's dial-in lines and an RS-232 interface which connects the 9825 to an acoustic coupler. The emulator software then supplies the capability of using the 9825 as an intelligent terminal through which data may be read from the flexible disks and sent over phone lines to the VAX.

Data transfer is accomplished with a VAX program which reads data sent from the terminal and retains it in storage files for access by the nonlinear theory programs.

SYMBOLS

A_c	microcrack growth rate shift factor
A_F	temperature-dependent material function
A_f	thermomechanical coupling factor
A_{ij}	expansion coefficients of bulk stress in terms of octahedral strains
A_n	constant
A_o	initial area
A_T	temperature shift factor (a_T)
a_η, a^*	(AHETA) damage related shift function
a	half sample width, grain ID radius
a_F	softening function
a_k	constant
a_{np}	expansion coefficients of correction modulus
A_1, A_2, A_3, A_4, A_6, A_i	constants
$2a$	biaxial sample width, grain ID
B	Cauchy-green deformation tensor
B	bulk modulus or a constant
$\bar{B}$	volume average deviatoric strain
B'	deviatoric deformation tensor
B_i	constant
B_{NC}, B_{NT}	Farris constants
B_o	constant
b	constant
$2b$	biaxial sample height (gage length)
$2b$	grain OD

C	softening function
CSD	Chemical Systems Division
C_x	rehealing parameter
C, C_1, C_2, C_i	constants
c	constant
D	damage
D_m, D_5, D_6, D_7 Di	constants
d	constant
E	modulus
E_1	relaxation function in bulk or constant
E_2	relaxation function in shear or constant
E_a	activation energy
E_c	case modulus
E_o	applied strain
E_p	propellant modulus
E_e	equilibrium modulus
E_{eff}	effective modulus
E_R	reference modulus and normalized coefficient for modulus
E_R	relaxation modulus
$E(t)$, $E_{rel}(t)$	linear viscoelastic relaxation modulus
e	product of F and virgin response function g
e_{ij}, e_{ij}^d	deviatoric strain tensor
$E(\xi)$	linear viscoelastic modulus
F	damage function or softening function
F	degrees Fahrenheit

f	force
F	strain magnification factor
$F(t)$	constant rate modulus
$F(\xi, \epsilon_m)$	damage curve at $_m$ damage level
FE	finite element
f_1, f_2	function
f	material parameter
(f)	deformation function
f_c	constant time rate of change of deformation invariant
$f(t)$	viscoelastic type function in kinetic
G	shear modulus
G. L.	gage length
G_c	corrected modulus
G_{eq}	equilibrium modulus
G_i	constant
G_r	relaxation modulus
G_{rel}	shear relaxation modulus
$G(t)$	shear relaxation modulus
g	virgin response function
$g( )$	function of
(g)	strain softening function
g_L	softening function for loading
g_u	softening function for unloading
H	function of damage
h	case thickness
h	function of damage in kinetic equation of evolution

HTPB	hydroxyl-terminated polybutadiene
I_d	volume dilatation
I_n	contribution to stress at time t_n
I	octahedral shear strain
$\| I_\gamma \|_{pi}$	L_p norm
J	creep function
J_1	creep function in bulk
J_2	creep function in shear
JANNAF	Joint Army Navy NASA Air Force
K, K_1-K_{10}	constants
K	temperature-dependent constant
K_I	stress intensity factor
$K_{ij}(x_k)$	stress at point x_k
$K'_{ij}(x_k)$	strain at point x_k
K_x	rehealing parameter
k	constant
L	length
L_x	constant
LCTE	linear coefficient of thermal expansion
M	constant
M_x, M_2, M_4	constants
m	constant
m, m_2, m_4	material parameters
N	number of cycles
N-L	nonlinear
NLCT	nonlinear constitutive theory

n	constant
P	terms of equation under summation
P	hydrostatic pressure
P_2, P_4	constants
P_{15}	used to normalize Y_3 to 1
$\overline{P}_r$	finite length correction factor
PBAN	polybutadiene acrylonitrile
p	constant
Q	terms of equation under summation
q	constant
R	function
R	healing
R_o	lower limit of R (healing)
R_o	strain maximum sensitivity
rms	root mean square
r, r_o	chemical bond radius or rotation
S	virgin stress and damage parameter constant
S	damage parameter
S	damage parameter
S_m	maximum damage
S_o	resultant stress
S_o	constant
S_r	certain measure of damage
S_t-S_τ	temperature-shifted time
S_x	constant
SF	stress free

T	temperature
T	peak stress time
T_a	material property and shift temperature
T_c	motor cure temperature
T_g	glass transition temperature
T_n, T_h	healing temperature
T_o	temperature at $t = 0$
T_o	stress-free temperature
T_R	reference temperature
TCM	thermorheologically complex material
TSM	thermorheologically simple material
t	time
t_n	time
t_n, t_h	healing time
t'	modified time
t_o^*	time to failure under constant load
U	chemical bond stretching rupture
UTP	United Technologies Propellant
V	volume
X_r, x_r	root of Y_3
x	$\equiv \epsilon/\epsilon_m$
x, y, z	coordinate axes
Y_1, Y_1, Y_2, Y_3	functions related to damage
y	$\equiv \epsilon_m$, maximum strain to time τ
α	kinetic constant
α	coefficient of thermal expansion

Symbol	Description
ω	material parameter
$\alpha,\ \alpha_i$	constant
α_c	case coefficient of linear expansion
α_p	propellant coefficient of linear expansion
β	constant
β	parameter
β	changing rate coefficient
γ	constant
γ	shear strain
γ	softening function
γ_a	adhesive failure
γ_c	cohesive failure
ΔE	modulus change
ΔL	change in length
ΔT	temperature change
ΔT_σ	thermal stress
Δv_p	negative volume change with hydrostatic pressure
δ	constant
δ_c	case $\alpha_c\ \Delta T$
δ_{ij}	Kronecker delta
δ_p	propellant $\alpha_p\ \Delta T$
ϵ	strain
$\dot{\epsilon}$	strain rate
ϵ_1	principal strain
ϵ_2	lateral strain
$\epsilon_{11},\ \epsilon_{22},\ \epsilon_{33}$	principal strains

ϵ^0, ϵ^0_r	pseudo strain
ϵ_m, ϵ_{max}	maximum strain
$\epsilon(t)$	strain at time t
ϵ_u	strain of unfilled polymer
ϵ_σ	strain due to mechanical stress
ϵ_θ	bore strain
ζ	neutral rate where damage remains constant
η	compressibility ($\eta = 0$ is incompressibility)
$\eta(t)$	related to damage function
θ	ratio of reload virgin stress
θ	axis
λ	extension ratio $(1 + \epsilon)$
λ	healing correction factor
λ	softening function
λ	width to height ratio
λ_2	grain OD/TD
μ	micron
μ	material parameter
ν	material parameter
ν_c	case Poisson's ratio
ν_p	propellant Poisson's ratio
ξ	reduced time
π	state of bonding
$\dot{\pi}$	rate mechanism underlying damage
π_α	second invariant of tension ($\alpha = \sigma$, β)
Σ	summation

σ	engineering stress or stress
σ	Cauchy-stress tensor
σ_B	bulk stress
σ_b	stress correction due to change in state of bonding
σ_c	stress correction
σ_{ij}^d	deviatoric stress
σ'	deviatoric stress
σ_ℓ	linear viscoelastic stress
σ_o	constant stress
σ_{kk}	bulk stress
σ_r	linear viscoelastic stress
$\sigma_{rr}(b)$	case-grain radial bond stress
$\sigma(t)$	stress at time t
$\sigma_f(t)$	fading memory stress
σ_∞	stress
τ	reduced time
τ	shear stress
τ	shifted time
ϕ	function of loading
ϕ	extension ratio
ϕ_1, ϕ_2	functions
$\dot{\phi}$	rate of loading function
ψ_n	nth component of stress correction
ω	normalized damage function
II_α	second invariant of tensor ($\alpha = \sigma$, B)
$\sqrt{II_B'}$	second invariant of deformation tensor

331

$\sqrt{II_{\sigma'}}$ second invariant of deviatoric stress

$|\cdot|$ denotes absolute value

∞ infinity